AD-A062 933 ROCKWELL INTERNATIONAL ANAHEIM CA ELECTRONICS RESEAR--ETC F/G 20/6
WAVEGUIDE OPTICS FOR COHERENT OPTICAL PROCESSING.(U)
JUN 78 D B ANDERSON , R R AUGUST, S K YAO F33615-77-C-1017

UNCLASSIFIED C77-210.13/501 AFAL-TR-78-83 NL

1 OF 3
AD
AO 62933

(2) LEVEL II

AFAL-TR-78-83

WAVEGUIDE OPTICS FOR COHERENT OPTICAL PROCESSING

D. B. ANDERSON
R. R. AUGUST
S. K. YAO
et. al.

ROCKWELL INTERNATIONAL CORPORATION
ELECTRONICS RESEARCH CENTER
3370 MIRALOMA AVENUE
ANAHEIM, CALIFORNIA 92803

JUNE 1978

TECHNICAL REPORT AFAL-TR-78-83
Final Report – January 1977 - January 1978

AIR FORCE AVIONICS LABORATORY
AIR FORCE WRIGHT AERONAUTICAL LABORATORIES
AIR FORCE SYSTEMS COMMAND
WRIGHT-PATTERSON AIR FORCE BASE, OHIO 45433

NOTICE

When Government drawings, specifications, or other data are used for any purpose other than in connection with a definitely related Government procurement operation, the United States Government thereby incurs no responsibility nor any obligation whatsoever; and the fact that the government may have formulated, furnished, or in any way supplied the said drawings, specifications, or other data, is not to be regarded by implication or otherwise as in any manner licensing the holder or any other person or corporation, or conveying any rights or permission to manufacture, use, or sell any patented invention that may in any way be related thereto.

This report has been reviewed by the Information Office (OI) and is releasable to the National Technical Information Service (NTIS). At NTIS, it will be available to the general public, including foreign nations.

This technical report has been reviewed and is approved for publication.

Michael C. Hamilton

MICHAEL C. HAMILTON
Project Engineer
Electro-Optics Tech & Appl Group

Kenneth R. Hutchinson

KENNETH R. HUTCHINSON, Chief
Electro-Optics Tech & Appl Group
Electronic Technology Division

FOR THE COMMANDER

Ronald F. Paulson

RONALD F. PAULSON, Acting Chief
Electro-Optics Technology Branch
Electronic Technology Division

"If your address has changed, if you wish to be removed from our mailing list, or if the addressee is no longer employed by your organization please notify AFAL/DHO-2 *,W-PAFB, OH 45433 to help us maintain a current mailing list".*

Copies of this report should not be returned unless return is required by security considerations, contractual obligations, or notice on a specific document.

AIR FORCE/56780/18 December 1978 — 75

SECURITY CLASSIFICATION OF THIS PAGE *(When Data Entered)*

REPORT DOCUMENTATION PAGE

READ INSTRUCTIONS BEFORE COMPLETING FORM

1. REPORT NUMBER: AFAL-TR-78-83	2. GOVT ACCESSION NO.
3. RECIPIENT'S CATALOG NUMBER	
4. TITLE (and Subtitle): WAVEGUIDE OPTICS FOR COHERENT OPTICAL PROCESSING.	5. TYPE OF REPORT & PERIOD COVERED: Final Technical Report. 77 Jan. 15 - 78 Jan. 15
6. PERFORMING ORG. REPORT NUMBER: C77-210.13/501	
7. AUTHOR(s): D. B. Anderson, S. K. Yao, V. G. Kreismanis, R. R. August, J. T. Boyd, C. M. Oania, B. R. Youmans	8. CONTRACT OR GRANT NUMBER(s): F33615-77-C-1017
9. PERFORMING ORGANIZATION NAME AND ADDRESS: Rockwell International, ~~Corporation~~ Electronics Research Center, 3370 Miraloma Ave. Anaheim, CA. 92803	10. PROGRAM ELEMENT, PROJECT, TASK AREA & WORK UNIT NUMBERS: 2001-02-53
11. CONTROLLING OFFICE NAME AND ADDRESS: Air Force Avionics Laboratory (DHO) Air Force Wright Aeronautical Laboratories Air Force Systems Command	12. REPORT DATE: June 1978
	13. NUMBER OF PAGES: 238
14. MONITORING AGENCY NAME & ADDRESS *(if different from Controlling Office)*: Wright Patterson ~~Air Force~~ Base; Dayton, OH 45433	15. SECURITY CLASS. *(of this report)*: Unclassified
	15a. DECLASSIFICATION/DOWNGRADING SCHEDULE

16. DISTRIBUTION STATEMENT *(of this Report)*

Approved for public release; distribution unlimited.

DDC RECEIVED JAN 8 1979 B

17. DISTRIBUTION STATEMENT *(of the abstract entered in Block 20, if different from Report)*

18. SUPPLEMENTARY NOTES

19. KEY WORDS *(Continue on reverse side if necessary and identify by block number)*

Thin-Film Waveguide, Generalized Luneburg Lenses, Reflectors, Spatial Filters, Waveguide Fan Out Array, Lens Diffraction Patterns

20. ABSTRACT *(Continue on reverse side if necessary and identify by block number)*

The results of an effort to further improve thin-film waveguide Luneburg lenses for implementation of the optical Fourier transform as may be employed for real-time wideband RF spectrum analysis is delineated. Overlay Ta_2O_5 thin-film waveguide Luneburg lenses on Corning 7059 waveguide on thermally-grown SiO_2 on a silicon substrate were demonstrated achieving the diffraction-limited results. The smallest beamwidth observed is 1.65 microns for an F/4 Luneburg lens design with side lobes below 17 dB decaying to approximately 30 dB.

DD FORM 1 JAN 73 1473 EDITION OF 1 NOV 65 IS OBSOLETE

Unclassified

SECURITY CLASSIFICATION OF THIS PAGE *(When Data Entered)*

A numercial procedure was developed and applied to compute the performance of these lenses using waveguide thickness profile ray traces to determine the ray intercepts in the image plane to provide the wavefront phase error and to determine the resulting intensity diffraction pattern. The procedure allows for introduction of profile errors and provides data for F/1, F/2.5 and F/4.5 lenses. A method to synthesize the edge shape so as to obtain the "true" lens thickness profile has been developed and applied, demonstrating diffraction-limited results. The effort included reduction of waveguide scattering, the creation of a spatial filter, improved reflectors by cleavage, and a waveguide fan-out array.

FOREWORD

This document is the final technical report by Rockwell International Corporation, Electronics Research Center, Anaheim, California, under Air Force Contract #F33615-77-C-1017 under Project 21172. It delineates the effort performed from 15 January 1977 through 15 January 1978. The author's submittal date was March 21, 1978. The Program Manager and Co-Principal Investigator was Mr. D. B. Anderson with Mr. R. R. August as a Co-Principal Investigator and with Mr. R. L. Davis as a Co-Principal Investigator during the first half of this effort. Dr. S. K. Yao and Mr. V. G. Kreismanis became Co-Principal Investigators during the latter half of this effort. Professor J. T. Boyd, University of Cincinnati, served as a consultant.

The contributions of Dr. W. H. Southwell, Rockwell International, Canoga Park, CA, are sincerely appreciated. Application of his computational procedures has greatly simplified and extended the data in an observable format and economical and expeditious fashion. Most of the results in Section II-B-5 are due to Mr. V. G. Kreismanis. Mask synthesis procedure is due to Dr. S. K. Yao. The processing preparation and deposition of various waveguides and lenses are due to Ms. C. M. Oania. The experimental characterization of lens performance and waveguide scattering is largely due to B. R. Youmans and V. G. Kreismanis.

Sincere appreciation is expressed to Mr. R. R. August of the Rockwell Electronics Research Center and to Mr. M. C. Hamilton, Air Force Avionics Laboratory, who jointly recognized and stimulated the application of thermally-oxidized silicon as a substrate for thin-film optical waveguide lenses.

Stimulating discussions with Mr. M. C. Hamilton, AFAL, beyond his duties as the Air Force Project Engineer, are greatly acknowledged.

TABLE OF CONTENTS

TABLE OF CONTENTS (CONT'D)

LIST OF ILLUSTRATIONS

LIST OF ILLUSTRATIONS (CONTINUED)

LIST OF ILLUSTRATIONS (CONTINUED)

LIST OF ILLUSTRATIONS (CONTINUED)

LIST OF ILLUSTRATIONS (CONTINUED)

LIST OF ILLUSTRATIONS (CONTINUED)

LIST OF ILLUSTRATIONS (CONTINUED)

LIST OF ILLUSTRATIONS (CONTINUED)

LIST OF ILLUSTRATIONS (CONTINUED)

LIST OF ILLUSTRATIONS (CONTINUED)

LIST OF ILLUSTRATIONS (CONTINUED)

LIST OF ILLUSTRATIONS (CONTINUED)

I. INTRODUCTION

A. BACKGROUND

The development of electronic integrated circuits and their application to our defense systems have led to increased reliability in life; reduced cost, size and weight; and reduced primary power requirements. The example set by this development has provided the justification for an increasing effort addressed to an integrated optical circuit technology with the expectation of realizing some of the same benefits for coherent optical signal processing, sensors and communication systems while simultaneously providing an increased information-handling capacity.

One important application of integrated optics is in the field of coherent optical signal processing executing the Fourier transform.[1-5] Optical signal processing is admirably suited to perform linear analog operations such as matrix products, the Fourier transform integration and related correlation and convolution.[6-8] The process employs a coherent source, modulation function(s) and the detection function to be performed throughout the signal spatial field with one or more Fourier transform lenses between. The optical signal function is usually performed for a two-dimensional image, whereas, an integrated optics format will limit the processing to a single transverse dimension as a function of time. For an application such as spectral analysis of microwave signals extending over a broad expanse of the spectrum, this one-dimensional characteristic is not a limitation.

The optical Fourier transform applied to spectral analysis of microwave signals is attractive because it provides a real-time, wide-open, continuous response. The schematic diagram of Figure 1 illustrates the essential components of an optical Fourier transform process applied to spectral analysis. Implementation in an integrated optics format of the spectrum analyzer will contain a coherent source (presumably, a DFB (GaAl)As laser[9]) coupled to a thin-film optical waveguide, an assortment of thin-film waveguide lenses[10,11] performing the beam expansion and the transform functions together with a spatial modulator (presumably, a surface elasto-optic Bragg-type interaction[12] within a common thin film) and a waveguide-coupled photodetector array[13] responsive to the laser with a temporal bandwidth encompassing the down-converted microwave signal.

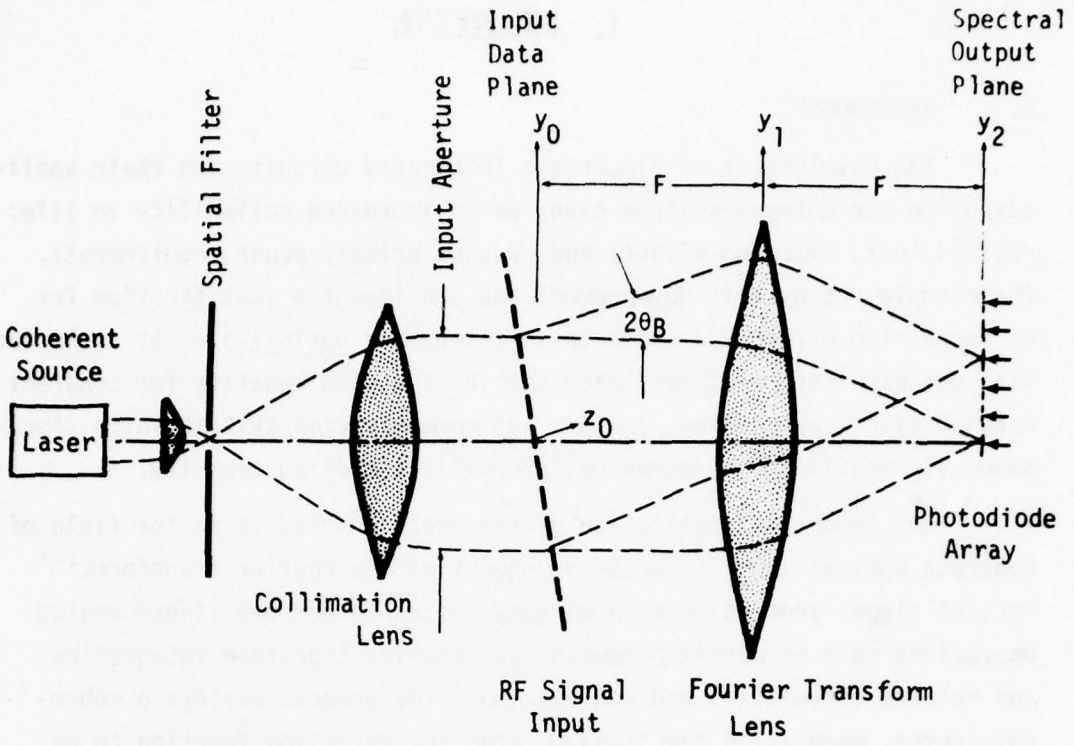

Figure 1. Coherent Optical Fourier Transform Signal Processing Schematic

The microwave signal is temporarily "stored" as a waveform in the spatial modulator which is simultaneously accessed by the optical field and transformed into its spectral components spatially separated by the lens and detector in an array. Use of an integrated optics format for the spectrum analyzer on a single substrate provides the necessary mechanical structure to obtain rigidity between the various optical elements. It provides the potential for a substantial reduction in size and weight of optical signal processing systems and provides the potential for a substantial reduction of cost, when the benefits of electronic integration are exploited by optical integration.

The optical Fourier transform process requires a series of lenses with sufficient aperture and resolution to encompass the time-spatial-bandwidth-product system requirements. Near diffraction-limited lens performance and low scattering are necessary to obtain a useful resolution and dynamic range. Lens systems designed to fulfill these requirements using conventional optical elements in three dimensions is a highly

developed art. The corresponding implementation of lenses in two-dimensional thin-film waveguides constitutes a developing technology of which this report constitutes the third-year's effort sponsored by the Air Force Avionics Laboratory. The first-year's effort[14] addressed various approaches to lenses, lens systems and reflectors as may be required for implementation of the optical Fourier transform function in an integrated optics format. The optical waveguide Luneburg lens and geodesic analogy received most of the attention. The second-year's effort[10,15] addressed the waveguide Luneburg lens implemented on a thermally-oxidized silicon substrate and developed a computational procedure to predict its performance as an inhomogeneous refractor. A portion of this second-year's effort addressed a companion component of the spectrum analyzer, specifically, waveguide-coupled photodetector array with charge-coupled device readout[16] which was carried out at the University of Cincinnati. The third-year's effort, reported herein, has continued to address waveguide Luneburg lenses on thermally-oxidized silicon substrate successfully achieving diffraction-limited performance, the reduction of waveguide and lens scattering, the implementation of a spatial filter, implementation of a channel waveguide fan-out structure and improved waveguide reflectors.

B. PROGRAM OBJECTIVE

Basic to the development of an integrated optical technology are the requirements for (1) a coherent source, (2) the general modulation function, both temporal and spatial, (3) the detection function and (4) a waveguide technology to appropriately interconnect all of these components. All of these components must be implemented on a planar structure or hybrid coupled together using a compatible processing technology.

Optical lens elements within thin-film waveguide medium have several additional design freedoms and some restrictions when compared with conventional optical systems. First, the lens system is entirely immersed in the thin-film waveguide which has an effective refractive index determined by the choice of materials and film thickness. The ambient waveguide effective refractive index may be greater than, or less than, the index employed for the lenses. The available range of refractive indices is restricted to values greater than that of the substrate bulk refractive index to preserve wave binding within the thin-film waveguide. Second, the use of nonplanar substrates permits the

formation of lenses of uniform refractive index by changes of the path length because the rays traverse geodesics. The maximum refractive index is usually limited by the thin-film waveguide material except for geodesics where the path length increase synthesizes the larger value. Third, inhomogeneous lens elements are feasible using homogeneous dielectrics and may be produced by graded waveguide film thickness. Consideration of these various ramifications was included in the initial effort, Optical Waveguide Lenses, I. One important conclusion derived from this initial effort suggested that generalized thin-film Luneburg lenses were a favored approach for optimization in integrated optics format.

Referring to Figure 1, the essential lens elements include a beam expansion system and a Fourier transform lens. In addition to the requirement for near diffraction-limited performance and low scattering, the design of these lenses must consider the length of the optical axis because of the Fourier transform "chip" substrate area limitations. Reasonable substrate dimensions are comparable to that employed in the integrated electronic circuit industry. Therefore, consideration of the telephoto effect so as to reduce the physical focal length of the Fourier transform lens received attention during the initial program, Optical Waveguide Lenses, I.[14] The required large compression of the physical focal length, field of view and field curvature negated further consideration of the telephoto effect in preference to a folded optical system. It was also necessary to develop plane refractors for folding so as to minimize the substrate area employed.

The second effort, Optical Waveguide Lenses, II,[15] addressed inhomogeneous thin-film waveguide lenses, lens systems and refractors for the waveguide material-structure and exploited thermally-oxidized silicon as an isolation layer between the waveguide and supporting silicon substrate. Typical Luneburg lenses employed Ta_2O_5 as an overlayer or underlayer in conjunction with Corning 7059 glass employed as the waveguide. The thermally oxidized silicon substrate with appropriate, careful processing has proven to yield the lowest scattering substrate thus far identified.

Interest in the thermally-oxidized silicon substrate was motivated by the potential advantage of integration of both optical and electronic components. This structure is of particular interest because the removal of the isolation oxide provides for waveguide coupling to a photodetector array in the substrate. The requirement for the spatial modulator for an optical Fourier transform "chip" can be satisfied with a piezoelectric ZnO overlay film to launch Rayleigh waves which may Bragg diffract in the optical waveguide.

The basic refractive element considered is the positive generalized Luneburg lens (with arbitrary optical focii equal to or greater than the lens diameter). Two of these lenses with comparative short focal length were employed to demonstrate a beam expansion system. A single lens with a longer focal length was folded using reflectors. This second effort included: (1) optimization of Luneburg lens radial refractive index profile to more closely approach diffraction-limited performance, (2) reduction of scattering losses due to waveguide films, substrate isolation layer and optical element boundaries, (3) establishment of lens reproducibility, alignment and positioning without regard to the specific profiles and (4) suppression of mode conversion within optical elements.

A part of this second program was directed to a waveguide-coupled photodetector array for use in the spatial frequency plane of the optical Fourier transform "chip." This waveguide-coupled photodetector array investigation was carried out by the Department of Electrical and Computer Engineering at the University of Cincinnati under a subcontract under the direction of Professor J. T. Boyd.

C. TECHNICAL APPROACH

Based upon the results of the preceding programs, Optical Waveguide Lenses, I, and Optical Waveguide Lenses, II, this effort, Waveguide Optics for Coherent Optical Processing, reported herein, has addressed generalized waveguide Luneburg lenses that yield diffraction-limited performance. Corning 7059 waveguide and Ta_2O_5 overlay lenses were employed using a thermally-oxidized silicon substrate. The thermally-oxidized silicon provides a smooth, low-loss isolation layer between the optical waveguide and the silicon substrate to prevent absorption losses of the waveguide evanescent field in the substrate. Generalized waveguide Luneburg lenses

are circular symmetric inhomogeneous refractors that can be void of all aberrations except circular field. These waveguide Luneburg lenses are formed by deposition through a circular mask where the edge of the mask is shaped to control the waveguide Luneburg lens radial refractive index profile. To obtain diffraction-limited performance requires that the radial refractive index profile fit a specific function. A significant achievement of the effort reported herein has been the synthesis of the mask edge shape so as to control the lens radial refractive index profile to yield essentially diffraction-limited results within the capability of its measurement. Other problems addressed in this program have included waveguide Luneburg lenses with both short and long focal lengths, namely, F/4 and F/25. Further, the effort has investigated various means to reduce lens and waveguide scattering and has provided means to measure both the in-plane and orthogonal out-of-plane scattering transverse to and longitudinal with the optical beam. A tolerance analysis for waveguide Luneburg lenses and the effect of lens focal length correction has been included.

Because the integrated optical spectrum analyzer must conserve substrate area and because some designs require a long focal length, means to realize improved reflectors were considered. Cleavage of the single crystal silicon substrate through the isolation layer and waveguide has yielded good reflection employing the total reflection phenomenon.

The integrated optical spectrum analyzer requires a high degree of transverse mode purity. Two types of spatial filters to obtain mode purity were investigated and demonstrated as an alternative to the requirement of the high degree of mode purity from the mode source. Absorptive and dispersive types were included.

Because the RF spectrum analyzer may employ a short focal length path for the Fourier transform with a beam width substantially less than a convenient waveguide coupled photodetector array period, a channel fan-out waveguide coupler was also included in this effort.

The following Technical Discussion is organized by subdivisions, reporting on the computational synthesis results for various Luneburg lenses, radial refractive index profiles and focal lengths, together with the measured lens diffraction patterns and data for the sundry components.

As a result of this effort, several scientific papers have been prepared for publication in the open literature. These manuscripts are included as appendices as follows:

A. D. B. Anderson and R. R. August, "Progress in Waveguide Lenses for Integrated Optics," Preprint for the Transactions of the Institute of Electronics and Communications Engineers of Japan, March 1978: Special Issue Integrated Optics and Optical Fiber Communication.

B. S. K. Yao, D. B. Anderson, C. M. Oania, and V. G. Kreismanis, "Mask Synthesis for Diffraction-Limited Waveguide Luneburg Lenses," Reprint presented at the Topical Meeting on Integrated and Guided Wave Optics, January 16, 1978, Salt Lake City, Utah.

C. J. T. Boyd and D. B. Anderson, "Effect of Optical Waveguide Scattering on the Integrated Optical Spectrum Analyzer Dynamic Range," To be published IEEE Journal of Quantum Electronics, June, 1978.

D. D. B. Anderson and R. R. August, "Fourier Transform Signal Processing in an Integrated Optical Format," Presented at the IEEE IOSA Conference on Lasers and Electro-Optical Systems, February 8, 1978, San Diego, California.

An effort has been made to avoid duplication between the Technical Discussion and the various appendices. Appendix A reports the status of thin-film waveguide Luneburg lenses and geodesic lenses as of mid-1977. Appendix B delineates progress through only the first step of the synthesis procedure for diffraction-limited lenses. The exposition contained in Appendix C is a full treatment of optical waveguide scattering and its effect upon the integrated optical spectrum analyzer dynamic range while Appendix D delineates Rockwell's "first-cut" approach to an integrated optical spectrum analyzer utilizing waveguide Luneburg lenses as developed under this effort. Appendix E, "Integrated Optical Spectrum Analyzer Signal Level Requirements," by Professor J. T. Boyd addresses the spectrum analyzer photodetector and CCD image array dynamic range to determine the Fourier transform's laser power requirements.

II. TECHNICAL DISCUSSION

A. MULTILAYER OPTICAL WAVEGUIDES

To provide a foundation for discussion of waveguide Luneburg lenses,[17] we will briefly summarize some of the more important properties of bound modes in dielectric waveguide.[18] In particular, we will consider the four-layer structure illustrated in Figure 2. It consists of a substrate having a refractive index of n_4 and superstrate having a refractive index of n_1, each with an infinite extent with one or two thin films between which serve as the optical waveguides or as a waveguide with isolation layer. The planar structure considered also has infinite extent in y with

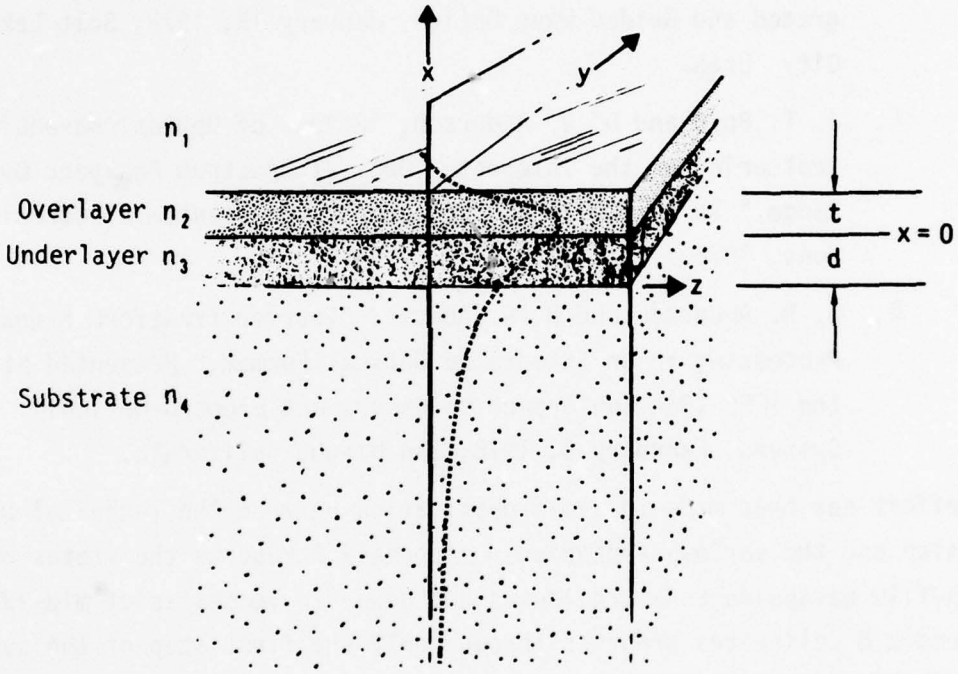

Figure 2. Cross Section of Asymmetrical Multilayer Planar Dielectric Waveguide Showing Zero - Order Mode Bound in Both Layers with Evanescent Field

optical propagation in the z-direction. For wave binding, it is necessary that (n_2 and/or n_3) be greater than (n_1 and n_4). We will not consider the modes bound to the substrate when it is of limited extent. The modes bound to this type of structure may be either transverse electric (TE_m) or transverse magnetic (TM_m) of order m. A transverse field component bounded

to both layers (overlayer and underlayer) is illustrated in Figure 2, showing the zero-order with the evanescent field extending into the superstrate and substrate. It is possible that the refractive index and the film thickness of these layers be such that wave binding occurs only in that region which has the highest index with an evanescent component in the other layers.

1. Dielectric Waveguide Modes

The transverse electric modes (TE) are the eigen solutions of the field equation where the time variation $e^{i\omega t}$ has been suppressed

$$\left[\frac{\partial^2}{2x^2} + \frac{\partial^2}{2z^2} + \omega^2 \varepsilon(x)\mu_o \right] E_y(x,z) = 0 \tag{1}$$

subject to the following boundary conditions: $E_y \to 0$ as x approaches $\pm \infty$, and the tangential components of E and H are continuous across the boundaries. The z dependence will be the same in all four regions for a given mode and can be written as

$$e^{-i\beta_m Z} \tag{2}$$

where m is the mode order. Additionally $\varepsilon(x)$ can be expressed as follows

$$\varepsilon(x) = \begin{cases} n_1^2 \varepsilon_o & x \geq t \\ n_2^2 \varepsilon_o & t > x > 0 \\ n_3^2 \varepsilon_o & 0 > x > -d \\ n_4^2 \varepsilon_o & -d \geq x \end{cases} \tag{3}$$

Applying the boundary conditions on E to the solutions of (1) the fields in the four regions can be written as

$$E_{m1} = A_m e^{-P_m(x-t)} \sin(h_m t + \phi_m) \sin \gamma_m e^{-i\beta_m z} \tag{4a}$$

$$E_{m2} = A_m \sin(h_m x + \phi_m) \sin \gamma_m e^{-i\beta_m z} \tag{4b}$$

$$E_{m3} = A_m \sin(\ell_m x + \gamma_m) \sin \phi_m e^{-i\beta_m z} \tag{4c}$$

$$E_{m4} = A_m e^{q_m(x+d)} \sin(-\ell_m d + \gamma_m) \sin \phi_m e^{-i\beta_m z} \tag{4d}$$

where A_m is a normalization constant, and P_m, h_m, ℓ_m and q_m are the transverse components of the propagation vector in regions 1, 2, 3, 4 respectively. P_m, h_m, ℓ_m, q_m and β_m are related by the following dispersion equations

$$P_m = (\beta_m^2 - \kappa^2 n_1^2)^{1/2} \tag{5a}$$

$$h_m = (k^2 n_2^2 - \beta^2_m)^{1/2} \tag{5b}$$

$$\ell_m = (k^2 n_3^2 - \beta^2_m)^{1/2} \tag{5c}$$

$$q_m = (\beta_m^2 - k^2 n_4^2)^{1/2} \tag{5d}$$

Application of the boundary conditions on H yields

$$\tan(h_m t + \phi_m) = -h_m/P_m \tag{6}$$

$$\tan \phi_m = (h_m/\ell_m) \tan \gamma_m \tag{7}$$

$$\tan(-\ell_m d + \gamma_m) = \ell_m/q_m \tag{8}$$

These equations when combined lead to the following transcendental equation

$$\frac{1}{\ell_m} \tan\left(\ell_m d + \tan^{-1} \frac{\ell_m}{q_m}\right) + \frac{1}{h_m} \tan\left(h_m t + \tan^{-1} \frac{h_m}{P_m}\right) = 0 \tag{9}$$

The roots of this equation are the allowed values of the propagation constants.

The transverse magnetic modes (TM) are the eigen solutions of the field equation

$$\left[\frac{\partial^2}{\partial x^2} + \frac{\partial^2}{\partial z^2} + \omega^2 \varepsilon(x) \mu_o\right] H_y(x,z) = 0 \tag{10}$$

The development of the TM modes is identical to that for the TE modes and again the allowed values of the propagation constants are roots of a transcendental equation, which is

$$\frac{n_3^2}{\ell_m} \tan\left(\ell_m d + \tan^{-1}\left[\frac{n_4^2}{n_3^2} \frac{\ell_m}{q_m}\right]\right) + \frac{n_2^2}{h_m} \tan\left(h_m t + \tan^{-1}\left[\frac{n_1^2}{n_2^2} \frac{h_m}{P_m}\right]\right) = 0 \tag{11}$$

2. Thin-Film Waveguide Dispersion Data

Tantalum pentoxide and Corning 7059 glass have been employed to form waveguides and lenses on thermally-grown SiO_2 substrates because they exhibit comparatively low scattering loss and may be deposited with reproducible properties and thickness profiles. Therefore, the dispersion for each has been calculated and the dispersion, when combined to form refractive lens elements, has also been calculated. Dispersion data is also presented for the multilayer structure when the field is trapped in only the dense layer and when it is trapped in both layers.

The single layer thin-film waveguide dispersion of Ta_2O_5 structure on Corning 7440 glass is shown in Figure 3 for both TE and TM modes as a function of the normalized film thickness. The thin-film waveguide dispersion of a Corning 7059 glass structure on an SiO_2 substrate is shown in Figure 4 for both TE and TM modes as a function of the normalized thickness. The effective refractive index approaches the bulk value for thick films and approaches the substrate for thin films. Each of these thin-film waveguide modes exhibit a cutoff where $n_e(m) = 1.47$ for Figure 3 and $n_e(m) = 1.47$ for Figure 4 in a dielectric waveguide structure. Cutoff means the lack of wave binding to the film. An asymmetric dielectric structure at cutoff leads to refraction into the substrate.

The dispersion for a two-layer structure for only the transverse electric modes is shown in Figures 5(a) and 5(b) where Ta_2O_5 is employed as the overlayer of variable thickness T and where the underlayer normalized thickness is constant ($kt = 2.37\ \pi$) which is equivalent to a 7059 layer having a thickness of 0.75 microns and an optical wavelength of 0.63 microns. Each of the dispersion curves of Figures 5(a) and 5(b) exhibit an inflection representing the transition region where wave binding occurs to only the dense overlayer and where wave binding occurs in both layers. Figure 5(b) is an expansion of Figure 5(a) in the region where wave binding occurs in both layers showing the effect of substrate refractive index.

The dispersion for a two-layer structure for only the transverse electric modes where 7059 is employed as the overlayer of fixed thickness and where the underlayer of Ta_2O_5 of variable thickness T is shown

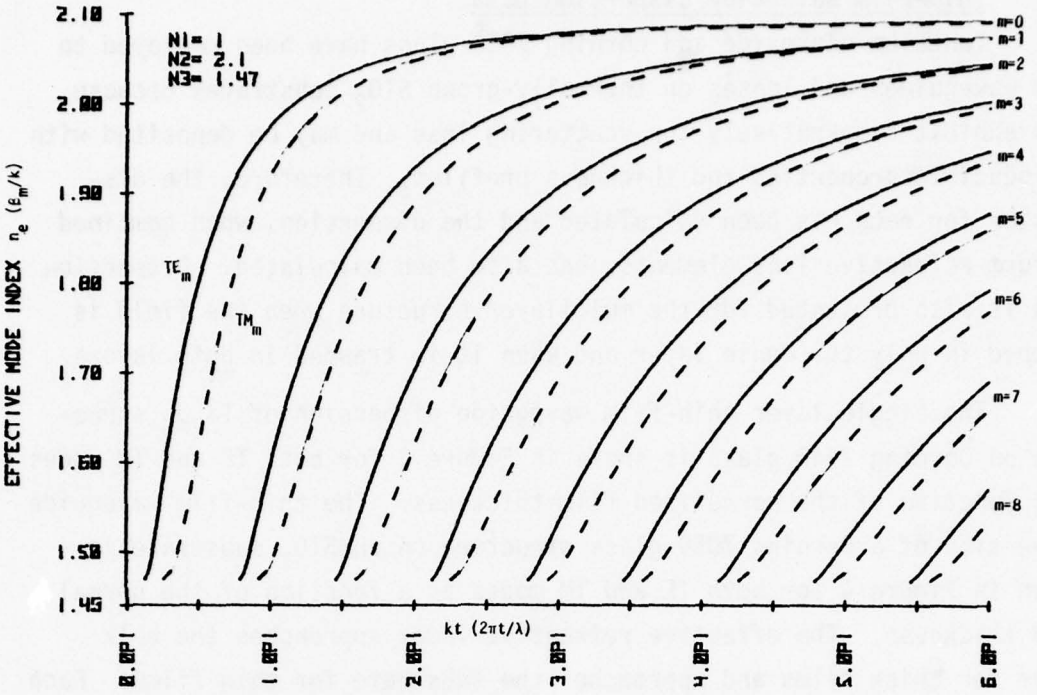

Figure 3. Effective Refractive Index Vs. Normalized Film Thickness for Ta_2O_5 Film on SiO_2 Substrate TE Modes —— TM Modes – – –

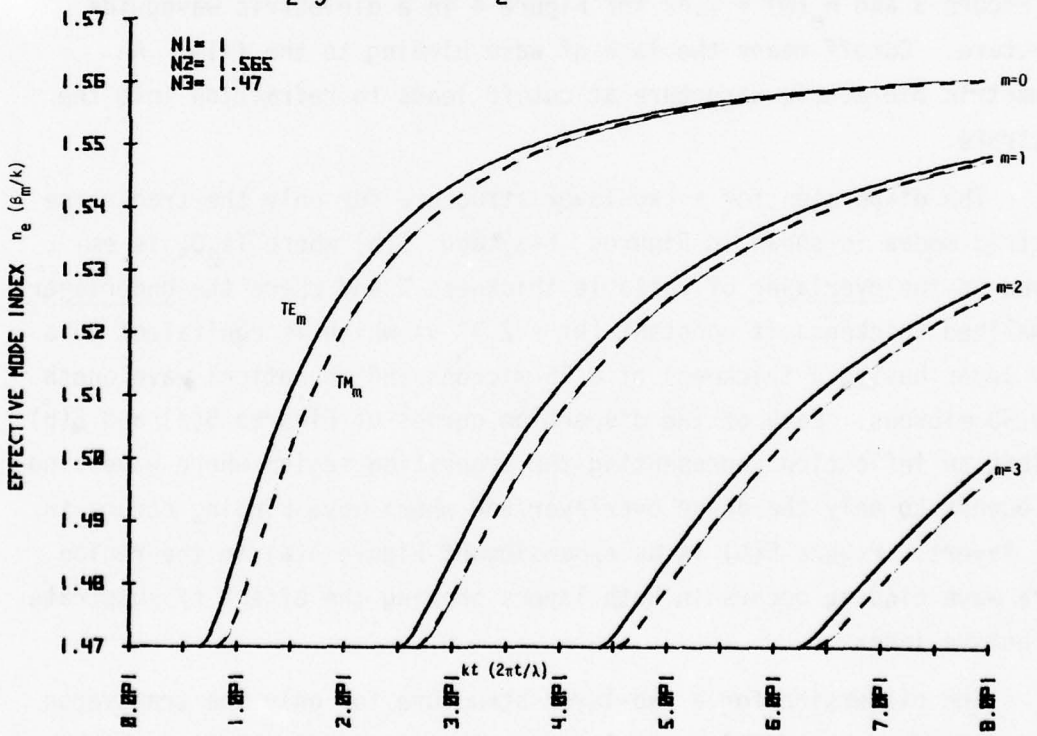

Figure 4. Effective Refractive Index Vs. Normalized Film Thickness for 7059 Glass Film on SiO_2 Substrate TE Modes —— TM Modes – – –

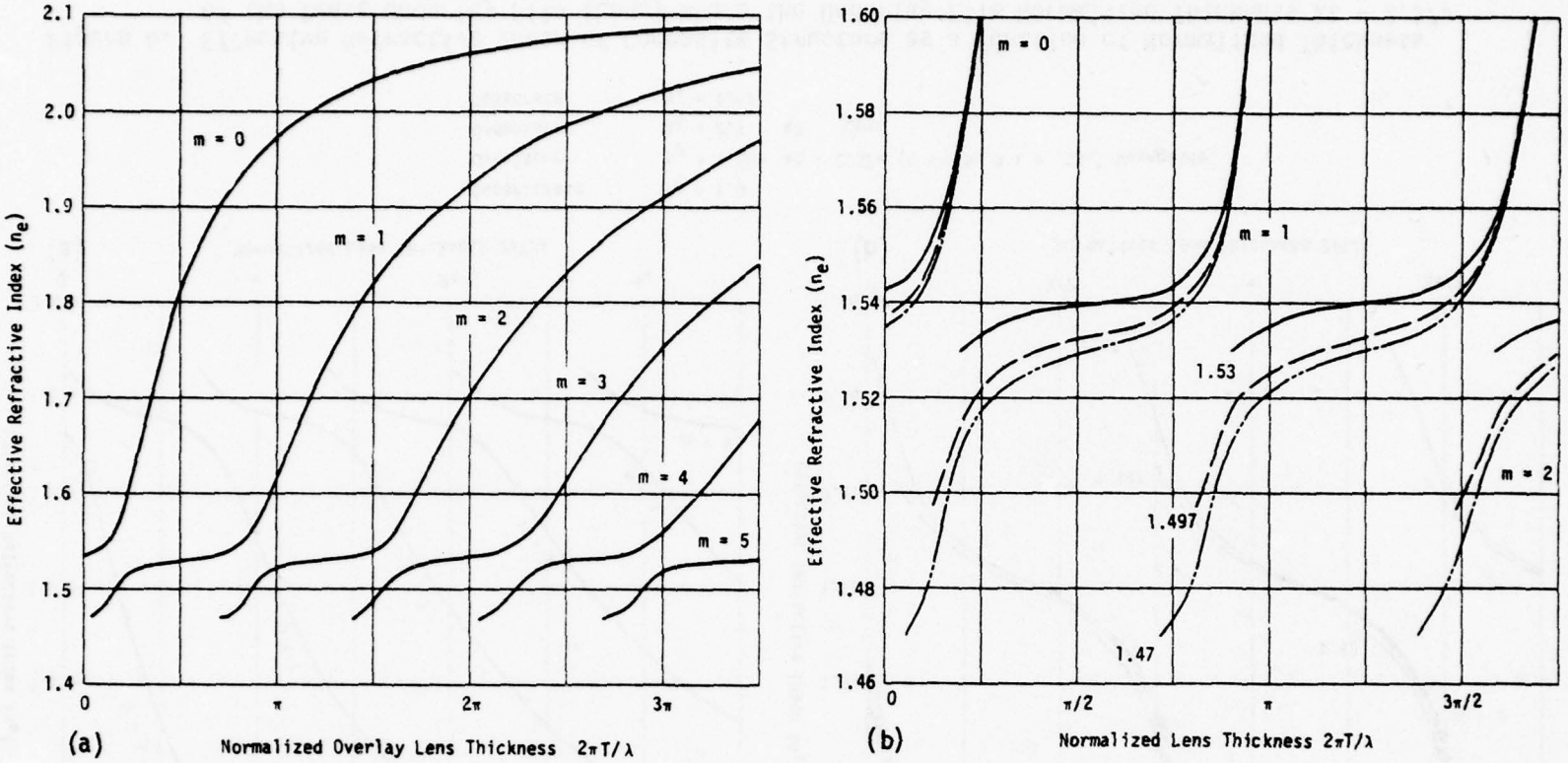

Superstrate	$n_1 = 1.0$
Overlayer	$n_2 = 2.1$ kT Lens
Underlayer	$n_3 = 1.565$ $kt = 2.37\pi$ ($t = .75\mu$ @ $\lambda = .63\mu$) Waveguide
Substrate	$n_4 = 1.47, 1.497, 1.53$

Figure 5. Effective Refractive Index of Composite Structure as a Function of Normalized Thickness of the Dense Overlay Film (Lens) Where the Overlay Film Normalized Thickness $kt = 2.37\pi$ for TE Modes Only (a), Expanded Scale Showing Effect of Three Substrates for TE Modes Only (b).

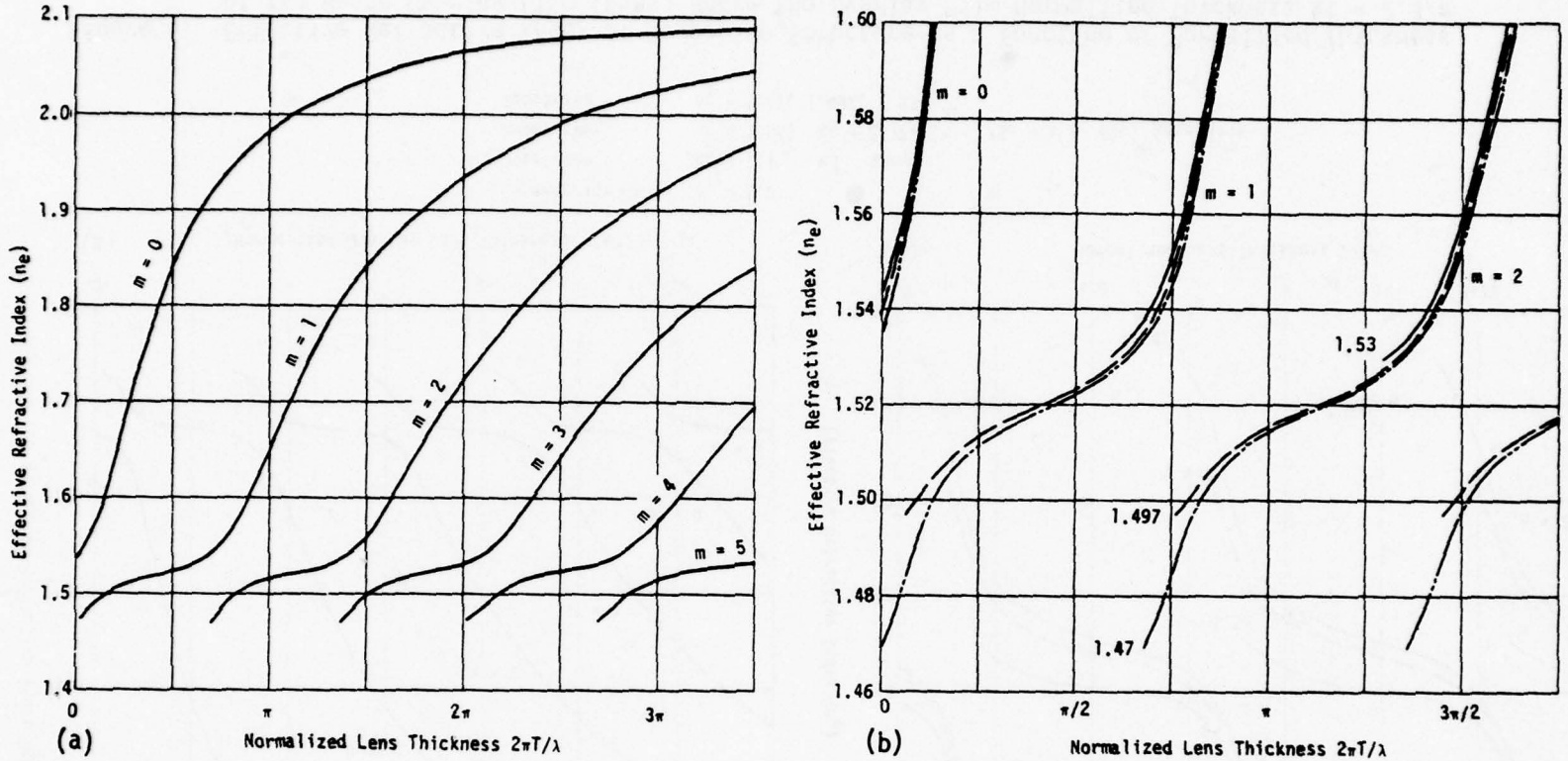

Superstrate	$n_1 = 1.0$
Overlayer	$n_2 = 1.565$ kt = 2.37π (t = .75u @ λ = .63u) Waveguide
Underlayer	$n_3 = 2.1$ kT Lens
Substrate	$n_4 = 1.47$

Figure 6. Effective Refractive Index of Composite Structure as a Function of Normalized Thickness of the Dense Underlay Film (Lens) Where the Underlay Film Normalized Thickness kt = 2.37π for TE Modes Only (a), Expanded Scale Showing Effect of Three Substrates for TE Modes Only (b).

in Figures 6(a) and 6(b). The fixed thickness waveguide ($kt = 2.37\ \pi$) is equivalent to a 7059 layer having a thickness of 0.75 microns for the optical wavelength of 0.63 microns. Each of the dispersion curves of Figures 6(a) and 6(b) again exhibit an inflection representing the transition region where wave binding occurs to only the dense underlayer and wave binding occurs in both layers. Figure 6(b) is an expansion of Figure 6(a) in the region where wave binding occurs in both layers showing the effect of substrate refractive index for the same three values of refractive index.

This dispersion data is sufficient for design of homogeneous and inhomogeneous refractors and reflector lens systems. In general, only transverse electric modes are employed in the lowest order to minimize loss. Restriction to the TE mode is achieved by input coupling polarization. The thickness of some lenses will permit the presence of a multiplicity of mode orders, however, most transitions are sufficiently gradual to minimize excitation of higher order modes. Location of the highest index layer adjacent to the substrate maximizes conversion to the next higher order mode which is odd. It is also possible to prohibit mode conversion by symmetry, that is, by interleaving the denser film between two separate halves of the waveguide.

The following sections consider thin-film waveguide generalized Luneburg lenses having circular symmetry requiring that the radial refractive index profile follow a prescribed function to obtain a focus of the radiation. The following numerical procedure will utilize the above analysis in the computations to derive the overlay waveguide-lens thickness such that it will satisfy the radial refractive index dependence. It will also include the effect of errors arising from the waveguide thickness and the lens radial functional thickness dependence.

B. INHOMOGENEOUS REFRACTIVE WAVEGUIDE LENSES

Conventional optical lens systems employ homogeneous dielectrics with spherical surfaces in various combinations to correct aberrations. Inhomogeneous materials with weak perturbations randomly distributed are avoided. Generally, materials with large inhomogeneous perturbations are not available and, thus, lenses requiring large refractive index variations such as Maxwell's fish-eye[19] and the Luneburg lens[20] have not been realized in the optical portion of the spectrum. Thin-film optical waveguide provides the opportunity to synthesize thin-film inhomogeneous dielectric lens using homogeneous materials by variation of the film thickness.

1. "Classical" Luneburg Lens[20]

Luneburg lens is an inhomogeneous positive refractor with radial symmetry which images a plane wavefront to a hemispherical spot located on the opposite boundary of the refractor. Ray traces through the "classical" Luneburg lens are illustrated in Figure 7. Interest in the Luneburg lens arises because of its 4π field of view and because it is free of all aberrations except field curvature. The cross section of a dielectric waveguide Luneburg lens is illustrated in Figure 8 where a circular overlay film is employed with prescribed radial thickness function. For integrated optics, its simplicity of fabrication in a thin-film structure realized reproducibly is an important attribute.[17] The circular symmetry is of particular interest where the substrate area is limited because folding of the optical axis may use the same lens for several purposes. The waveguide Luneburg lens has a further advantage that all refractive index variations are continuous, smooth and slow functions with respect to the optical wavelength. Mode conversion in the lens is suppressed by the graded thickness profile and by symmetry.

The Luneburg lenses may be generalized to form a perfect geometric image of two given concentric circles on each other.[21] The perfect focusing property may be achieved in various regions. If one of the circles is of infinite radius, the lens may be designed to focus on another circle outside of, at the boundary, or inside of, the Luneburg lens. Luneburg found a solution for the refractive index function which had a conjugate foci for two given points outside of the lens. The solution for a parallel beam array which focuses on the opposite lens interface requires that the

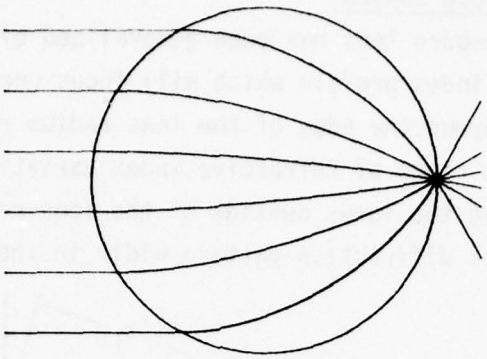

Figure 7. Ray Trajectory Through Luneburg Lens Where f-Number = 0.5, which is Equivalent to Morgan's S = 1.

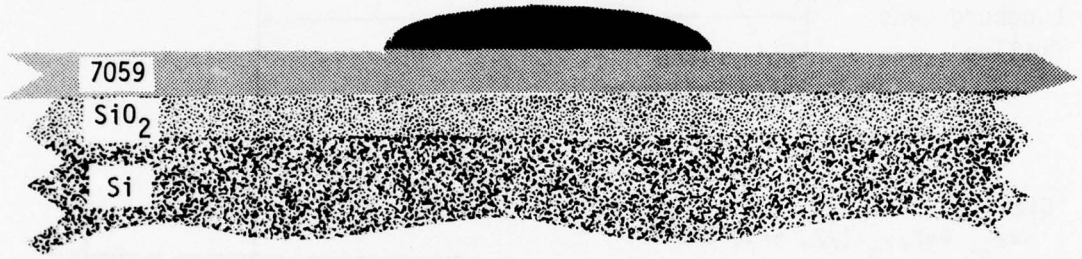

Figure 8. Cross Section of a Waveguide Luneburg Lens using a Dense Ta_2O_5 Overlay Lens on Corning 7059 Waveguide on a Thermally-Oxidized Silicon Substrate.

refractive index n(r,m)

$$n(r,m) = n_e(m)\sqrt{2 - (r/r_o)^2} \qquad r \le r_o \tag{12}$$

where n_e is the refractive index of the medium surrounding the lens, r_o is the lens radius, and r is the radial coordinate for mode (m). Southwell has developed a technique for ray tracing through Luneburg lenses which has been employed to generate Figure 7 (The corresponding diffraction pattern is depicted in Figure 14.).

2. Generalized Luneburg Lenses

The "classic" Luneburg lens has been generalized by Morgan[21] developing a radial refractive index profile which will focus one circle on another in the region beyond the edge of the lens radius r_o. The increased focal length reduces the range of refractive index variation required to form the lens. Extending the focus outside of the lens region increases the f-number and thus the diffraction pattern width in the focal region.

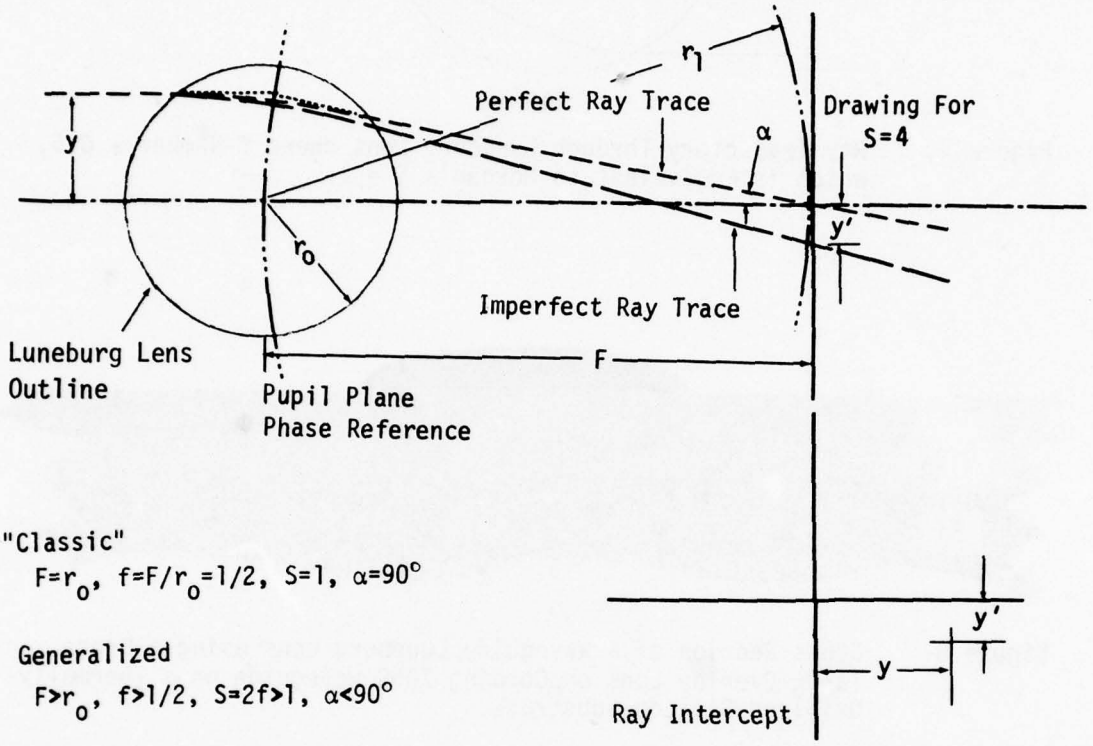

Figure 9. Ray Trace Geometry Through Luneburg Lens and Ray Trace Intercept Plot.

The geometry of a generalized Luneburg lens is depicted in Figure 9 showing a perfect ray trace. An imperfect ray trace is also included in Figure 9 from which a ray intercept plot is developed which is also included in Figure 9. In the following section, numerous ray traces are calculated yielding the ray intercept plot from which the phase wavefront has been derived followed by the calculated intensity diffraction pattern. This procedure has provided the means to calculate generalized Luneburg lens performance starting from waveguide thickness profiles with various functional errors to determine the allowed tolerances as determined by degradation of the diffraction pattern.

The functional radial refractive index profile for some generalized Luneburg lenses can be obtained from a paraxial approximation in the region where the f-number is >1.5. The normalized refractive index profile is given by

$$\frac{n(r,m)}{n_e(m)} = \exp\left(\frac{\sqrt{n_e(m)^2 r_o^2 - r^2 n^2(r,m)}}{\pi n_e(m) r_1}\right) \quad . \tag{13}$$

In the above equation, r is the radial coordinate from the lens center along the waveguide surface, r_o is the radius of the lens region, the focal length is r_1=F and $n_e(m)$ is the effective refractive index for the waveguide mode (m) of interest. Note that the above equation is not solved for n(r,m), but n(r,m) is readily determined from Eq. (13) numerically as a function of r_1. Using Eq. (13), Figure 10 depicts the normalized effective refractive index profile as a function of the normalized lens radius for several values of f-numbers. It indicates that the transverse profile becomes more uniform having a lower refractive index over a larger central region of the lens as the focal length is increased.

Note that Equation (13) depends upon the waveguide mode order and, therefore, a waveguide which will support more than a single mode will have a separate foci for each of the modes of which only one can yield a diffraction-limited pattern.

For the classic Luneburg lens $n(0,0)/n_e(0)=\sqrt{2}$, a high index layer like Ta_2O_5 or Nb_2O_5 is required on Corning 7059 for F/D = 0.5. Generalized Luneburg lenses with longer focal lengths may be formed with these materials using thinner films or using films with lower index and thicker layers. Generalized Luneburg lenses have been realized using an "all" 7059 thin film when F/D>6. Lenses which are formed from a single composition by changes of the layer thickness exhibit substantially less scattering and further suppress the excitation of higher order modes.

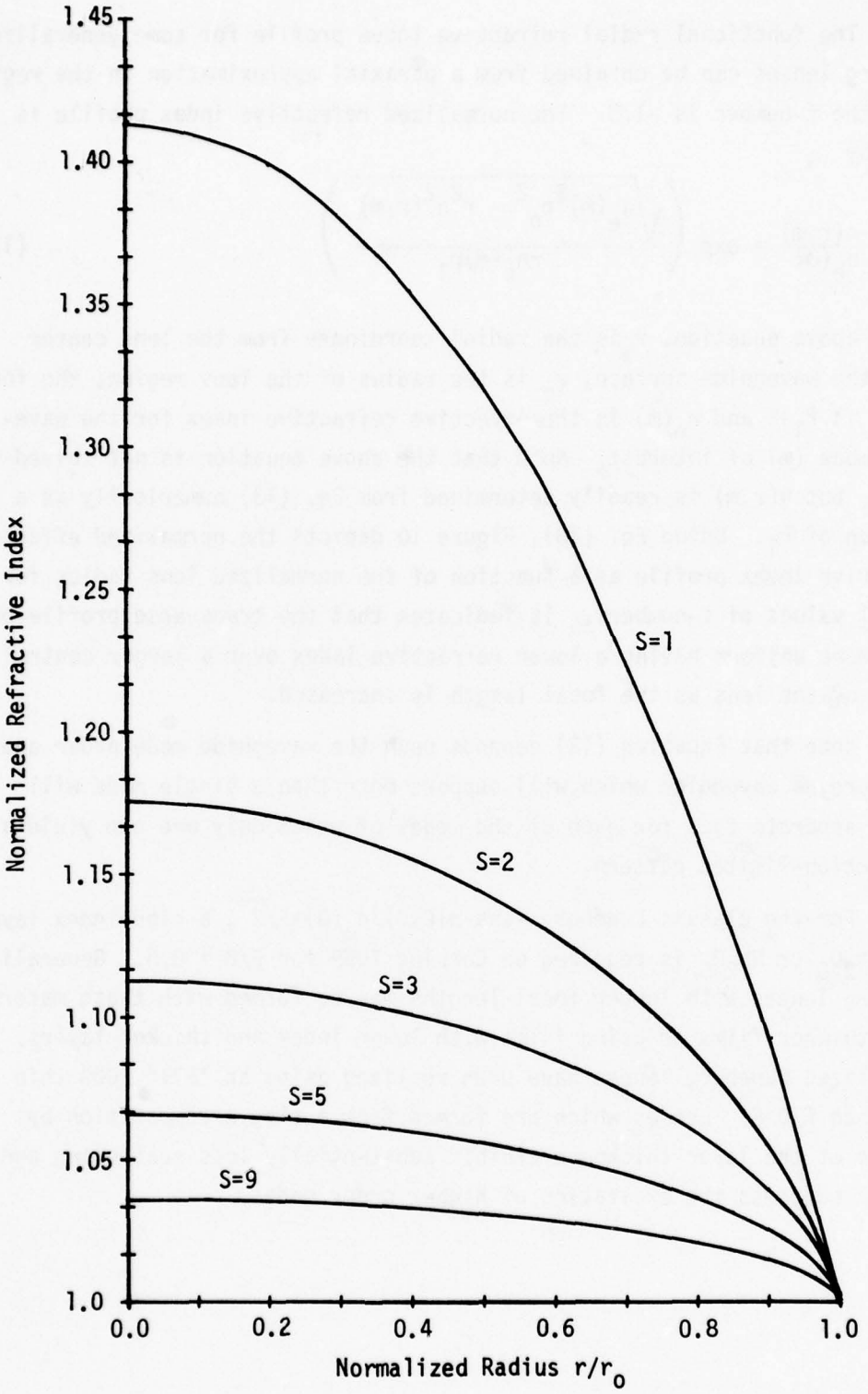

Figure 10. Normalized Refractive Index Profile for Generalized Luneburg Lenses for Various f-Number = S/2 (after Morgan and Southwell).

3. Generalized Luneburg Lens Analysis

Southwell's[22,23] analytical approximation is derived for Luneburg's integral equation from which the index profile for the generalized Luneburg lens may be extracted to sufficient accuracy for ray-tracing to diffraction-limited performance. This expression was derived as an expansion based on a consideration of known behavior at certain limits. The expression consists of five parameters which depend on the generalized Luneburg lens focal length. Two of these parameters are determined from the "boundary" limits and the others are determined using a least-squares procedure. This analytical expression provides a convenient means for obtaining the radial index n(r) for ray-tracing purposes. It also provides a means of conveniently determining integrated optical Luneburg lens thickness profiles.

A spherically symmetric index distribution n(r) which gives a perfect image of an infinite object satisfies[20] the integral equation

$$n = \exp[\omega(\rho,s)], \tag{14}$$

where $\rho=rn$ and

$$\omega(\rho,s) = \frac{1}{\pi} \int_{\rho}^{1} \frac{\arcsin(x/s)}{(x^2-\rho^2)^{1/2}}\, dx \ , \tag{15}$$

in which the optical guided wave index of refraction variable n is normalized to the optical guided wave index of refraction n_e of the homogeneous waveguide medium surrounding the lens such that $n \geq 1$. Both the radius variable r and the image distance parameter s as measured from the center of the lens are normalized with respect to the generalized Luneburg lens radius r_o such that $0 \leq r \leq 1$ and $s \geq 1$. The full aperture f-number for these lenses turns out to be approximately s/2 for $s \geq 1$.

For the case s=1, the above integral may be evaluated in closed form yielding the "classical" Luneburg lens. To obtain a closed form analytical approximation for the generalized Luneburg lens given by Equation (15), a change of variable is required. Letting $x' = x/s$ and $\rho=0$, the value of the generalized Luneburg lens refractive index maxima which occurs at the center is given by Equation (14) and

TABLE I. THE FUNCTION $\omega(o,s)$ USING EQ. (16) $n_{max} = \exp[\omega(o,s)]$

s	$\omega(o,s)$	$n_{max}(r=0)$
1	0.34657359	1.41421356
2	0.161532974	1.17531121
3	0.106778890	1.11268820
4	0.0798585731	1.08313387
5	0.0638050027	1.06588453
6	0.0531341389	1.05457109
7	0.0455246840	1.04657684
8	0.0398234213	1.04062701
9	0.0353921041	1.03602586
10	0.0318487205	1.03236132
17	0.0187277137	1.01890418

$$\omega(o,s) = \frac{1}{\pi}\int_0^{1/s} \frac{\arcsin x'}{x'}\, dx' \qquad (16)$$

The refractive index maxima for Luneburg lenses are given in Table I as well as by the ordinate of Figure 10.

To investigate the Luneburg refractive index profile for $\rho \neq o$, a new variable $y=x-\rho$ is employed for Equation (15) which becomes

$$\omega(\rho,s) = \frac{1}{\pi}\int^{1-\rho} \frac{\arcsin\left(\frac{y+\rho}{s}\right)}{(y+2\rho)^{1/2} y^{1/2}}\, dy \quad . \qquad (17)$$

We may now remove the $y^{-1/2}$ singularity by performing an integration by parts,

$$\omega(\rho,s) = \frac{1}{\pi}\left[2 \arcsin\left(\frac{1}{s}\right)\frac{(1-\rho)^{1/2}}{(1+\rho)^{1/2}} - \int_0^{1-\rho}\left(\left[s^2-(y+\rho)^2\right]^{-1/2} - \frac{\arcsin\frac{y+\rho}{s}}{(y+2\rho)}\right)\frac{y^{1/2}dy}{(y+2\rho)^{1/2}}\right] \quad . \tag{18}$$

From Equation (18), it is observed that as $\rho\to 1$, which is near the edge of the lens and in the limit as $y\to 0$, the integrand of Equation (18) behaves as $y^{1/2}$. Thus, it is found that the integral portion behaves as $(1-\rho)^{3/2}$, which is a higher order term compared to the first term on the right side of Equation (18). Thus, in the limit as $\rho\to 1$ the integral may be ignored and $\omega(\rho,s)$ behaves like

$$\omega(\rho,s) \underset{\rho\to 1}{=} \frac{\sqrt{2}}{\pi}\arcsin\left(\frac{1}{s}\right)(1-\rho)^{1/2} \quad . \tag{19}$$

Furthermore, the integral of Equation (18) indicated that the next order term will have a $(1-\rho)^{3/2}$ behavior. Therefore, it is reasonable to suggest a power series for the function $\omega(\rho,s)$ as follows

$$\omega(\rho,s) = p_1(1-\rho)^{1/2} + p_2(1-\rho)^{3/2} + p_3(1-\rho)^{5/2} + p_4(1-\rho)^{7/2} + p_5(1-\rho)^{9/2} \tag{20}$$

Obviously,

$$p_1 = \frac{\sqrt{2}}{\pi}\arcsin\left(\frac{1}{s}\right) \tag{21}$$

and

$$p_5 = \omega(o,s) - p_1 - p_2 - p_3 - p_4 \quad . \tag{22}$$

Thus, only three of the p coefficients are as yet unspecified. To determine these remaining coefficients, we fit the numerical values of data given in Equation (18) to the function $\omega(\rho,s)$ given by Equation (20). More points are included near the $\rho=1$ region in order to more heavily weight

TABLE II

RESULTS OF FITTING EQ. (20) TO THE DATA IN TABLE I.

The values listed for SUM are the sum of the squares of the errors for the 29 points. p_5 was determined by Eq. (22).

	s=2	s=3	s=5	s=9
SUM	3.9101×10^{-11}	5.8134×10^{-12}	1.7893×10^{-12}	5.3512×10^{-13}
p_1	0.235687835	0.152976535	.0906399959	.0501194645
p_2	-7.47500358×10^{-2}	-4.22494061×10^{-2}	-2.34300068×10^{-2}	-1.26356394×10^{-2}
p_3	6.72894476×10^{-3}	-1.93175172×10^{-3}	-2.51100017×10^{-3}	-1.63934418×10^{-3}
p_4	-5.14447054×10^{-3}	-8.25244897×10^{-4}	-1.49192458×10^{-4}	-4.07947091×10^{-5}
p_5	-9.89299661×10^{-4}	-1.19124255×10^{-3}	-7.44793717×10^{-4}	-4.11582122×10^{-4}

the region when the greatest change is occurring. Table II is a tabulation of the results of the curve-fit for the 29 "data" points determined from the numerical integration of Equation (18). The deviation of this approximation from the exact formula has been examined and is found to be less than 10^{-6}.

Having an analytical expression for $\omega(\rho,s)$, we are now in a position to extract $n(r)$ numerically for any specified value of r. To do this, we define a function F,

$$F(n) = \exp[\omega(\rho,s)] - n. \tag{23}$$

For a given r and s, we extract the value of n that makes F(n) vanish using Newton's iterative method. A tabulation of results is given in Table III. Plots of these profiles are shown in Figure 10.

In addition to a numerical value of n, the ray-trace algorithms[22] also require values for dn/dr and d^2n/dr^2. The analytical expressions for dn/dr and d^2n/dr^2 in terms of r and the numerical value for n can be derived using implicit differentiation of Equation (23) using Equation (20) for $\omega(\rho,s)$. The results are

TABLE III

NORMALIZED REFRACTIVE INDEX PROFILES FOR GENERALIZED LUNEBURG LENSES

r	s=2	s=3	s=5	s=9
0	1.175311212	1.112688200	1.065884534	1.036025859
0.05	1.174999407	1.112507930	1.065788087	1.035976411
0.10	1.174071705	1.111969546	1.065500332	1.035828873
0.15	1.172521576	1.111069129	1.065018948	1.035581965
0.20	1.170340993	1.109801290	1.064340603	1.035233817
0.25	1.167519780	1.108158811	1.063460759	1.034781859
0.30	1.164044879	1.106132212	1.062373426	1.034222692
0.35	1.159899514	1.103709214	1.061070836	1.033551908
0.40	1.155062156	1.100874045	1.059543028	1.032763858
0.45	1.149505212	1.097606509	1.057777265	1.031851324
0.50	1.143193243	1.093880684	1.055757219	1.030805062
0.55	1.136080437	1.089663045	1.053461790	1.029613132
0.60	1.128106836	1.084909633	1.050863316	1.028259883
0.65	1.119192434	1.079561599	1.047924746	1.026724355
0.70	1.109227400	1.073537799	1.044594938	1.024977603
0.75	1.098054844	1.066721643	1.040800259	1.022977928
0.80	1.085437716	1.058935566	1.036428193	1.020661529
0.85	1.070987513	1.049884988	1.031290974	1.017921692
0.90	1.053981685	1.039009952	1.025027636	1.014552365
0.91	1.050159236	1.036524794	1.023580201	1.013768729
0.92	1.046155078	1.033902395	1.022045349	1.012935510
0.93	1.041942017	1.031119755	1.020407545	1.012043672
0.94	1.037484456	1.028146025	1.018645667	1.011080865
0.95	1.032734249	1.024938133	1.016729693	1.010029408
0.96	1.027623448	1.021432662	1.014614324	1.008862349
0.97	1.022050589	1.017529080	1.012225136	1.007534739
0.98	1.015851602	1.013049431	1.009422596	1.005960167
0.99	1.008726930	1.007614146	1.005874179	1.003921693
1.00	1	1	1	1

$$\frac{dn}{dr} = \frac{-n^2 G}{2(1-rn)^{1/2}+nrG} \tag{24}$$

$$\frac{d^2n}{dr^2} = \frac{2n^3\left[G^2\ (1-rn)^{1/2}+H\right]}{\left[2(1-rn)^{1/2}+nrG\right]^3} + \frac{2}{n}\left(\frac{dn}{dr}\right)^2 \tag{25}$$

where

$$G = p_1 + 3p_2(1-rn) + 5p_3(1-rn)^2 + 7p_4(1-rn)^3 + 9p_5(1-rn)^4 \tag{26}$$

and

$$H = -p_1 + 3p_2(1-rn) + 15p_3(1-rn)^2 + 35p_4(1-rn)^3 + 63p_5(1-rn)^4 \ . \tag{27}$$

The design of the waveguide Luneburg lens requires a specification of the kind of waveguide mode and its order. For a dense overlay lens on a waveguide on an isolation substrate, the equations governing the relationship between the waveguide effective index of refraction n and the overlay lens thickness t are given by Equations (9) and (11) for the TE modes and TM modes, respectively. When rewritten as explicit form for the lens overlay thickness required to produce certain waveguide effective index, Equation (9) becomes

$$ht = \begin{cases} \tan^{-1}\left[\dfrac{h\left[1 - \frac{\ell}{q}\tan(\ell d)\right] + \frac{ph}{\ell}\left[\frac{\ell}{q} + \tan(\ell d)\right]}{\frac{h^2}{\ell}\left[\frac{\ell}{q} + \tan(\ell d)\right] - p\left[1 - \frac{\ell}{q}\tan(\ell d)\right]}\right] & n<n_3 \\ \tan^{-1}\left[\dfrac{h\left[(q+\ell)e^{2\ell d} + q - \ell\right] + \frac{ph}{\ell}\left[(q+\ell)e^{2\ell d} - q + \ell\right]}{\frac{h^2}{\ell}\left[(q+\ell)e^{2\ell d} - q + \ell\right] - p\left[(q+\ell)e^{2\ell d} + q - \ell\right]}\right] & n\geq n_3. \end{cases} \tag{28}$$

for the TE modes. If all the parameters, p, h, ℓ, q, are replaced by $\frac{p}{n_1^2}, \frac{h}{n_2^2}, \frac{\ell}{n_3^2}, \frac{q}{n_4^2}$, Equation (28) can be employed for the TM modes.

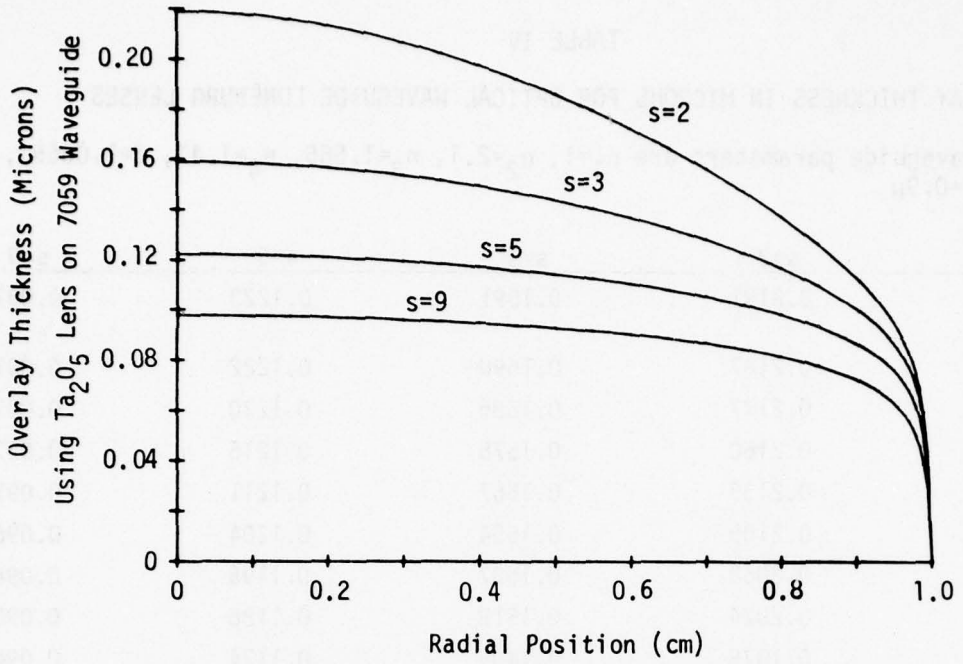

Figure 11. Waveguide Overlay Thickness Profile for Generalized Luneburg Lenses Using Ta_2O_5 on Corning 7059 (d=1.0665μ) on SiO_2 Which is Tabulated in Table IV.

Consequently, a Luneburg lens waveguide thickness profile can be obtained from the above numerical determination of n(r). Some numerical examples have been calculated for a Ta_2O_5 lens overlay having a refractive index of 2.1 using a Corning 7059 waveguide having a refractive index of 1.565 and a thickness of 1.0665μ on a SiO_2 substrate having a refractive index of 1.47 and using a wavefront of 0.9μ. Figure 11 illustrates the waveguide lens thickness profile with the corresponding numerical data tabulated in Table IV for s=2, 3, 5, 9.

To test the accuracy of the approximation of Eq. 20, we have ray traced the s=2 case using Southwell's procedure which provides the wavefront phase errors and the intensity diffraction patterns. Figure 12, Section (a), is a plot showing six rays traced through an s=2 Luneburg lens. Nineteen rays were traced and the resulting wavefront phase error at λ = 0.9μ was determined. This wavefront phase error result is shown in Figure 12, Section(b), with a corresponding intensity diffraction pattern shown on a logarithmic scale in Section(c)of this figure. Note that the refractive index profile as derived from Eq. 20 produces diffraction-limited results.

TABLE IV

OVERLAY THICKNESS IN MICRONS FOR OPTICAL WAVEGUIDE LUNEBURG LENSES

The waveguide parameters are $n_1=1$, $n_2=2.1$, $n_3=1.565$, $n_4=1.47$, $d=1.0665\mu$, and $\lambda=0.9\mu$

r (cm)	s=2	s=3	s=5	s=9
0	0.2191	0.1591	0.1223	0.0979
0.05	0.2187	0.1590	0.1222	0.0979
0.10	0.2177	0.1585	0.1220	0.0978
0.15	0.2160	0.1578	0.1216	0.0975
0.20	0.2135	0.1567	0.1211	0.0972
0.25	0.2105	0.1554	0.1204	0.0968
0.30	0.2068	0.1537	0.1196	0.0963
0.35	0.2024	0.1518	0.1186	0.0957
0.40	0.1975	0.1495	0.1174	0.0949
0.45	0.1920	0.1469	0.1160	0.0940
0.50	0.1860	0.1440	0.1141	0.0930
0.55	0.1794	0.1406	0.1126	0.0918
0.60	0.1722	0.1370	0.1105	0.0905
0.65	0.1646	0.1328	0.1081	0.0888
0.70	0.1563	0.1282	0.1054	0.0869
0.75	0.1472	0.1229	0.1022	0.0846
0.80	0.1374	0.1169	0.0983	0.0817
0.85	0.1262	0.1097	0.0935	0.0780
0.90	0.1130	0.1006	0.0870	0.0727
0.91	0.1099	0.0984	0.0853	0.0713
0.92	0.1067	0.0960	0.0835	0.0697
0.93	0.1031	0.0933	0.0814	0.0679
0.94	0.0993	0.0903	0.0790	0.0657
0.95	0.0949	0.0869	0.0762	0.0632
0.96	0.0898	0.0827	0.0728	0.0601
0.97	0.0835	0.0774	0.0682	0.0559
0.98	0.0749	0.0699	0.0616	0.0499
0.99	0.0597	0.0562	0.0496	0.0395
1.00	0	0	0	0

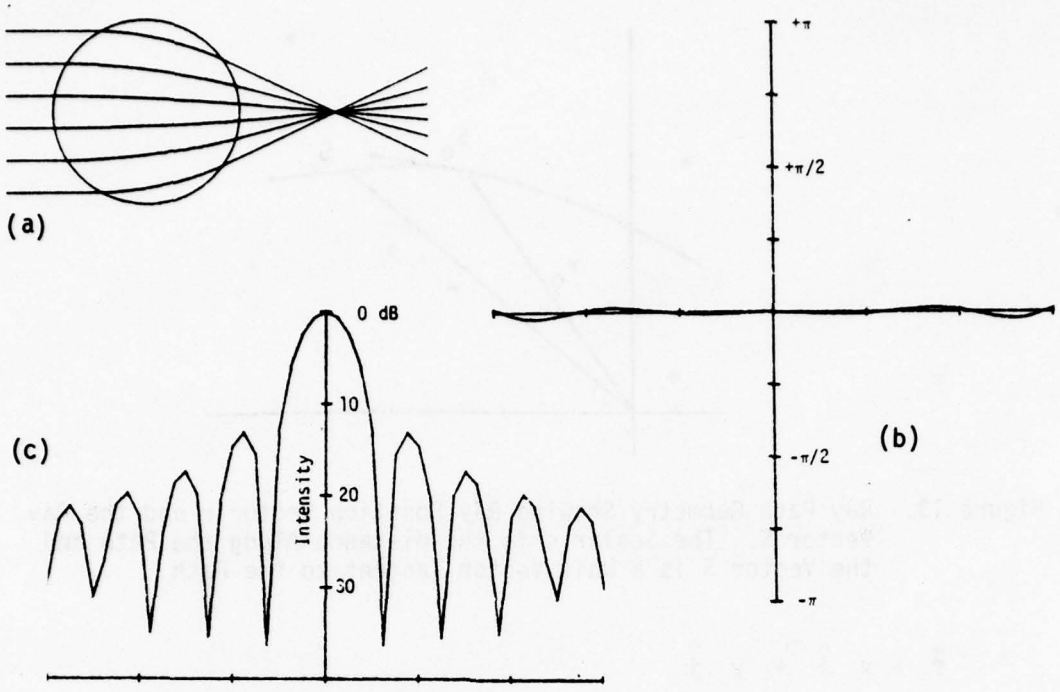

Figure 12. Ray Traces of an s=2 Generalized Luneburg Lens Using the Index Profile Derived from Eq. 14 , the Wavefront Phase Error in the Pupil Plane (b), and the Corresponding Intensity Diffraction Pattern Using a Logarithmic Scale in the Image Plane (c).

4. Inhomogeneous Lens Analysis

Southwell's procedure[22] for gradient-index ray-tracing techniques to evaluate the performance on inhomogeneous optical lenses is derived herein for reference because of its application to generalized waveguide Luneburg lenses. Using the thin-film waveguide parameter including the lens thickness profile, the wavefront phase error and intensity diffraction patterns are derived. The procedure is applied to a classical Luneburg lens index profile for which exact results are known. The procedure yields better than diffraction-limited accuracy within reasonable computer running time. Restricting our interest to lens index profiles having circular symmetry, the ray path position vector $\vec{r}$ shown in Fig. 13 can be described in a coordinate system with its origin at the center of symmetry of the index profile. The position of the ray is described by the components of $\vec{r}$. Defining the ray parameter s as a scalar distance along the ray path measured from an arbitrary reference point on the ray, the unit ray direction vector $\vec{S}$, which is tangent to the ray curve, is therefore

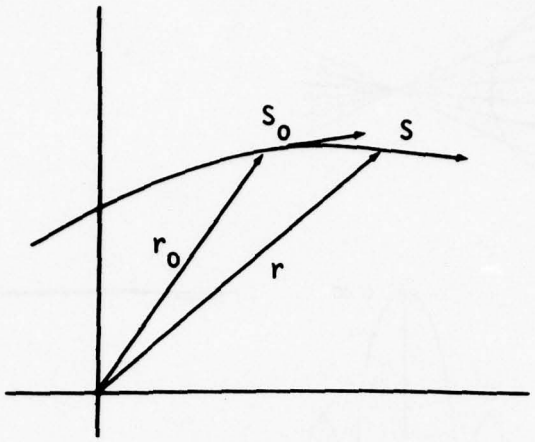

Figure 13. Ray Path Geometry Showing Ray Position Vector r and the Ray Vector S. The Scalar s is the distance Along the Path and the Vector S is a Unit Vector Tangent to the Path.

$$\vec{r} = x\,\hat{i} + y\,\hat{j} \tag{29}$$

$$\vec{S} = \frac{d\vec{r}}{ds} = \alpha\,\hat{i} + \beta\,\hat{j} \tag{30}$$

where α and β are the directional cosines of the ray. The characteristics, namely the position and direction vectors, of the ray at any point $(s+\Delta s)$ may be obtained from the ray characteristics at the previous point (s) by Taylor's series expansion. That is

$$\vec{r}(s_o + \Delta s) = \vec{r}(s_o) + \left.\frac{d\vec{r}}{ds}\right|_{s=s_o} (\Delta s) + \frac{1}{2!}\left.\frac{d^2\vec{r}}{ds^2}\right|_{s=s_o} (\Delta s)^2 + \frac{1}{3!}\frac{d^3\vec{r}}{ds^3}(\Delta s)^3 + \ldots \tag{31}$$

$$\vec{S}(s_o + \Delta s) = \vec{S}(s_o) + \vec{K} \cdot (\Delta s) + \frac{1}{2}\frac{d\vec{K}}{ds} \cdot (\Delta s)^2 + \ldots \tag{32}$$

Noting that $\frac{d\vec{r}}{ds}$ is the ray direction vector, the second derivative of $\vec{r}$ is the curvature vector $\vec{K} = d^2\vec{r}/ds^2 = d\vec{S}/ds$. With these two Taylor expansions, the ray can be traced point by point to any distance, provided that the ray characteristics of an initial point and the necessary derivatives are given.

In order to obtain the necessary derivatives, use can be made of the equation of motion for the ray position in a gradient index medium, which is

$$\frac{d}{ds}\left[n\,\frac{d\vec{r}}{ds}\right] = \nabla n \tag{33}$$

where ∇n is the index gradient

$$\nabla n = \frac{\partial n}{\partial x}\,\hat{i} + \frac{\partial n}{\partial y}\,\hat{j} \quad . \tag{34}$$

Expanding Eq. (33), we obtain the curvature vector

$$\vec{K} = \frac{1}{n}\,[\nabla n - (\nabla n \cdot \vec{S})\,\vec{S}\,] \, . \tag{35}$$

Before obtaining the last required derivative dK/ds, we rewrite Eq. (35), making use of the symmetry in n

$$\vec{K} = f(r)\,[\vec{r} - (\vec{r} \cdot \vec{S})\,\vec{S}\,] \tag{36}$$

where

$$f(r) = \frac{1}{nr}\,\frac{dn}{dr} \quad . \tag{37}$$

Differentiating Eq. (36), we have

$$\frac{d\vec{K}}{ds} = \frac{1}{r}\,\frac{df}{dr}\,(\vec{S} \cdot \vec{r})[\vec{r} - (\vec{r} \cdot \vec{S})\vec{S}] - f[(\vec{r} \cdot \vec{K})\vec{S} + (\vec{r} \cdot \vec{S})\vec{K}] \tag{38}$$

where we have used the general relationships,

$$\frac{dg}{ds} = \vec{S} \cdot \nabla g, \quad \text{and } \nabla g(r) = \frac{1}{r}\,\frac{dg}{dr}\,\vec{r} \tag{39}$$

The ray tracing algorithm, therefore, is as follows:

(1) From the known position and directions (x_o, y_o, α_o, β_o) and index gradient, evaluate the curvature $\vec{K}$ and its derivative, Eqs. (35) and (38) at that point.

(2) Select an incremental step size Δs and evaluate the new position and angle from Eqs. (31) and (32).

(3) Considering our new position and angle as known, go back to Step (1) and repeat the sequence until the exit surface is reached or until the region is encountered when the index gradient vanishes.

We note that this algorithm requires the index, the gradient dn/dr, and the second derivative d^2n/dr^2 at each point. In case of ray tracing for an ideal generalized Luneburg lens, the power series for the index n, dn/dr, and d^2n/dr^2 are given by Eqs. (20), (32) and (33), using the five P parameters. In case of ray tracing from either a measured or a computed thin film Luneburg lens thickness profile, the index profile is obtained from thickness profile as numerical data points. The derivatives dn/dr and d^2n/dr^2 can be readily differentiated numerically from the index profile data.

It is necessary to consider the problem of precisely locating the ray position as it exits the lens region because any error here will result at a focal plane error; i.e., aberration; of the same magnitude. For computational efficiency, the step size Δs is large compared to the required tolerances. Thus, an interpolation is required once the ray has stepped outside the lens.

The procedure we take for locating the edge is as follows. We first define the function F

$$F = r_o^2 - r^2 \tag{40}$$

where r_o is the lens radius and $r^2 = x^2 + y^2$ as determined by the ray position. By considering the last point inside the lens as the base point, we see that r becomes a function of the step size Δs. The function F then may be considered a function of Δs, $F = F(\Delta s)$. The problem of locating the edge is then solved by finding the root Δs that makes $F(\Delta s) = 0$. This may be done using Newton's method

$$(\Delta s)_e = (\Delta s)_o - F \Big/ \frac{dF}{d(\Delta s)}\Big|_{\Delta s = \Delta s_o} \quad . \tag{41}$$

Since the functional dependence of F on Δs is given through Eq. (31), we have

$$\frac{\partial F}{\partial(\Delta s)} = -2r \quad \frac{dr}{d(\Delta s)} = -2\vec{r} \cdot \vec{s} \quad . \tag{42}$$

Initially $(\Delta s)_0 = 0$ at our base point inside the lens and the derivative in Eq. (41) has already been evaluated. It is thus a simple matter to apply Eq. (41) until $|F| < 10^{-8}$ or some prescribed small quantity.

There are two factors to be considered when determining a value for the step size Δs. They are computing time and accuracy. When tracing diffraction-limited systems, the ray trace must provide an exit height accurate to some fraction of a wavelength. This may require extremely small step size and, consequently, long computing time.

With a classic Luneberg lens profile, the ray tracing error due to finite incremental step size Δs can be evaluated because the theoretical result will have no aberrations. Southwell has shown that for diffraction limited ray tracing, the ray trace error must be smaller than a few wavelength and that the ray trace step size may be approximately a few tens of wavelength. To reduce the computing time, a compensation scheme based on extrapolation of ray trace error due to finite step size has been developed by Southwell.

The spot diagrams determined by ray tracing may be employed to determine the optical phase front error through the system. These phase errors are then expressed in a pupil function (which is a function of the pupil coordinates) and is then Fourier transformed and squared to form the image diffraction pattern.

To derive the wavefront errors from ray trace intercept data, we draw upon the theory of Hamilton's angle characteristic function $T(\beta)$, which represents the optical path length along the path through the system described by the entrance height y_0. This function is also expressed as a function of the exit angle β. The theory states that the ray intercept error y in the image plane is given by

$$y = -\frac{\partial T}{\partial \beta} \quad . \tag{43}$$

To utilize this theory, we assume that the optical path length may be expressed as a power series in the exit angle coordinate β,

$$T = c_1\beta^2 + c_2\beta^4 + c_3\beta^6 + \ldots \tag{44}$$

Since we are dealing with symmetric systems we consider only even powers of β. The ray trace intercepts y_i and the associated angles β_i can be obtained by ray tracing. After a few traces, the y_i, β_i are fitted to a least square deviation fashion to the function

$$\frac{\partial T}{\partial \beta} = (2c_1\beta + 4c_2\beta^3 + 6c_3\beta^5 + \ldots) . \tag{45}$$

This procedure determines the c coefficients for the optical path length in Eq. (44).

Prior to fitting the intercept data to the expression (45), it is convenient to first normalize the β's. By doing this, the wavefront error function (44) is then automatically expressed in terms of normalized aperture coordinates. The preceding statement is valid strictly for systems with a linear relationship between aperture and exit angle. Although this is only approximately true, it is sufficiently close for our case.

The phase error is $2\pi/\lambda$ times the optical path error. Figure 14(a) is a plot of the phase error of the Luneberg lens of Figure 7 using extrapolation on the rays with $\Delta s = 0.1$ cm for the initial step size. Since we expect zero phase error, the amount shown represents the residual ray tracing error. We note that it is considerably less than $\pi/4$ and consequently represents a diffraction-limited wavefront.

The pupil function is given by the expression

$$P = \exp[i2\pi T(y/y_0)/\lambda], \tag{46}$$

where the function T is expressed in terms of normalized aperture position y/y_0 . The square of the Fourier transform of P yields the diffraction pattern in the image plane. This is performed using the discrete fast Fourier transform algorithm. Figure 14(a) is the diffraction pattern for the "classic" Luneburg lens as traced in Figures 7 and 14(a).

To further test the system, we moved the detector plane slightly away from the edge of the lens and repeated the evaluation. The corresponding wavefront phase error and its diffraction pattern are depicted in Figure 14(b).

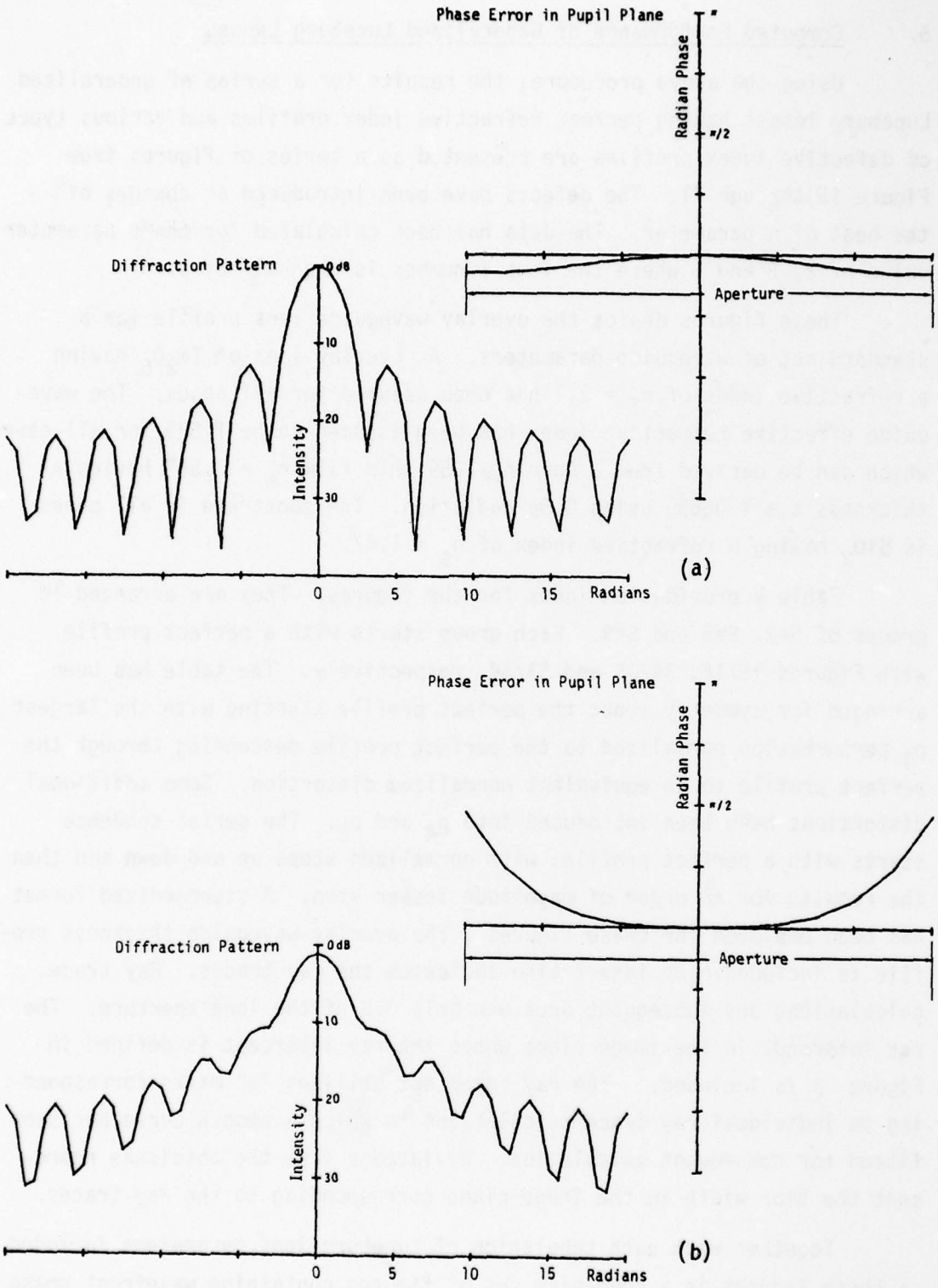

Figure 14. Wavefront Phase Error and Corresponding Intensity Diffraction Pattern for "Classic" Geodesic Lens Ray Traced in Figure 7 for Perfect Radial Profile (a) and Where the Image Plane Has Been Displaced by λ Yielding the Defocus Aberration (b).

5. Computed Performance of Generalized Luneburg Lenses

Using the above procedure, the results for a series of generalized Luneburg lenses having perfect refractive index profiles and various types of defective index profiles are presented as a series of figures from Figure 15 through 71. The defects have been introduced as changes of the best of n parameter. The data has been calculated for the s parameter value of 2, 5 and 9 where the lens f-number is one-half of s.

These figures depict the overlay waveguide lens profile for a standard set of waveguide parameters. An overlay lens of Ta_2O_5 having a refractive index of $n_1 = 2.1$ has been assumed for all cases. The waveguide effective refractive index has been assumed to be 1.535 for all cases which can be derived from a Corning 7059 thin film $n_w = 1.565$ having a thickness $t = 1.0665\mu$ using 0.9μ radiation. The substrate in all cases is SiO_2 having a refractive index of $n_s = 1.47$.

Table V provides an index for the figures. They are arranged in groups of S=2, S=5 and S=9. Each group starts with a perfect profile with Figures 15/16, 34/35 and 53/54, respectively. The table has been arranged for symmetry about the perfect profile starting with the largest p_1 perturbation normalized to the perfect profile descending through the perfect profile to an equivalent normalized distortion. Some additional distortions have been introduced into p_4 and p_2. The serial sequence starts with a perfect profile, with normalized steps up and down and then the results for an order of magnitude lesser step. A standardized format has been employed for these figures. The overlay waveguide thickness profile is included. An insert also indicates the ray traces. Ray trace calculations and subsequent data use only 0.8 of the lens aperture. The ray intercept in the image plane where the ray intercept is defined in Figure 9 is included. The ray intercept utilizes "x" marks corresponding to individual ray trace calculations to which a smooth curve has been fitted for subsequent calculation. Deviations from the abscissae represent the blur width in the image plane corresponding to the ray traces.

Together with each tabulation of Luneburg lens parameters included in these figures is a companion set of figures containing wavefront phase error and the corresponding intensity diffraction pattern. The wavefront phase error and intensity diffraction pattern are presented for the

TABLE V. INDEX OF FIGURES FOR PERFECT AND DISTORTED LUNEBURG LENS PROFILES
(Arranged for Symmetry About the Perfect Profile with Decreasing P_1)

Lens Distortion	S=2	S=5	S=9
$1.05P_1$, $1.35P_2$	Fig. 29/30	Fig. 48/49	Fig. 67/68
$1.04P_1$, $10.0P_4$	Fig. 23/24	Fig. 42/43	Fig. 61/62
$1.0004P_1$, $1.1P_4$	Fig. 27	Fig. 46	Fig. 65
$1.02P_n$	Fig. 17/18	Fig. 36/37	Fig. 55/56
$1.0002P_n$	Fig. 21	Fig. 40	Fig. 59
Perfect Profile	Fig. 15/16	Fig. 34/35	Fig. 53/54
$0.9998P_n$	Fig. 22	Fig. 41	Fig. 60
$0.98P_n$	Fig. 19/20	Fig. 38/39	Fig. 57/58
$0.9996P_1$, $-1.1P_4$	Fig. 28	Fig. 47	Fig. 66
$0.96P_1$, $-10.0P_4$	Fig. 25/26	Fig. 44/45	Fig. 63/64
$0.9995P_1$, $0.997P_2$	Fig. 33	Fig. 52	Fig. 71
$0.95P_1$, $0.7P_2$	Fig. 31/32	Fig. 50/51	Fig. 69/70

paraxial focus. Data for lenses containing a distorted profile include the perfect overlay waveguide lens thickness profile together with the defective profile. For some cases where S=5 and S=9, the distortion is not apparent, however, is listed, and its physical effect will be apparent by referring to the corresponding S=2 case. Inspection of Figures 16, 35 and 54 for S=2, S=5 and S=9, respectively, shows the wavefront phase error and the corresponding intensity diffraction pattern. The

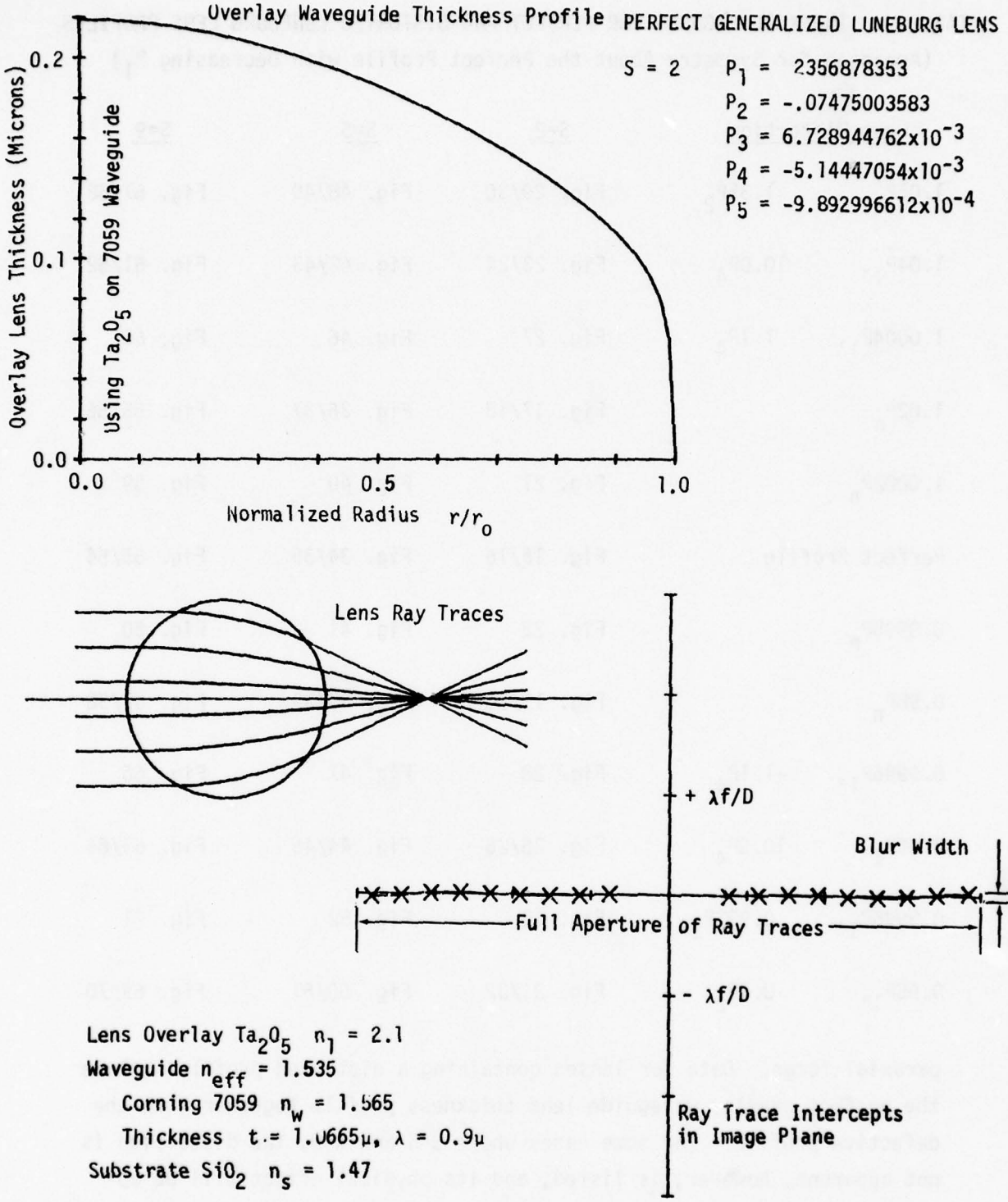

Figure 15. Tabulation of Generalized Luneburg Lens Parameters with Corresponding Overlay Waveguide Lens Thickness Radial Profile, Ray Traces through this Lens and the Intercept Error in the Image Plane, S = 2 (Perfect Luneburg Lens).

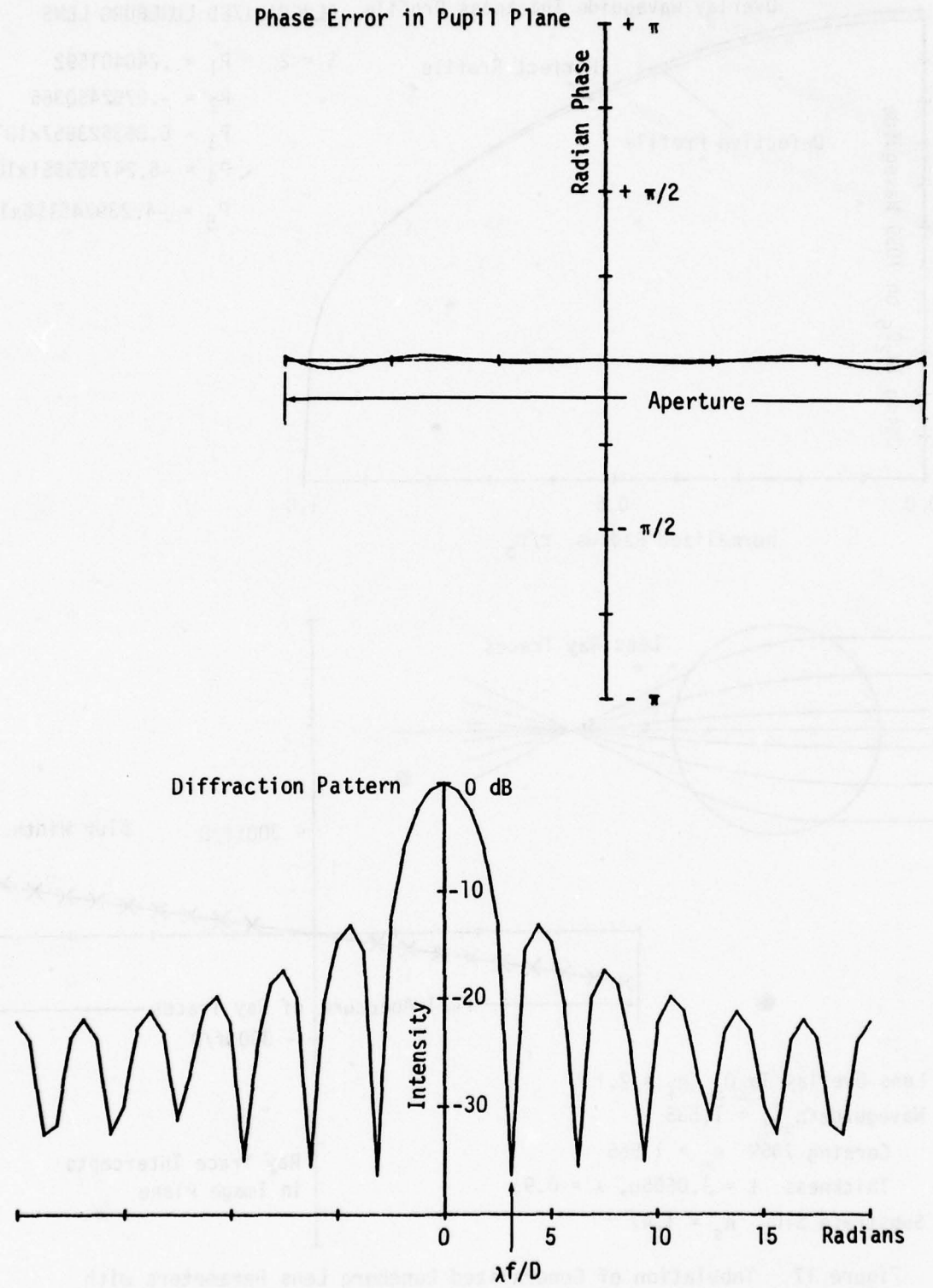

Figure 16. Wavefront Phase Error and Corresponding Intensity Diffraction Pattern for Generalized Luneburg Lens Delineated in Figure 15.

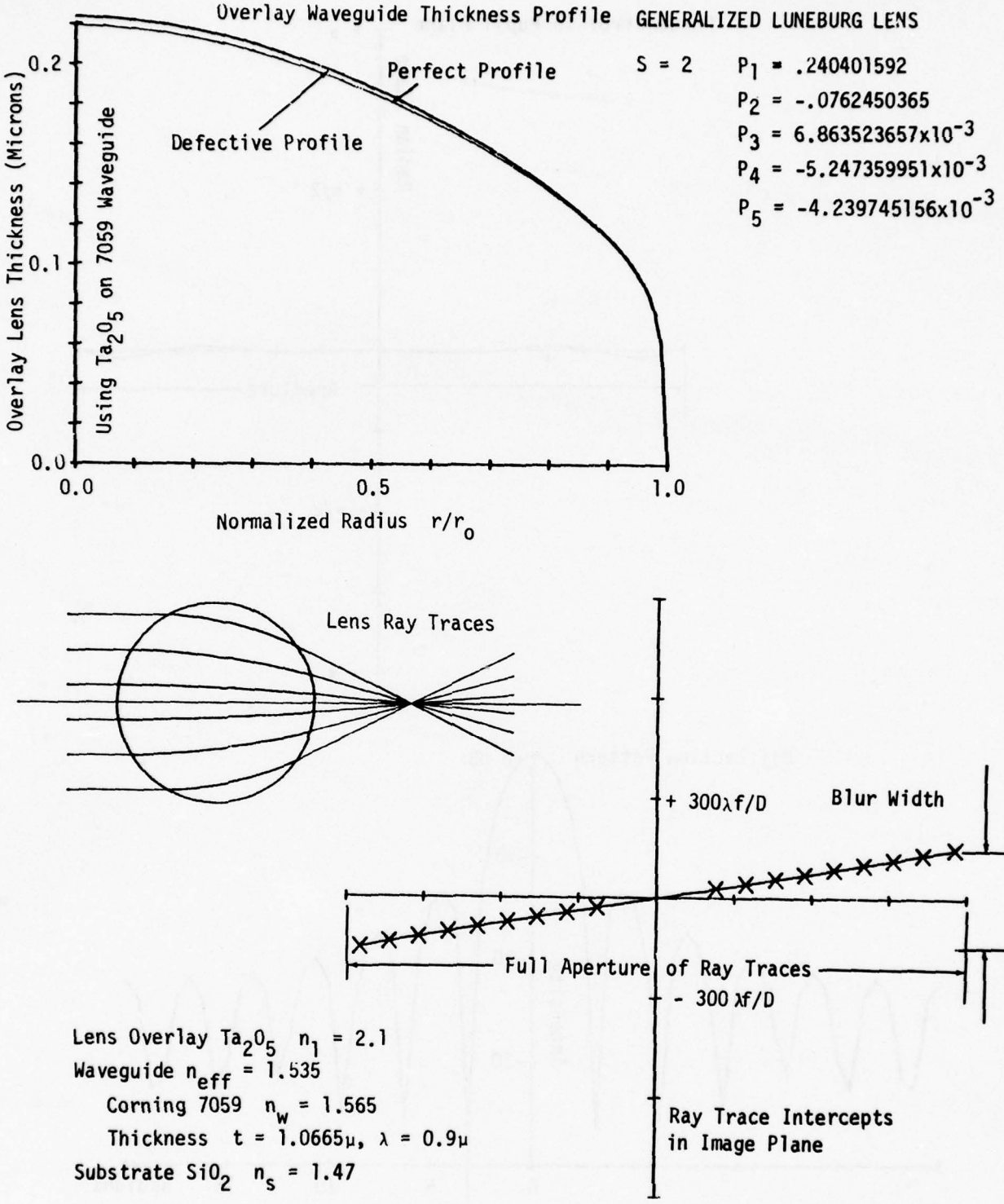

Figure 17. Tabulation of Generalized Luneburg Lens Parameters with Corresponding Overlay Waveguide Lens Thickness Radial Profile, Ray Traces through this Lens and the Intercept Error in the Image Plane, S = 2 (1.02 P_1, 1.02 P_2, 1.02 P_3, 1.02 P_4, 4.2856 P_5).

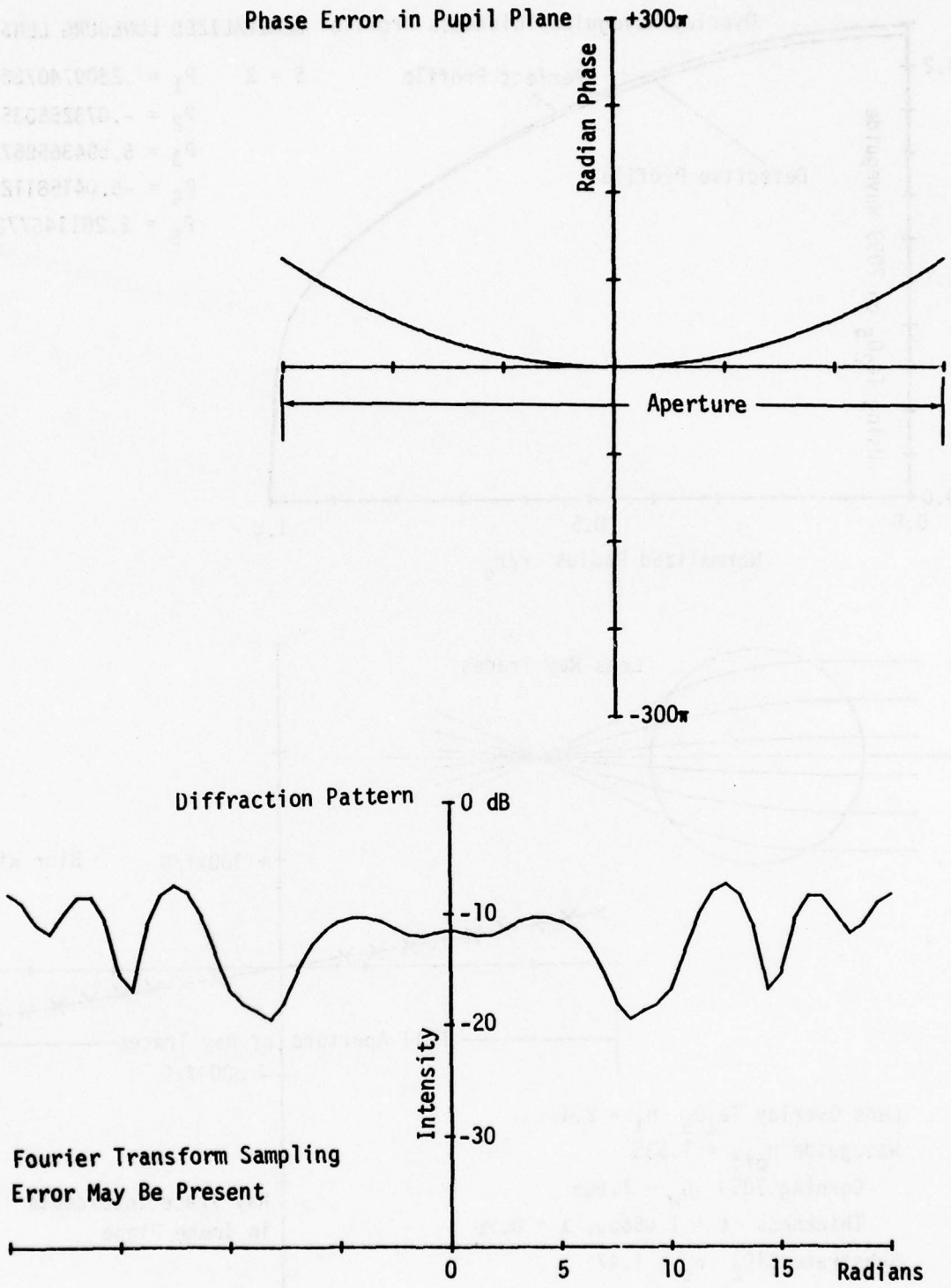

Figure 18. Wavefront Phase Error and Corresponding Intensity Diffraction Pattern for Generalized Luneburg Lens Delineated in Figure 17.

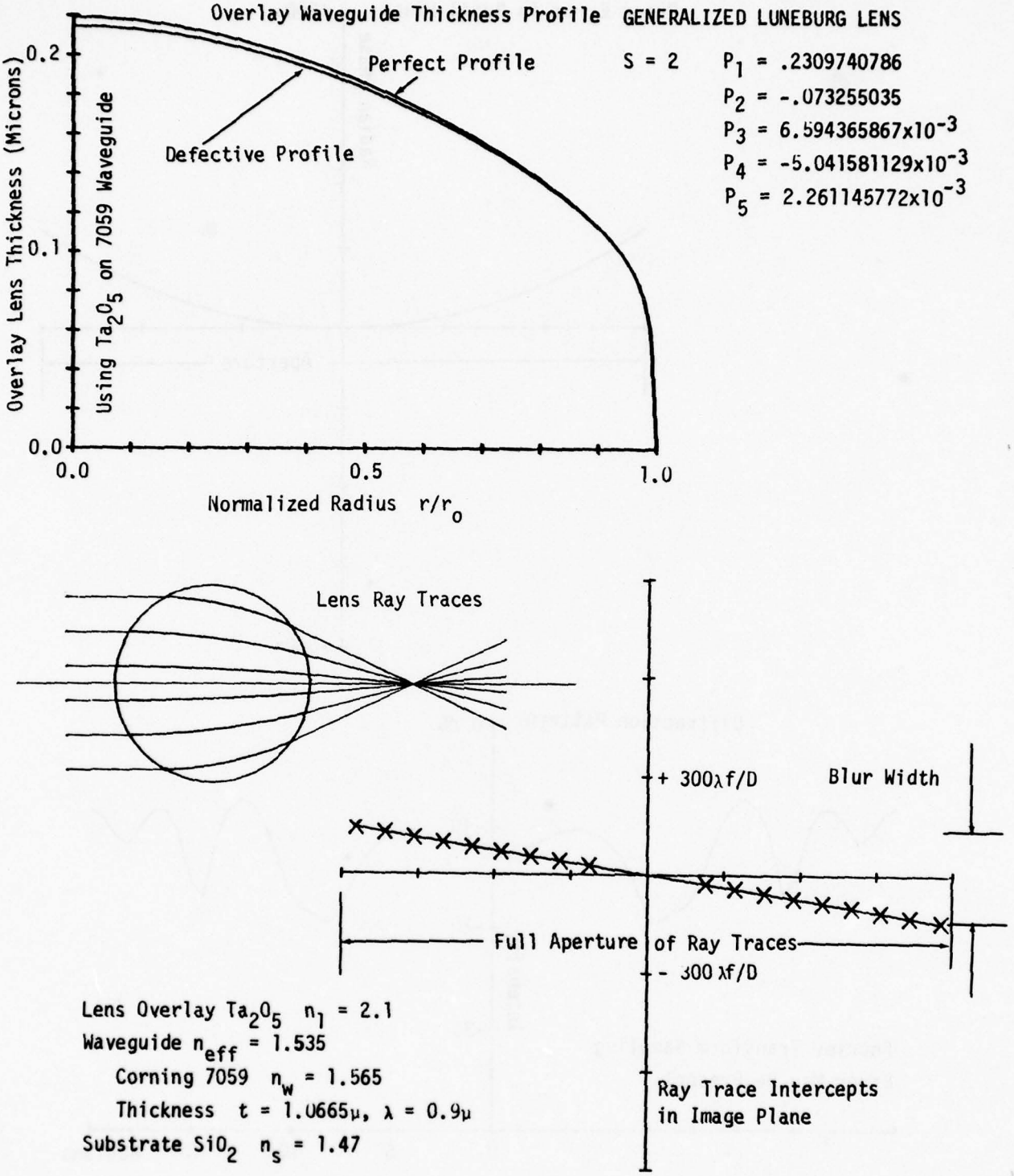

Figure 19. Tabulation of Generalized Luneburg Lens Parameters with Corresponding Overlay Waveguide Lens Thickness Radial Profile, Ray Traces through this Lens and the Intercept Error in the Image Plane, S = 2 (.98 P_1, .98 P_2, .98 P_3, .98 P_4, -2.2856 P_5).

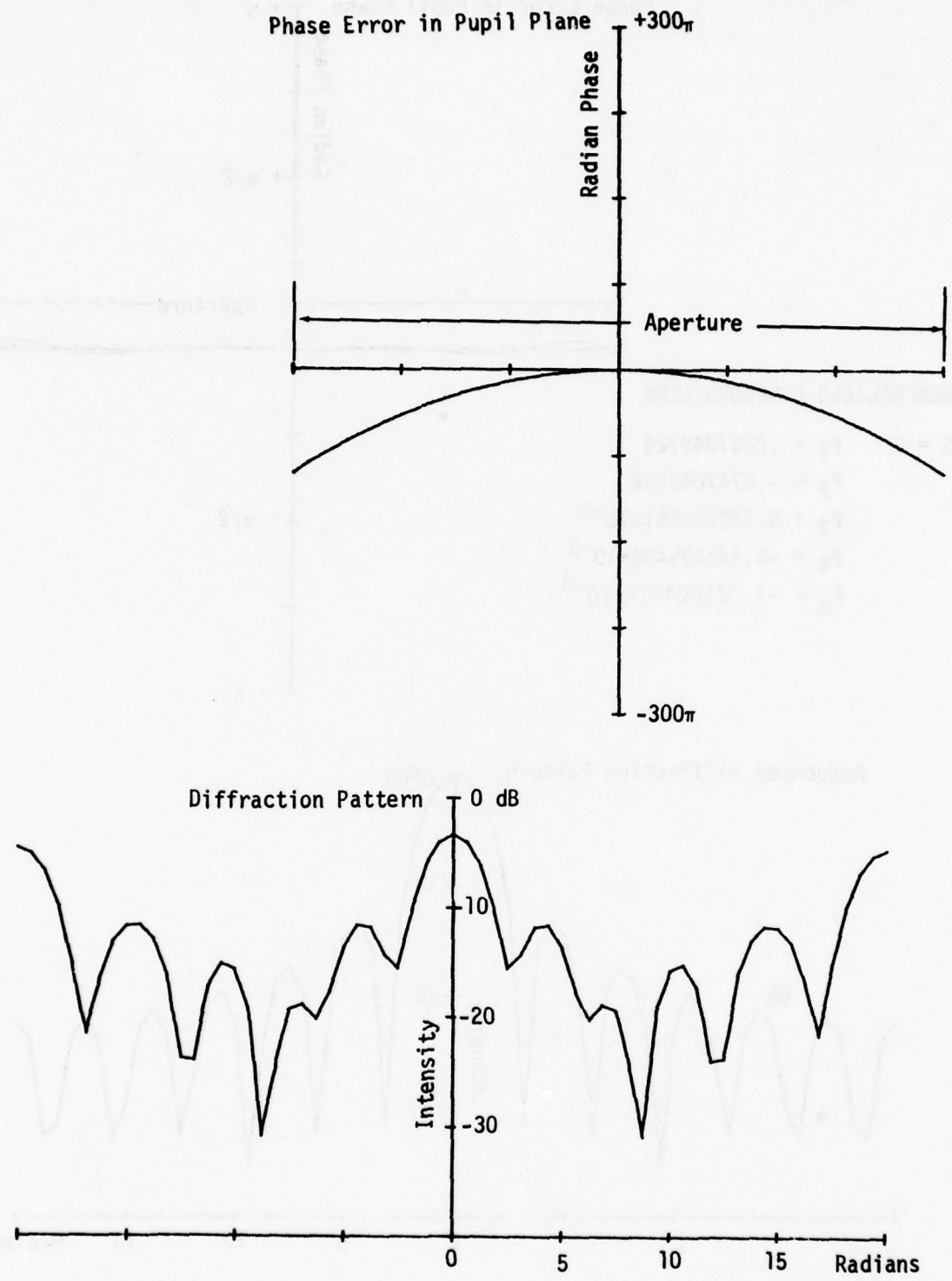

Figure 20. Wavefront Phase Error and Corresponding Intensity Diffraction Pattern for Generalized Luneburg Lens Delineated in Figure 19.

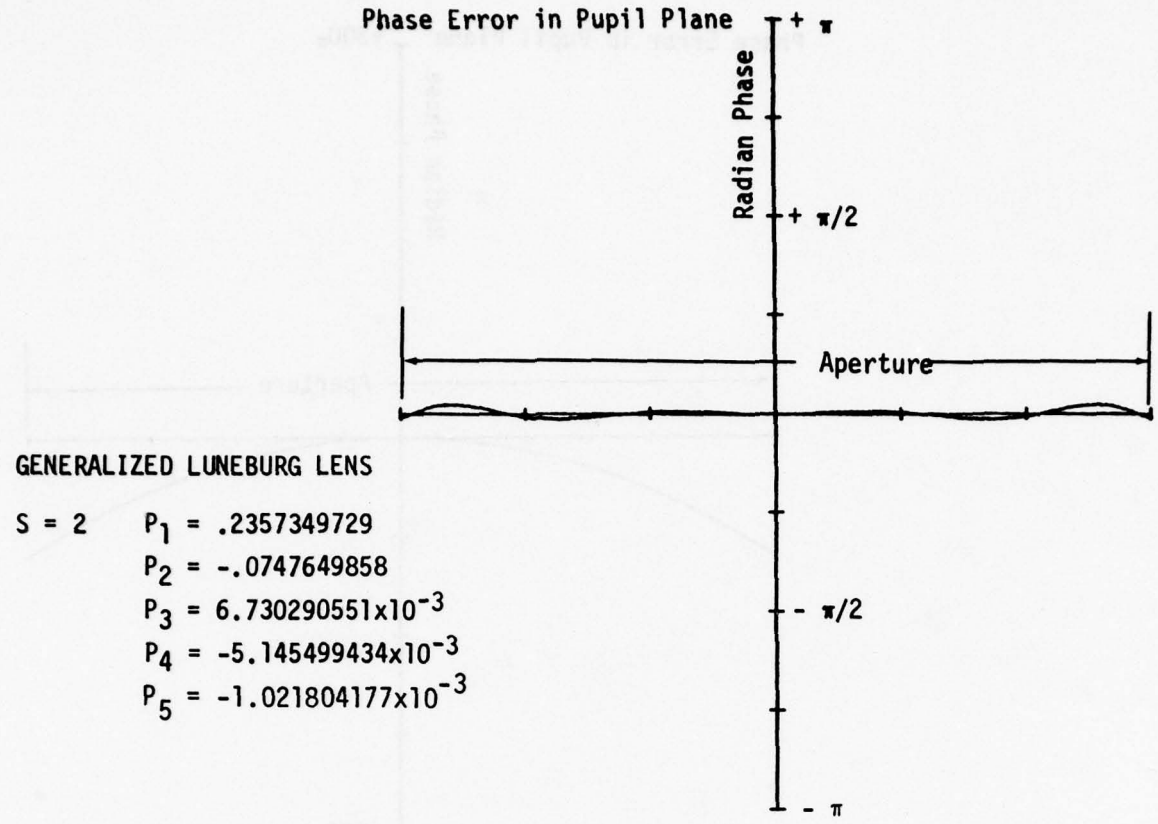

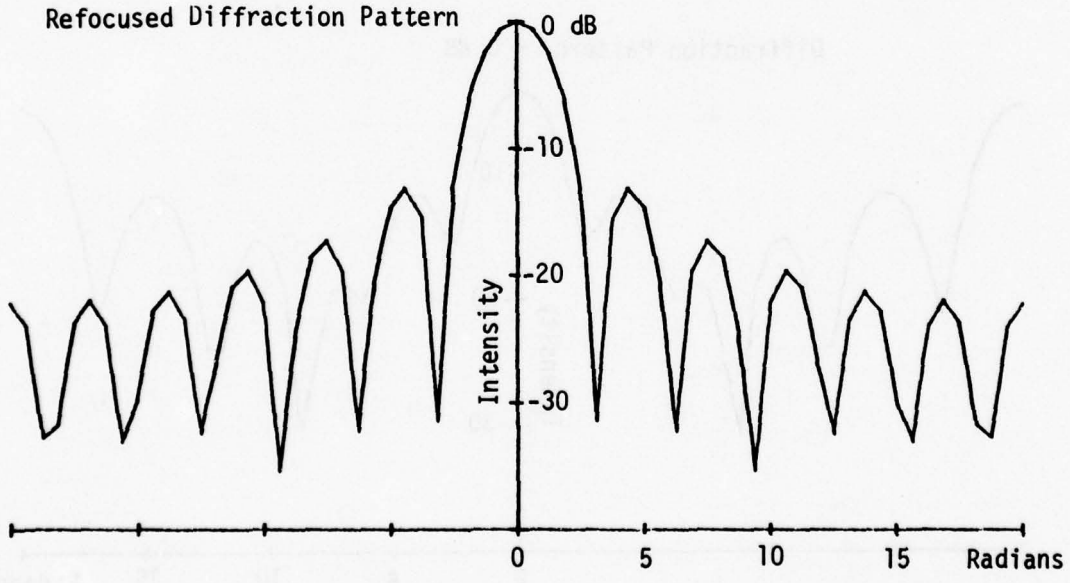

Figure 21. Wavefront Phase Error and Corresponding Intensity Diffraction Pattern for Generalized Luneburg Lens Delineated in Figure 17, S = 2 (1.0002 P_1, 1.0002 P_2, 1.0002 P_3, 1.0002 P_4, 1 .0328 P_5).

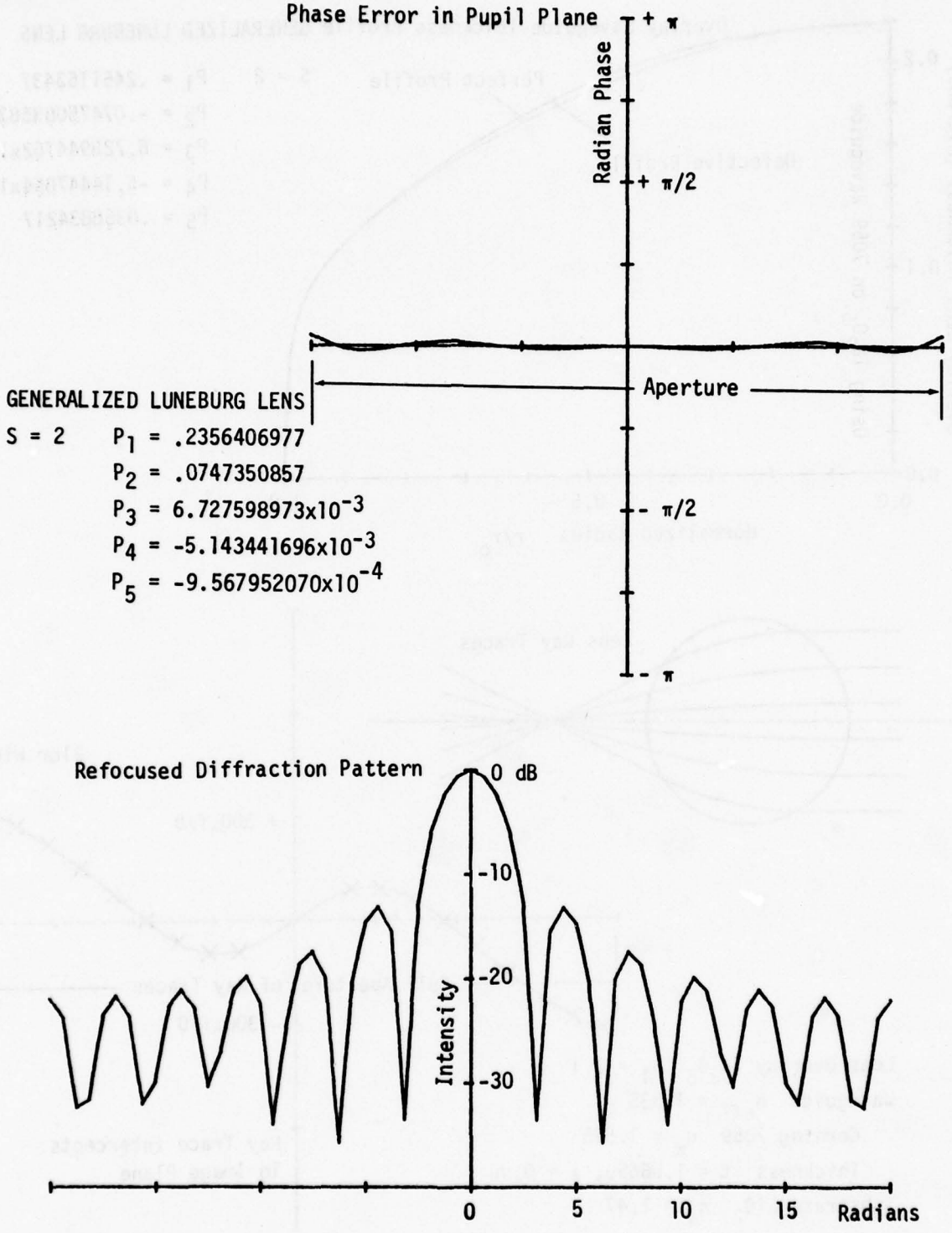

Figure 22. Wavefront Phase Error and Corresponding Intensity Diffraction Pattern for Generalized Luneburg Lens Delineated in Figure 19, S = 2 (.9998 P_1, .9998 P_2, .9998 P_3, .9998 P_4, .9671 P_5).

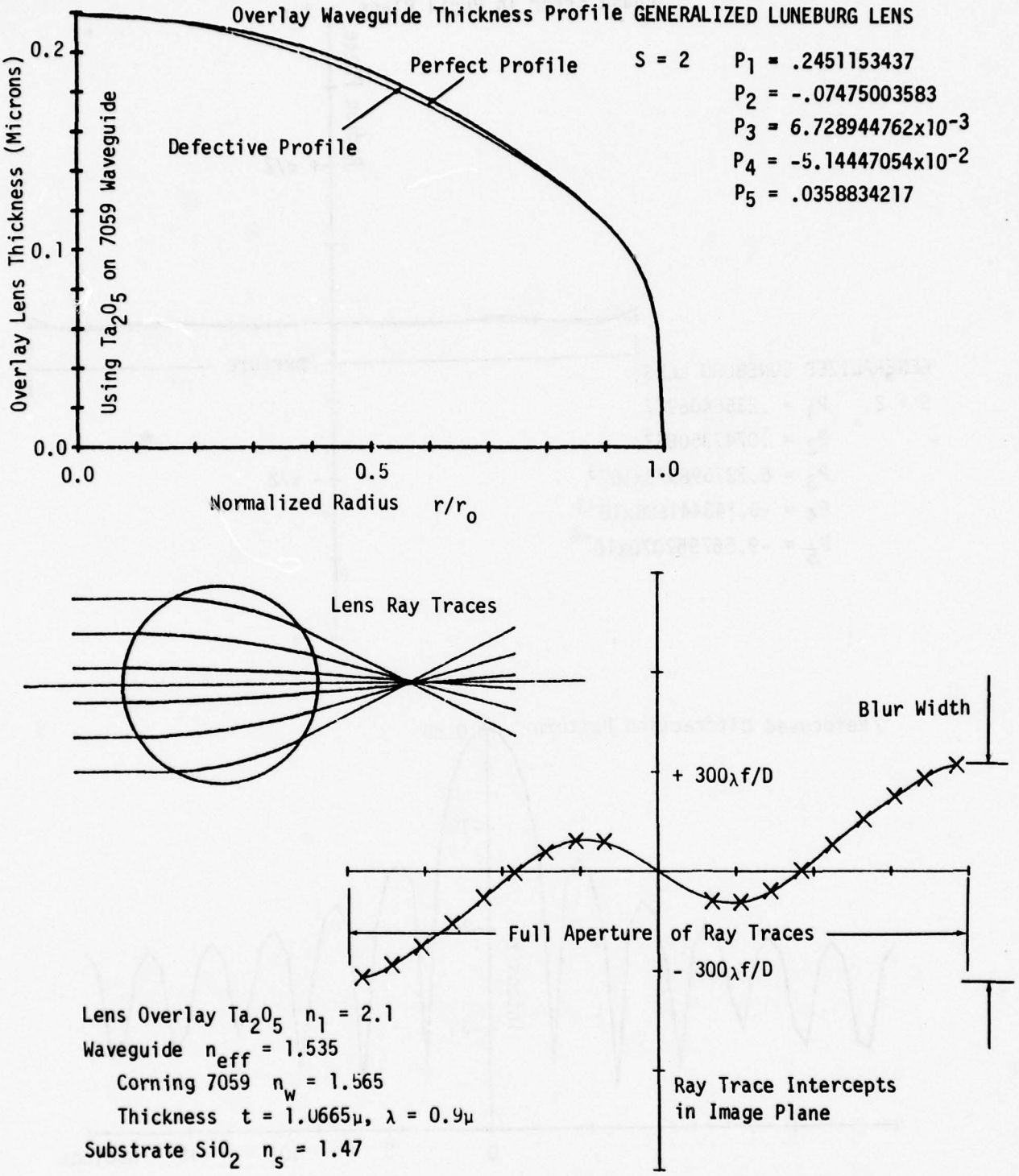

Figure 23. Tabulation of Generalized Luneburg Lens Parameters with Corresponding Overlay Waveguide Lens Thickness Radial Profile, Ray Traces through this Lens and the Intercept Error in the Image Plane, S = 2 (1.04 P_1, 10 P_4, -36.2715 P_5).

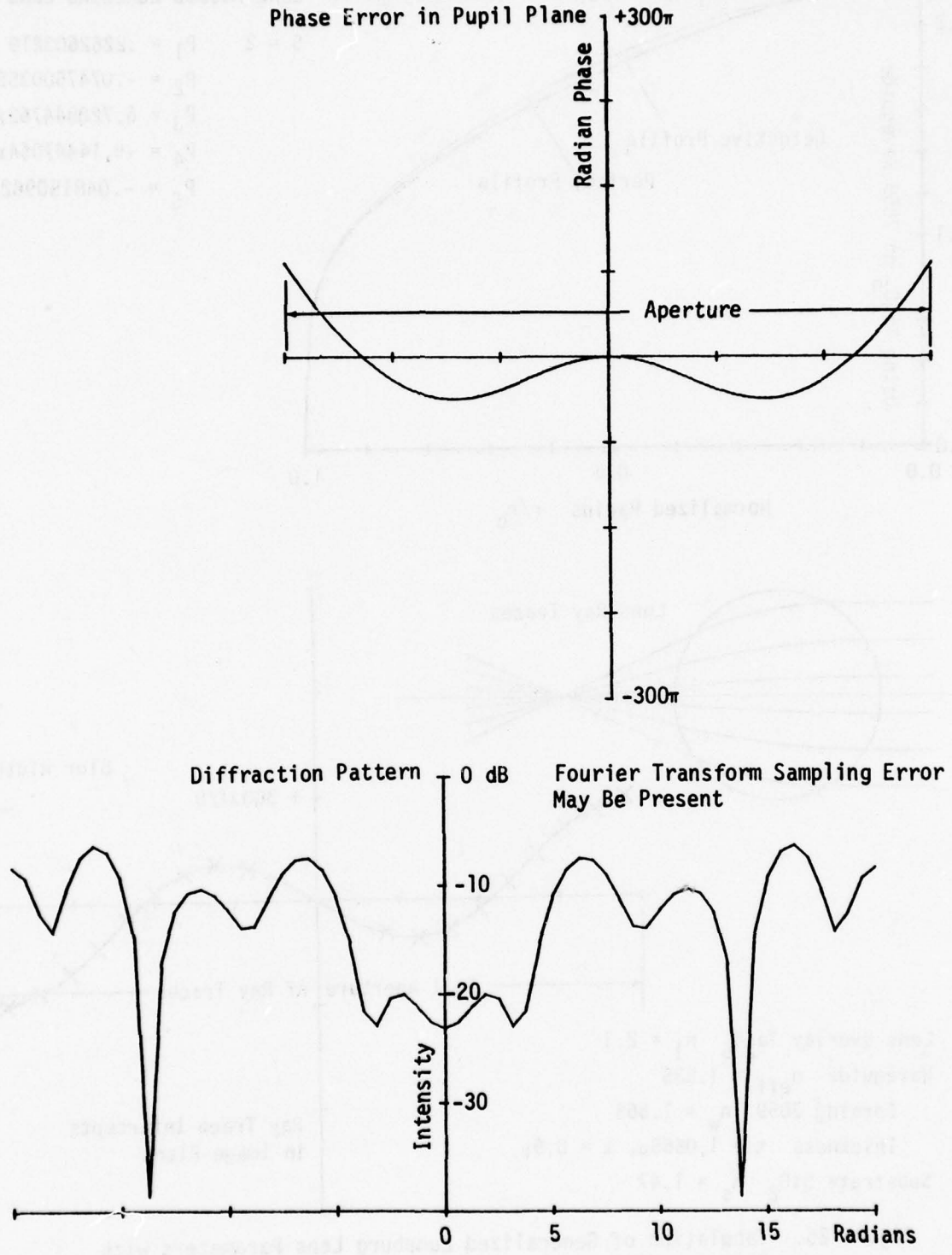

Figure 24. Wavefront Phase Error and Corresponding Intensity Diffraction Pattern for Generalized Luneburg Lens Delineated in Figure 23.

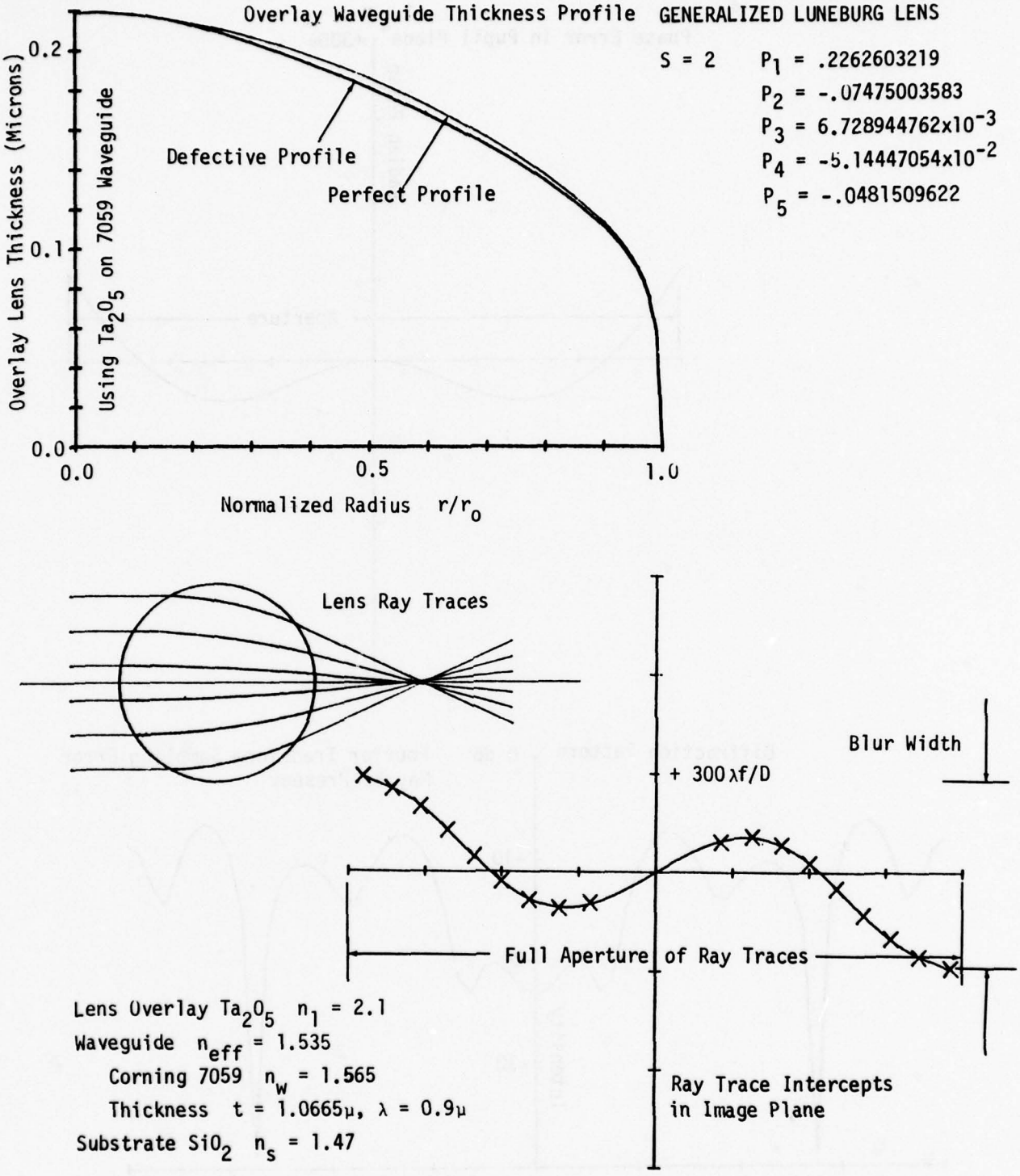

Figure 25. Tabulation of Generalized Luneburg Lens Parameters with Corresponding Overlay Waveguide Lens Thickness Radial Profile, Ray Traces through this Lens and the Intercept Error in the Image Plane, S = 2 (.96 P_1, P_2, P_3, -10 P_4, 48.6717 P_5).

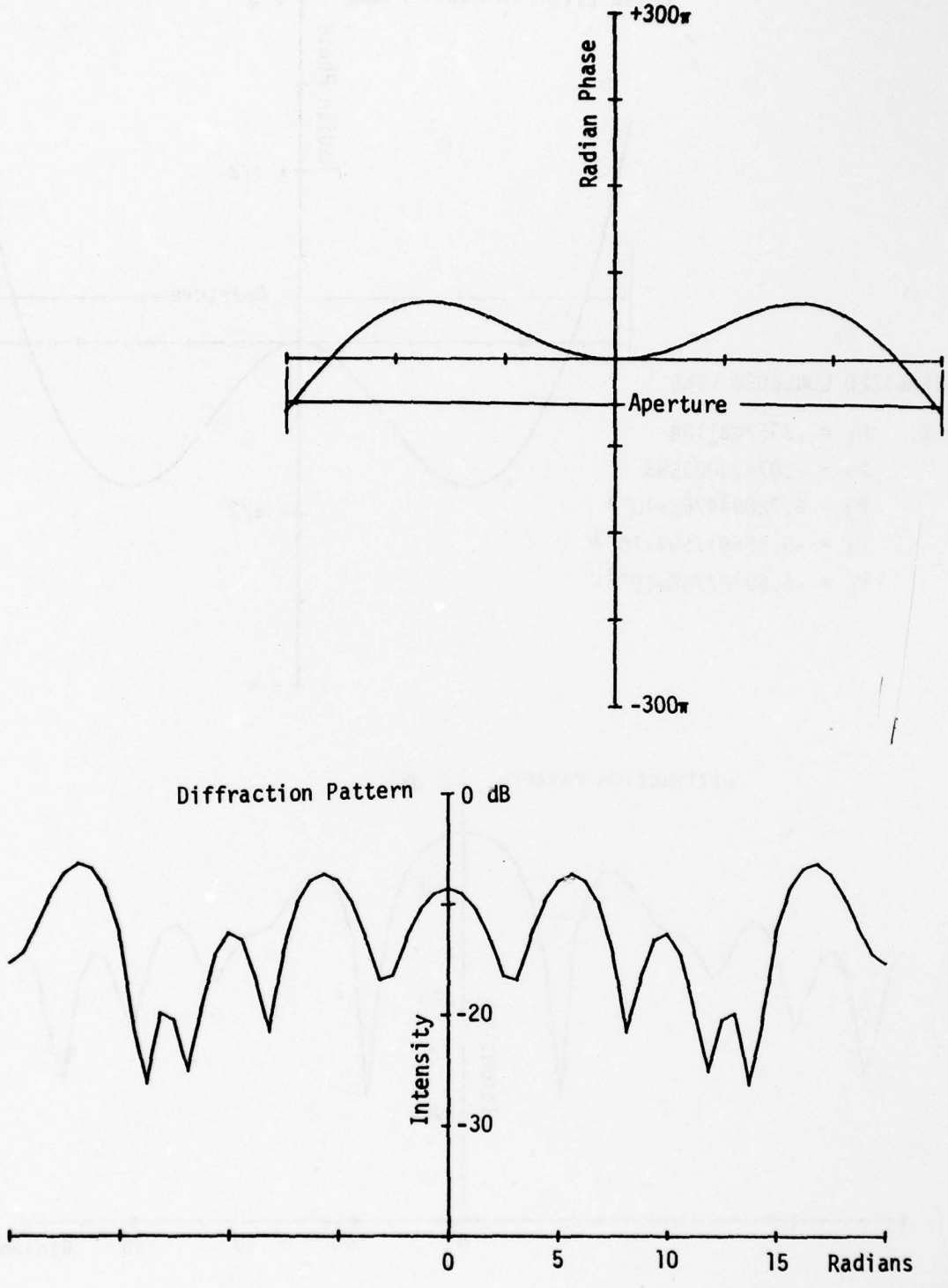

Figure 26. Wavefront Phase Error and Corresponding Intensity Diffraction Pattern for Generalized Luneburg Lens Delineated in Figure 25.

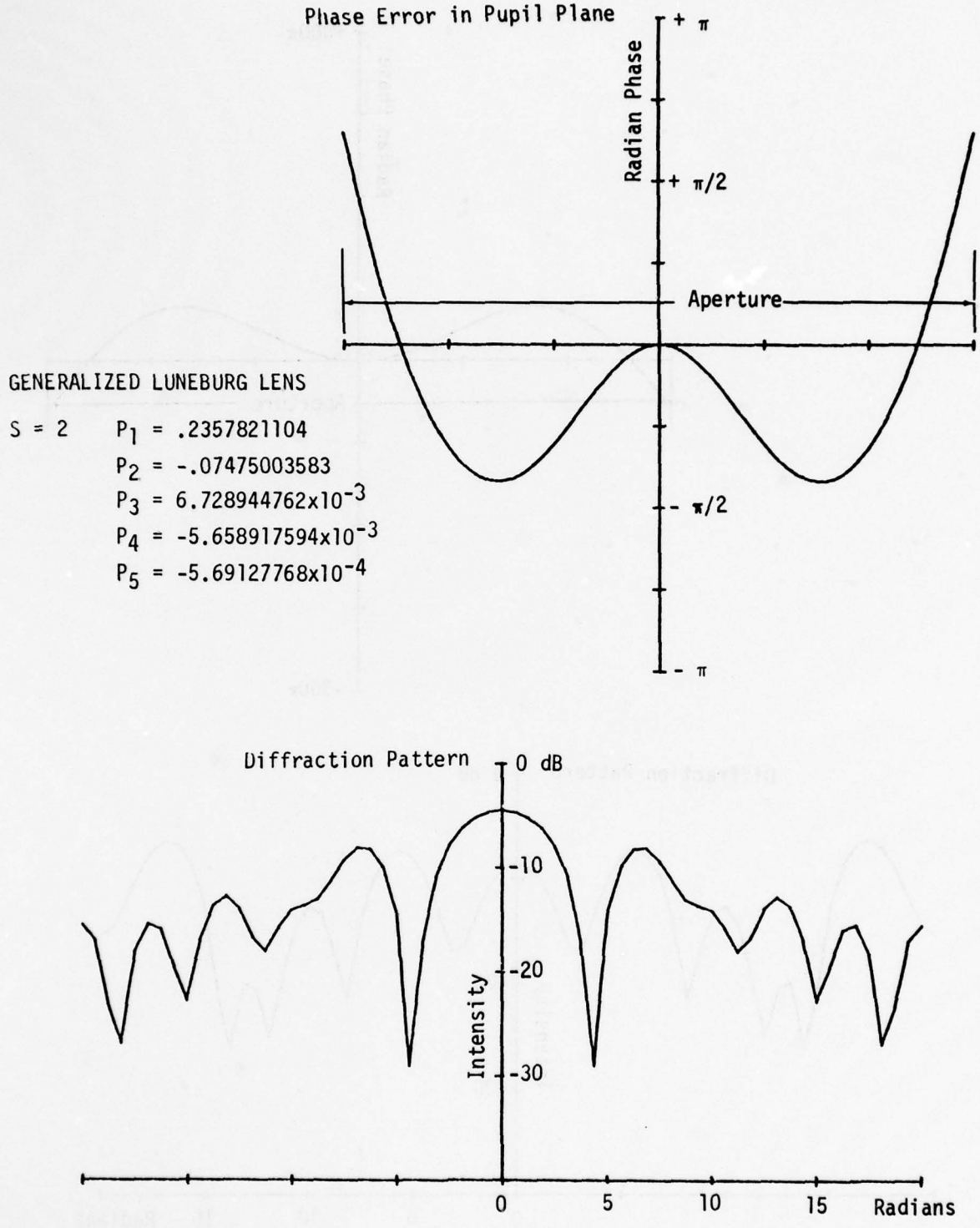

Figure 27. Wavefront Phase Error and Corresponding Intensity Diffraction Pattern for Generalized Luneburg Lens Delineated in Figure 23, S = 2 (1.0004 P_1, 1.1 P_4, .5752 P_5).

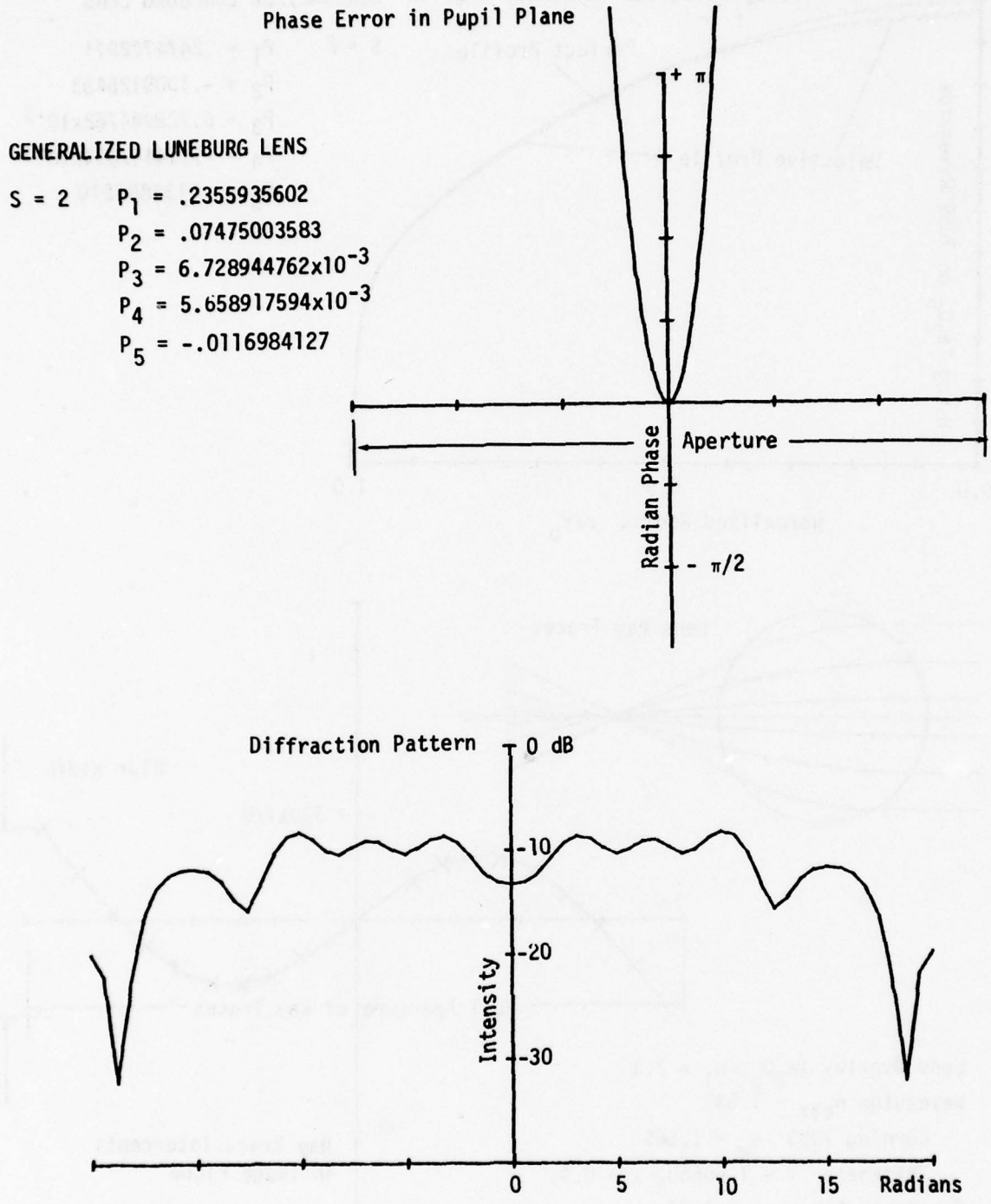

Figure 28. Wavefront Phase Error and Corresponding Intensity Diffraction Pattern for Generalized Luneburg Lens Delineated in Figure 25, S = 2 (.9996 P_1, P_2, P_3, -1.1 P_4, 11.8249 P_5).

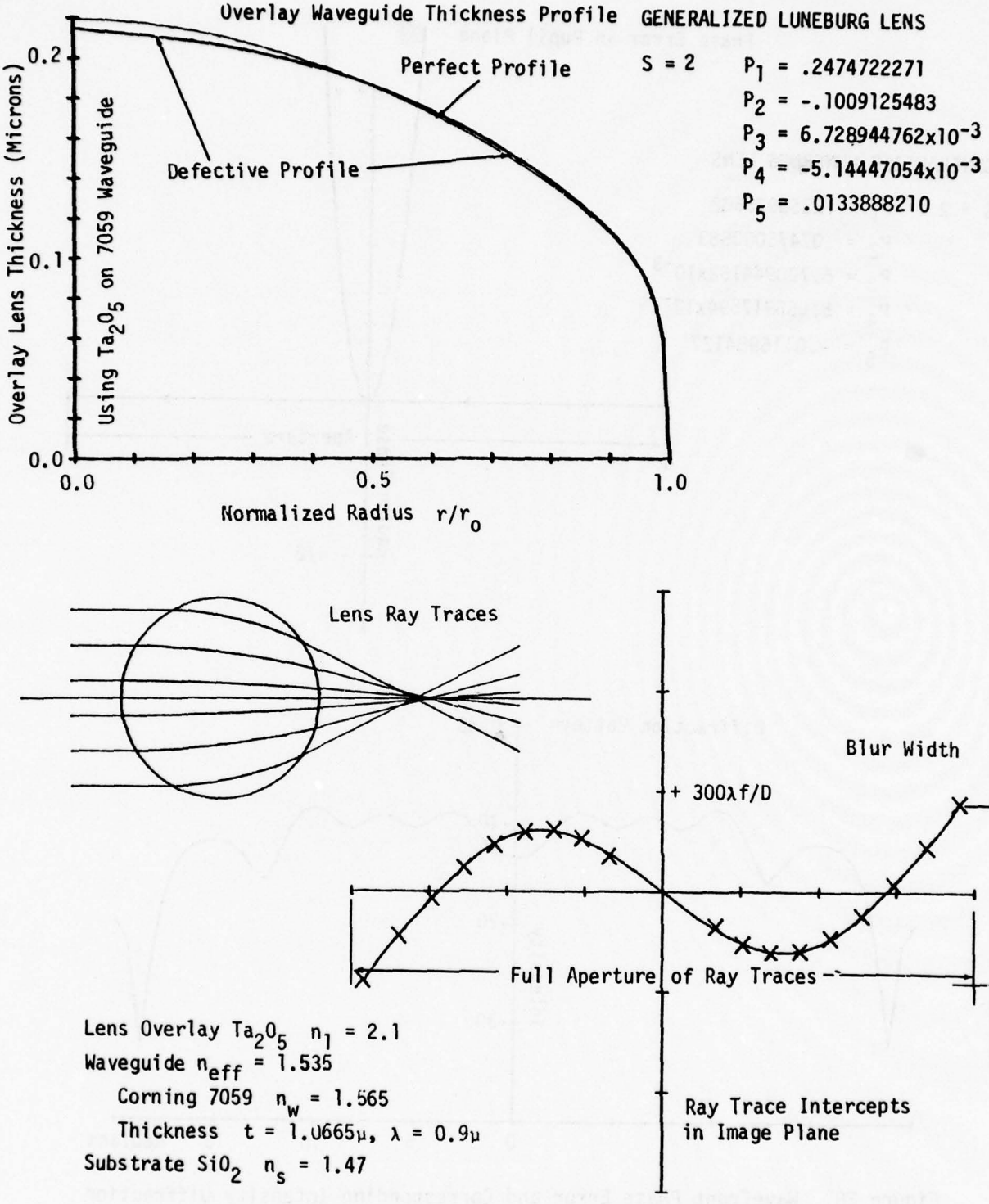

Figure 29. Tabulation of Generalized Luneburg Lens Parameters with Corresponding Overlay Waveguide Lens Thickness Radial Profile, Ray Traces through this Lens and the Intercept Error in the Image Plane, S = 2 (1.05 P_1, 1.35 P_2, -13.5336 P_5).

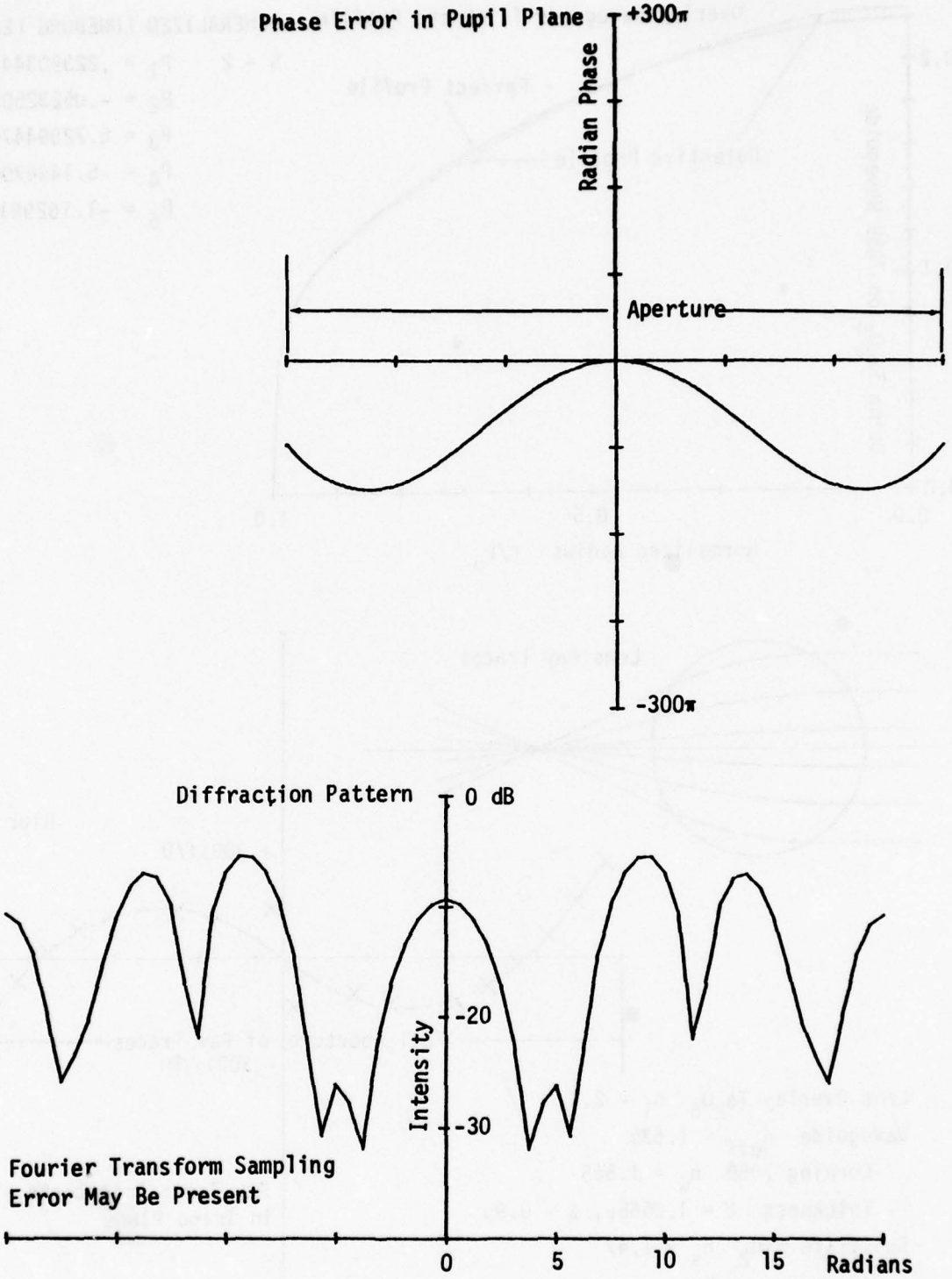

Figure 30. Wavefront Phase Error and Corresponding Intensity Diffraction Pattern for Generalized Luneburg Lens Delineated in Figure 29.

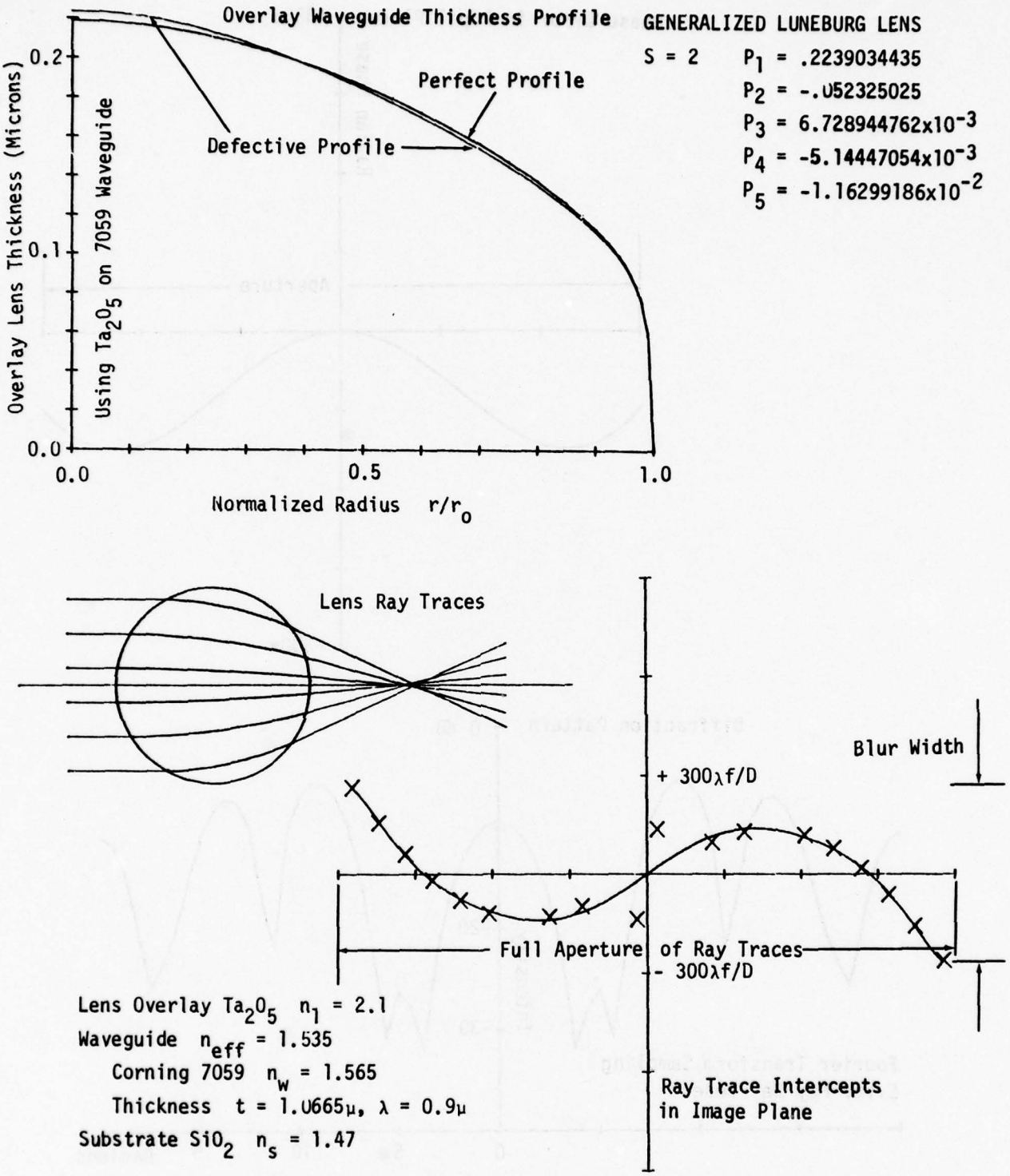

Figure 31. Tabulation of Generalized Luneburg Lens Parameters with Corresponding Overlay Waveguide Lens Thickness Radial Profile, Ray Traces through this Lens and the Intercept Error in the Image Plane, S = 2 (.95 P_1, .7 P_2, 11.7550 P_5).

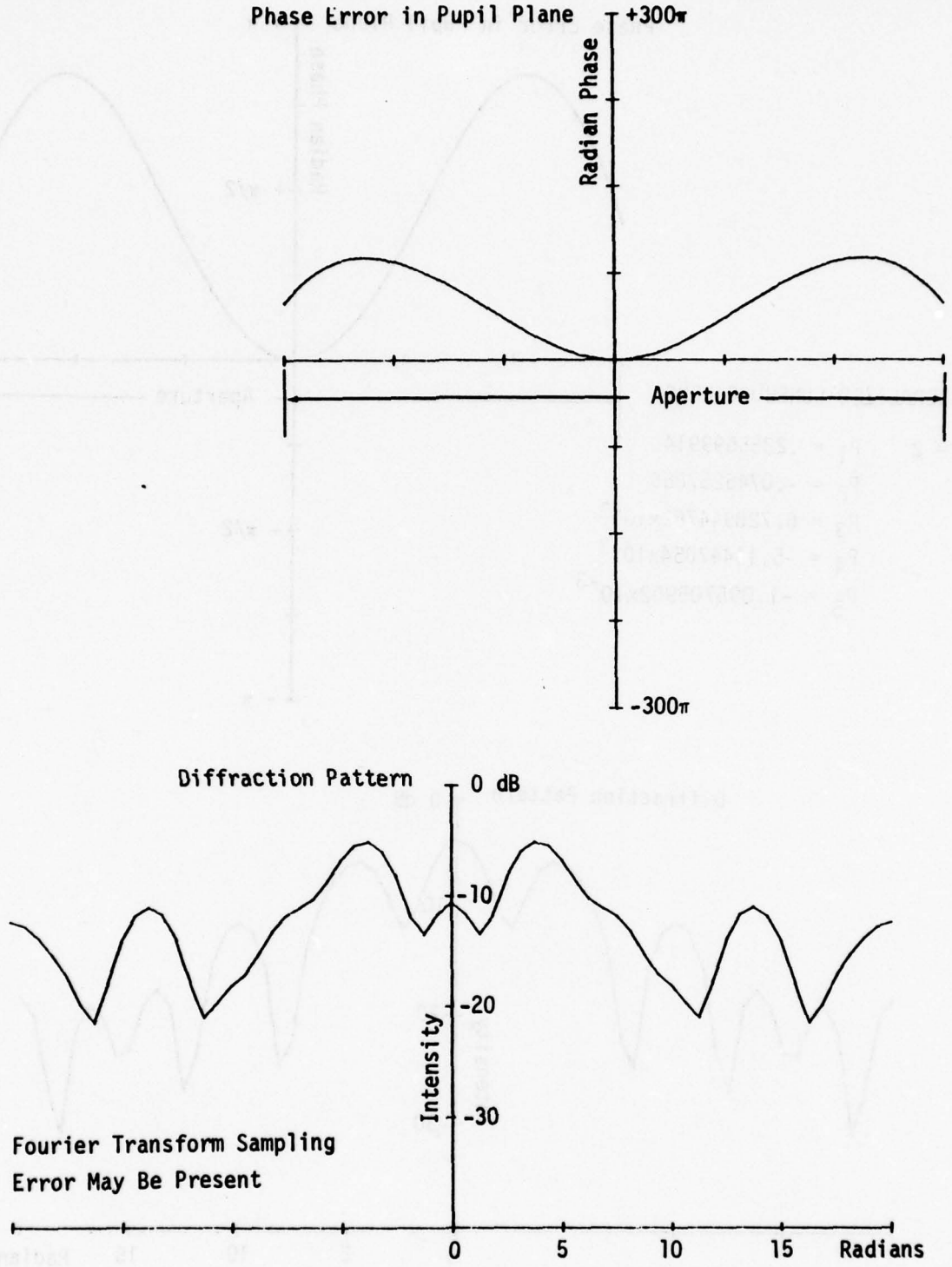

Figure 32. Wavefront Phase Error and Corresponding Intensity Diffraction Pattern for Generalized Luneburg Lens Delineated in Figure 31.

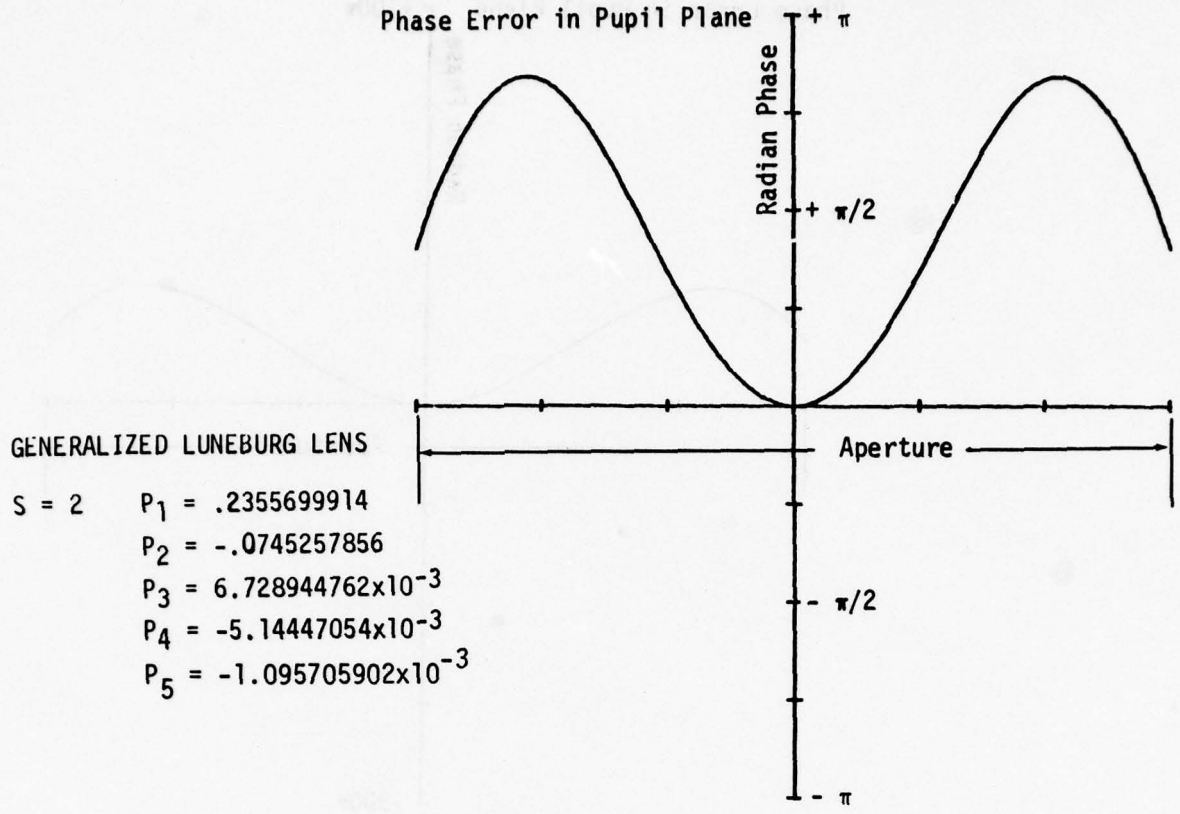

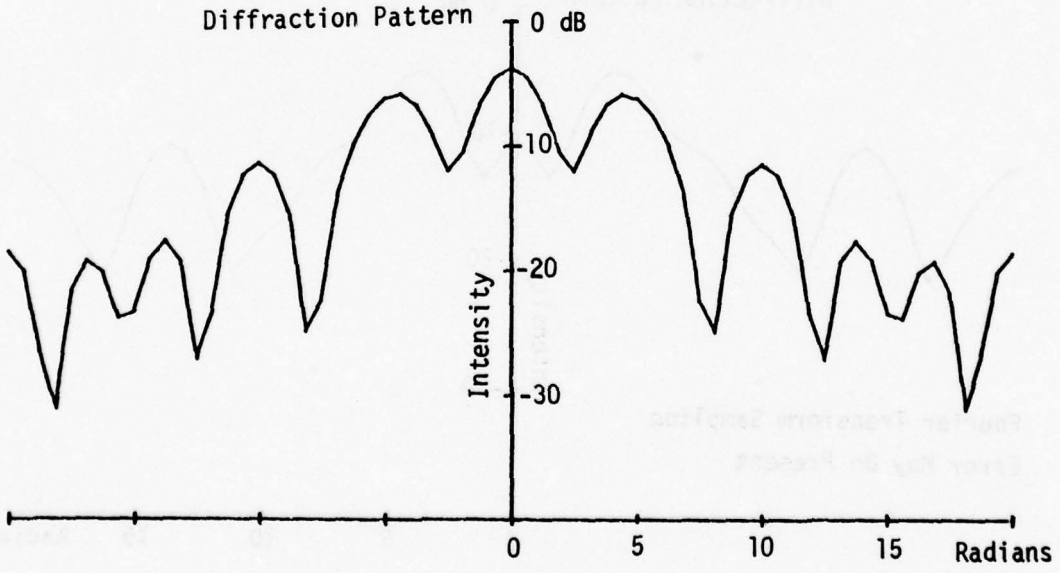

Figure 33. Wavefront Phase Error and Corresponding Intensity Diffraction Pattern for Generalized Luneburg Lens Delineated in Figure 31, S = 2 (.9995 P_1, .997 P_2, 1.1075 P_5).

wavefront phase errors for the perfect profile are due to the computational residues arising from limitation of the computational time. In each case, the intensity diffraction pattern is the expected $\text{sinc}^2 x$ function which has the expected single lobe and side lobes due to use of a uniform elimination function.

Some of the computed results do not show a single principle lobe type of diffraction pattern. This is due to the introduction of excessive errors in the waveguide thickness profile. There are two optical means to suppress this effect, i.e., stopping down the aperture or the introduction of a tapered illumination function. The computer program can be altered to accommodate various aperture distributions and their limits. Some of the figures for the S=2 case are identical to those contained in the preceding Optical Waveguide Lenses II Report AFAL-TR-77-60; however, they have been included herein again for comparison with the S=5 and S=9 cases.

Now referring to Figure 17, it does not produce a well-defined single principle lobe diffraction pattern because of the defective profile caused by the introduction of a 2% increase of all the P_n values except P_5. Inspection of the ray intercept clearly indicates that the computational plane is displaced from the true focusing because of its tilt which is also apparent from the curvature of the wavefront phase error. Using a new computational image plane, a much better well-defined principle lobe diffraction pattern can be obtained. Figure 19 shows the results for a corresponding 2% decrease of all P_n values except P_5 leading to a distorted diffraction pattern which can be refocused by shifting of the image plane in the opposite direction. Figures 21 and 22 also show these same effects to a much lesser degree because the distortion introduced is 0.02% which has been refocused yielding results nearly identical to Figure 16. Inspection of Figures 40 and 41 for S=5 and Figures 59 and 60 for S=9 show similar results; however, these have not required refocusing. This is because the central lens thickness has not been changed appreciably.

It is also apparent that stopping down the lens aperture will remove some marginal rays and refocusing will partially negate the effect of defective profiles. This can be observed by inspection of the lens ray traces and ray intercepts such as in Figures 23/24, 25/26, 29/30, and 31/32. This

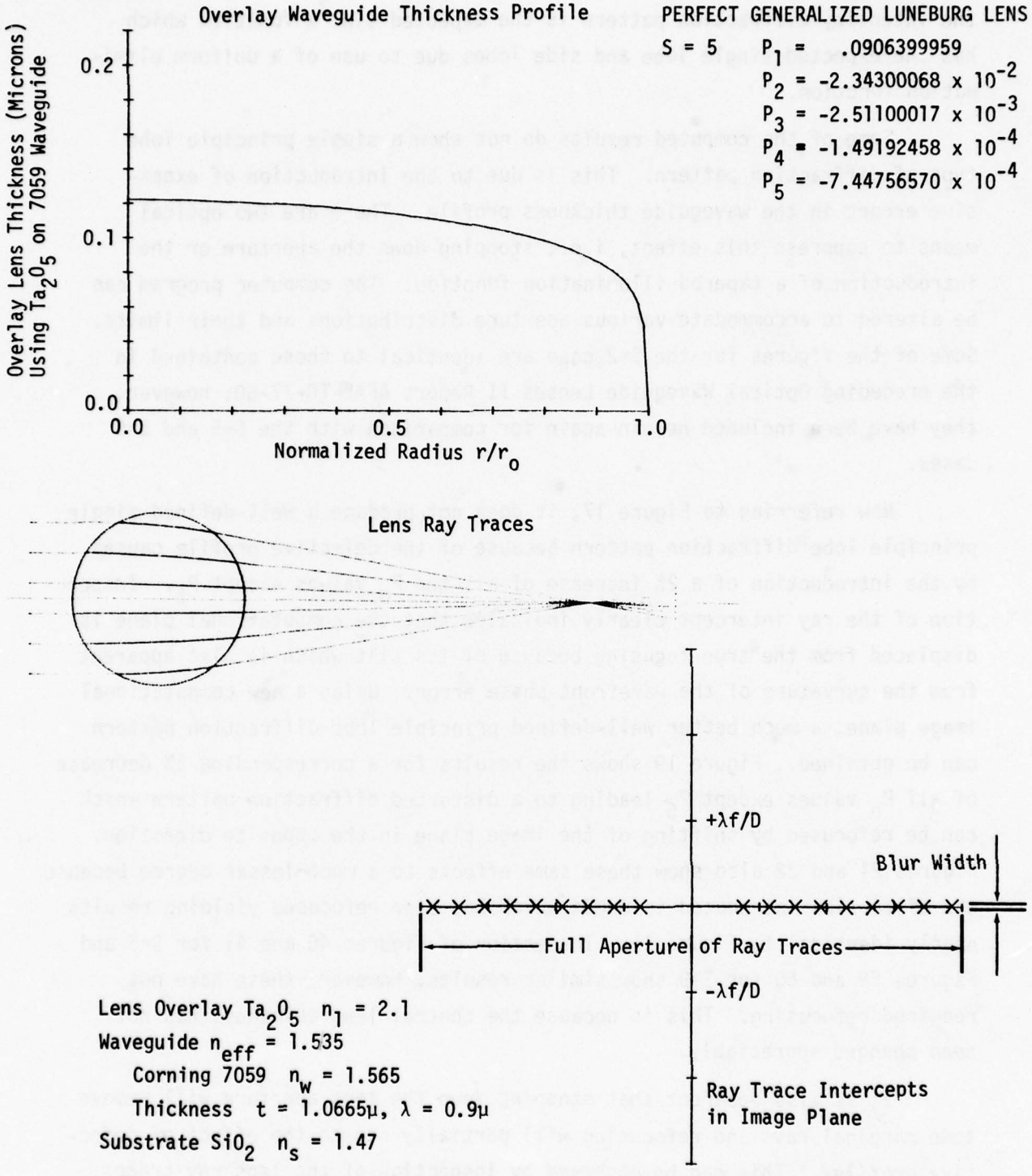

Figure 34. Tabulation of Generalized Luneburg Lens Parameters with Corresponding Overlay Waveguide Lens Thickness Radial Profile, Ray Traces through this Lens and the Intercept Error in the Image Plane, S = 5 (Perfect Luneburg Lens).

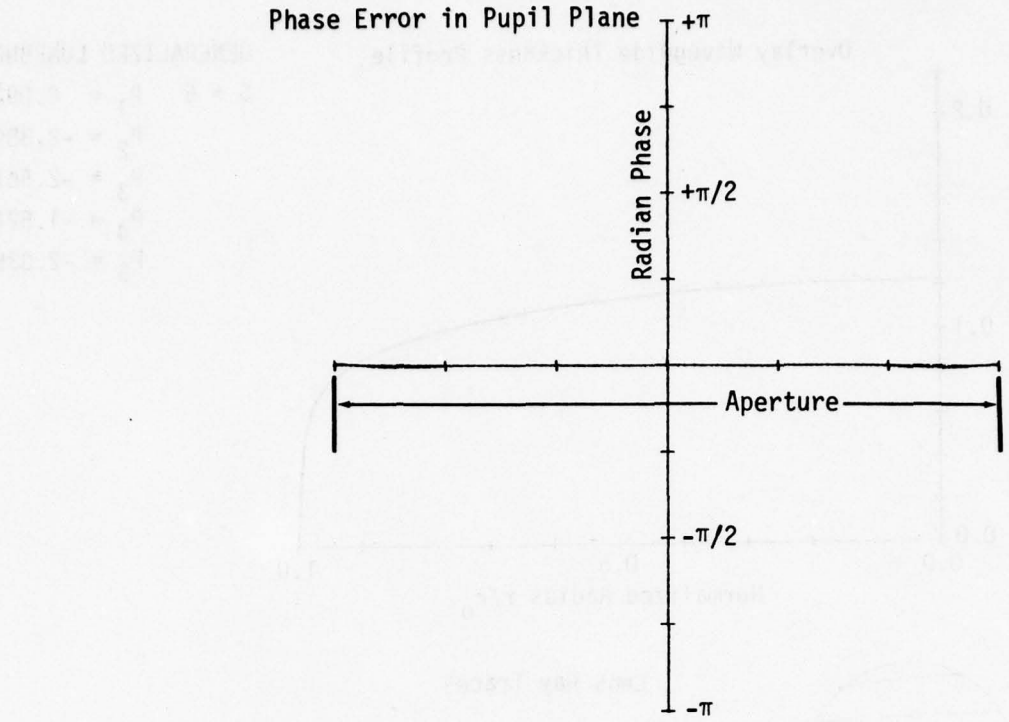

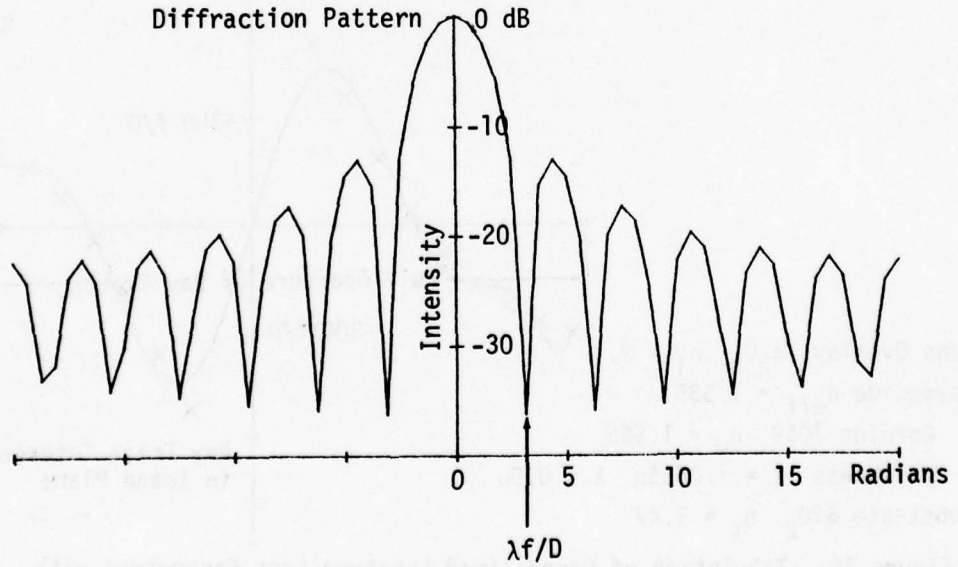

Figure 35. Wavefront Phase Error and Corresponding Intensity Diffraction Pattern for Generalized Luneburg Lens Delineated in Figure 34.

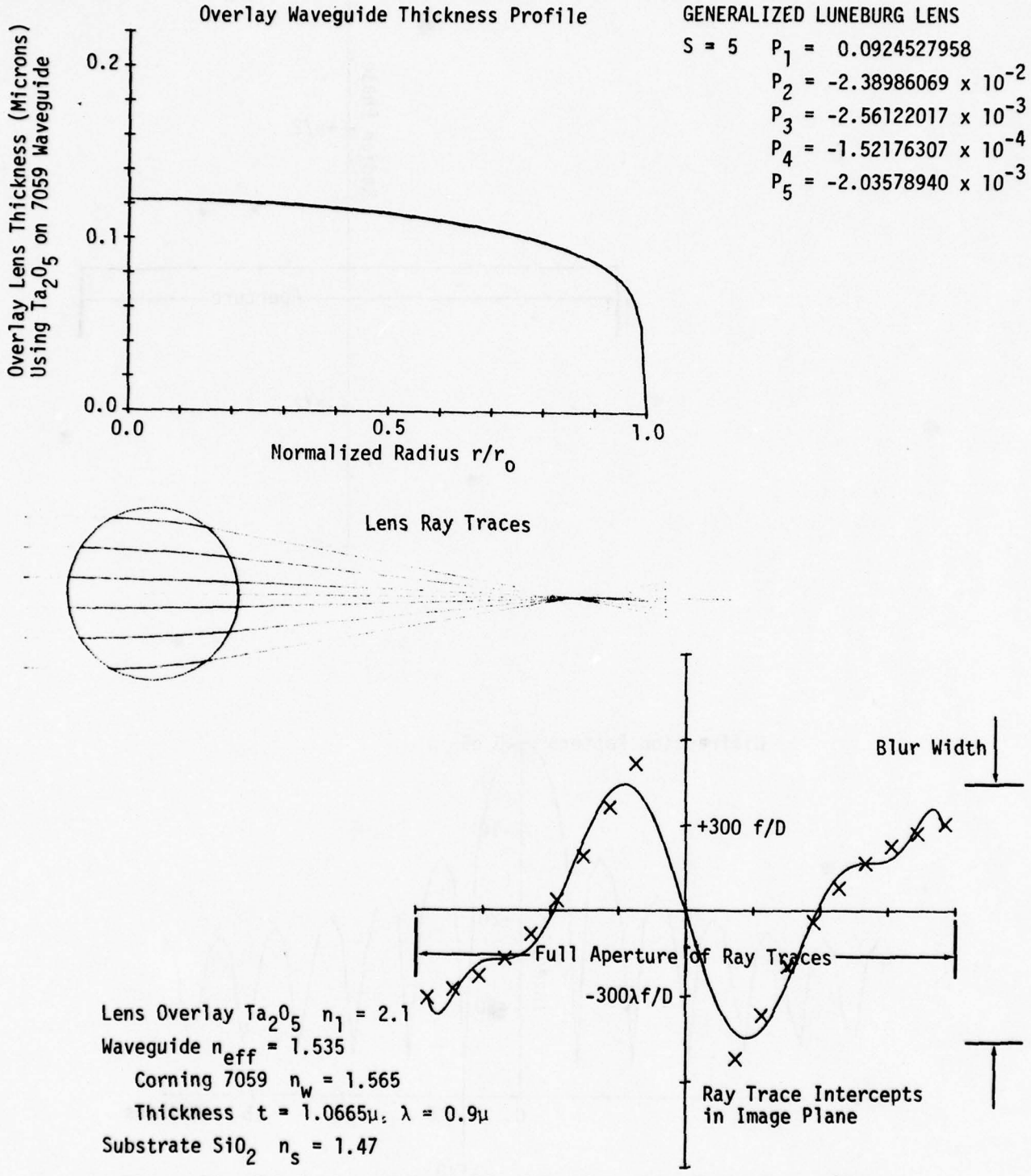

Figure 36. Tabulation of Generalized Luneburg Lens Parameters with Corresponding Overlay Waveguide Lens Thickness Radial Profile, Ray Traces through this Lens and the Intercept Error in the Image Plane, S = 5 (1.02 P_1, 1.02 P_2, 1.02 P_3, 1.02 P_4, 2.7333 P_5).

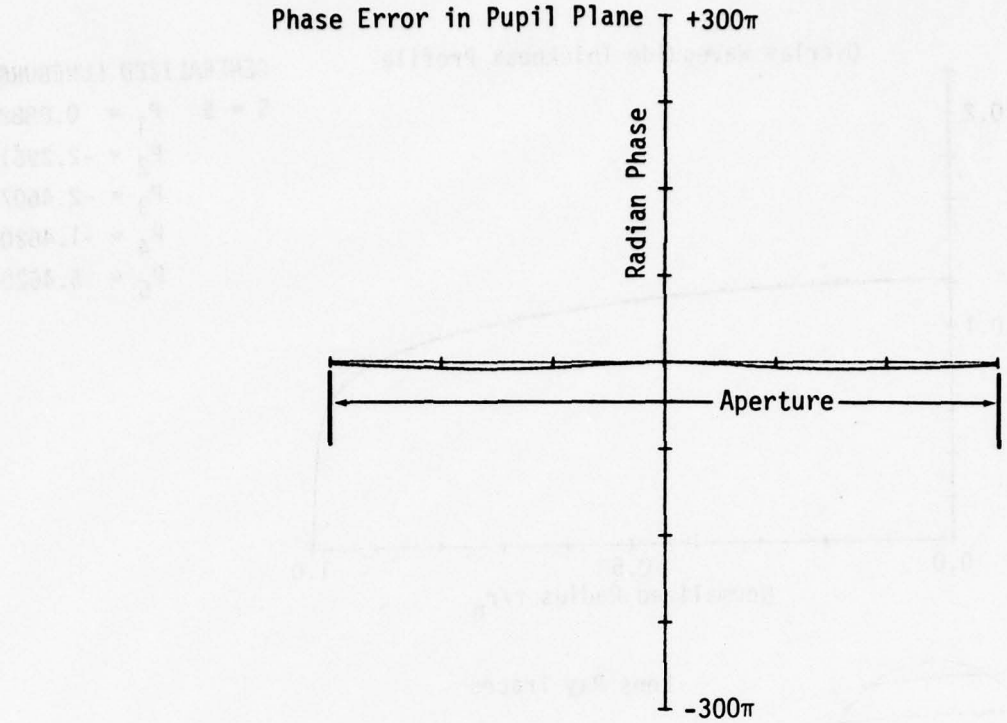

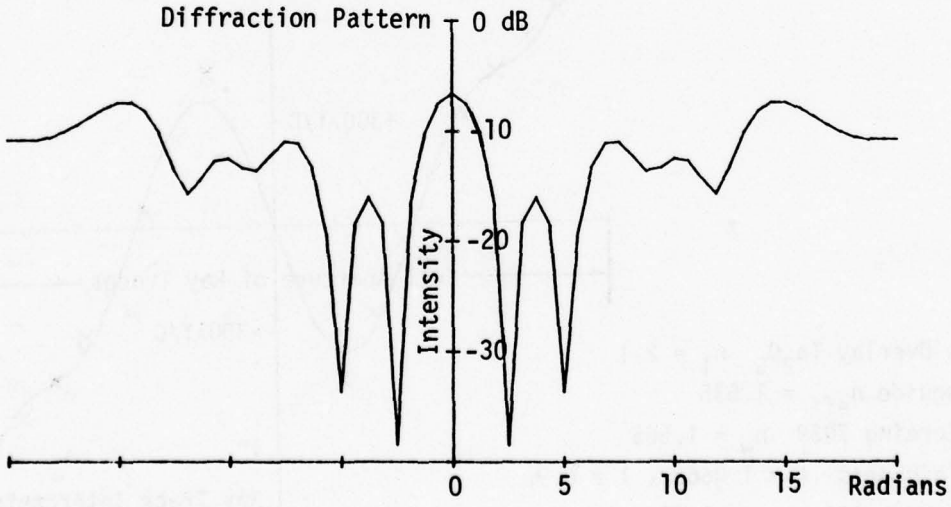

Figure 37. Wavefront Phase Error and Corresponding Intensity Diffraction Pattern for Generalized Luneburg Lens Delineated in Figure 36.

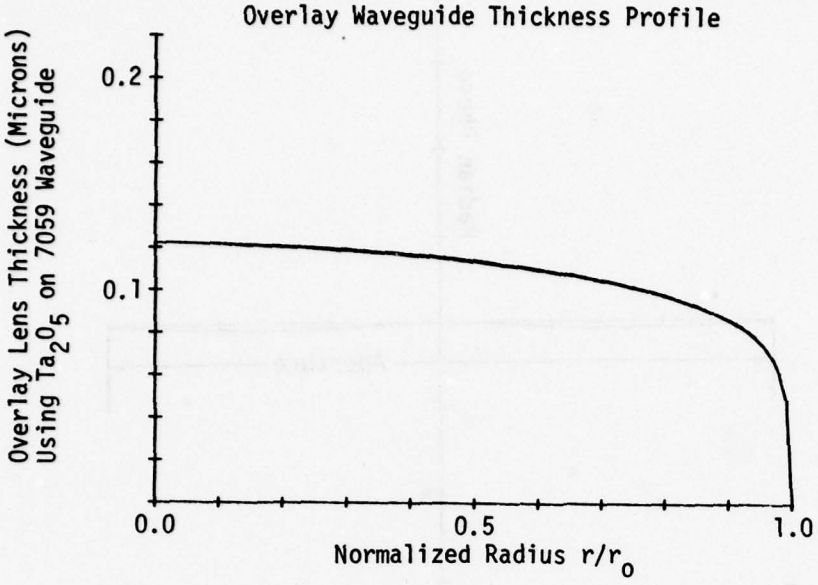

GENERALIZED LUNEBURG LENS

S = 5 P_1 = 0.0888271959

P_2 = $-2.29614066 \times 10^{-2}$

P_3 = $-2.46078016 \times 10^{-3}$

P_4 = $-1.46208608 \times 10^{-4}$

P_5 = $5.46202460 \times 10^{-4}$

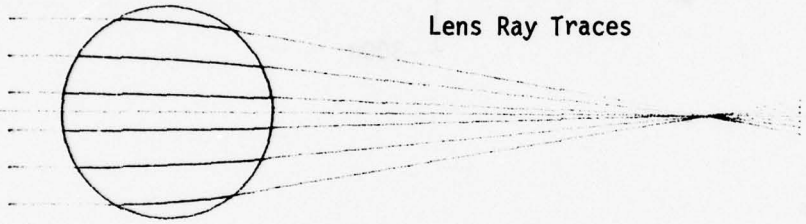

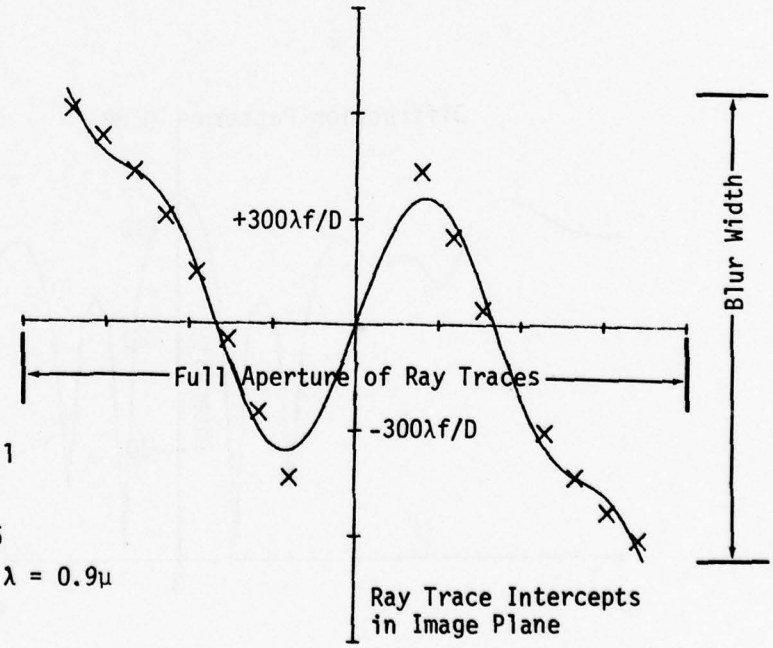

Lens Overlay Ta_2O_5 n_1 = 2.1

Waveguide n_{eff} = 1.535

Corning 7059 n_w = 1.565

Thickness t = 1.0665μ, λ = 0.9μ

Substrate SiO_2 n_s = 1.47

Figure 38. Tabulation of Generalized Luneburg Lens Parameters with Corresponding Overlay Waveguide Lens Thickness Radial Profile, Ray Traces through this Lens and the Intercept Error in the Image Plane, S = 5 (.98 P_1, .98 P_2, .98 P_3, .98 P_4, -.7333 P_5).

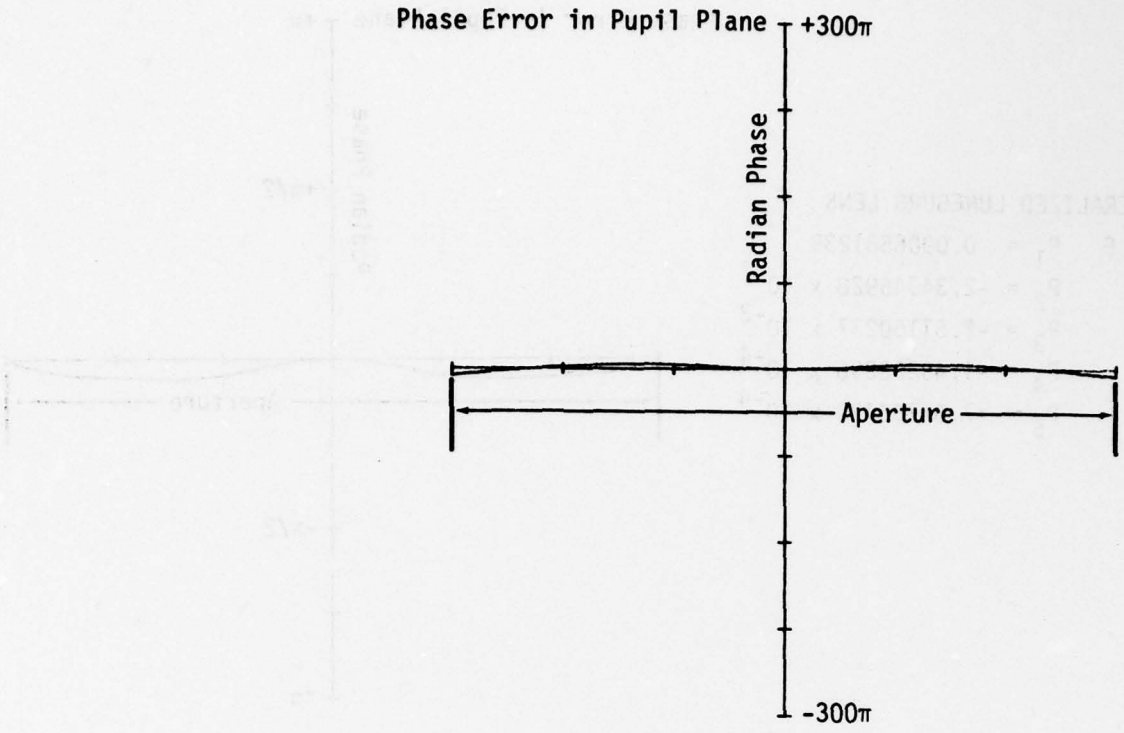

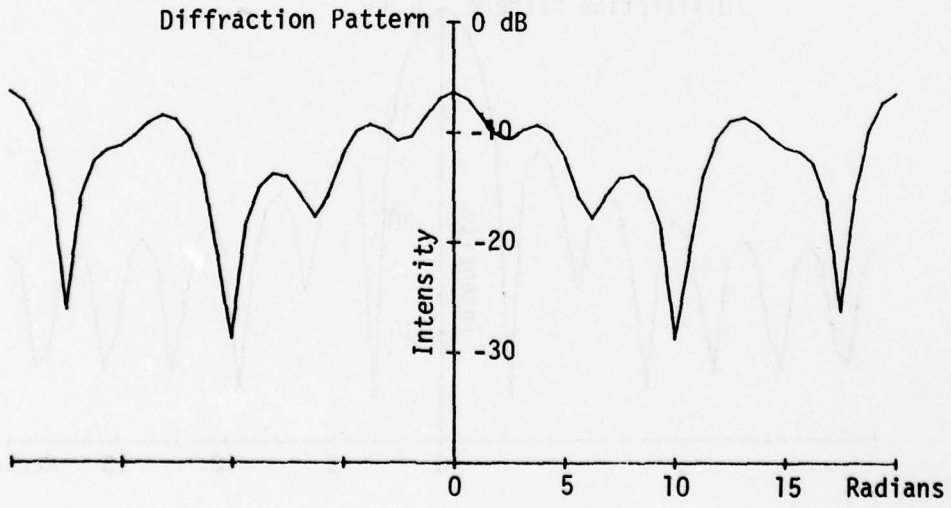

Figure 39. Wavefront Phase Error and Corresponding Intensity Diffraction Pattern for Generalized Luneburg Lens Delineated in Figure 38.

GENERALIZED LUNEBURG LENS

S = 5 P_1 = 0.0906581239

P_2 = $-2.34346928 \times 10^{-2}$

P_3 = $-2.51150237 \times 10^{-3}$

P_4 = $-1.49222296 \times 10^{-4}$

P_5 = $-7.57703430 \times 10^{-4}$

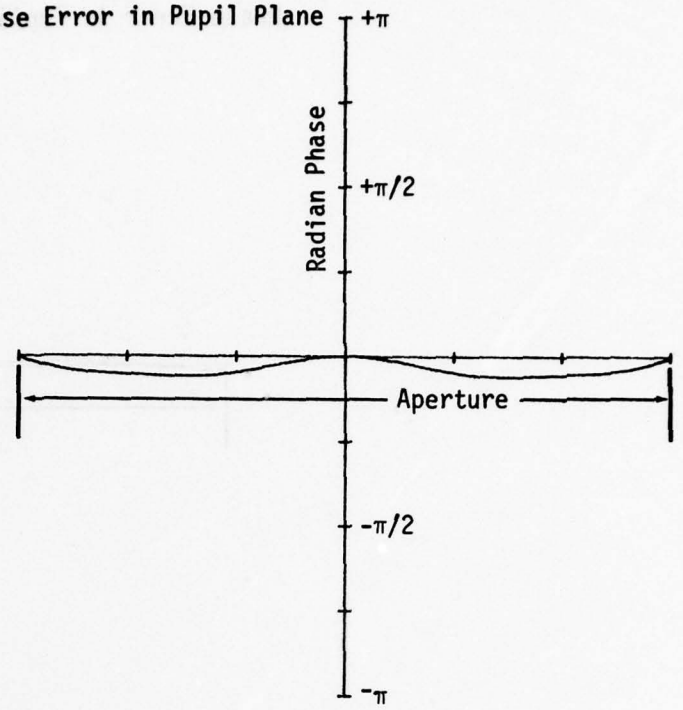

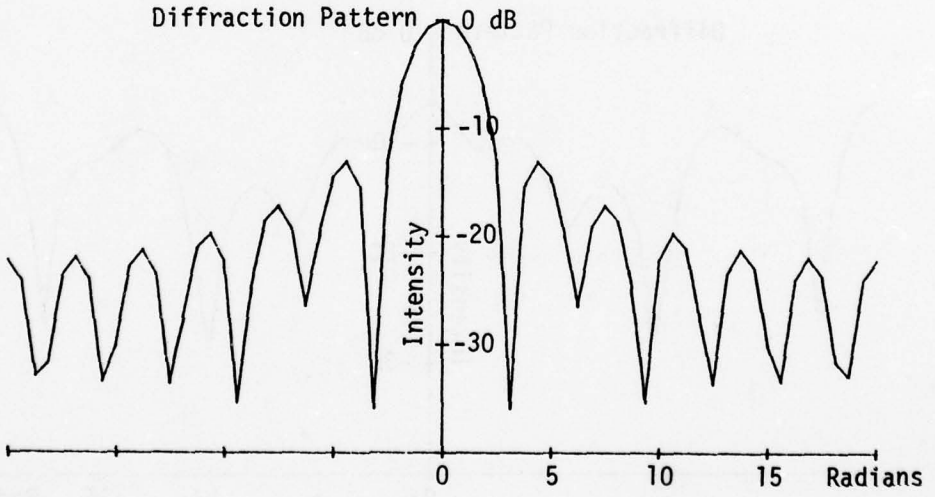

Figure 40. Wavefront Phase Error and Corresponding Intensity Diffraction Pattern for Generalized Luneburg Lens Delineated in Figure 36, S = 5 (1.0002 P_1, 1.0002 P_2, 1.0002 P_3, 1.0002 P_4, 1.0173 P_5).

GENERALIZED LUNEBURG LENS

S = 5 P_1 = 0.0906218679

P_2 = $-2.34253208 \times 10^{-2}$

P_3 = $-2.51049797 \times 10^{-3}$

P_4 = $-1.49162619 \times 10^{-4}$

P_5 = $-7.31883510 \times 10^{-4}$

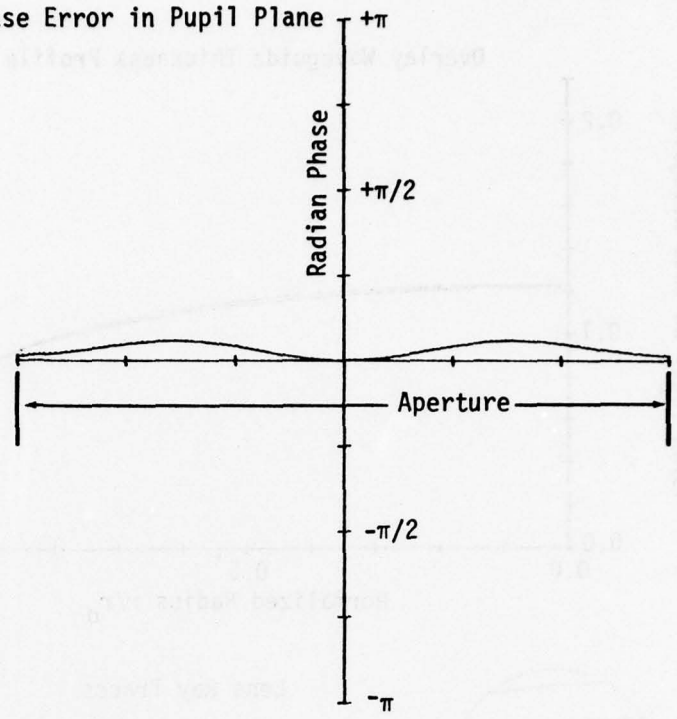

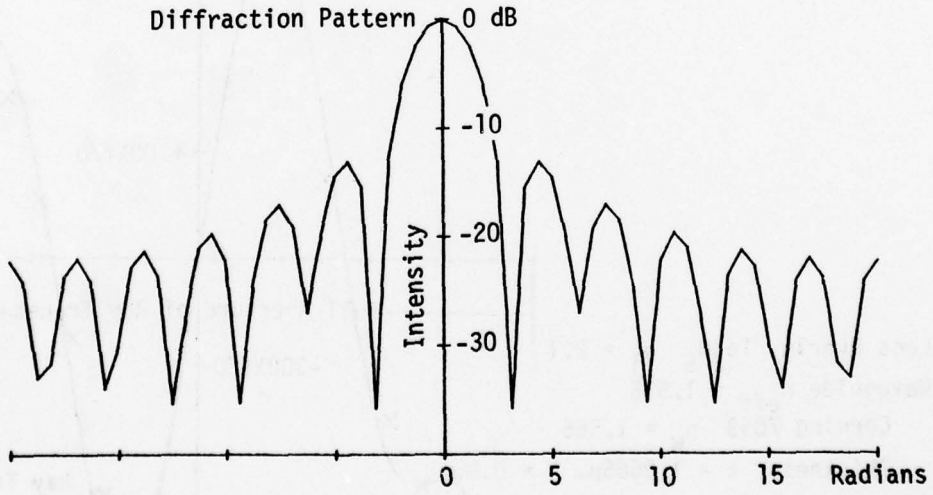

Figure 41. Wavefront Phase Error and Corresponding Intensity Diffraction Pattern for Generalized Luneburg Lens Delineated in Figure 38, S = 5 (.9998 P_1, .9998 P_2, .9998 P_3, .9998 P_4, .9826 P_5).

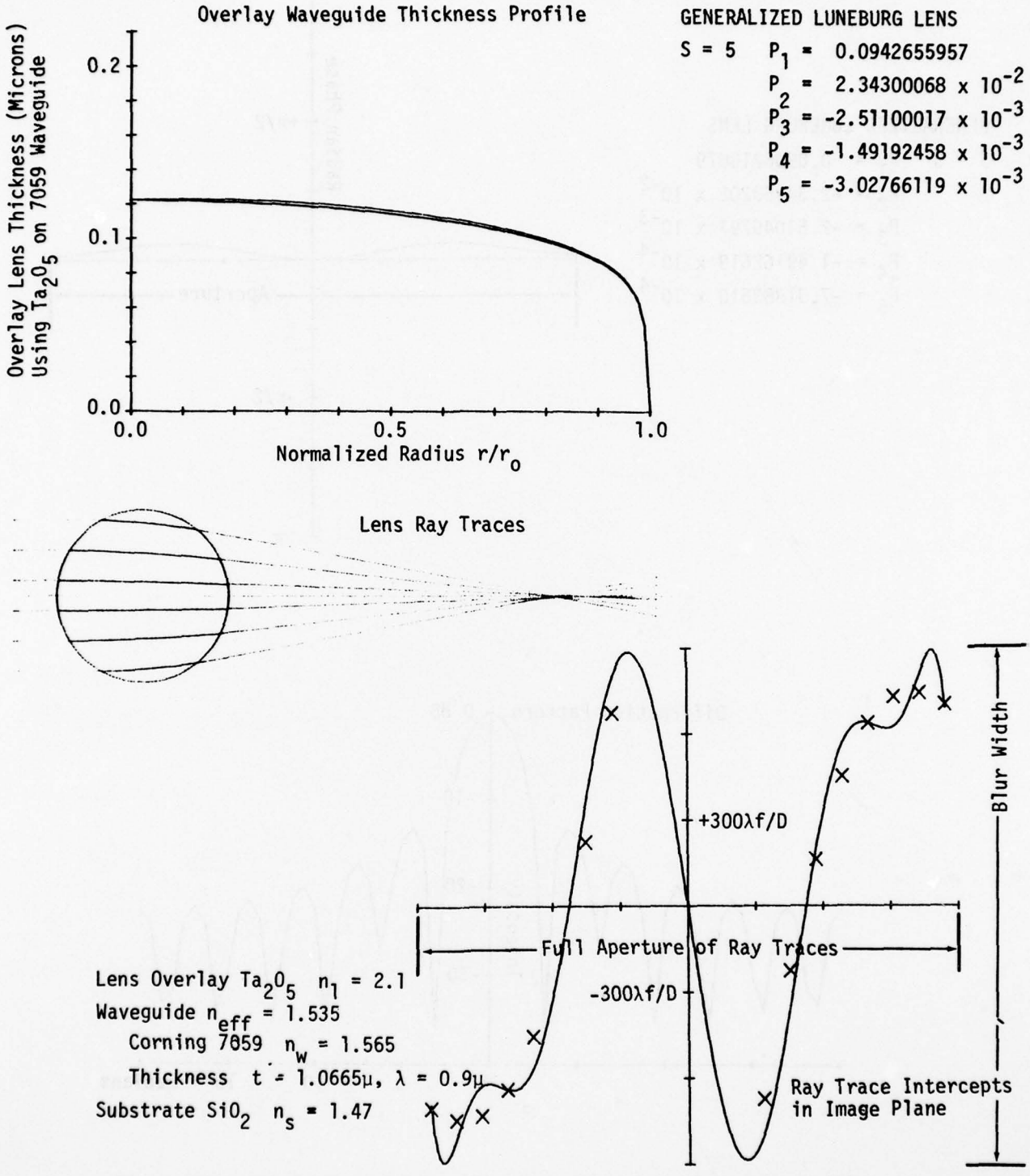

Figure 42. Tabulation of Generalized Luneburg Lens Parameters with Corresponding Overlay Waveguide Lens Thickness Radial Profile, Ray Traces through this Lens and the Intercept Error in the Image Plane, S = 5 (1.04 P_1, 10 P_4, 4.0653 P_5).

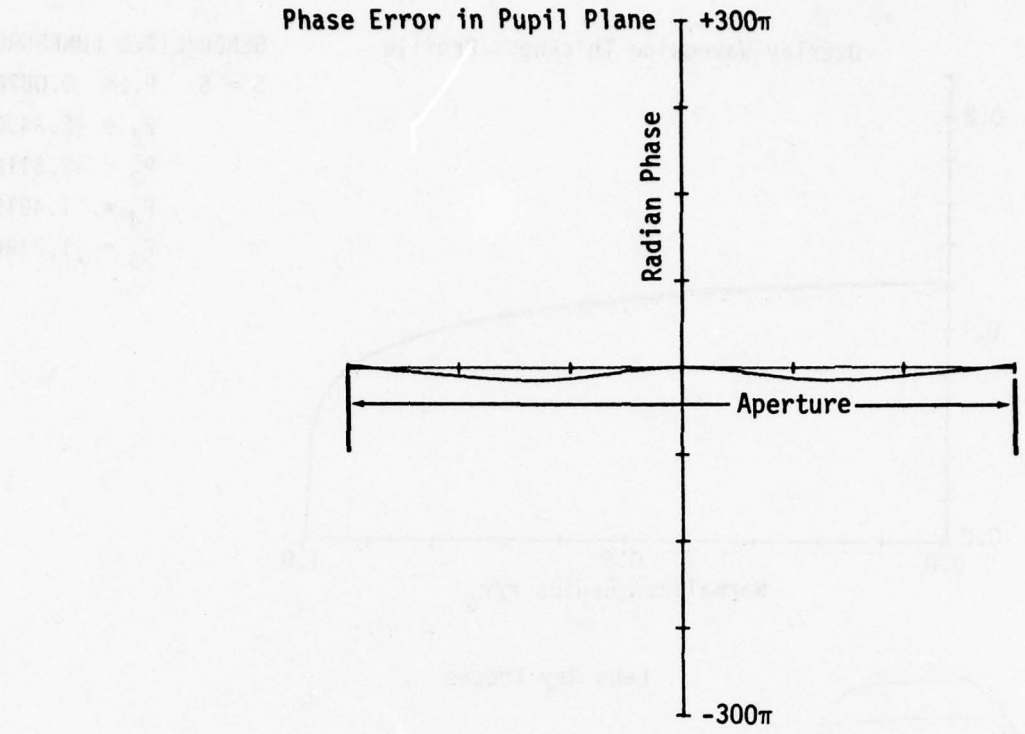

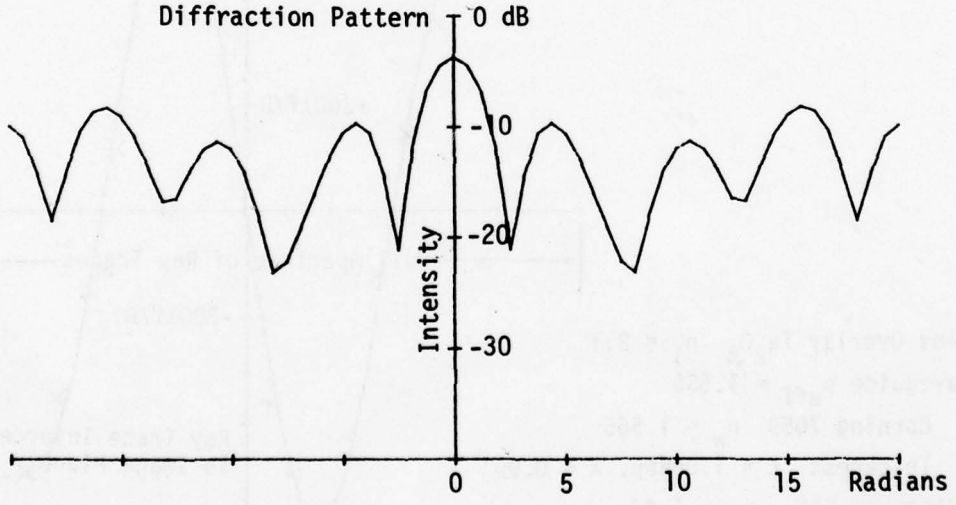

Figure 43. Wavefront Phase Error and Corresponding Intensity Diffraction Pattern for Generalized Luneburg Lens Delineated in Figure 42.

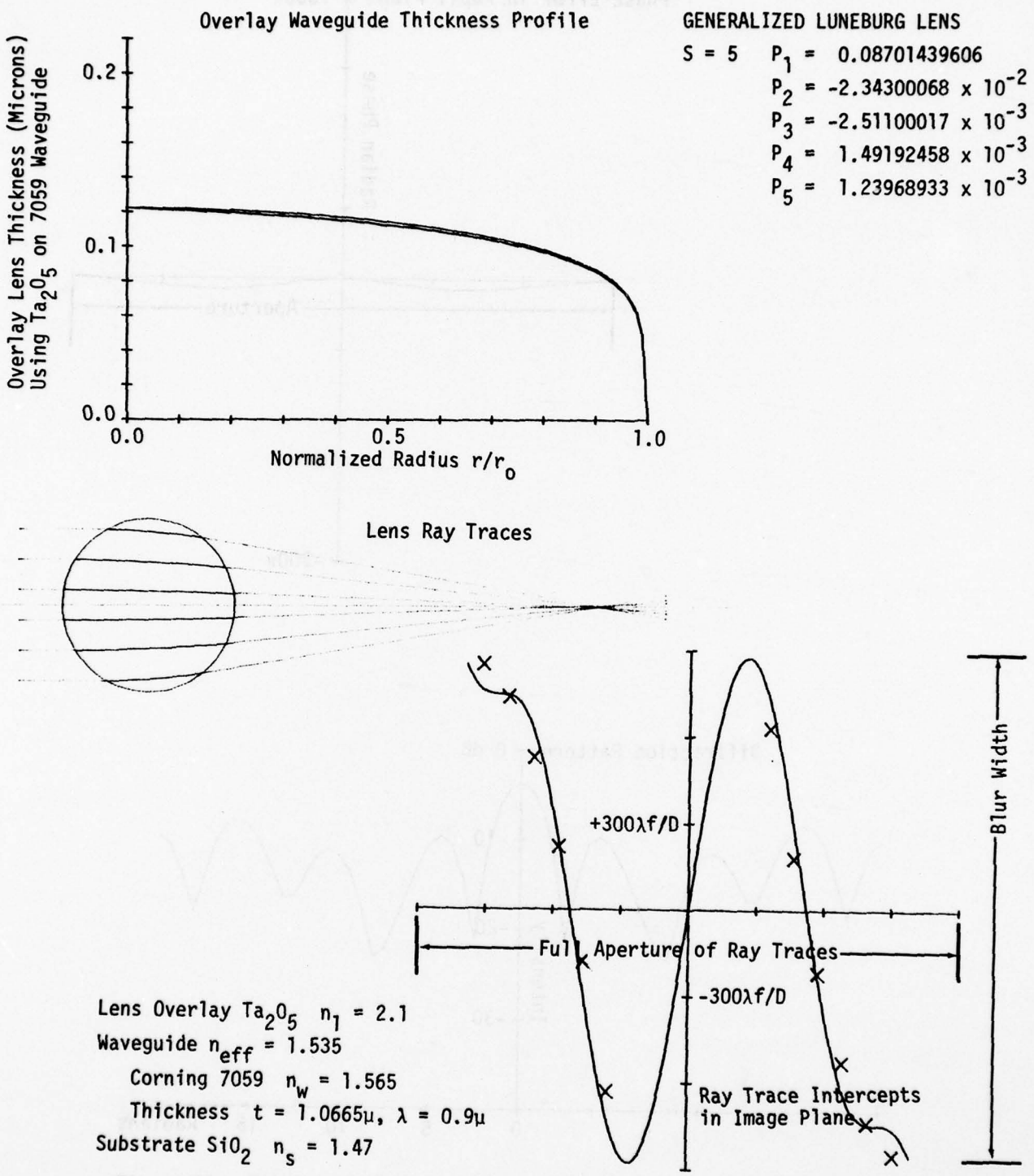

Figure 44. Tabulation of Generalized Luneburg Lens Parameters with Corresponding Overlay Waveguide Lens Thickness Radial Profile, Ray Traces through this Lens and the Intercept Error in the Image Plane, S = 5 (.96 P_1, P_2, P_3, -10 P_4, -1.6646 P_5).

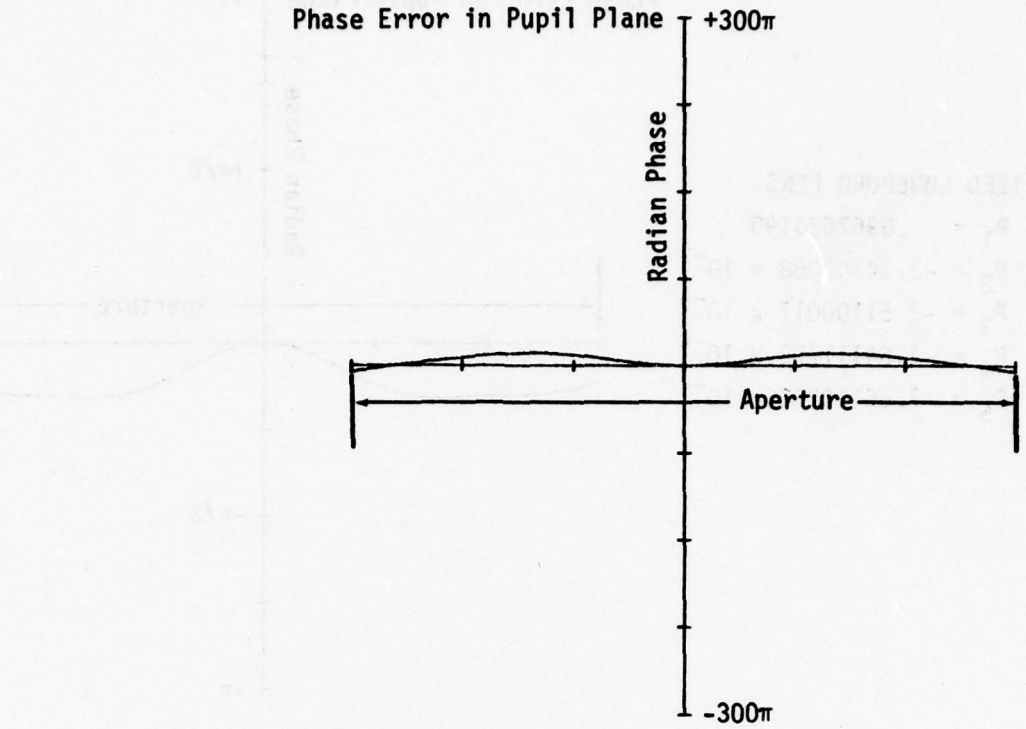

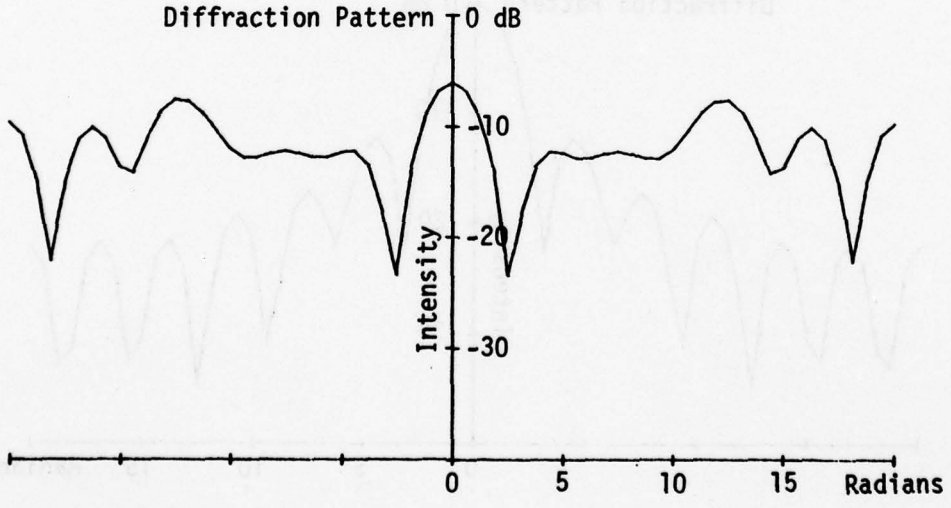

Figure 45. Wavefront Phase Error and Corresponding Intensity Diffraction Pattern for Generalized Luneburg Lens Delineated in Figure 44.

GENERALIZED LUNEBURG LENS

S = 5 P_1 = .0967625190

P_2 = $-2.34300068 \times 10^{-2}$

P_3 = $-2.51100017 \times 10^{-3}$

P_4 = $-1.64111703 \times 10^{-4}$

P_5 = $-7.66130230 \times 10^{-4}$

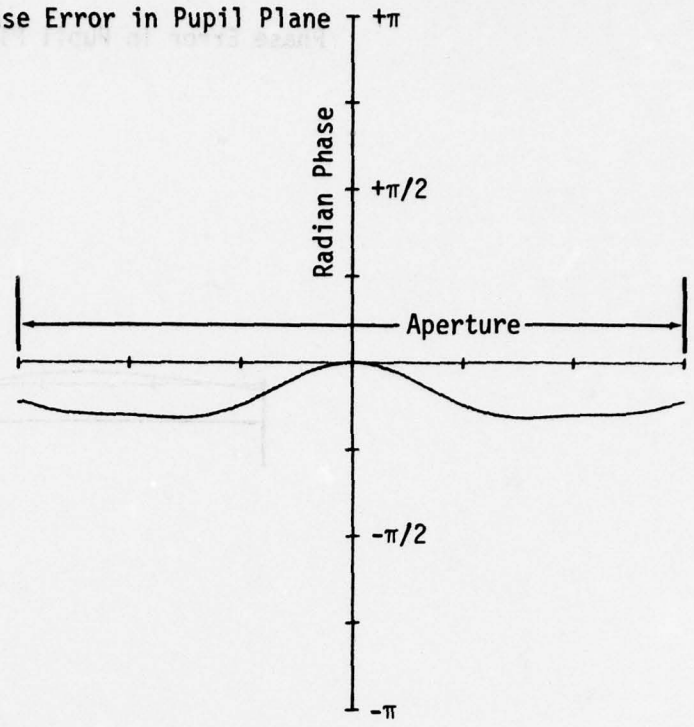

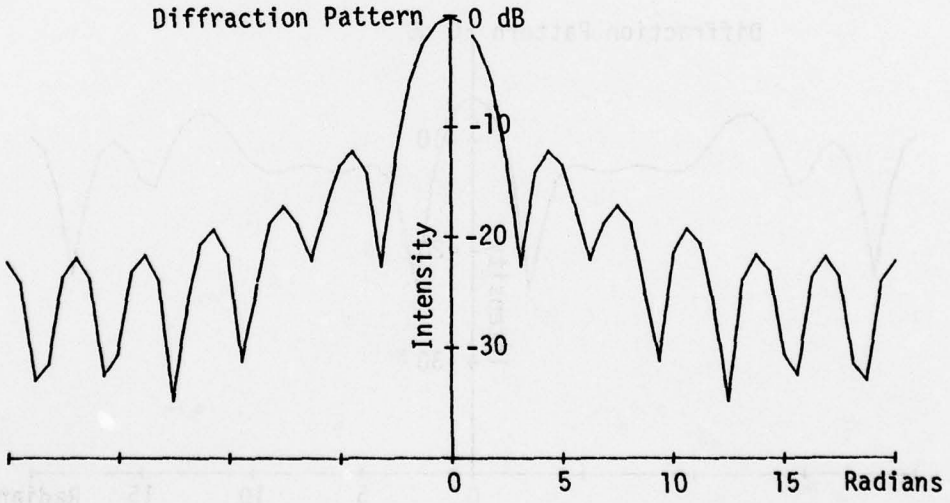

Figure 46. Wavefront Phase Error and Corresponding Intensity Diffraction Pattern for Generalized Luneburg Lens Delineated in Figure 42, S = 5 (1.0004 P_1, 1.1 P_4, 1.0287 P_5).

GENERALIZED LUNEBURG LENS

S = 5 P_1 = 0.0906037399

P_2 = $-2.34300068 \times 10^{-2}$

P_3 = $-2.51100017 \times 10^{-3}$

P_4 = $1.64111703 \times 10^{-4}$

P_5 = $-1.02184163 \times 10^{-3}$

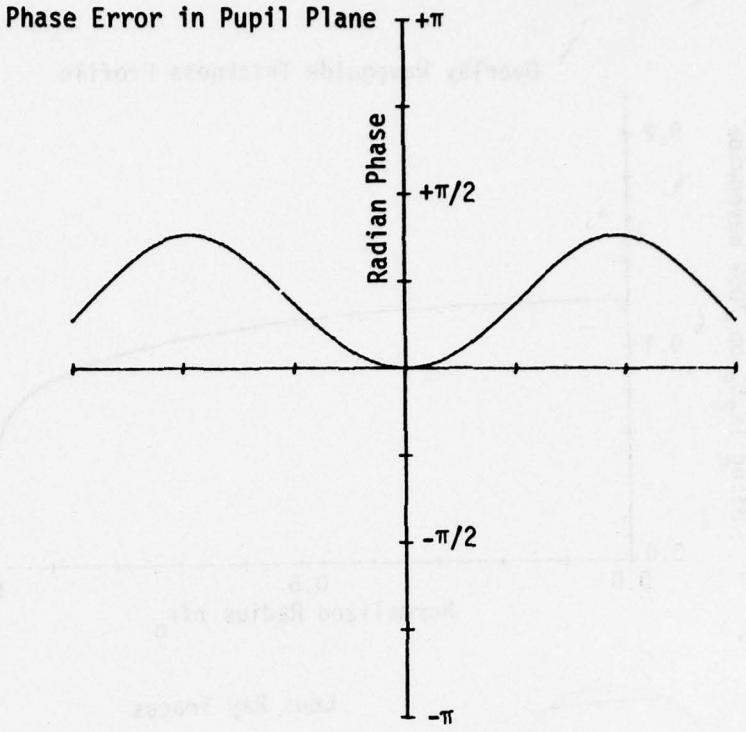

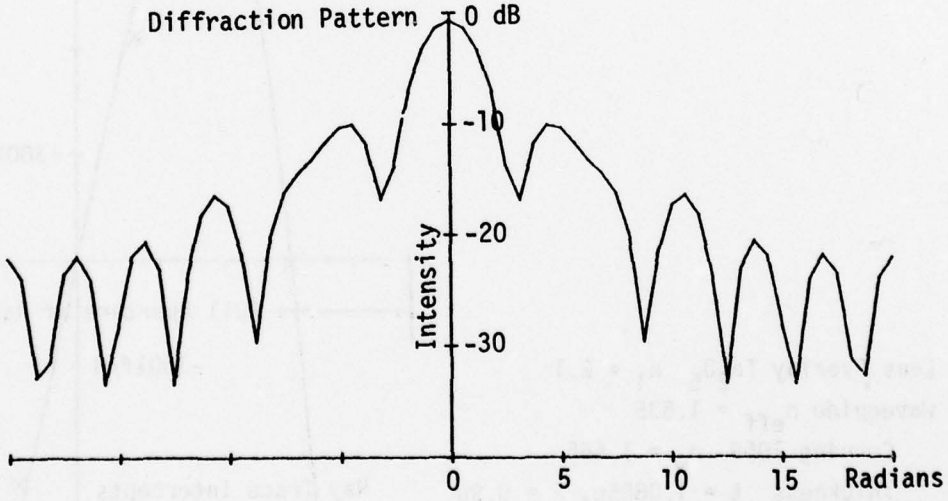

Figure 47. Wavefront Phase Error and Corresponding Intensity Diffraction Pattern for Generalized Luneburg Lens Delineated in Figure 44, S = 5 (.9996 P_1, P_2, P_3, -1.1 P_4, 1.3720 P_5).

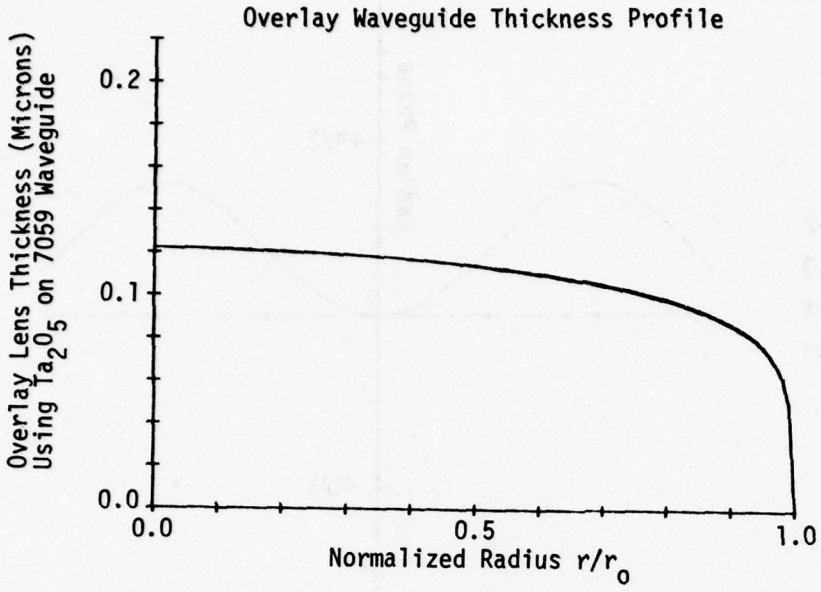

GENERALIZED LUNEBURG LENS

S = 5 P_1 = 0.0951719957

P_2 = $-3.16305091 \times 10^{-2}$

P_3 = $-2.51100017 \times 10^{-3}$

P_4 = $-1.49192458 \times 10^{-4}$

P_5 = $2.92370911 \times 10^{-3}$

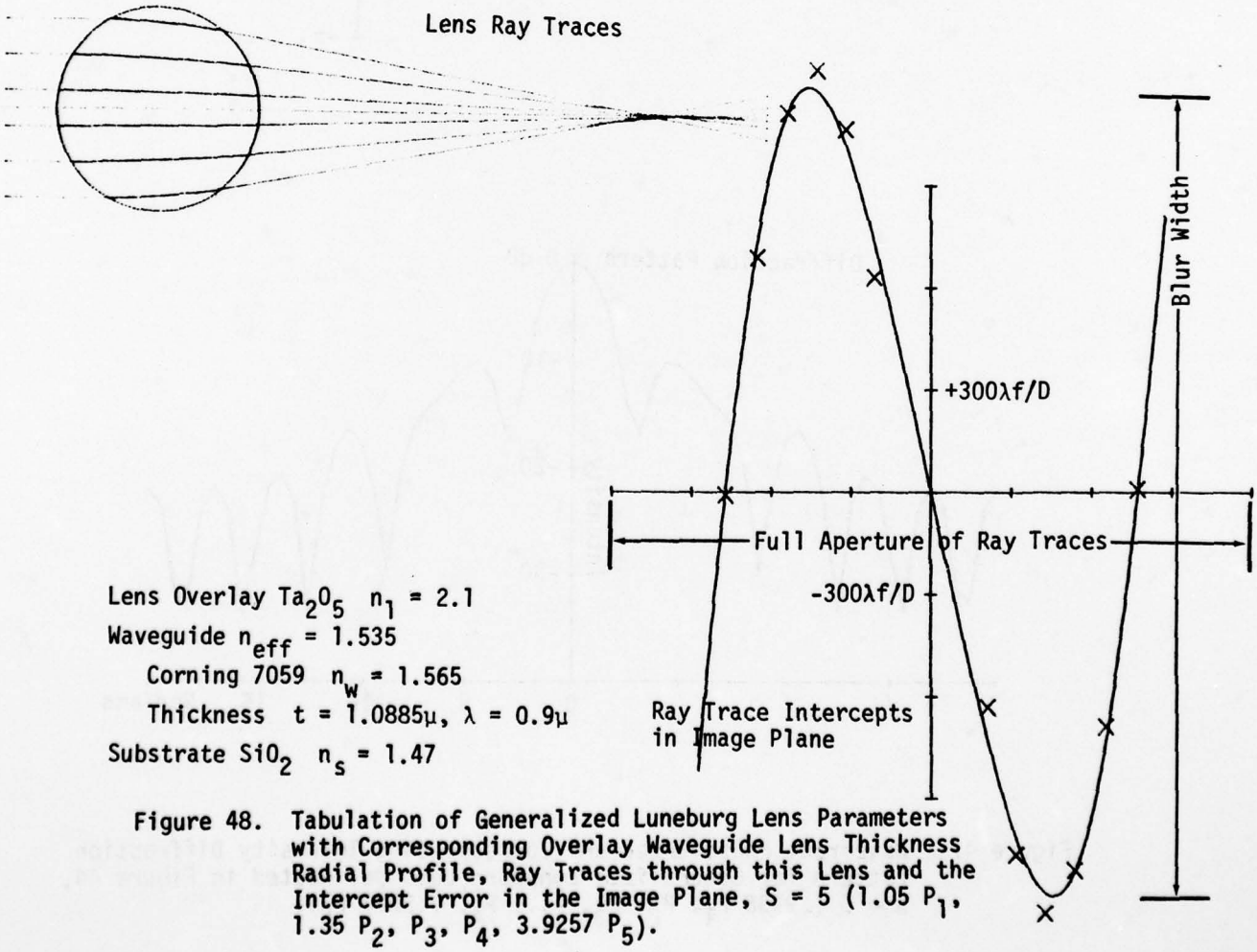

Lens Overlay Ta_2O_5 n_1 = 2.1

Waveguide n_{eff} = 1.535

Corning 7059 n_w = 1.565

Thickness t = 1.0885μ, λ = 0.9μ

Substrate SiO_2 n_s = 1.47

Figure 48. Tabulation of Generalized Luneburg Lens Parameters with Corresponding Overlay Waveguide Lens Thickness Radial Profile, Ray Traces through this Lens and the Intercept Error in the Image Plane, S = 5 (1.05 P_1, 1.35 P_2, P_3, P_4, 3.9257 P_5).

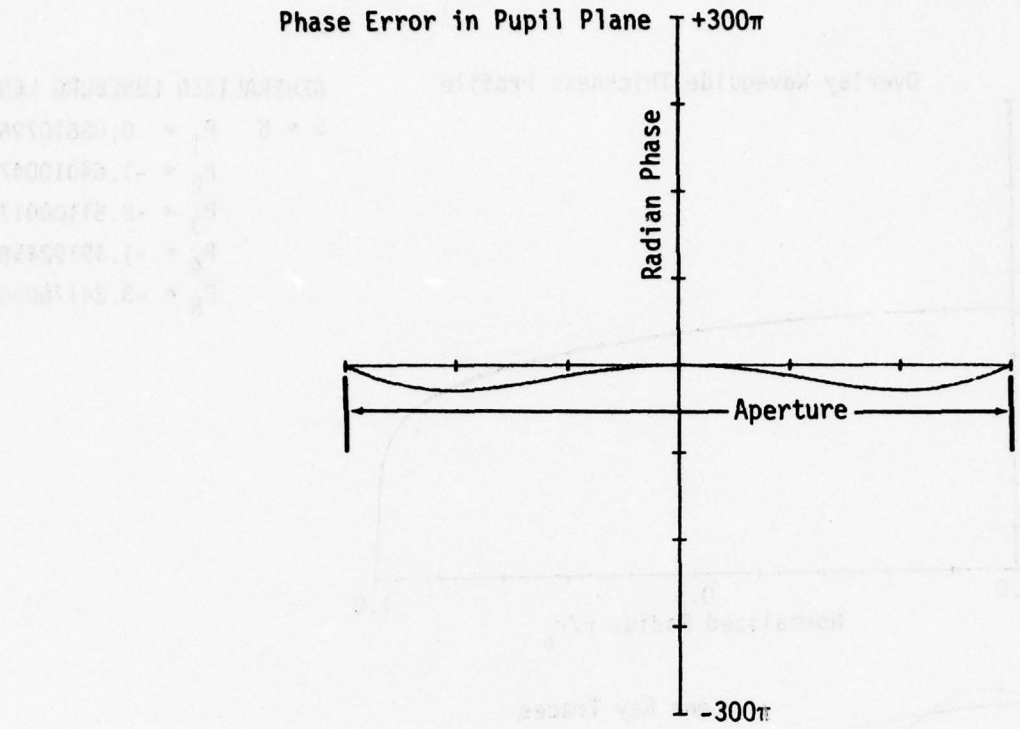

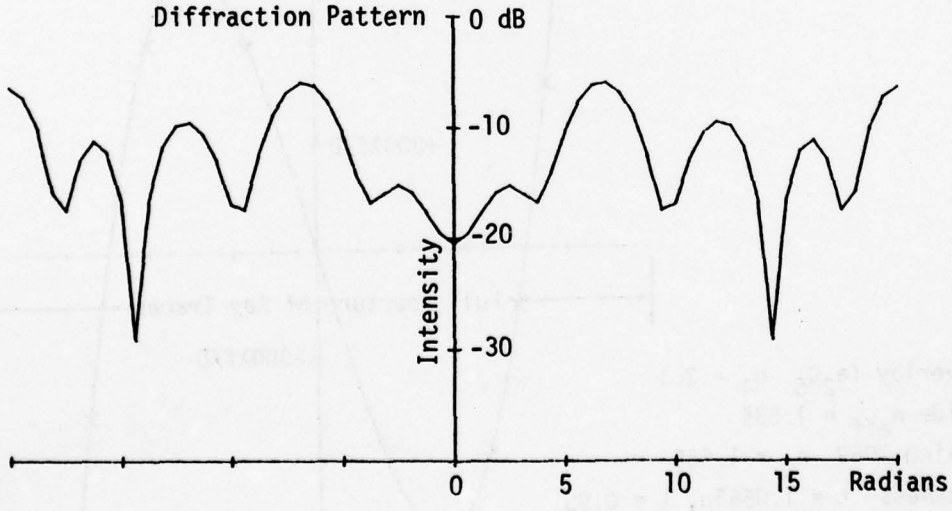

Figure 49. Wavefront Phase Error and Corresponding Intensity Diffraction Pattern for Generalized Luneburg Lens Delineated in Figure 48.

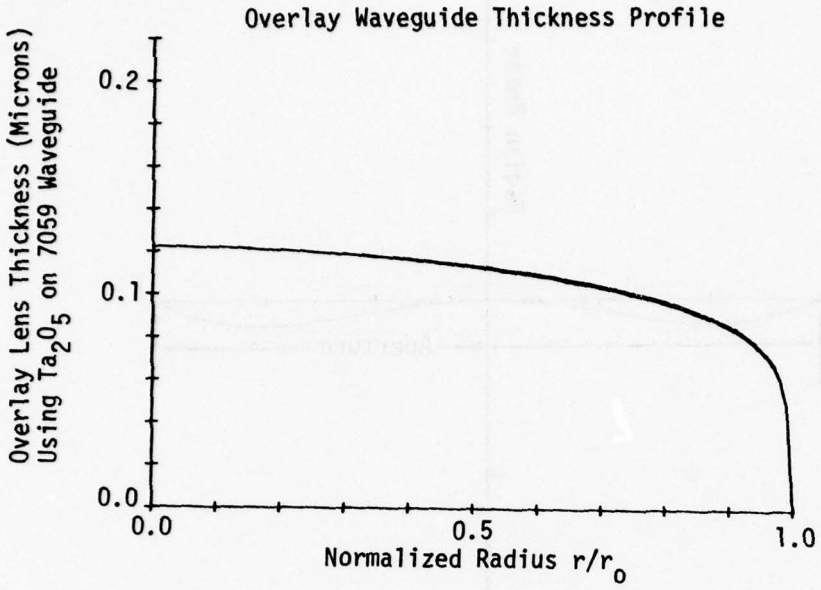

GENERALIZED LUNEBURG LENS

S = 5 P_1 = 0.0861079610

P_2 = -1.64010047 x 10^{-2}

P_3 = -2.51100017 x 10^{-3}

P_4 = -1.49192458 x 10^{-4}

P_5 = -3.24176066 x 10^{-3}

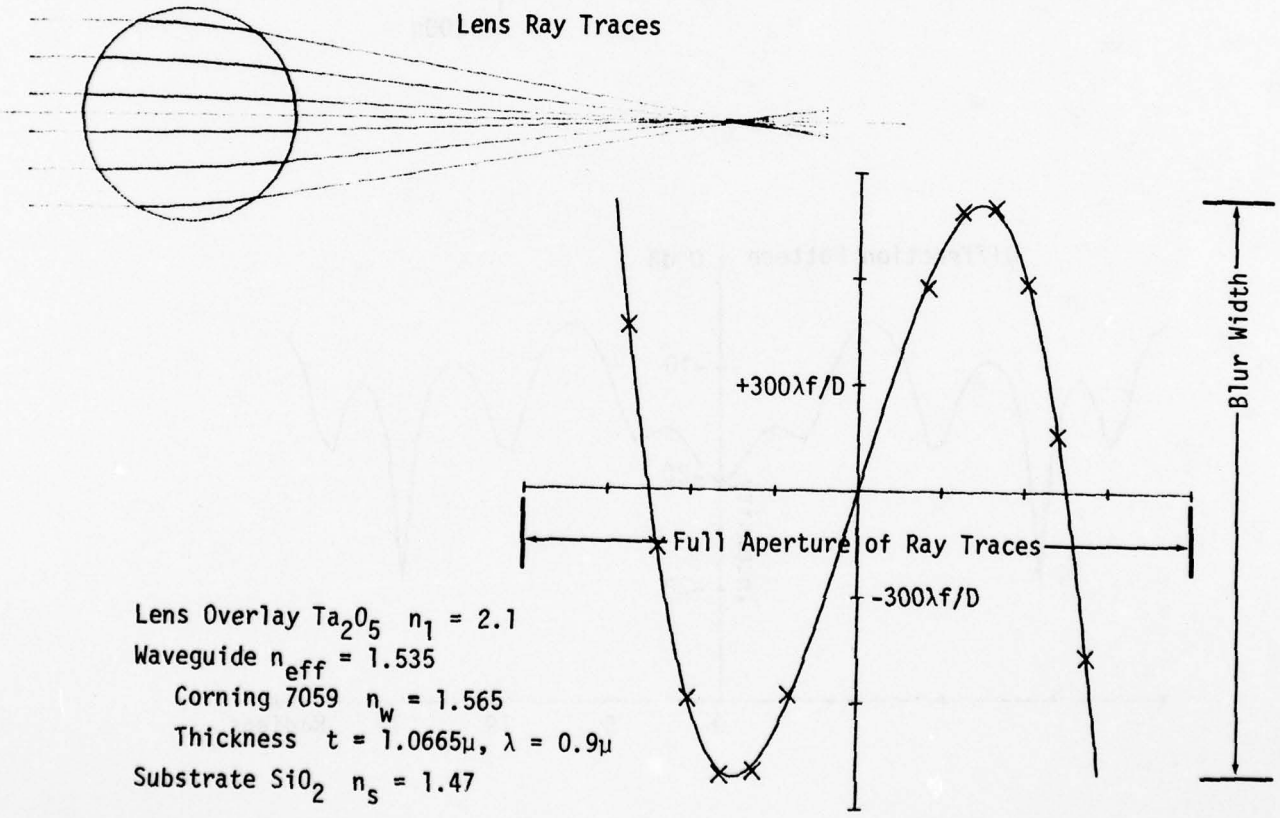

Lens Overlay Ta_2O_5 n_1 = 2.1

Waveguide n_{eff} = 1.535

Corning 7059 n_w = 1.565

Thickness t = 1.0665μ, λ = 0.9μ

Substrate SiO_2 n_s = 1.47

Figure 50. Tabulation of Generalized Luneburg Lens Parameters with Corresponding Overlay Waveguide Lens Thickness Radial Profile, Ray Traces through this Lens and the Intercept Error in the Image Plane, S = 5 (.95 P_1, .7 P_2, 4.3528 P_5).

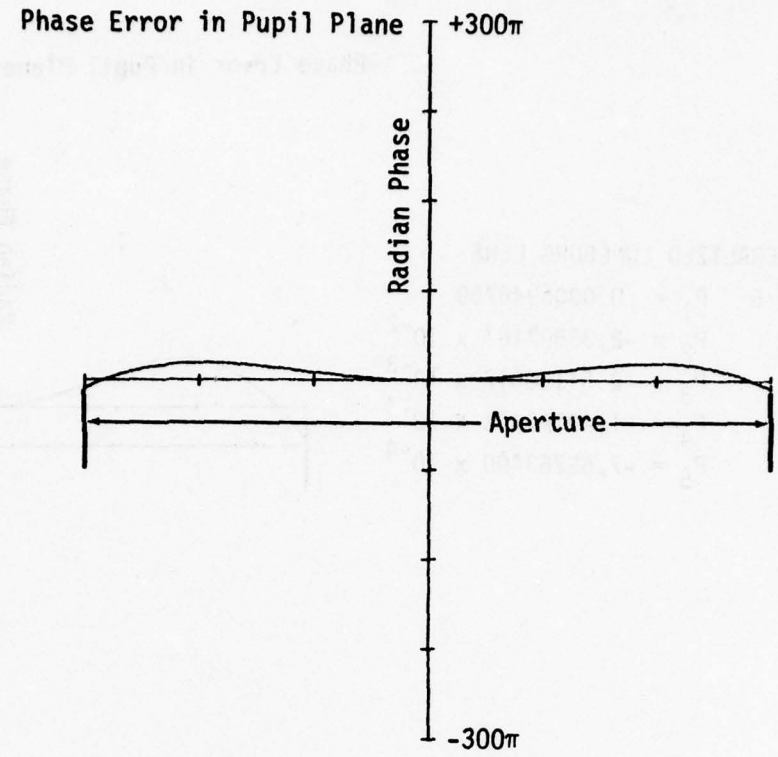

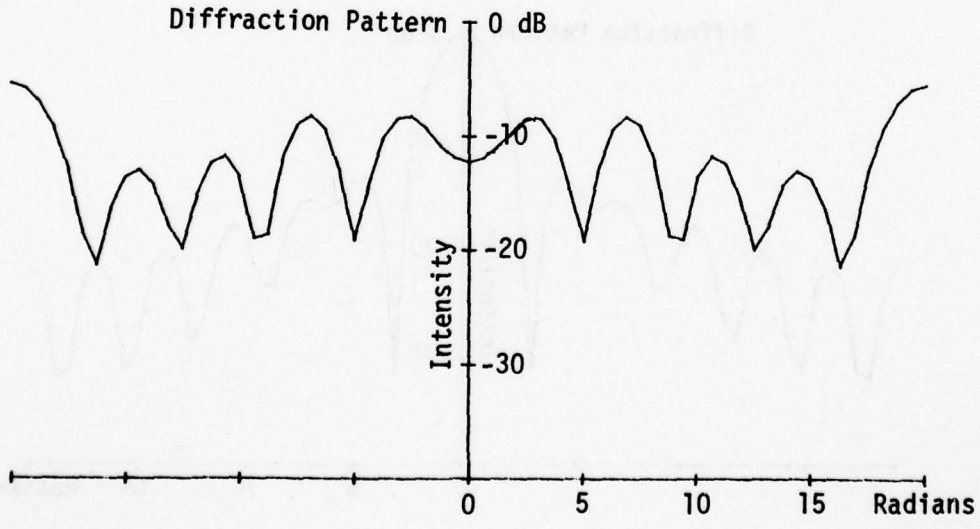

Figure 51. Wavefront Phase Error and Corresponding Intensity Diffraction Pattern for Generalized Luneburg Lens Delineated in Figure 50.

GENERALIZED LUNEBURG LENS

S = 5 P_1 = 0.0905946759

P_2 = $-2.33597167 \times 10^{-2}$

P_3 = $-2.51100017 \times 10^{-3}$

P_4 = $-1.49192458 \times 10^{-4}$

P_5 = $-7.69763490 \times 10^{-4}$

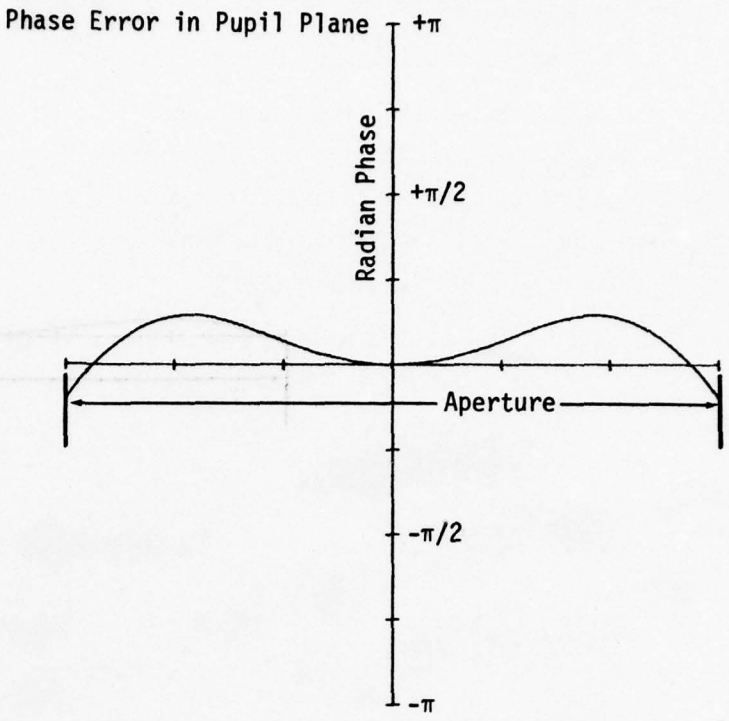

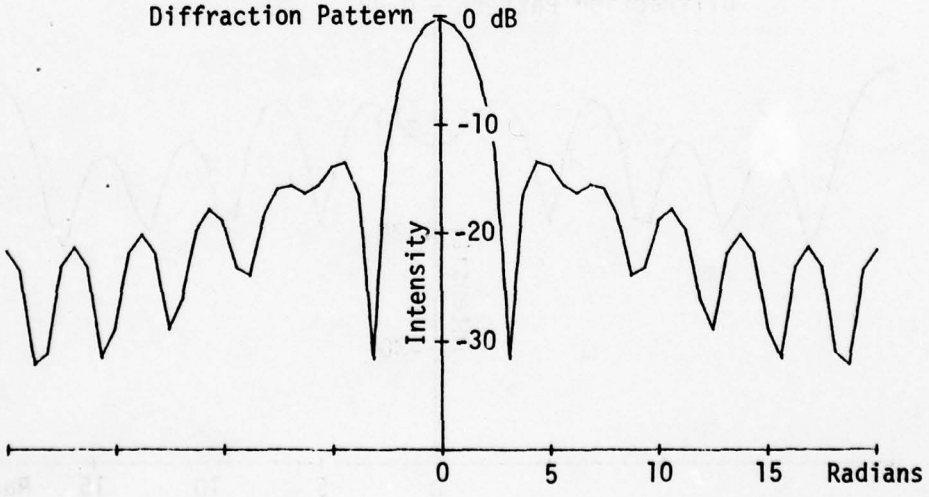

Figure 52. Wavefront Phase Error and Corresponding Intensity Diffraction Pattern for Generalized Luneburg Lens Delineated in Figure 50, S = 5 (.9995 P_1, .997 P_2, 1.0336 P_5).

effect is more pronounced for the S = 5 and S =9 lenses, however, requires a more severe limit imposed upon the aperture.

As the S value is increased, these lenses trend toward a more homogeneous lens where its refractive power is concentrated near the edge. This dictates that the mask contour employed to form these lenses should accurately conform to a circle measured to a fraction of the optical wavelength.

Inspection of the S = 2 perfect profile and various types of defective profiles illustrate that the defects considered represent zonal errors. For Figures 17/18 and 19/20, the error is concentrated in a single circle zone. For Figures 23/24 and 25/26, the errors are concentrated as a circular ring located near $r/r_0 = 0.5$. For Figures 29/30 and 31/32, zonal errors are introduced of opposite effect near the center and near $r/r_0 = 0.7$. These types of errors are not pictorially apparent for the S = 5 and 9 sequence; however, the pattern has been preserved and should be inferred by reference to Table V.

Subsequent experimental data will depict ray traces through various waveguide Luneburg lenses and diffraction patterns. The resulting diffraction patterns contain a variety of defects which may be attributed to spherical aberration in the coupling of convergent/divergent beams for measurements, Mie and Rayleigh scattering in and on the waveguide and lens, and imperfections of the input beam due to scattering, particularly at the input coupling prism edge. For some of the lens data, the lens loss is notinsignificant. Data for scattering out of the waveguide above the substrate is presented, while scattering into the isolation layer and substrate is largely absorbed. All of these real effects tend to mask the inherent lens diffraction pattern. Thus, achievement of near diffraction-limited performance is emphasized for attainment of the appropriate beamwidth, suppression of near-in side lobes below 13 - 17 dB and suppression of wide angle side lobes as far as possible.

AD-A062 933 ROCKWELL INTERNATIONAL ANAHEIM CA ELECTRONICS RESEAR--ETC F/G 20/6
WAVEGUIDE OPTICS FOR COHERENT OPTICAL PROCESSING.(U)
JUN 78 D B ANDERSON , R R AUGUST, S K YAO F33615-77-C-1017

UNCLASSIFIED C77-210.13/501 AFAL-TR-78-83 NL

2 OF 3
AD
AD 62933

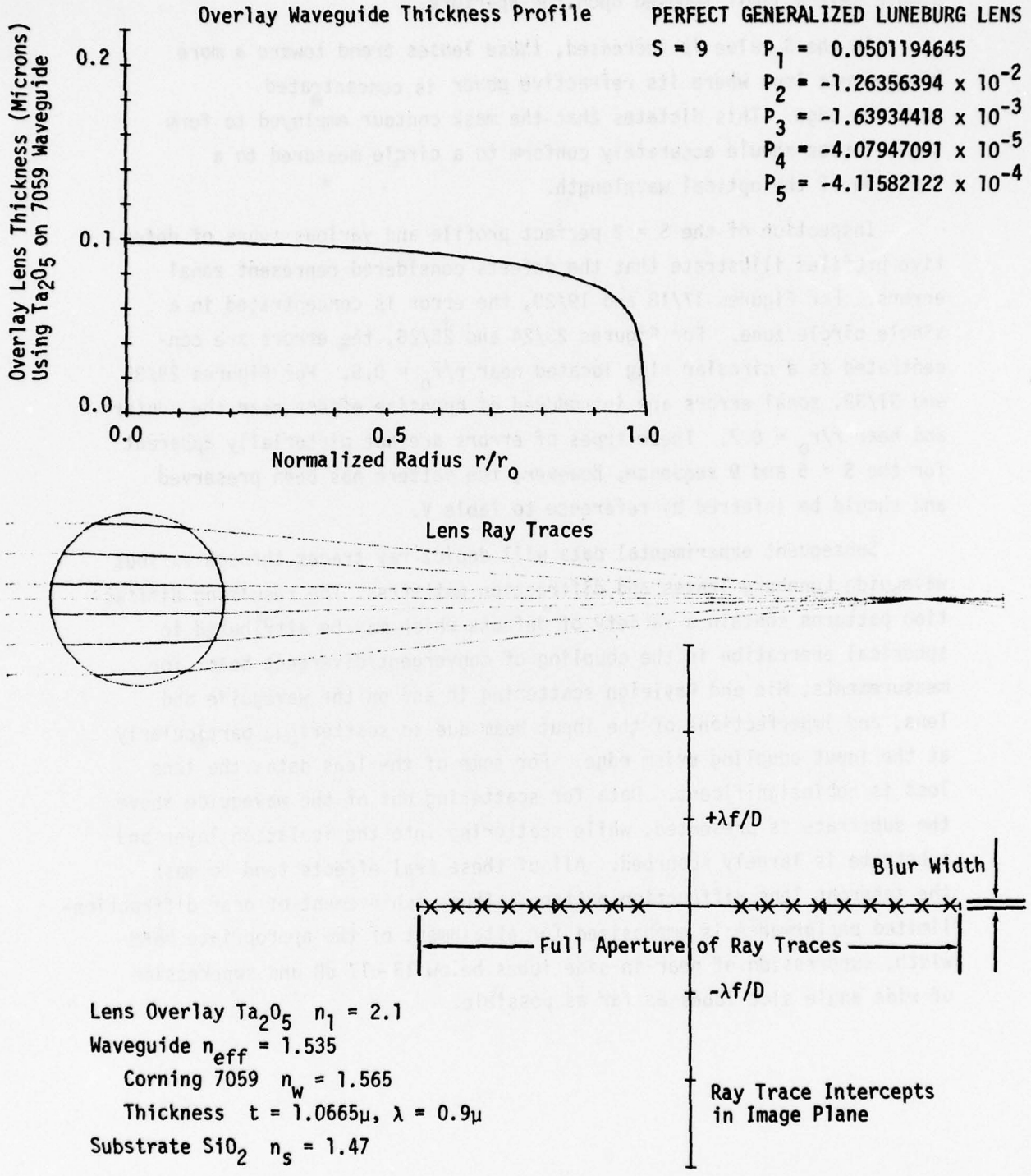

Figure 53. Tabulation of Generalized Luneburg Lens Parameters with Corresponding Overlay Waveguide Lens Thickness Radial Profile, Ray Traces through this Lens and the Intercept Error in the Image Plane, S = 9 (Perfect Luneburg Lens).

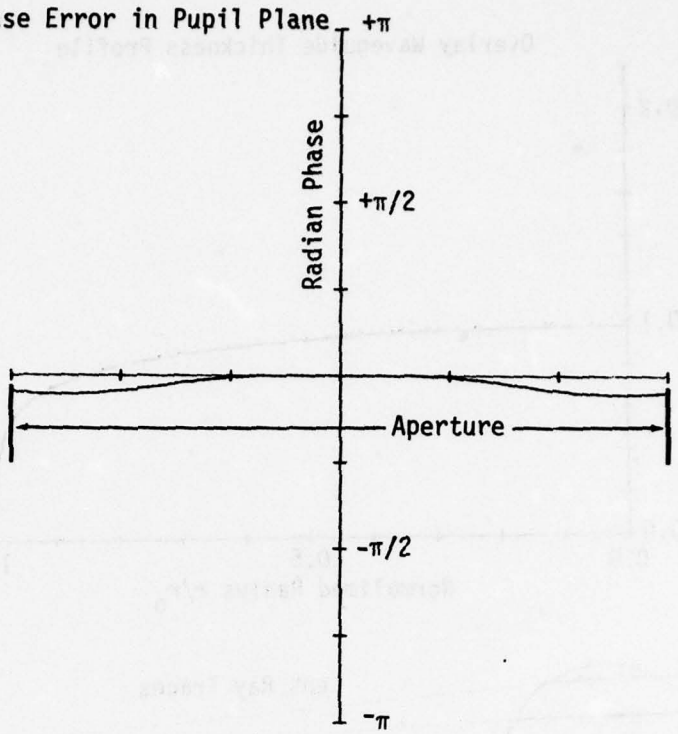

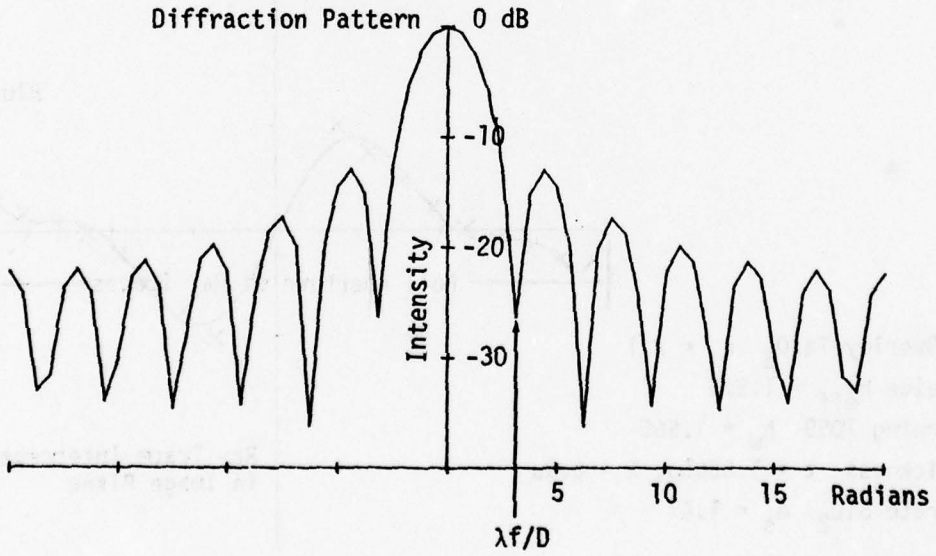

Figure 54. Wavefront Phase Error and Corresponding Intensity Diffraction Pattern for Generalized Luneburg Lens Delineated in Figure 53.

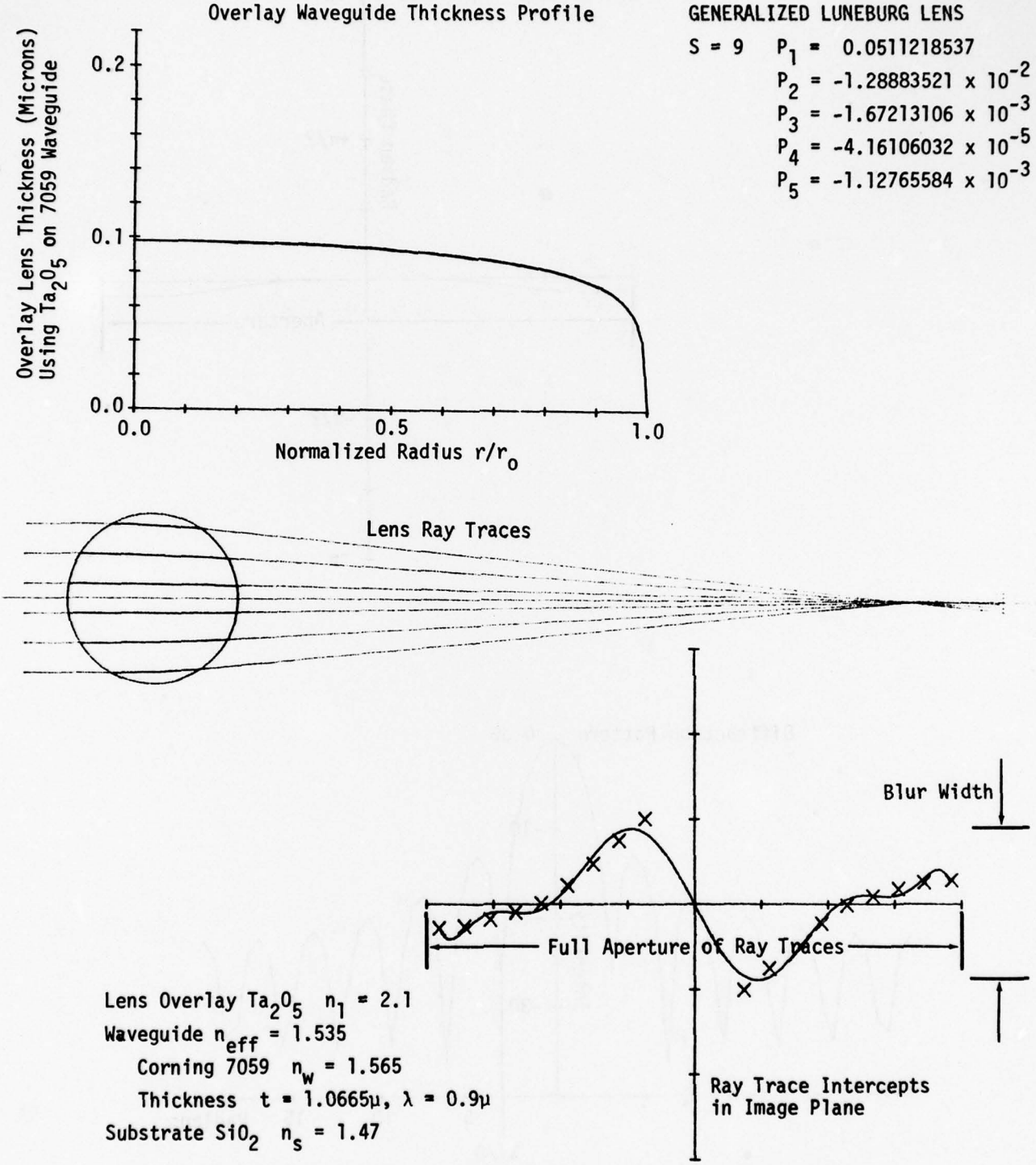

Figure 55. Tabulation of Generalized Luneburg Lens Parameters with Corresponding Overlay Waveguide Lens Thickness Radial Profile, Ray Traces through this Lens and the Intercept Error in the Image Plane, S = 9 (1.02 P_1, 1.02 P_2, 1.02 P_3, 1.02 P_4, 3.1015 P_5).

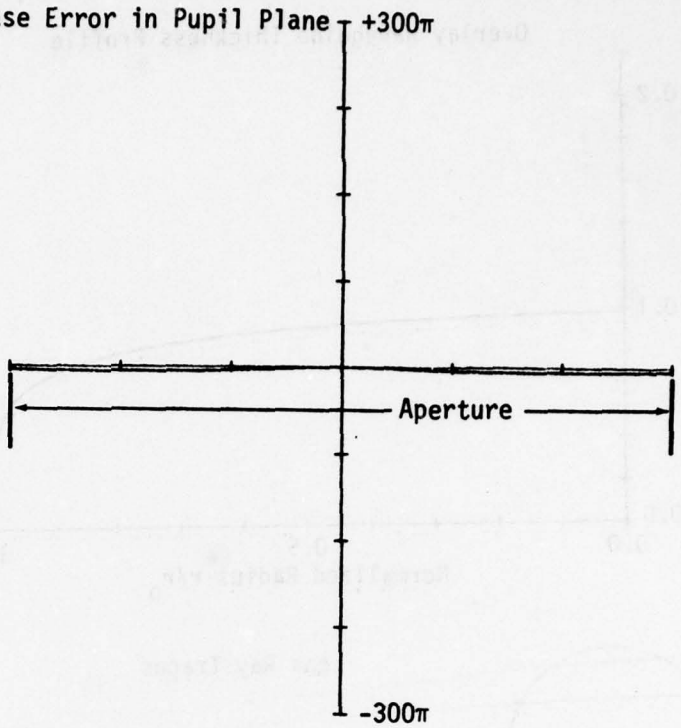

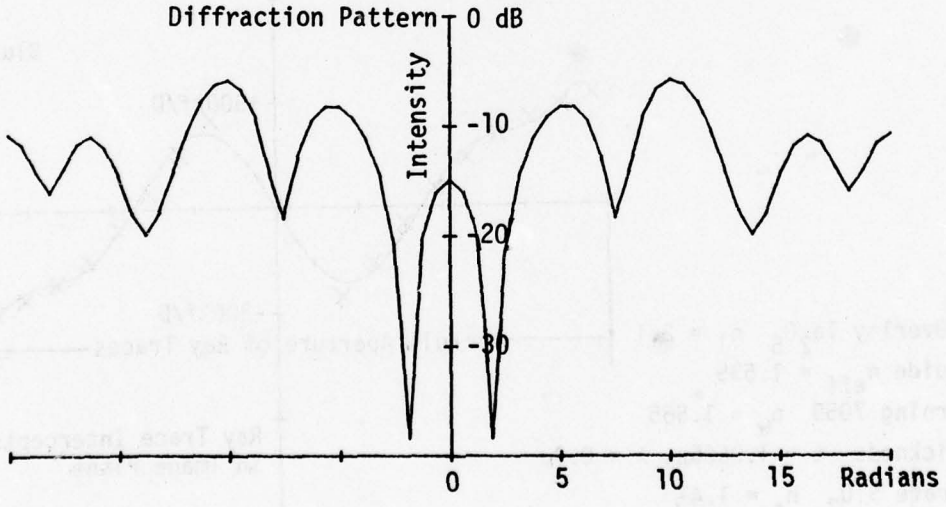

Figure 56. Wavefront Phase Error and Corresponding Intensity Diffraction Pattern for Generalized Luneburg Lens Delineated in Figure 55.

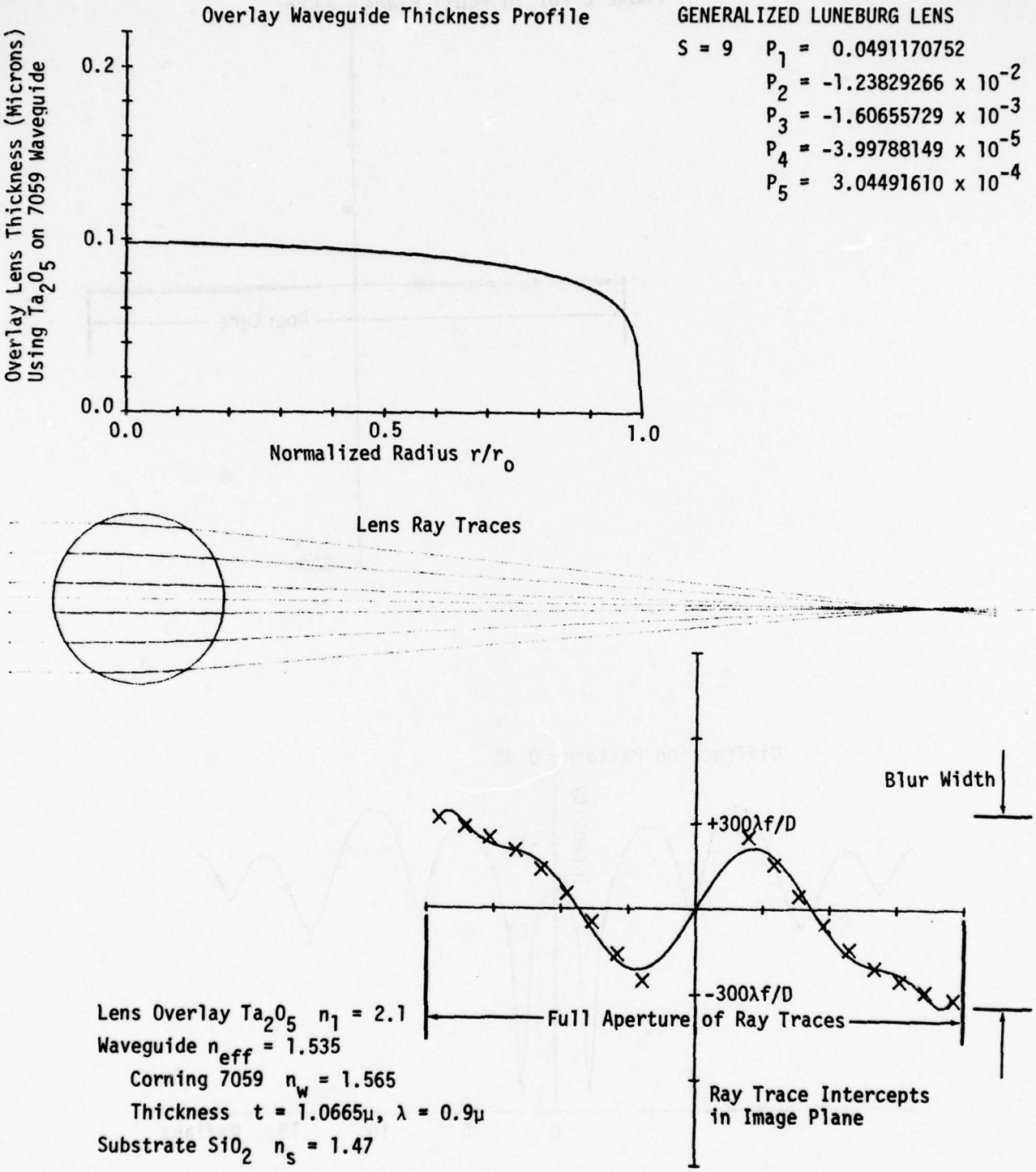

Figure 57. Tabulation of Generalized Luneburg Lens Parameters with Corresponding Overlay Waveguide Lens Thickness Radial Profile, Ray Traces through this Lens and the Intercept Error in the Image Plane, S = 9 (.98 P_1, .98 P_2, .98 P_3, .98 P_4, -.7398 P_5).

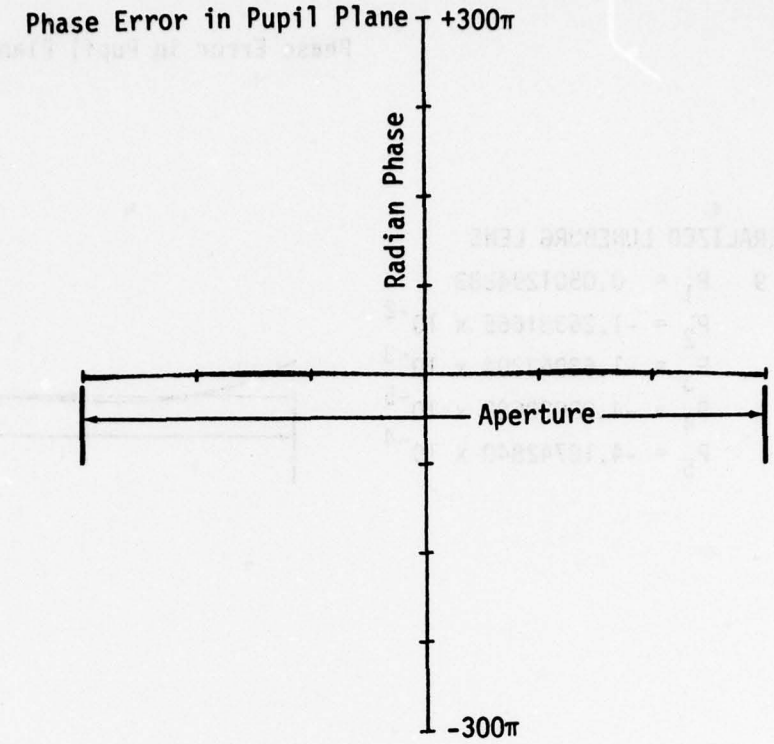

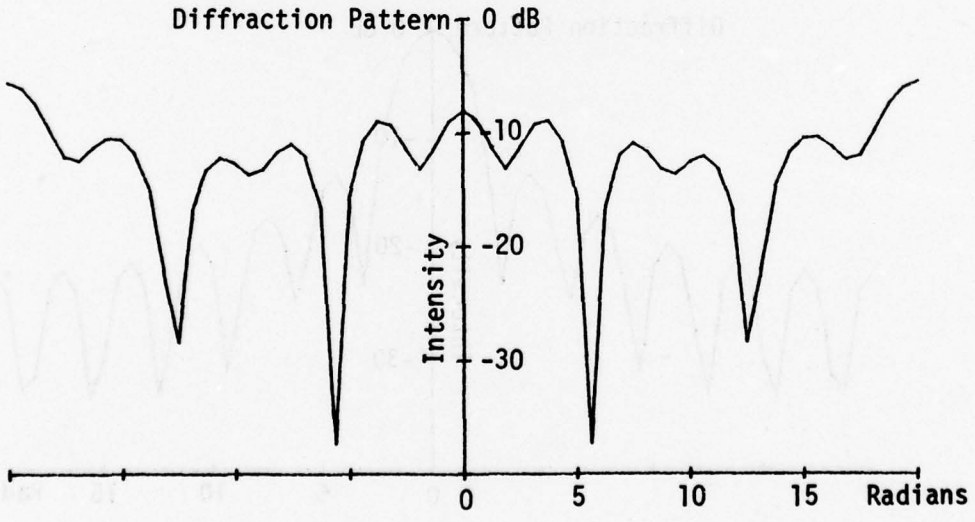

Figure 58. Wavefront Phase Error and Corresponding Intensity Diffraction Pattern for Generalized Luneburg Lens Delineated in Figure 57.

GENERALIZED LUNEBURG LENS

S = 9 P_1 = 0.0501294883

P_2 = $-1.26381665 \times 10^{-2}$

P_3 = $-1.63967204 \times 10^{-3}$

P_4 = $-4.08028680 \times 10^{-5}$

P_5 = $-4.18742840 \times 10^{-4}$

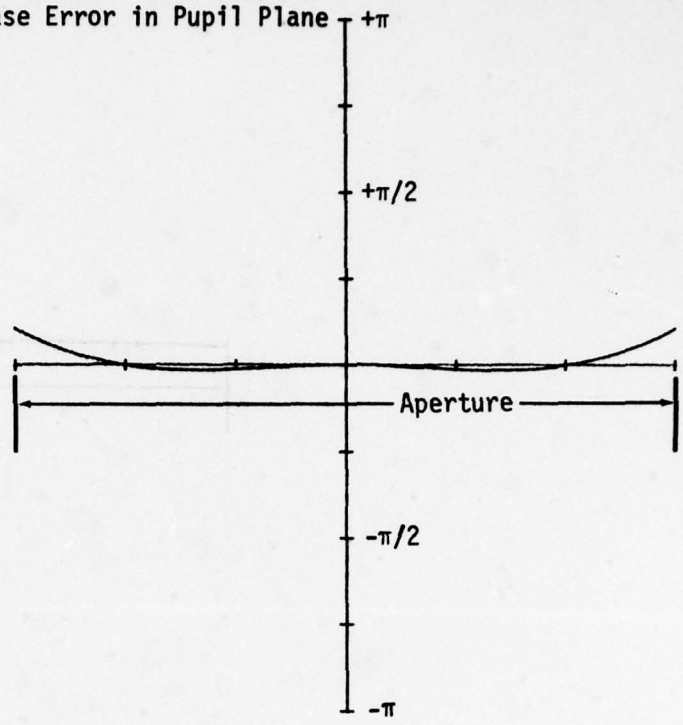

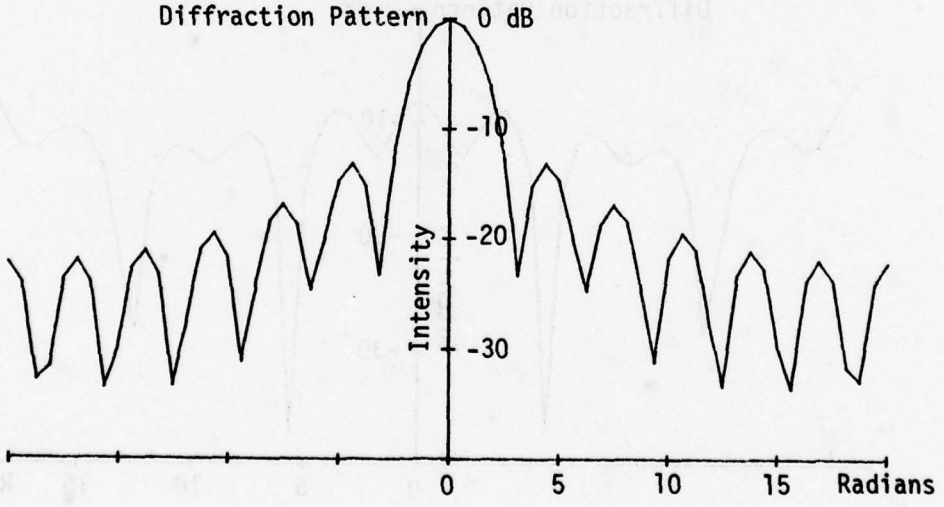

Figure 59. Wavefront Phase Error and Corresponding Intensity Diffraction Pattern for Generalized Luneburg Lens Delineated in Figure 55, S = 9 (1.0002 P_1, 1.0002 P_2, 1.0002 P_3, 1.0002 P_4, 1.0174 P_5).

GENERALIZED LUNEBURG LENS

S = 9 P_1 = 0.0501094406

P_2 = $-1.26331122 \times 10^{-2}$

P_3 = $-1.63901631 \times 10^{-3}$

P_4 = $-4.07865501 \times 10^{-5}$

P_5 = $-4.04421380 \times 10^{-4}$

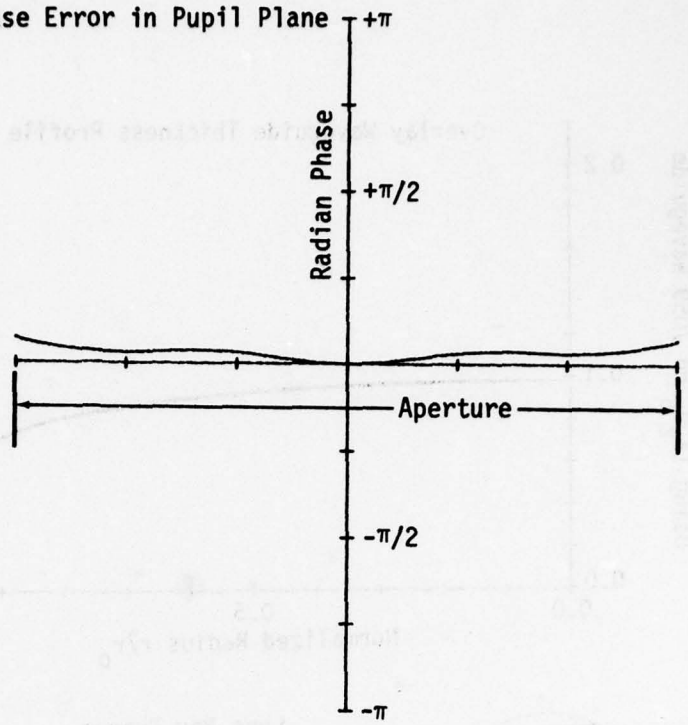

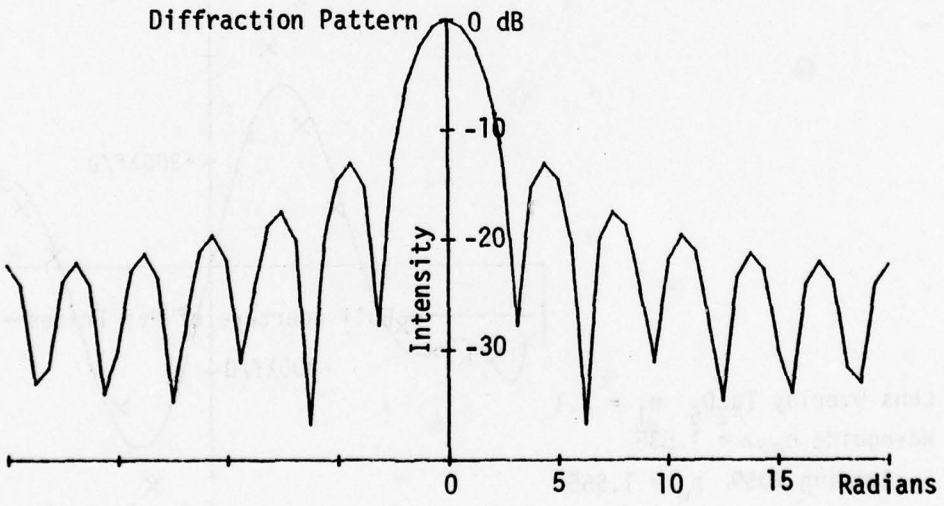

Figure 60. Wavefront Phase Error and Corresponding Intensity Diffraction Pattern for Generalized Luneburg Lens Delineated in Figure 57, S = 9 (.9998 P_1, .9998 P_2, .9998 P_3, .9998 P_4, .9826 P_5).

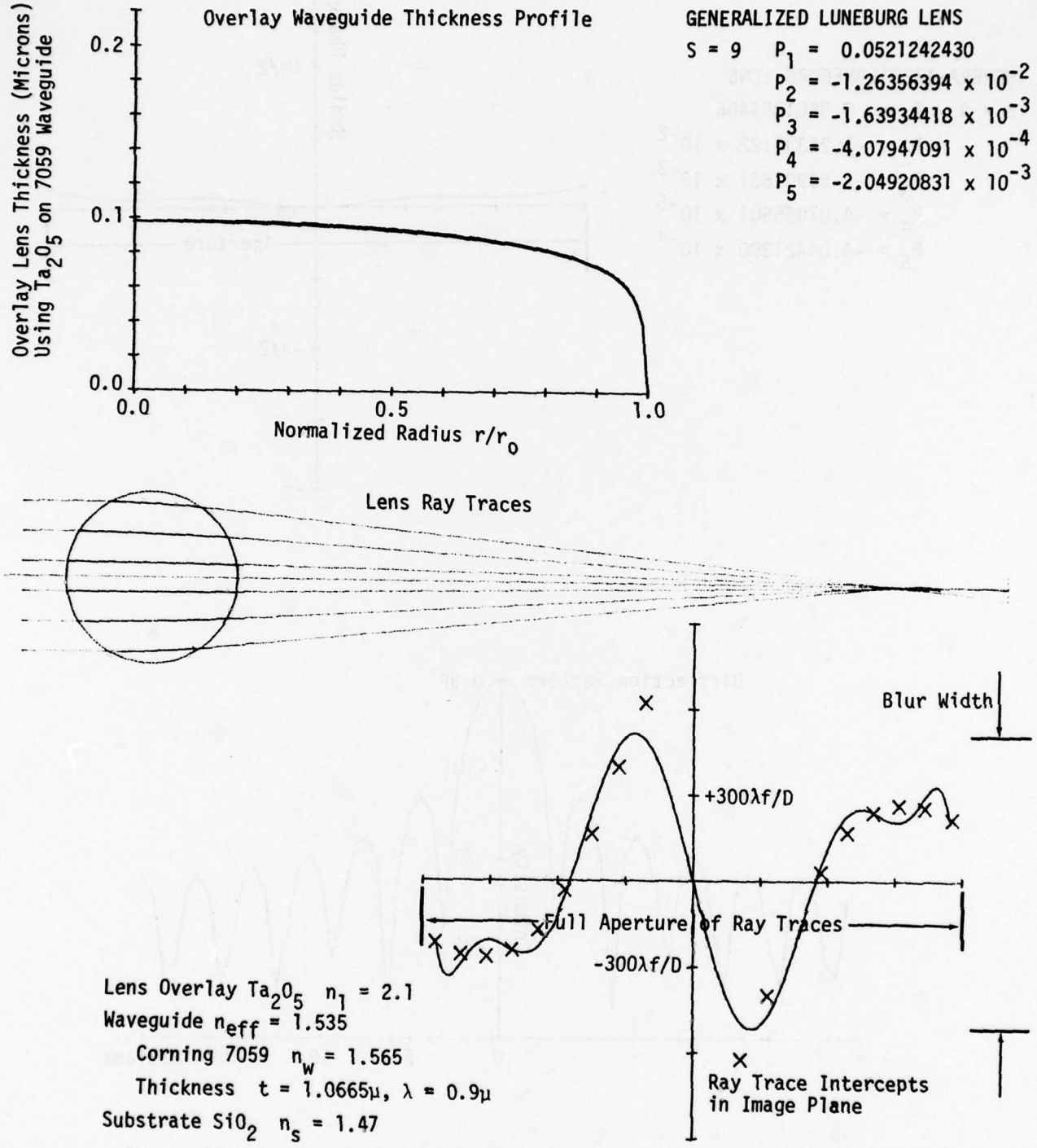

Figure 61. Tabulation of Generalized Luneburg Lens Parameters with Corresponding Overlay Waveguide Lens Thickness Radial Profile, Ray Traces through this Lens and the Intercept Error in the Image Plane, S = 9 (1.04 P_1, 10 P_4, 4.9788 P_5).

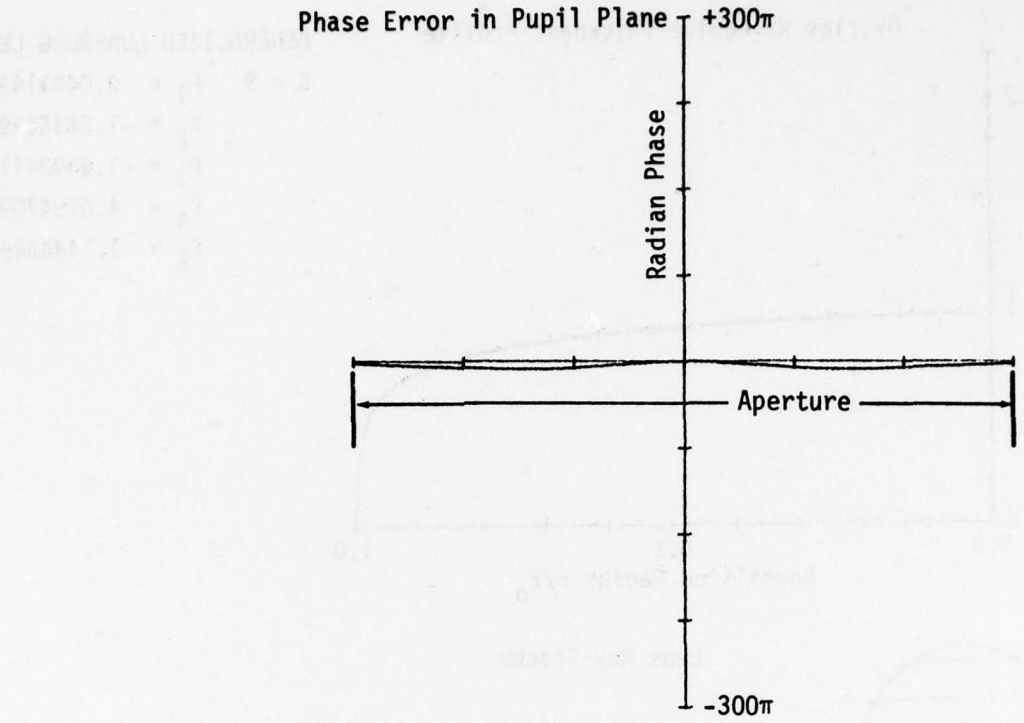

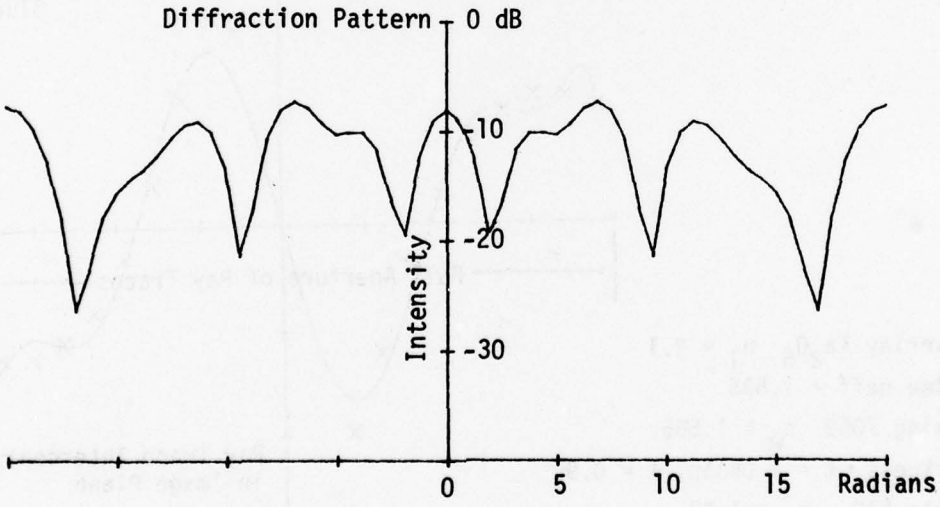

Figure 62. Wavefront Phase Error and Corresponding Intensity Diffraction Pattern for Generalized Luneburg Lens Delineated in Figure 61.

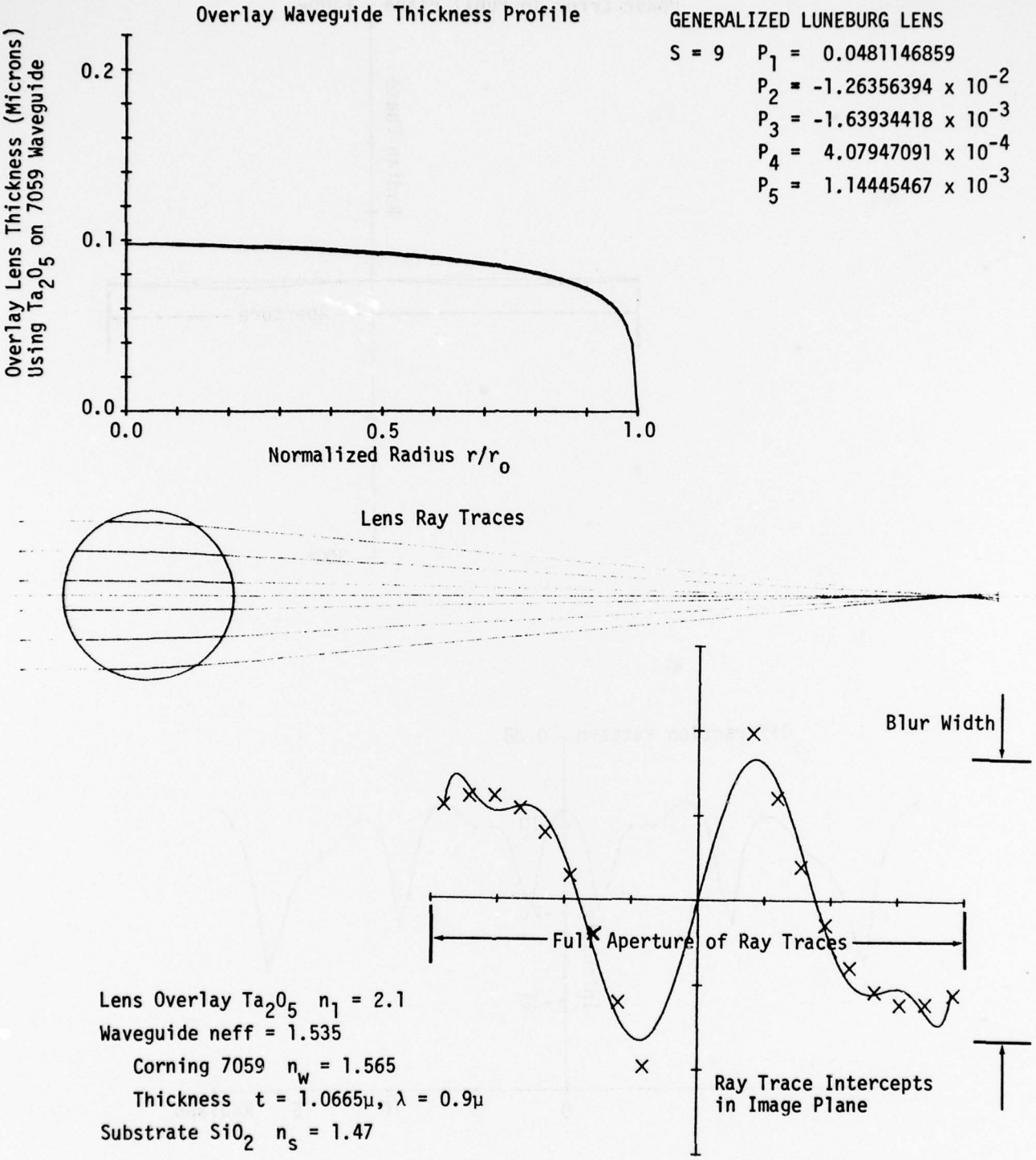

Figure 63. Tabulation of Generalized Luneburg Lens Parameters with Corresponding Overlay Waveguide Lens Thickness Radial Profile, Ray Traces through this Lens and the Intercept Error in the Image Plane, S = 9 (.96 P_1, P_2, P_3, -10 P_4, -2.7806 P_5).

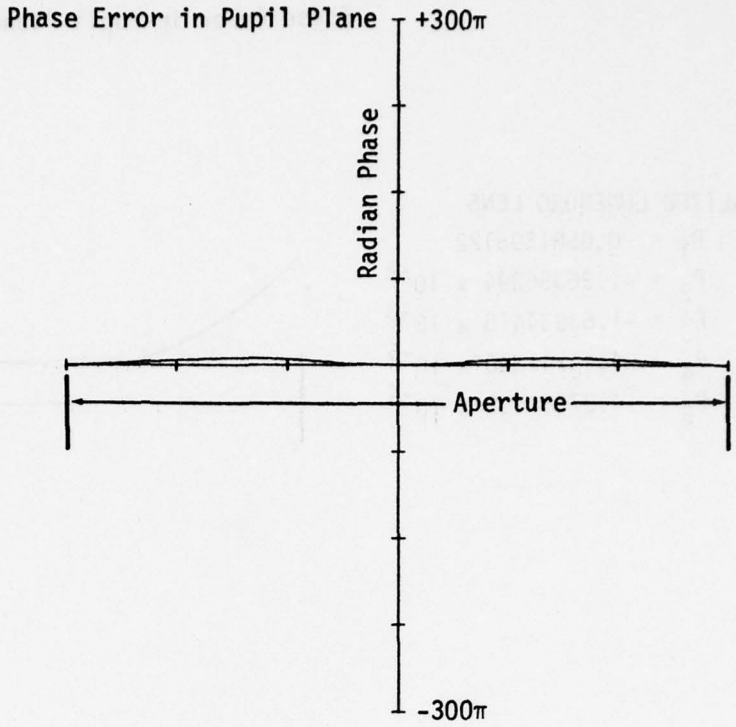

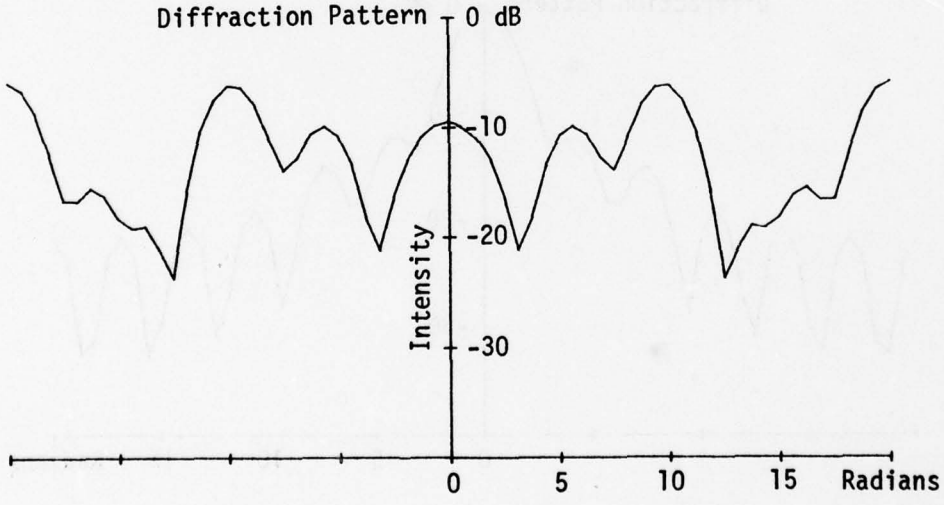

Figure 64. Wavefront Phase Error and Corresponding Intensity Diffraction Pattern for Generalized Luneburg Lens Delineated in Figure 63.

GENERALIZED LUNEBURG LENS

S = 9 P_1 = 0.0501395122

$P_2 = -1.26356394 \times 10^{-2}$

$P_3 = -1.63934418 \times 10^{-3}$

$P_4 = -4.48741800 \times 10^{-5}$

$P_5 = -4.27550430 \times 10^{-4}$

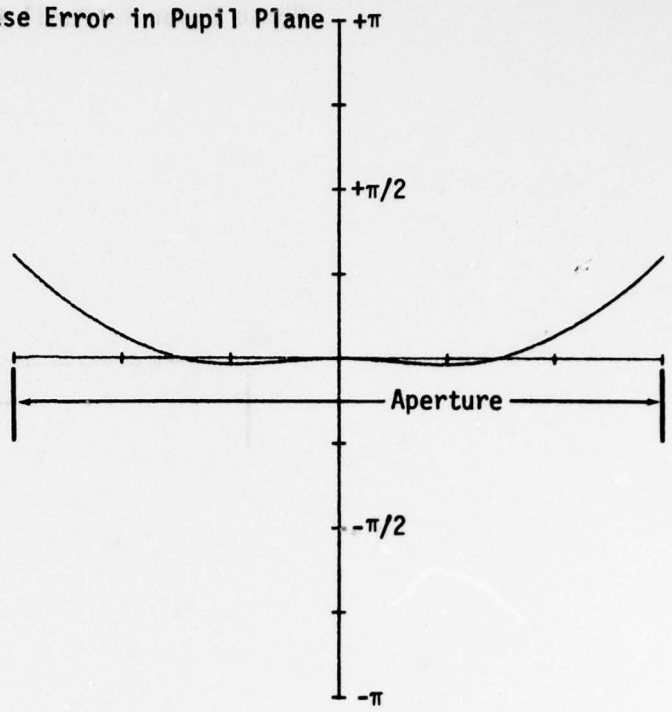

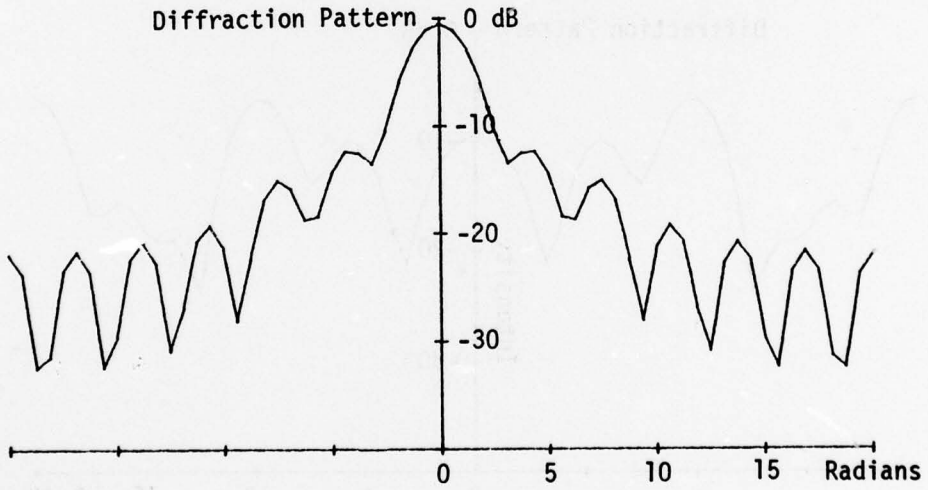

Figure 65. Wavefront Phase Error and Corresponding Intensity Diffraction Pattern for Generalized Luneburg Lens Delineated in Figure 61, S = 9 (1.0004 P_1, 1.1 P_4, 1.0387 P_5).

GENERALIZED LUNEBURG LENS

S = 9 P_1 = 0.0500994167

P_2 = $-1.26356394 \times 10^{-2}$

P_3 = $-1.63934418 \times 10^{-3}$

P_4 = $4.48741800 \times 10^{-5}$

P_5 = $-4.77203210 \times 10^{-4}$

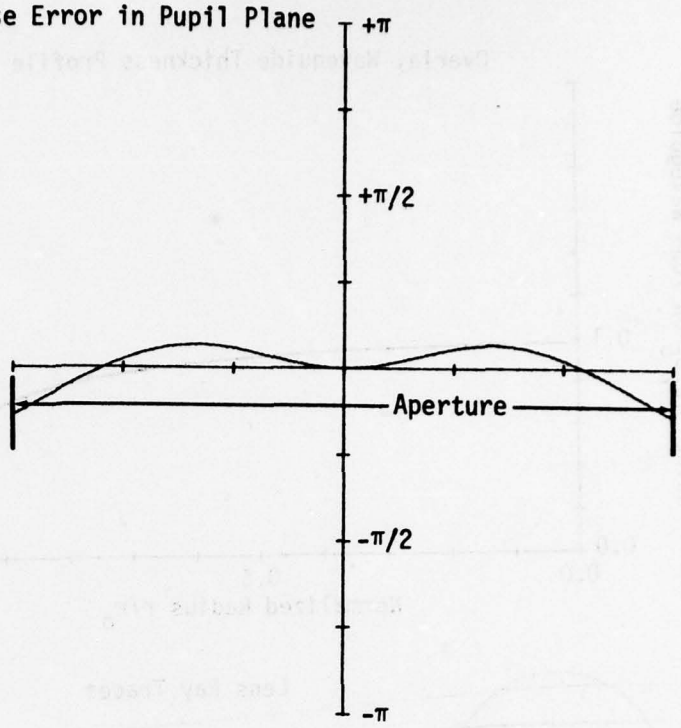

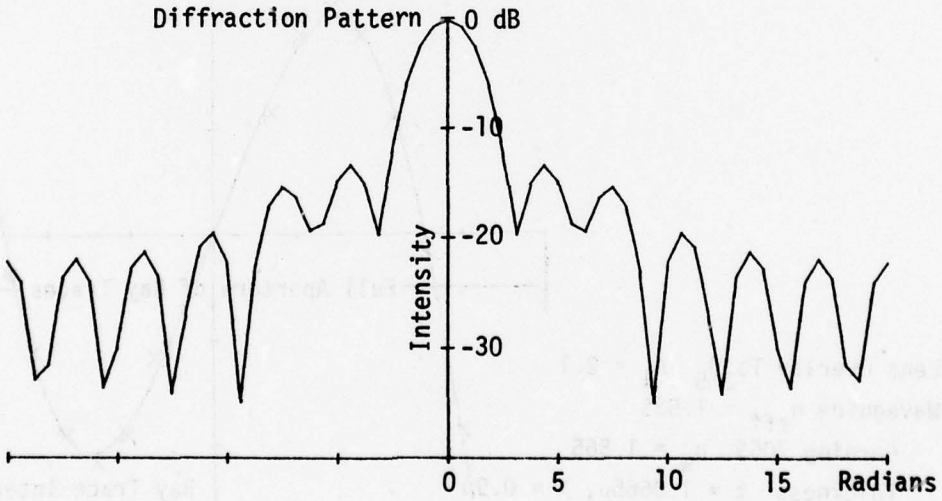

Figure 66. Wavefront Phase Error and Corresponding Intensity Diffraction Pattern for Generalized Luneburg Lens Delineated in Figure 63, S = 9 (.9996 P_1, P_2, P_3, -1.1 P_4, 1.1594 P_5).

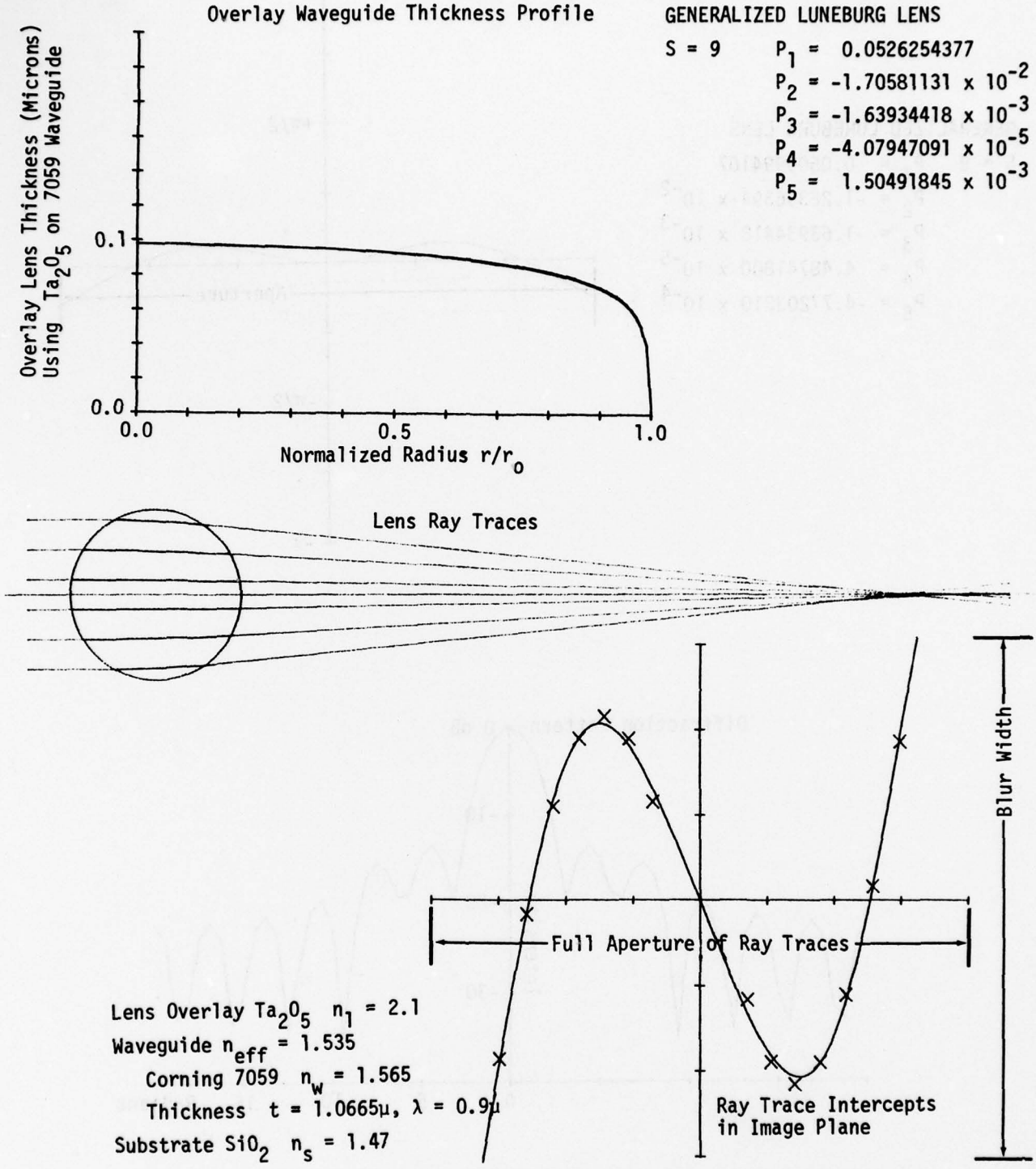

Figure 67. Tabulation of Generalized Luneburg Lens Parameters with Corresponding Overlay Waveguide Lens Thickness Radial Profile, Ray Traces through this Lens and the Intercept Error in the Image Plane, S = 9 (1.05 P_1, 1.35 P_2, P_3, P_4, -3.6564 P_5).

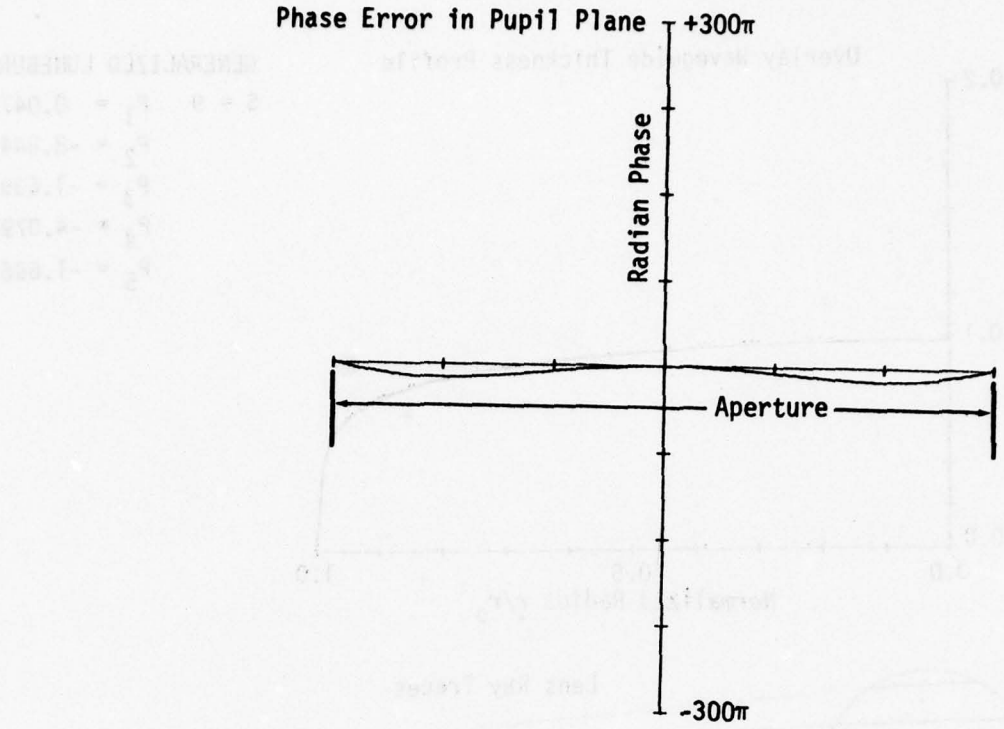

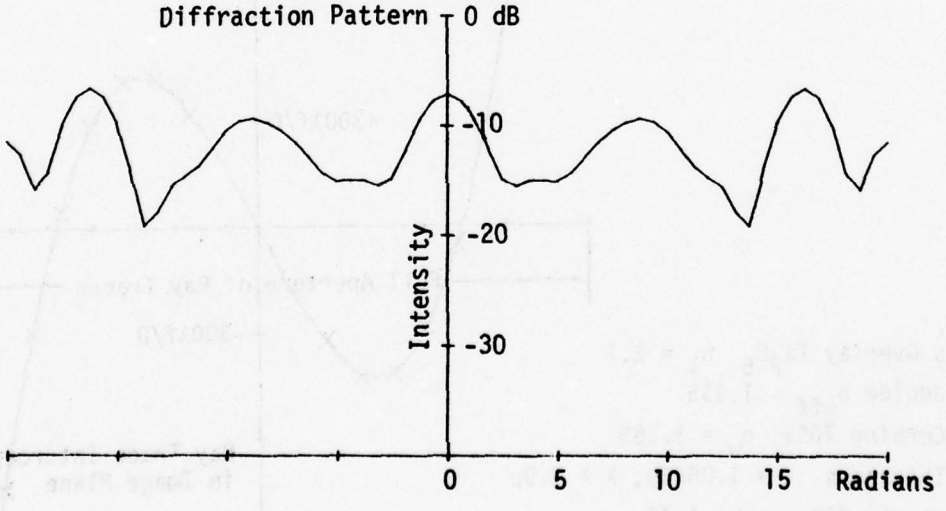

Figure 68. Wavefront Phase Error and Corresponding Intensity Diffraction Pattern for Generalized Luneburg Lens Delineated in Figure 67.

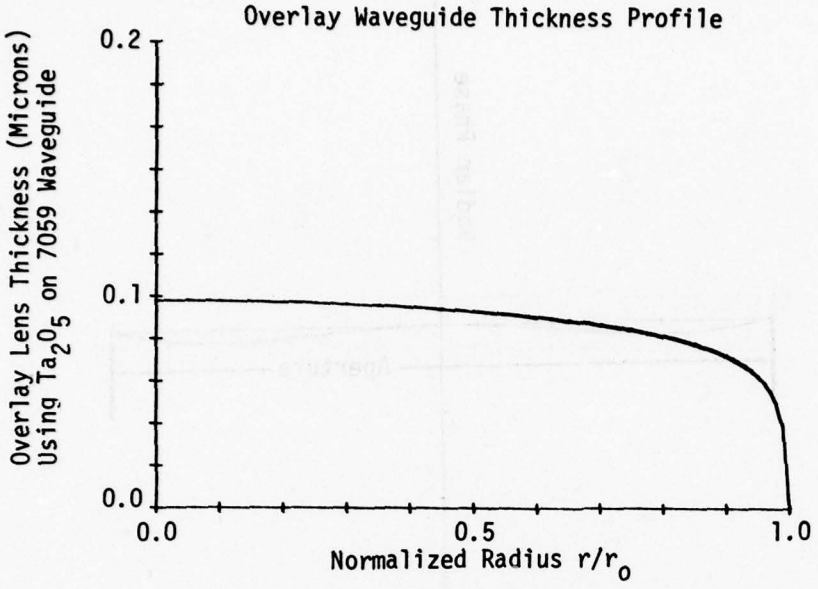

GENERALIZED LUNEBURG LENS

S = 9 P_1 = 0.0476134912

P_2 = -8.84494758 x 10^{-3}

P_3 = -1.63934418 x 10^{-3}

P_4 = -4.07947091 x 10^{-5}

P_5 = -1.69630071 x 10^{-3}

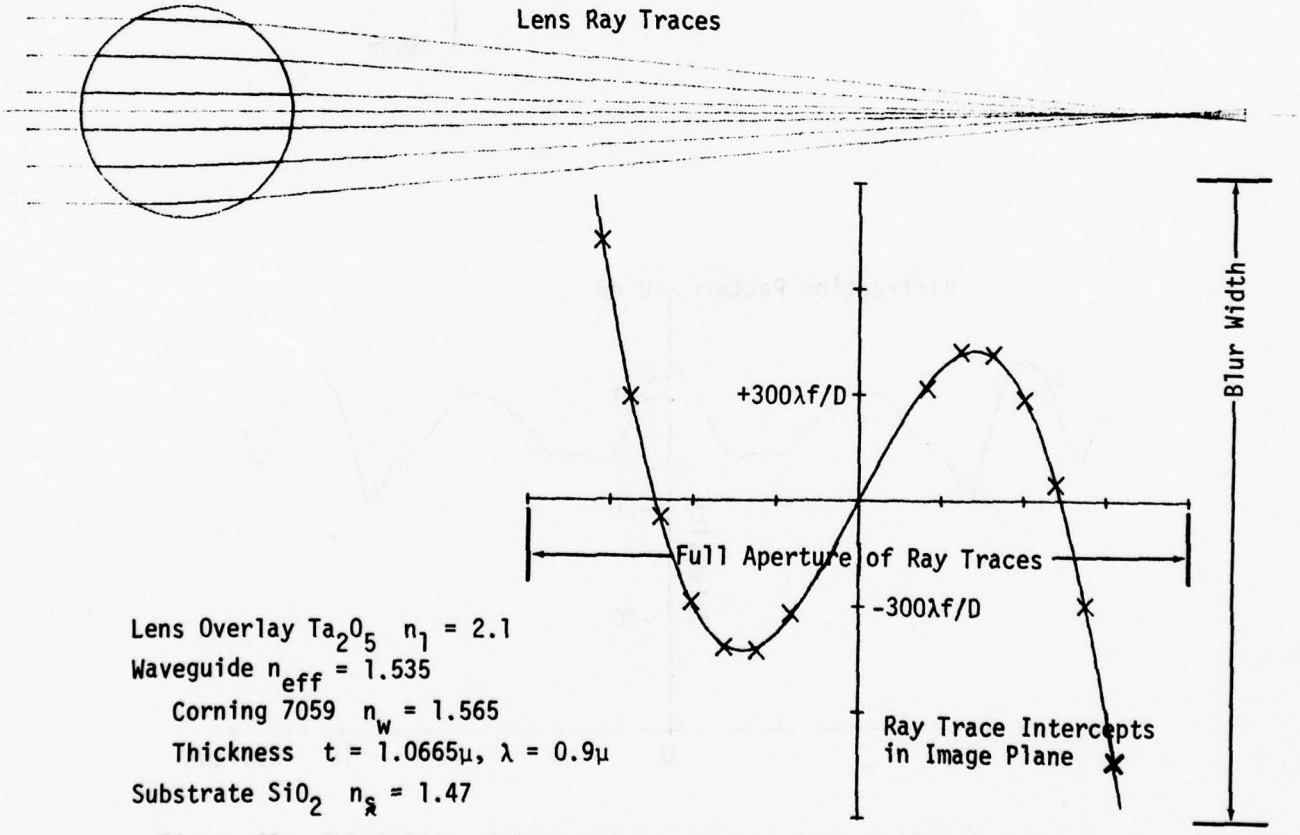

Lens Overlay Ta_2O_5 n_1 = 2.1

Waveguide n_{eff} = 1.535

Corning 7059 n_w = 1.565

Thickness t = 1.0665μ, λ = 0.9μ

Substrate SiO_2 n_s = 1.47

Figure 69. Tabulation of Generalized Luneburg Lens Parameters with Corresponding Overlay Waveguide Lens Thickness Radial Profile, Ray Traces through this Lens and the Intercept Error in the Image Plane, S = 9 (.95 P_1, .7 P_2, 4.1214 P_5).

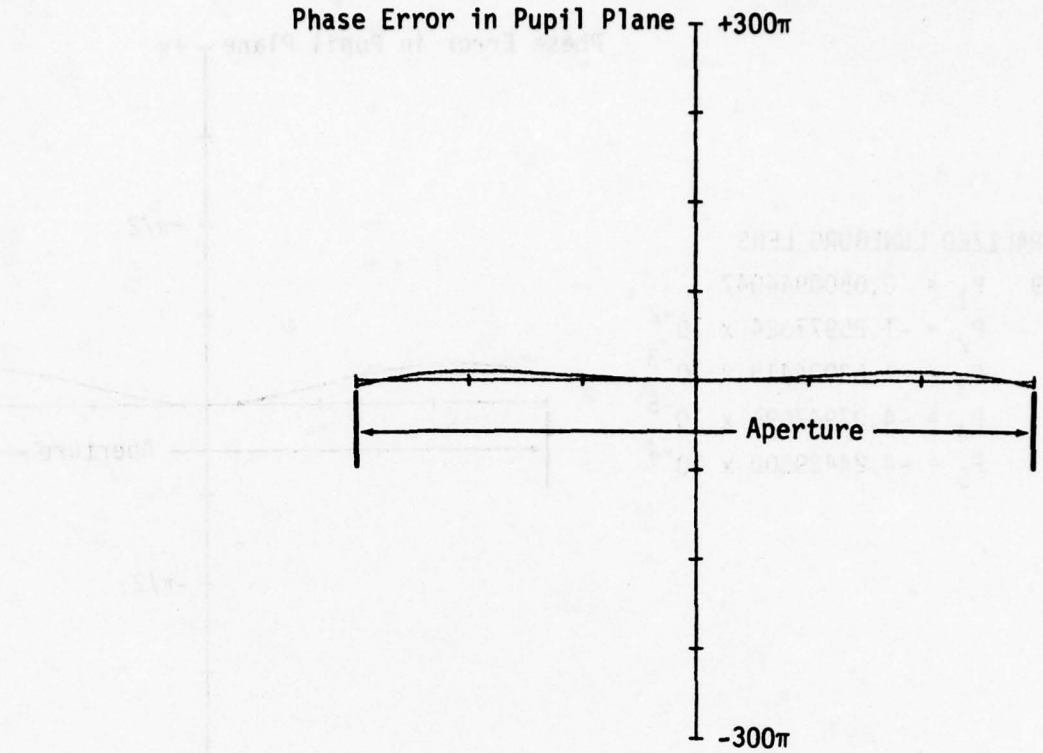

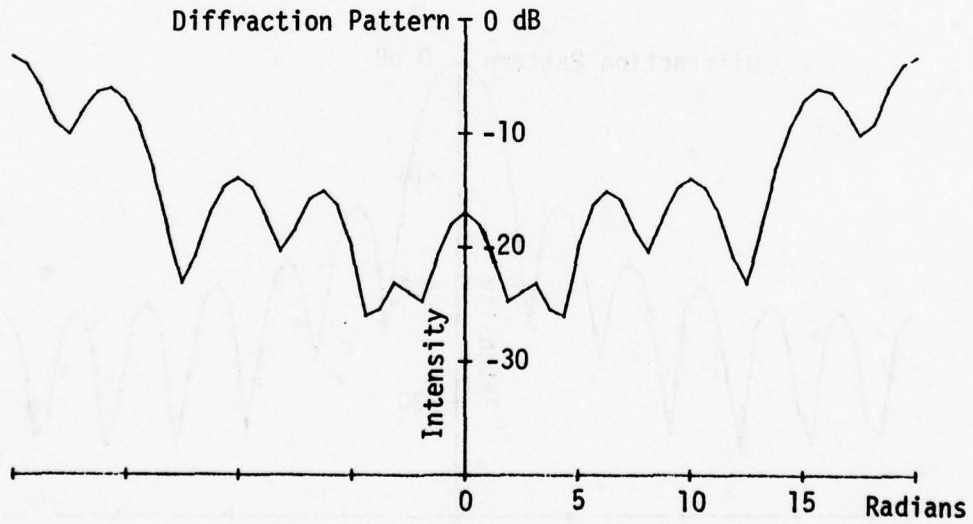

Figure 70. Wavefront Phase Error and Corresponding Intensity Diffraction Pattern for Generalized Luneburg Lens Delineated in Figure 69.

GENERALIZED LUNEBURG LENS

S = 9 P_1 = 0.0500944047

P_2 = $-1.25977324 \times 10^{-2}$

P_3 = $-1.63934418 \times 10^{-3}$

P_4 = $-4.07947091 \times 10^{-5}$

P_5 = $-4.24429300 \times 10^{-4}$

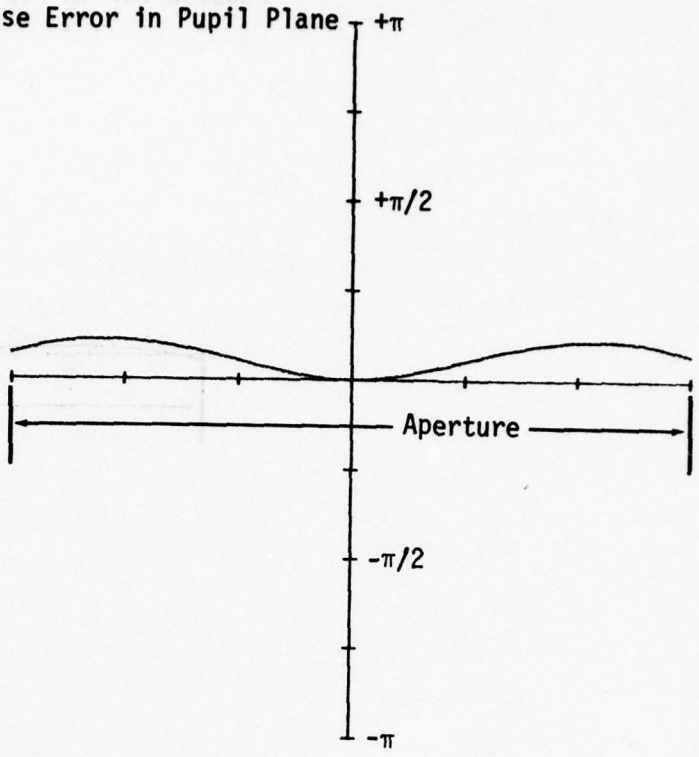

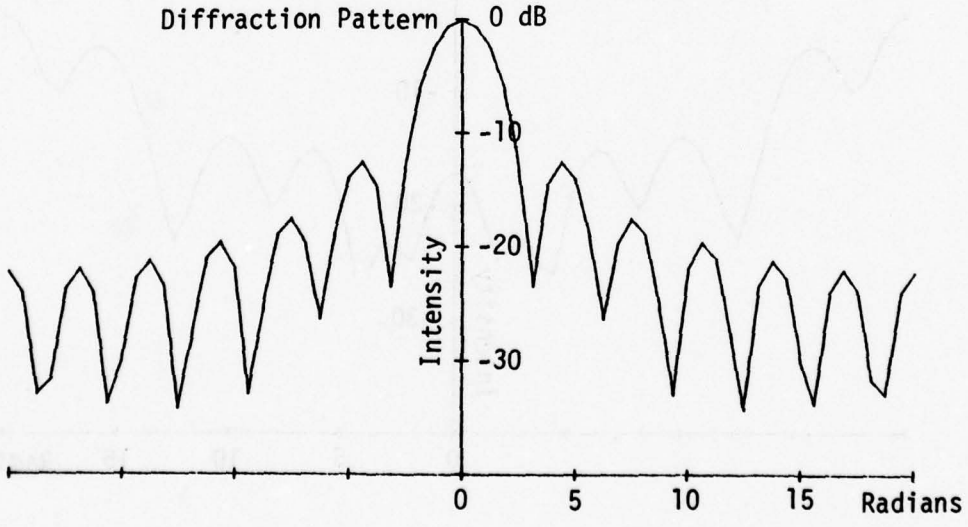

Figure 71. Wavefront Phase Error and Corresponding Intensity Diffraction Pattern for Generalized Luneburg Lens Delineated in Figure 69, S = 9 (.9995 P_1, .997 P_2, 1.0312 P_5).

6. Computer Simulation of the Luneburg Lens Deposition Mask

The preceding analysis has accurately defined the overlay Luneburg lens thickness profile necessary to produce diffraction-limited results and the effects of defective profiles as exemplified by their diffraction patterns.

One method to form thin-film waveguide lenses is by deposition through an appropriate mask. The RF sputter process has been employed throughout for this purpose. The cross section of the RF sputter deposition sample is depicted in Figure 72. Argon ions are accelerated toward the Ta or Nb cathode target where bombardment releases molecules that are oxidized during their flight until collision. In the sputtering environment employed, the mean-free-pathlength is greater than the thickness of the mask and, thus, effects of collision and diffusion are avoided. A Lambertian distribution has been assumed and verified. Thus, the molecular beam arrives at the mask entrance with a predictable angular momentum distribution $A(\theta,v)$. Where the mask produces a shadow, integration over the particle velocity range provides an angular distribution function $A_d(\theta)$. The distribution function, $A_d(\theta)$, was experimentally measured with a knife-edge mask confirming the Lambertian source. Based upon this knowledge, the effect of a shadow mask upon sputtering has been predicted with the aid of a computer.

The shadow mask computation is relatively simple when the mask has circular symmetry. The coordinates employed to compute the distribution are illustrated in Figure 73. For an arbitrary point P_0, the thickness distribution becomes

$$T(x_0,y_0) = \iint_S \frac{A(\theta)\cos\theta}{R^2} \, dxdy \tag{47}$$

where

$$\theta = \cos^{-1} \frac{D}{\sqrt{(x_1-x_0)^2+(y_1-y_0)^2}} \, , \; R = \sqrt{(x_1-x_0)^2+(y_1-y_0)^2+z_1^2}$$

and (dxdy) is an infinitesimally small area of the mask entrance window, and S is the portion of the entrance window which is visible from point P.

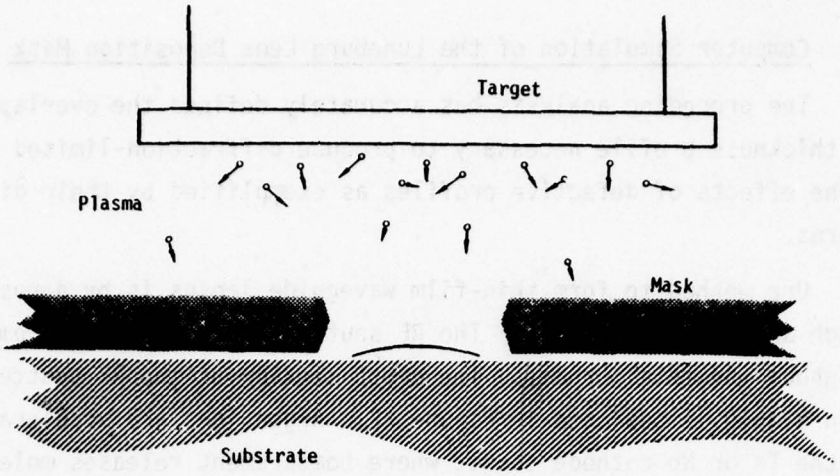

Figure 72. Cross Section of RF Sputter Deposition Chamber Used to Profile Luneburg Lenses and Taper Waveguide Films.

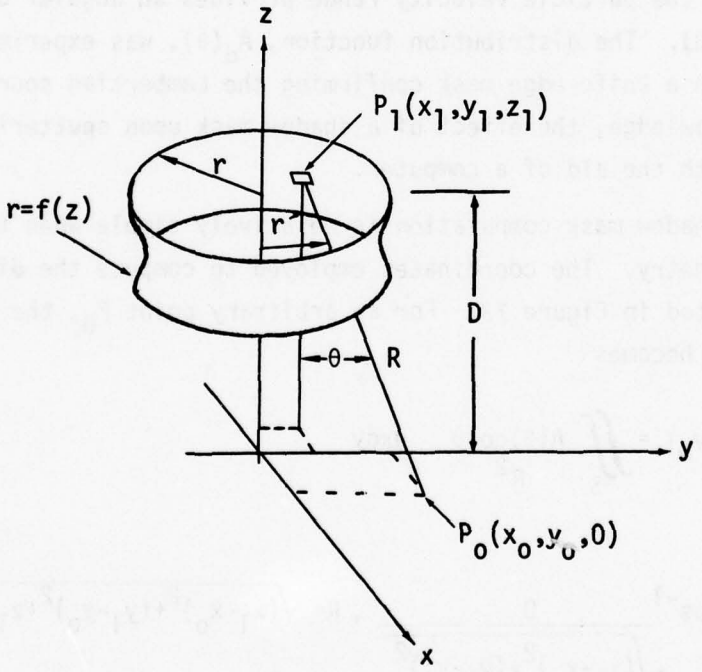

Figure 73. Coordinate System for Luneburg Lens Mask Edge Synthesis.

The distance, D, in Figure 73 extends from the plane containing the top of the mask to the substrate surface.

The determination of the effective window function, S, for a mask contour of a general cylinder is also illustrated by Figure 73 The edge contour is conveniently described by $r = f(z)_0$. The line of sight between points P_0 and P_1 is given by the solution of

$$\begin{aligned} z_1 y + (y_0 - y_1)z - z_1 y_0 &= 0 \\ z_1 x + (x_0 - x_1)z - z_1 x_0 &= 0 \end{aligned} \tag{48}$$

which defines two planes each parallel to the x or the y axis while containing the line of sight P_0P_1. At any point on this line, the distance to the axis of rotation of the mask is, therefore,

$$r' = \left[\left(\frac{(x_0 - x_1)z}{z_1} - x_0 \right)^2 + \left(\frac{(y_0 - y_1)z}{z_1} - y_0 \right)^2 \right]^{1/2} . \tag{49}$$

If the line of sight is not interrupted by the edge of the shadow mask, the following function must not have real solution.

$$(r')^2 - r^2 \geq 0, \quad \left(\frac{(x_0 - x_1)z}{z_1} - x_0 \right)^2 + \left(\frac{(y_0 - y_1)z}{z_1} - y_0 \right)^2 - f^2(z) = 0$$

For f(z) described by quadratic functions, analytic result may be easily obtained. For f(z) of higher order functions, numerical evaluation must be employed. Anytime when the above function becomes greater than or equal to zero, it means that interference with line of sight is occurring. Thus, the deposition distribution function becomes

$$T(x_0, y_0) = \iint_W \frac{A(\theta)\cos\theta G}{R^2} \, dxdy \tag{50}$$

where W is the entrance window and G is a logic function which is one (or zero) when the line of sight is clear (or interrupted).

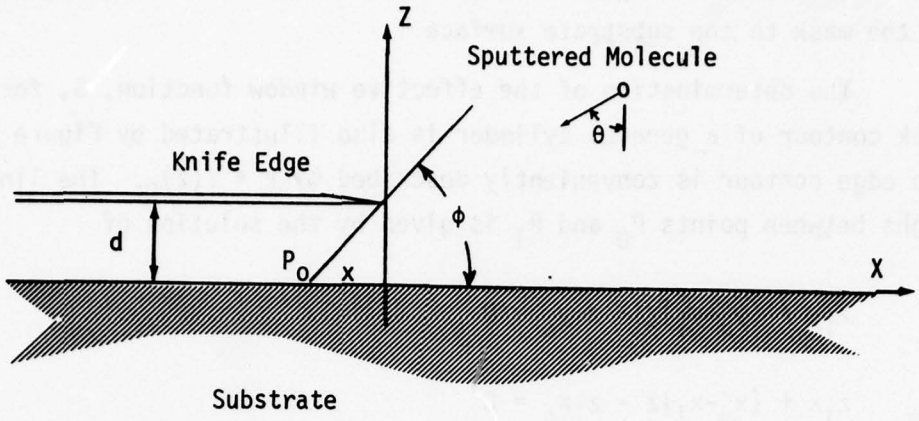

Figure 74. Coordinate System for Knife-Edge Shadow Mask.

The anglular distribution of sputtered material depends upon the ion angle of arrival, the target and sputtering system geometry, and film growth properties. For the vacuum environment employed, the ions experience a mean-free path length greater than the shadowing mask thickness, while the target source extends over the full angular range of the shadow mask acceptance angle. The angular distribution of sputtered particles has been measured with a small pinhole and with a knife edge for calibration, and has been found to confirm the assumed cosine or Lambertian distribution.

Assume that the knife edge is located at a distance d above the substrate, as shown in Figure 74, and that the deposited film thickness profile is B (x) which can be measured. From Figure 74 it is noted that the relationship between the coordinate x and the deposition acceptance angle $\phi(x)$ is $x = d \cot\phi$. Because the physical deposition rate at any point is actually dependent on the deposition acceptance angle available to that point, i.e.,

$$B(x) = \tau \int_{90°}^{\phi(x)} \frac{A_d(\theta)}{r} \, r d\theta \tag{51}$$

$$= \tau \int_{90°}^{\tan^{-1}\frac{d}{x}} A_d(\theta) \, d\theta \tag{52}$$

where τ is the deposition time, the angular deposition rate may be

obtained by taking the derivative of B (x) followed by a change of variable, i.e.,

$$\frac{dB(x)}{dx} = \frac{-\tau d}{(x^2+d^2)} A_d(x) \tag{53}$$

$$A_d(x) \xrightarrow[x=d\ \cot\Theta]{} A_d(\theta) \quad . \tag{54}$$

Thus, from the above, the angular deposition rate is found to closely approximate the cosine angular distribution.

With the computer model we have iterated a sample conical mask and computed the resulting deposition thickness profile. A cross section of the conical mask and its descriptive parameters is depicted in Figure 75 (a). The effect of changing the conical angle is depicted in Section (b) of the Figure. The effect of the mask spacing above the substrate is depicted in Section (c), and the effect of mask aperture diameter is depicted in Section (d). The accuracy of these computations has been confirmed by a stylus probe, including measurements of the slope and steps for a number of shadow masks.

From these variational effects depicted in Figure 75, a first iteration approximation to a Luneburg lens thickness profile was developed using two conical sections as illustrated by the cross section in Figure 76. The resulting calculated thickness profile is indicated together with an experimentally measured segment near the edge of the deposition. Using the preceding computer simulation programs, the thickness profile is converted to a refractive index profile with ray traces through the lens calculated to find the ray intercept errors at the focus. Figure 77 depicts the calculated ray intercepts for the thickness profile of Figure 76 derived from the conical mask. The insert illustrates the ray traces. The experimental points concerning the calculations have been taken from the measured ray traces photographed for Figure 78 using a waveguide Luneburg lens formed with mask SK-1. The mask SK-1 is only a first approximation and referring to Figure 77, can only be used out to 0.5 of its radius. Diffraction data for a number of waveguide Luneburg lenses fabricated with mask SK-1 are included in the next section.

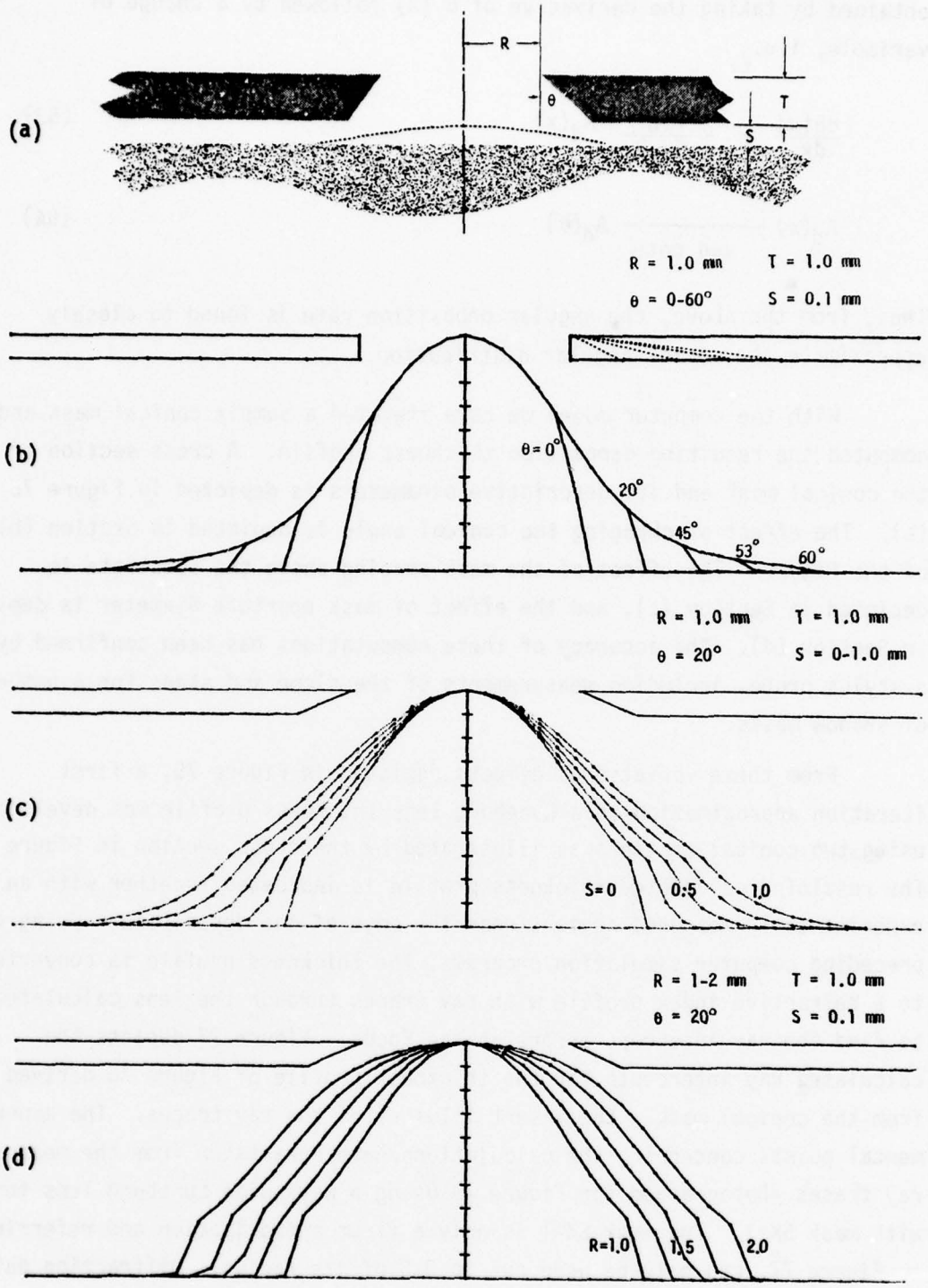

Figure 75. Cross Section of Mask (a) and Calculated Thin-Film Deposition Profiles for Variable Cone Angle (b) Variable Mask Spacing Above Substrate (c) and for Variable Mask Aperture Diameter (d).

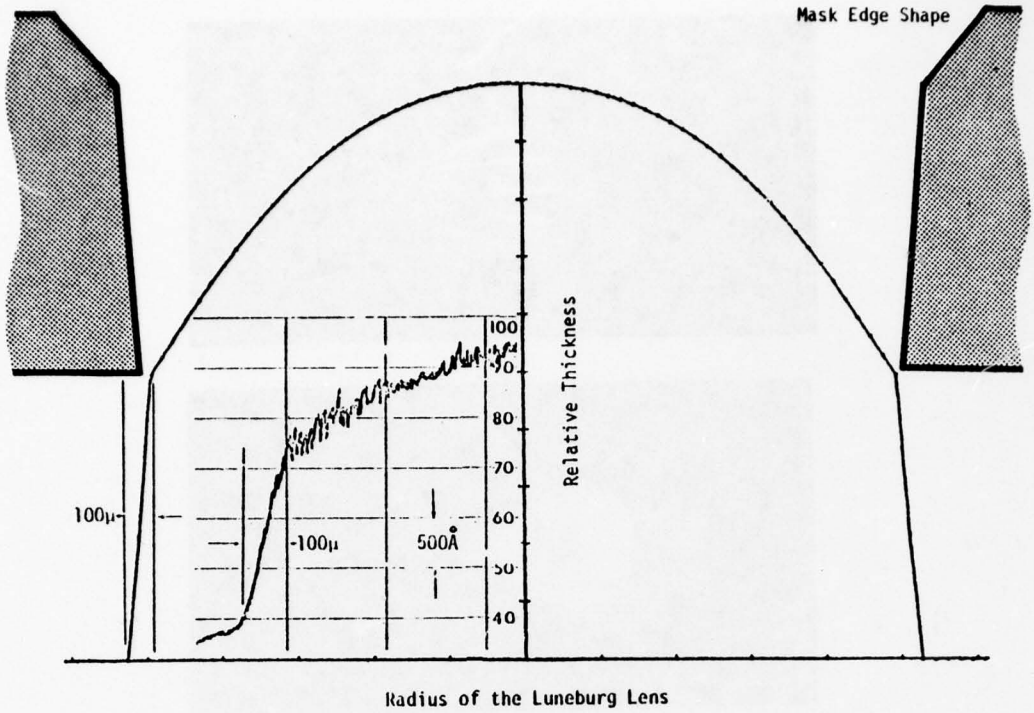

Figure 76. Computed Luneburg Lens Thickness Profile for SK-1 Mask Edge Shape Indicated with a Confirming Measured Stylus Thickness Profile.

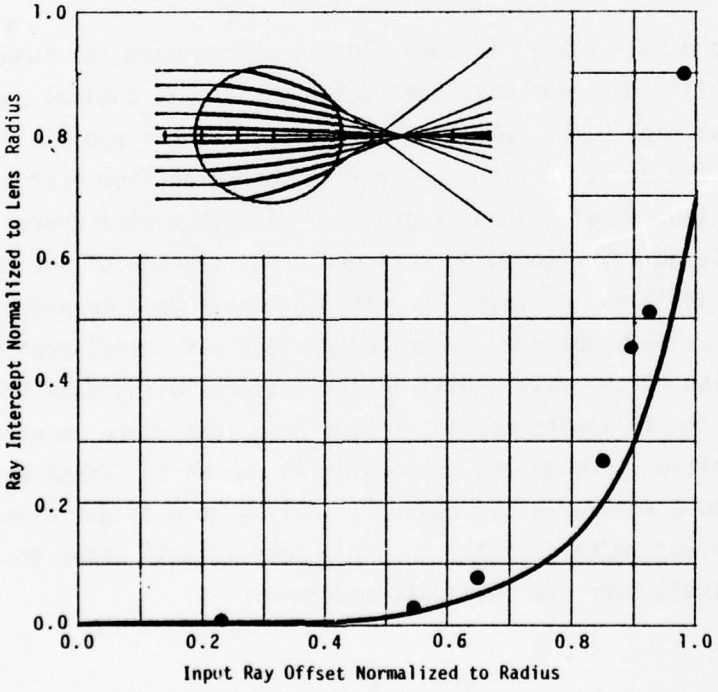

Figure 77. Calculated and Measured Ray Intercept for Waveguide Luneburg Lens Using Mask SK-1 and Photographic Data of Figure 78.

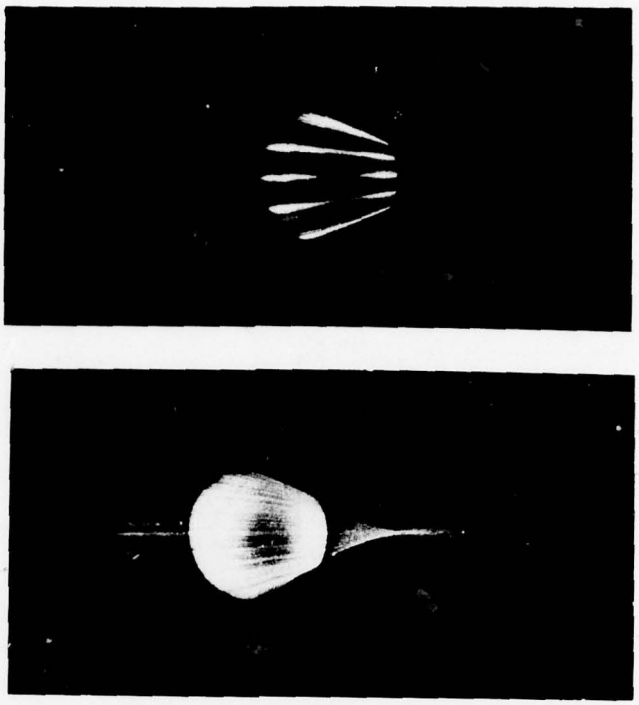

Figure 78. Measured Ray Traces for Waveguide Luneburg Lens Formed With Mask SK-1.

A second mask (SK-2) to more closely approximate the ideal lens thickness profile has been developed which employs 12 conical segments to shape the mask edge. The resulting computed thickness profile is depicted in Figure 79 and compared with the profile generated from mask SK-1 and the Luneburg lens ideal thickness profile. A much closer approximation has been achieved. The computed enlarged cross section of the improved mask SK-2 is depicted in Figure 80. Its thickness is 6 mm and its diameter is 8 mm. This computer generated profile was transferred directly for fabrication of the mask. Diffraction patterns using mask SK-2 are presented in the following section including a lens where an error was made by deposition through the wrong side of the mask. These masks have been scaled to a smaller size; however, scaling to a larger diameter will require a corresponding increase in the target size in order to extend coverage entirely over the full mask aperture.

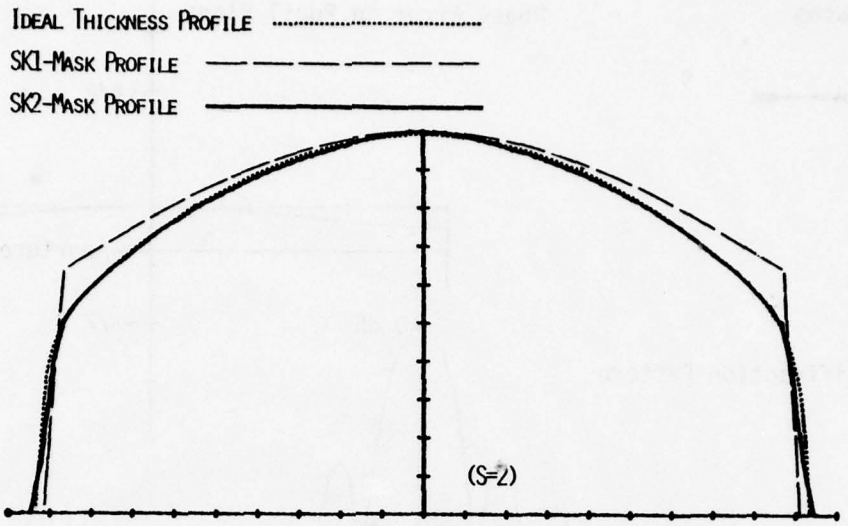

Figure 79. Sputtered Deposition Profiles for Waveguide Luneburg Lens Using Computer-Generated Masks.

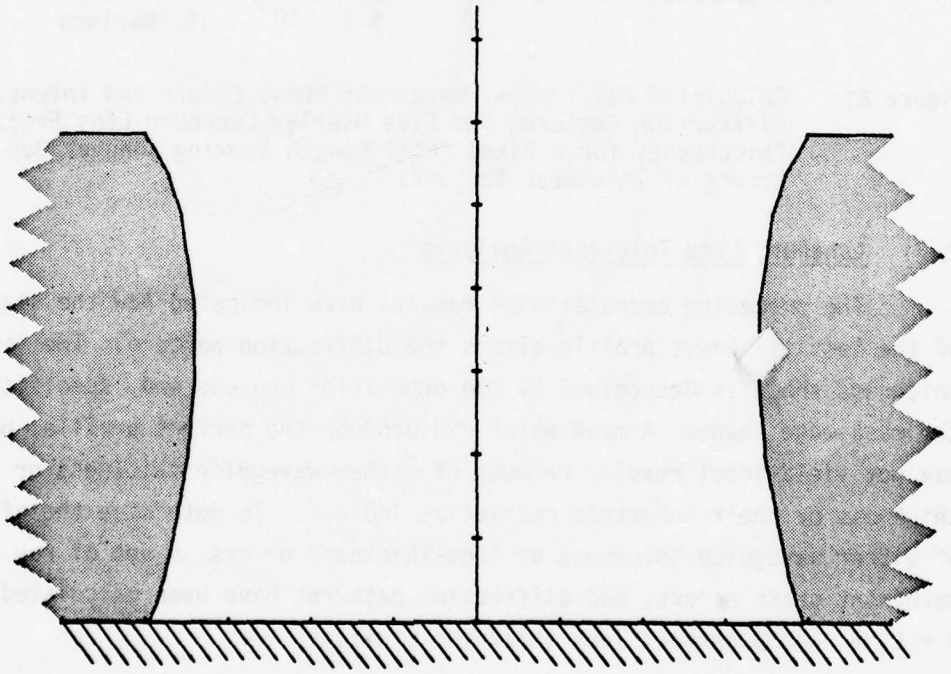

Figure 80. Computed Cross Section of SK-2 Mask Employed for Optical Waveguide Luneburg Lenses Which yield Diffraction-Limited Results (Mask Thickness 6mm and Diameter 8mm).

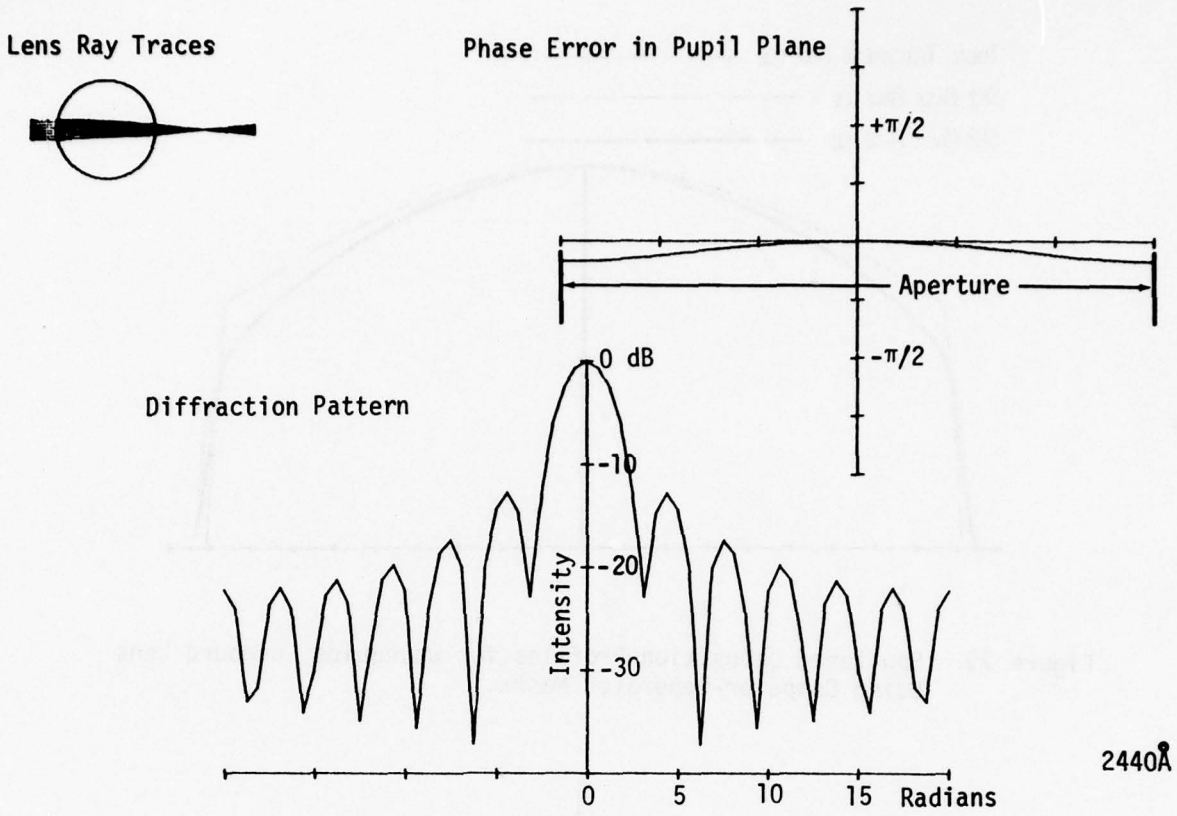

Figure 81 Calculated Ray Traces, Wavefront Phase Errors and Intensity Diffraction Patterns for Five Overlay Luneburg Lens Fractional Thicknesses for a Fixed Focal Length Showing Changes Due to Errors of Thickness for S=2.

7. Luneburg Lens Tolerance Analysis

The preceding computational results have indicated how the shape of the lens thickness profile alters the diffraction pattern. The lens-thickness shape is determined by the deposition process and, specifically, the mask-edge shape. A mask which can produce the perfect profile, however, may not yield ideal results because of either waveguide thickness or lens thickness or their incorrect refractive indices. To determine the effect of either waveguide-thickness or lens-thickness errors, a set of ray traces, wavefront phase errors, and diffraction patterns have been calculated for S = 2, 5, and 9 perfect lens thickness profiles.

The lens thickness has been increased and has been decreased to represent an incorrect deposition time. The resulting ray traces, wavefront phase errors, and diffraction patterns are depicted in the collage of Figures 81, 82, and 83. The nominal central lens thickness of 2240Å, 1281Å, and 1013Å yield focal lengths of 1.040 cm, 2.499 cm, and 4.01 cm for

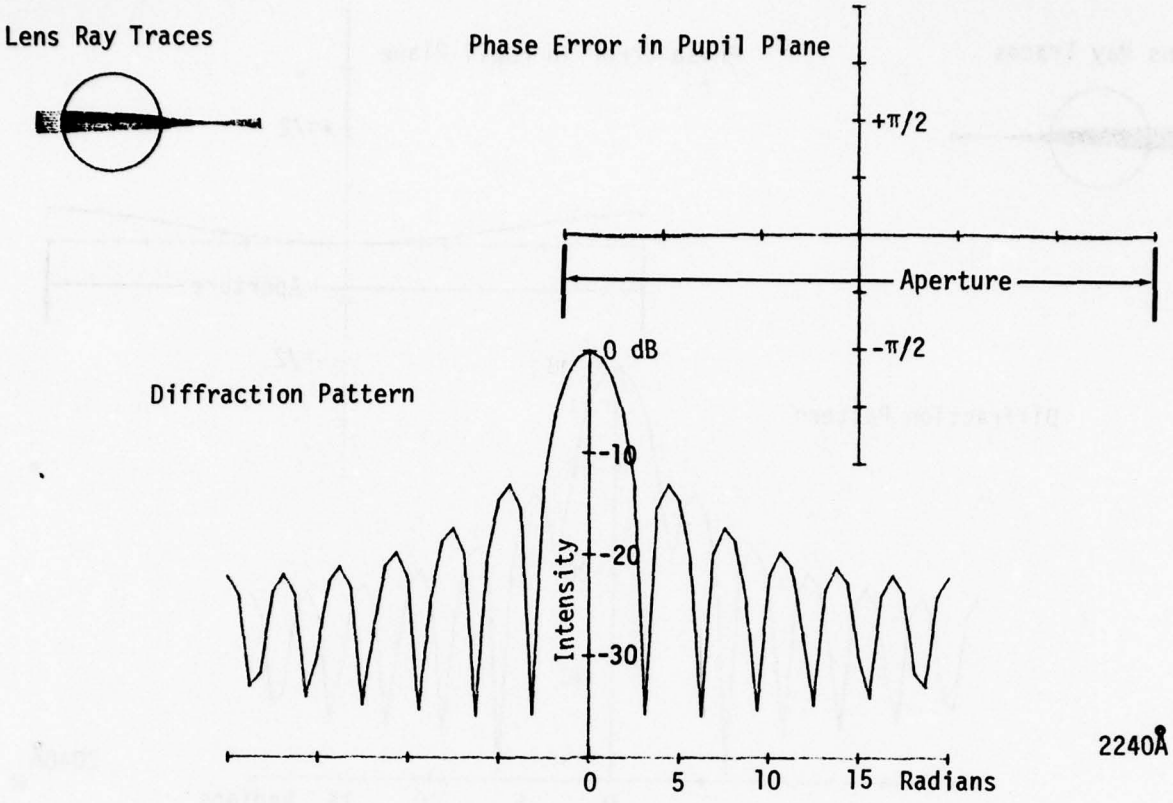

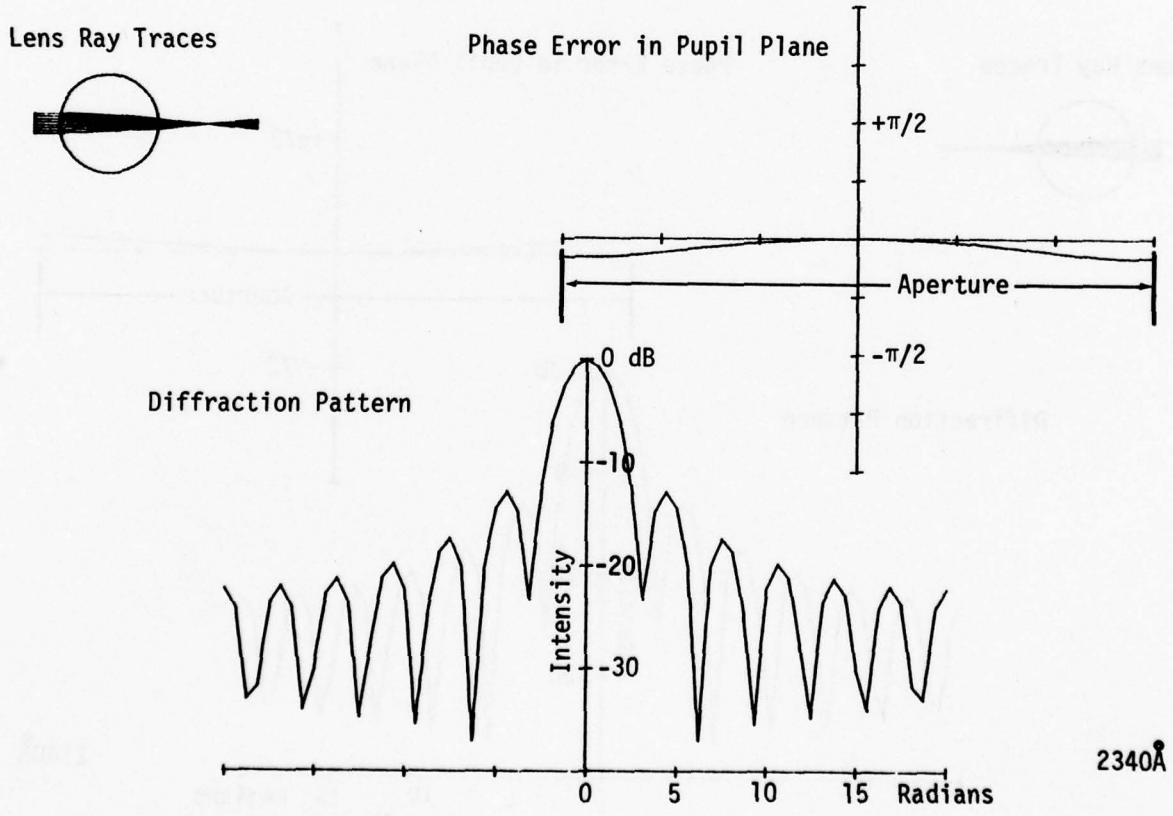

Figure 81. (Continued)

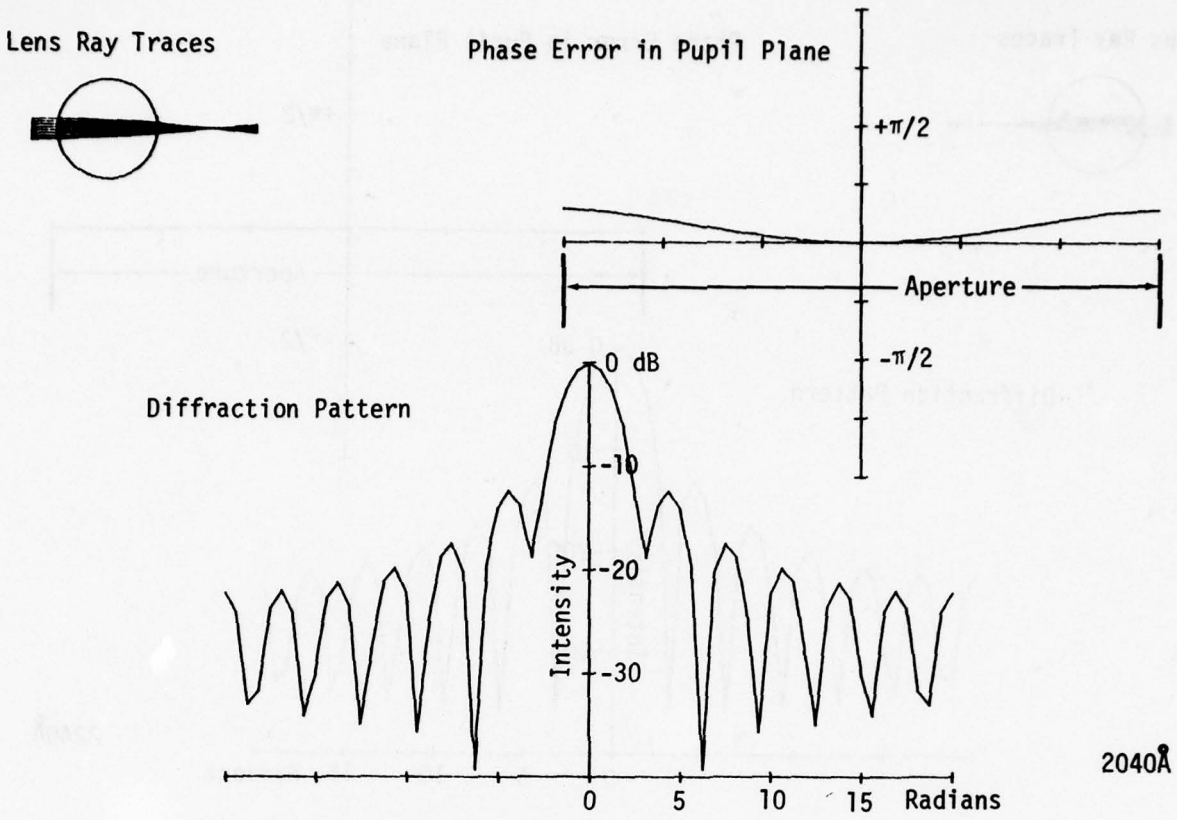

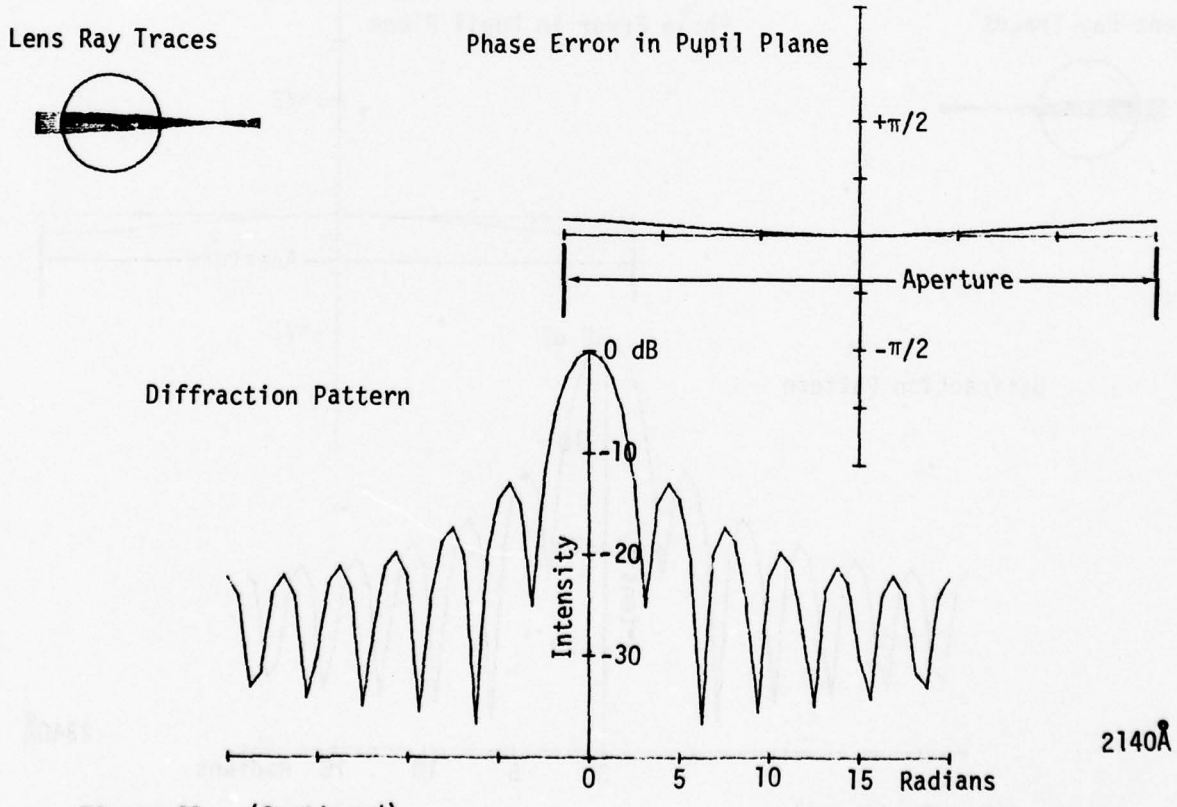

Figure 81. (Continued)

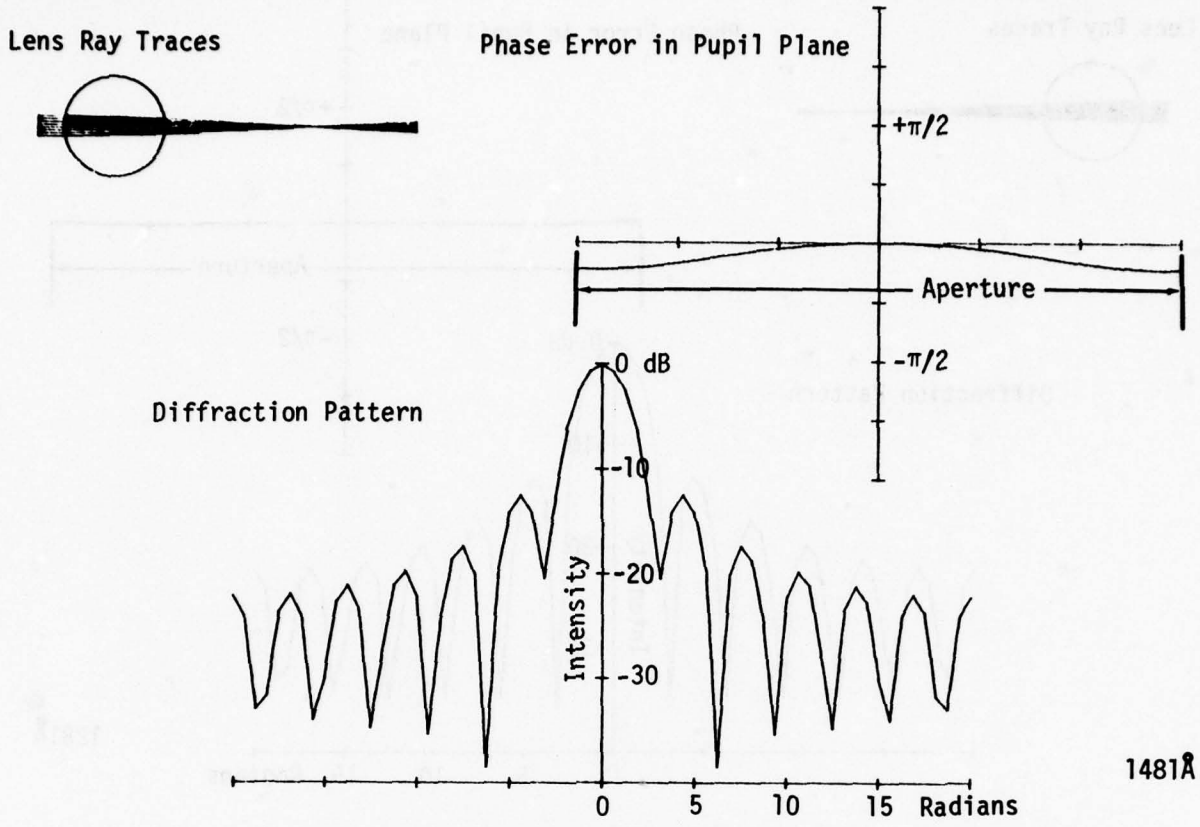

Figure 82. Calculated Ray Traces, Wavefront Phase Errors and Intensity Diffraction Patterns for Five Overlay Luneburg Lens Fractional Thicknesses for a Fixed Focal Length Showing Changes Due to Errors of Thickness for S=5.

the S = 2, 5, and 9 cases respectively. These thickness profiles have been increased and decreased ± 100 and ± 200Å at the center of the lens and in proportion to the lens thickness out to the edge. Inspection of the resulting diffraction patterns shows that an error of thickness introduces a slight spherical aberration which produces a slight increase of the adjacent side lobes and fill-in of the first null. It should be noted that the phase error introduced by a ± 200Å thickness error produces an approximate $\pi/8$ wavefront phase error for all of the S values computed and, thus, similar diffraction patterns. However, for a given error of thickness, the effect upon the focal length of S = 9 lenses is much more than that of S = 2 lens design. This effect upon the lens focal length is apparent in Figure 84.

Although the calculations have been performed by varying the lens thickness, comparable results are obtained by varying the waveguide thick-

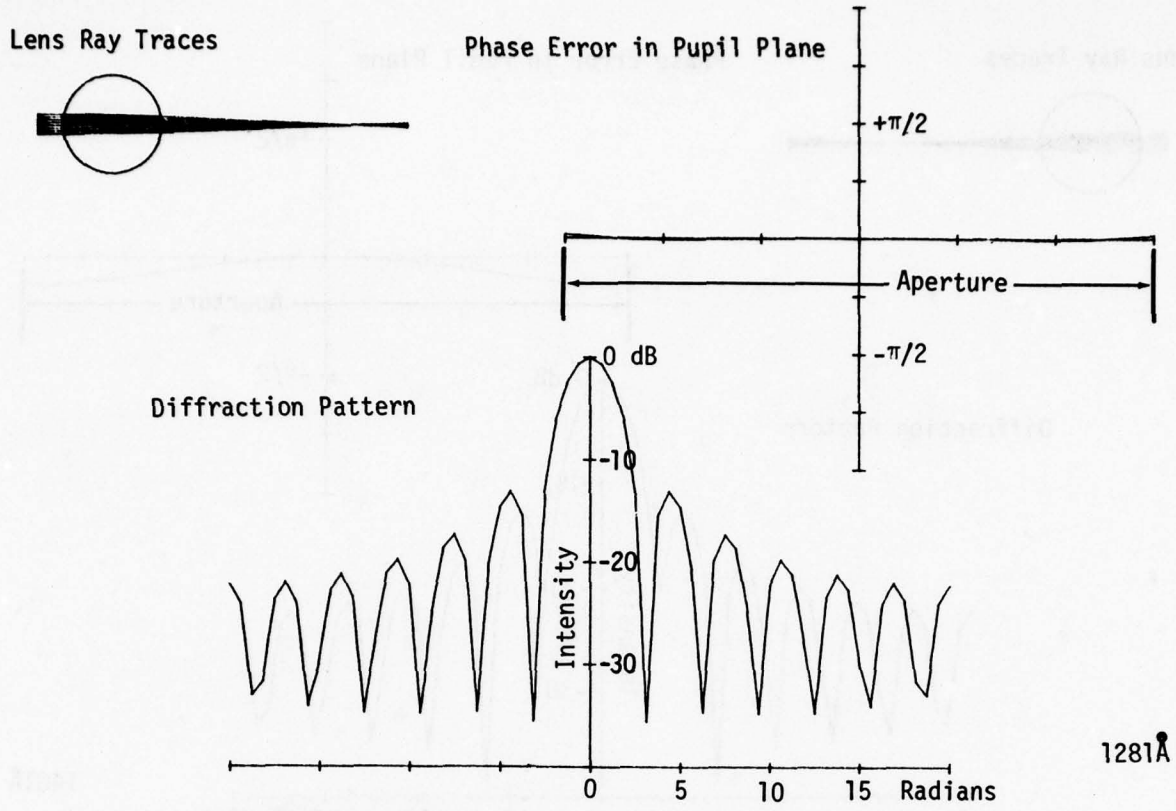

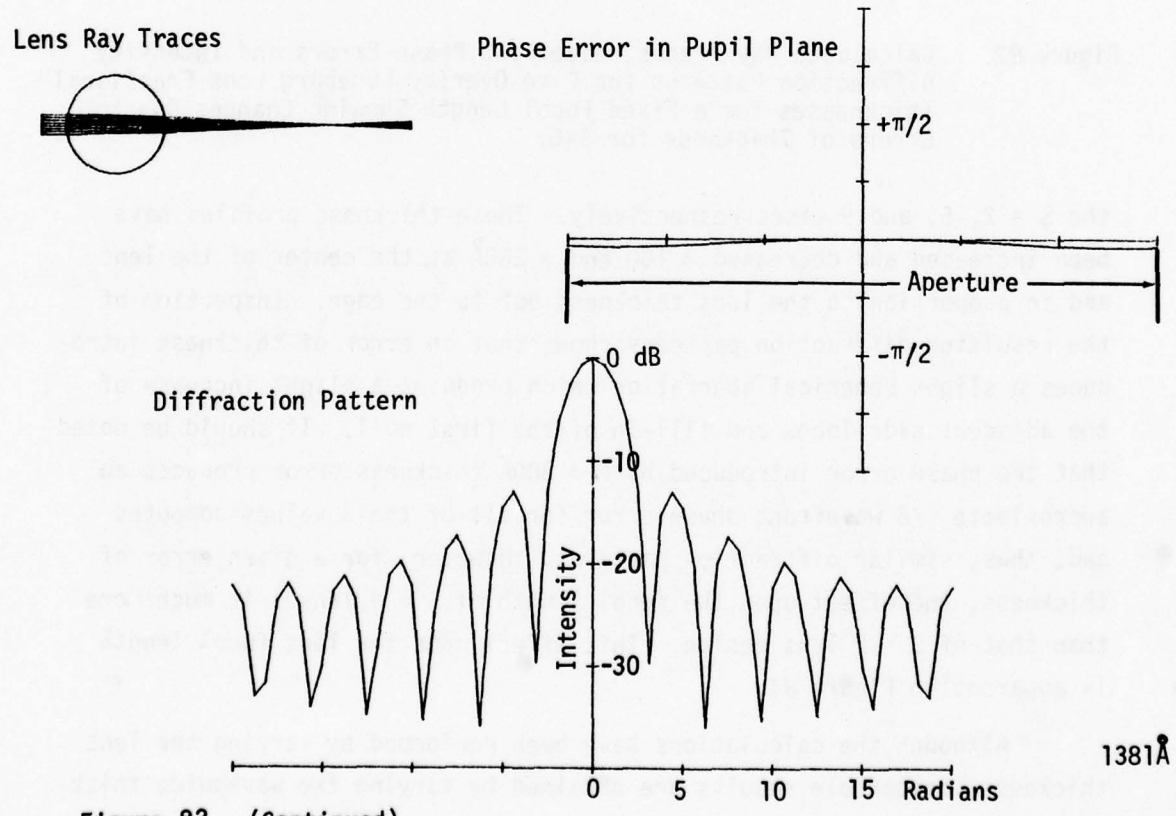

Figure 82. (Continued)

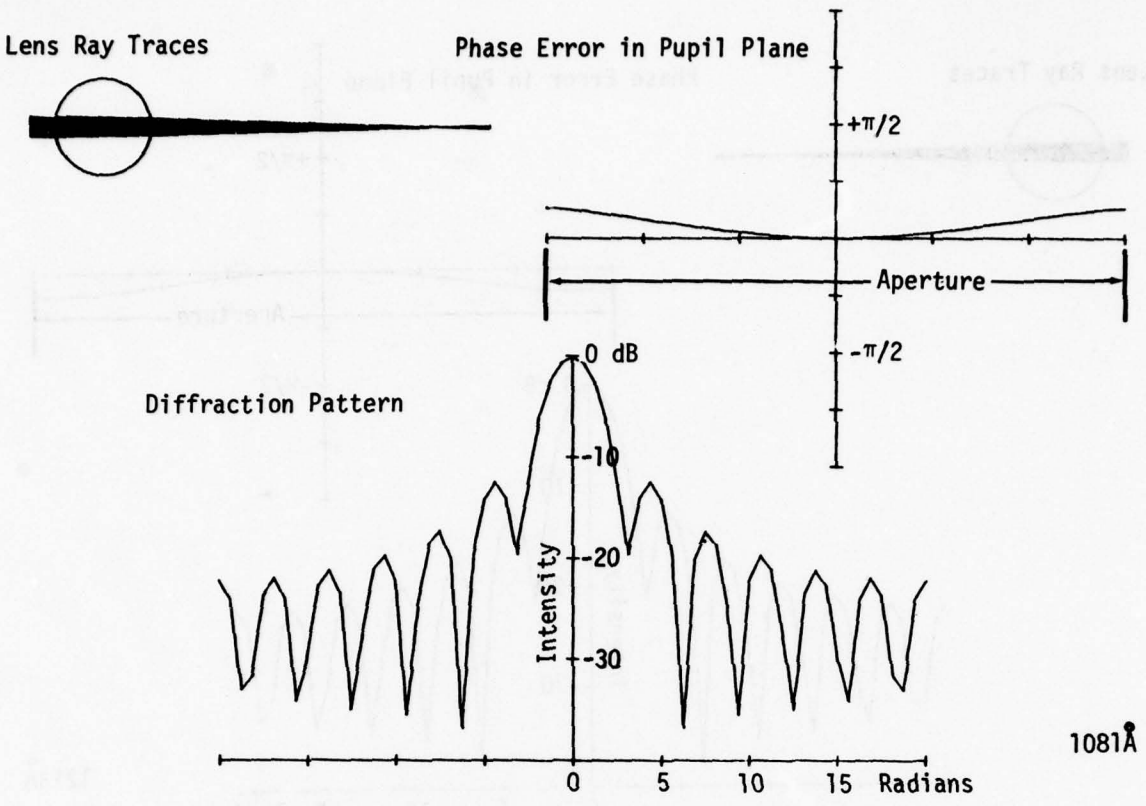

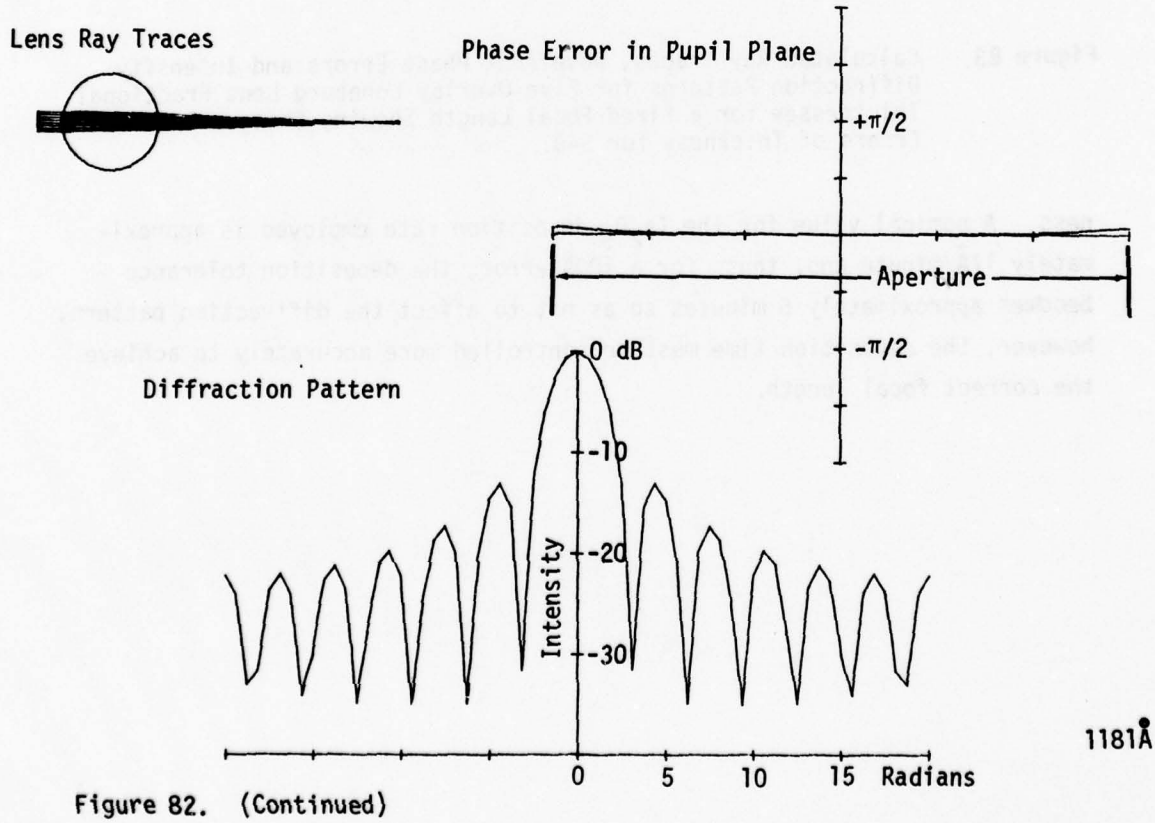

Figure 82. (Continued)

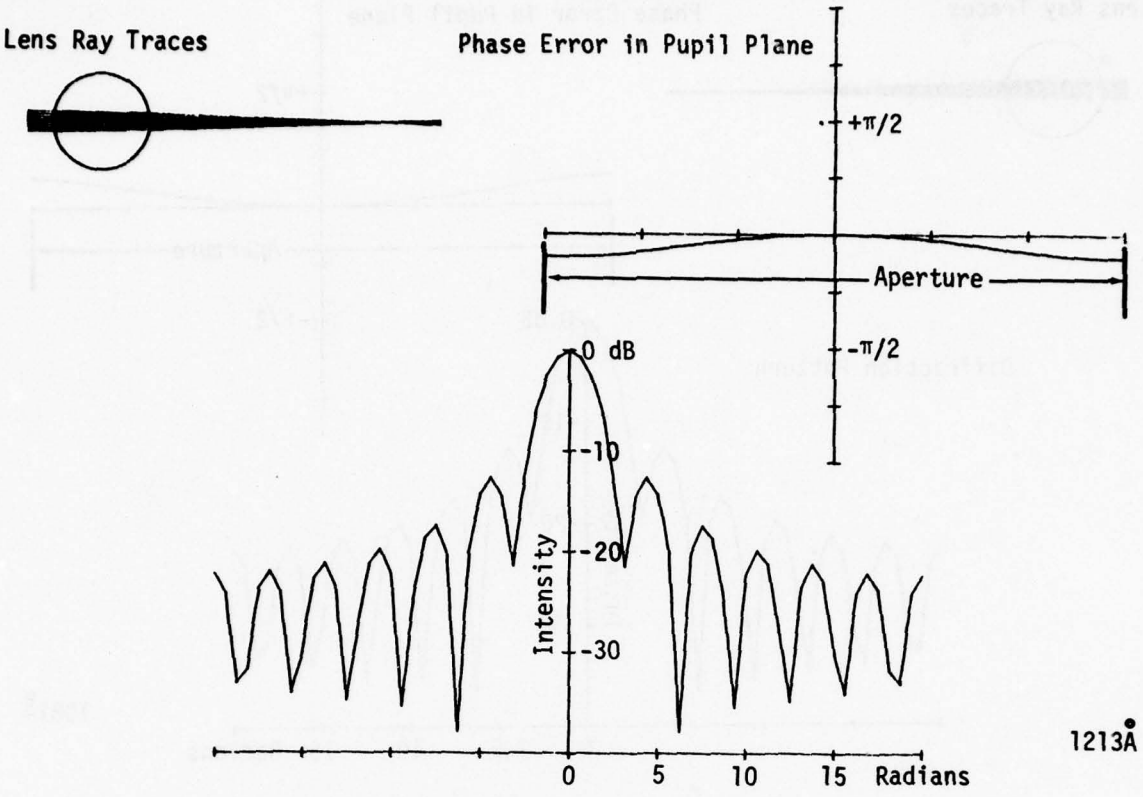

Figure 83. Calculated Ray Traces, Wavefront Phase Errors and Intensity Diffraction Patterns for Five Overlay Luneburg Lens Fractional Thicknesses for a Fixed Focal Length Showing Changes Due to Errors of Thickness for S=9.

ness. A nominal value for the Ta_2O_5 deposition rate employed is approximately 17Å/minute and, thus, for a 100Å error, the deposition tolerance becomes approximately 6 minutes so as not to affect the diffraction pattern, however, the deposition time must be controlled more accurately to achieve the correct focal length.

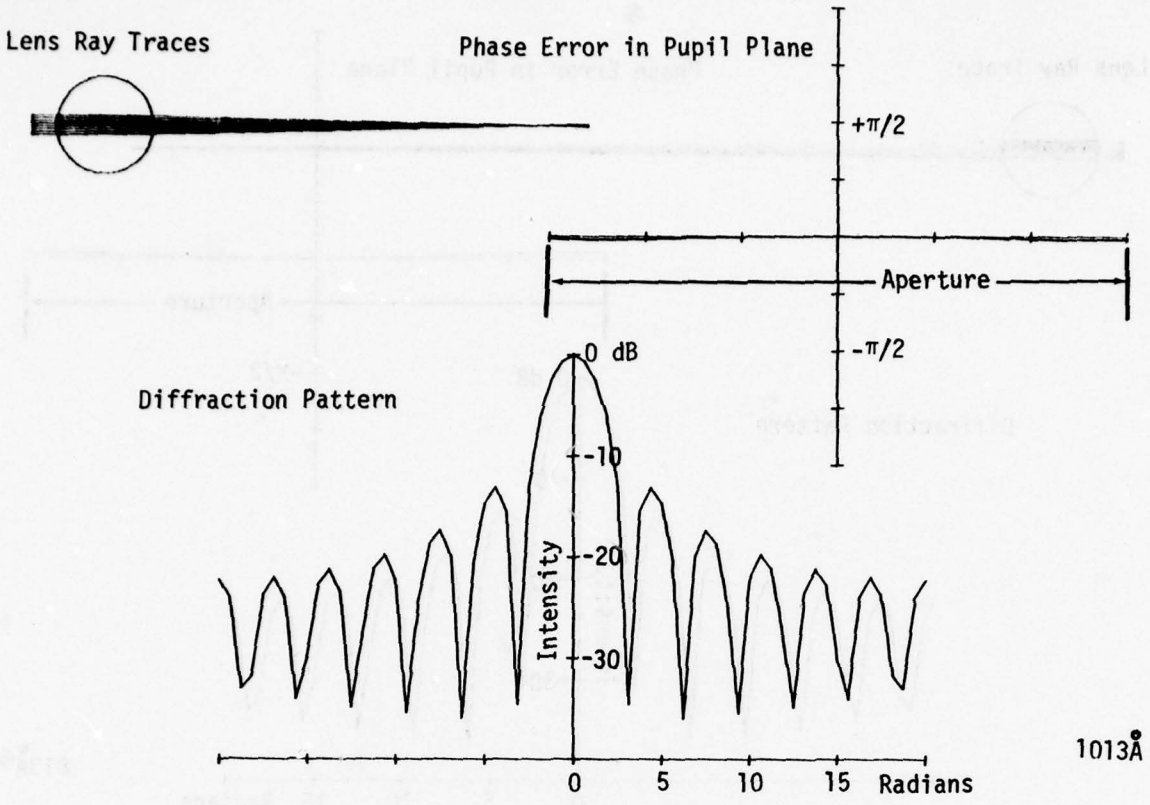

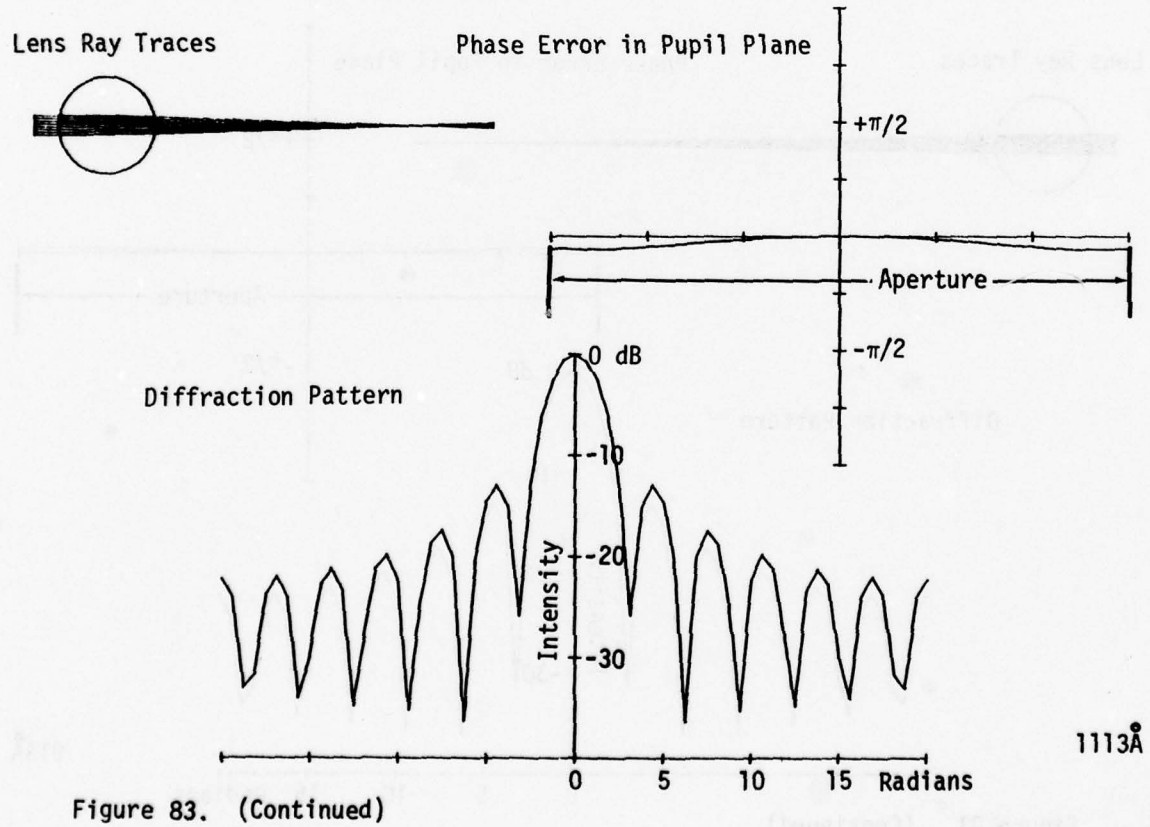

Figure 83. (Continued)

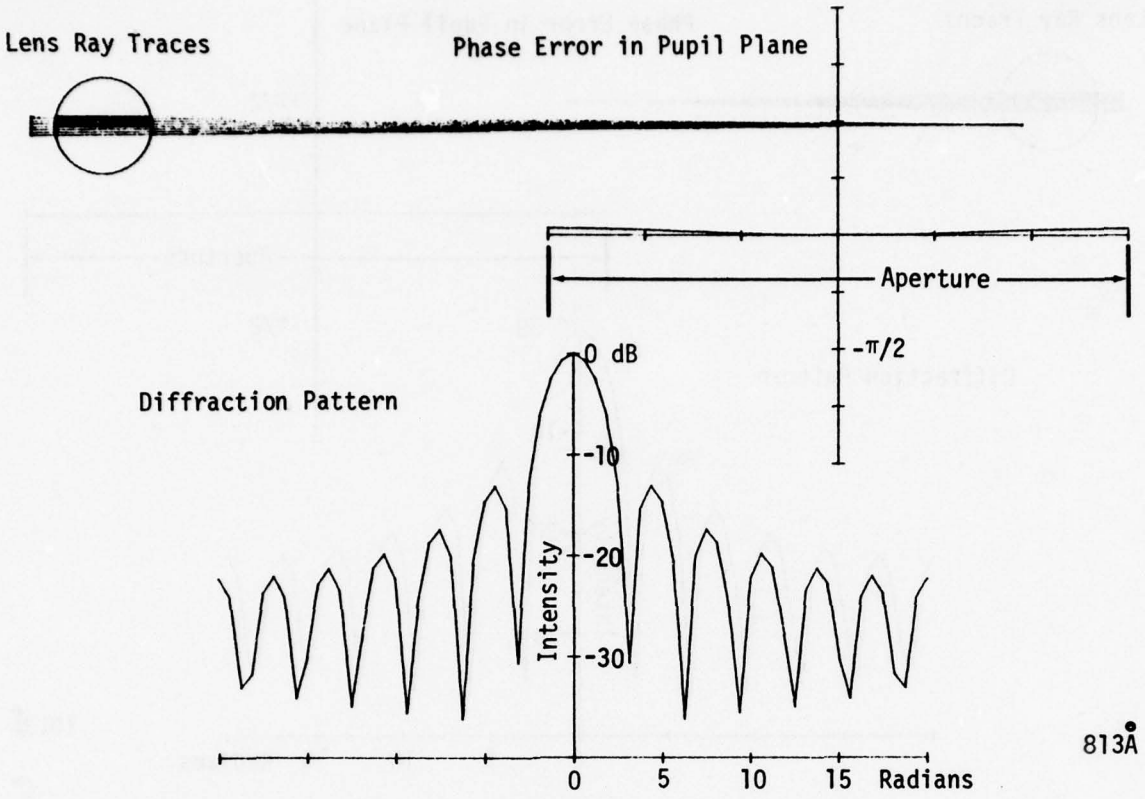

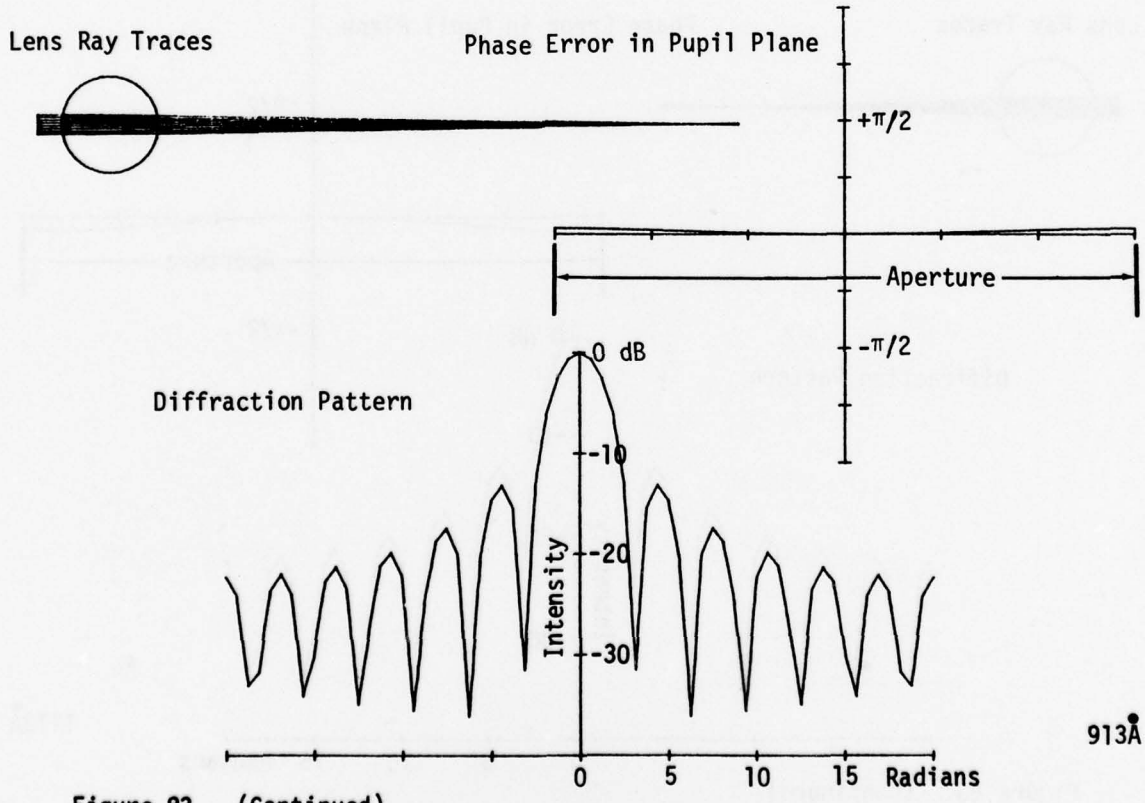

Figure 83. (Continued)

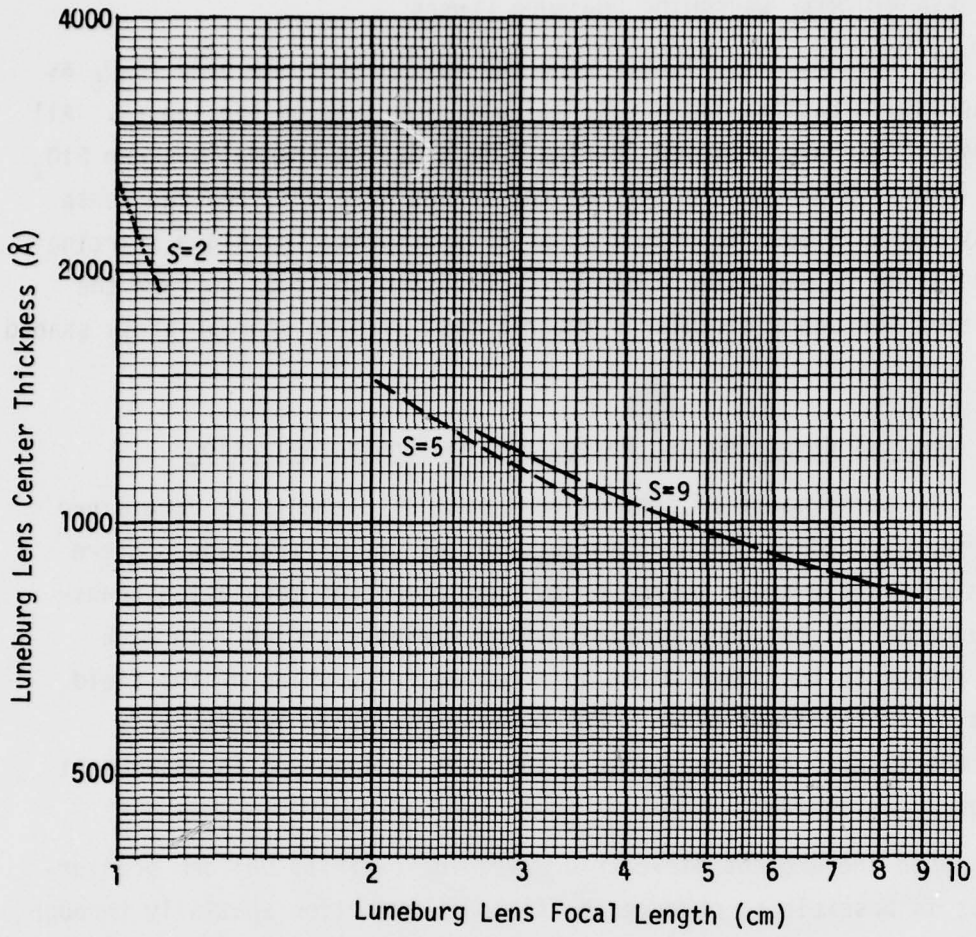

Figure 84. Calculated Waveguide Luneburg Lens Focal Length for S=2, S=5 and S=9 Perfect Profiles Where a Fractional Thickness Error Has Been Introduced to Simulate the Effect of an Error of the Deposition Time.

C. EXPERIMENTAL WAVEGUIDE LUNEBURG LENSES

All the waveguide lenses reported herein have employed Ta_2O_5 as the highest refractive index material used for forming the lenses. All the waveguides have employed Corning 7059 glass on thermally-grown SiO_2 on silicon as a substrate. All of the lenses have utilized the dense overlay and have been deposited by an RF-sputtering technique starting with metallic Ta and using a reactive process with Ar-O_2 to form the deposition through a circular symmetric mask with an appropriately shaped edge.

1. Optical Waveguide and Waveguide Lens Characterization

The performance of conventional optical elements is determined by various procedures such as measurement of the diffraction pattern for an accurately known source or by measurement of modulation transfer function for periodic sources having variable period. In each case, access to the image plane is required for probing of the field intensity in the image plane. For optical waveguide lenses, this technique is not practical because the lens is immersed in an ambient dielectric waveguide.

When the ambient dielectric waveguide exhibits uniform scattering, it is possible to observe the field distribution spatially through the scattering mechanism. However, in general the lens and waveguide which exhibit sufficient scattering for this type of observation also represents an unsatisfactory lens for use in an optical Fourier transform.

The technique employed to measure the diffraction pattern of waveguide lenses has utilized a reimaging procedure with several types of coupling. A schematic of the reimaging apparatus is depicted in Figure 85. Prism couplers are employed to launch beams within the thin-film waveguide which traverses the lens under investigation. Four types of coupling have been employed to extract the field which is relayed and reimaged with magnification where it is possible to probe the field distribution in this latter plane. A narrow-slit aperture with an optical fiber has been employed to probe the field distribution. The slit-fiber probe is scanned in any of the three major axes providing a signal to drive a recorder while the optical signal is detected, amplified and

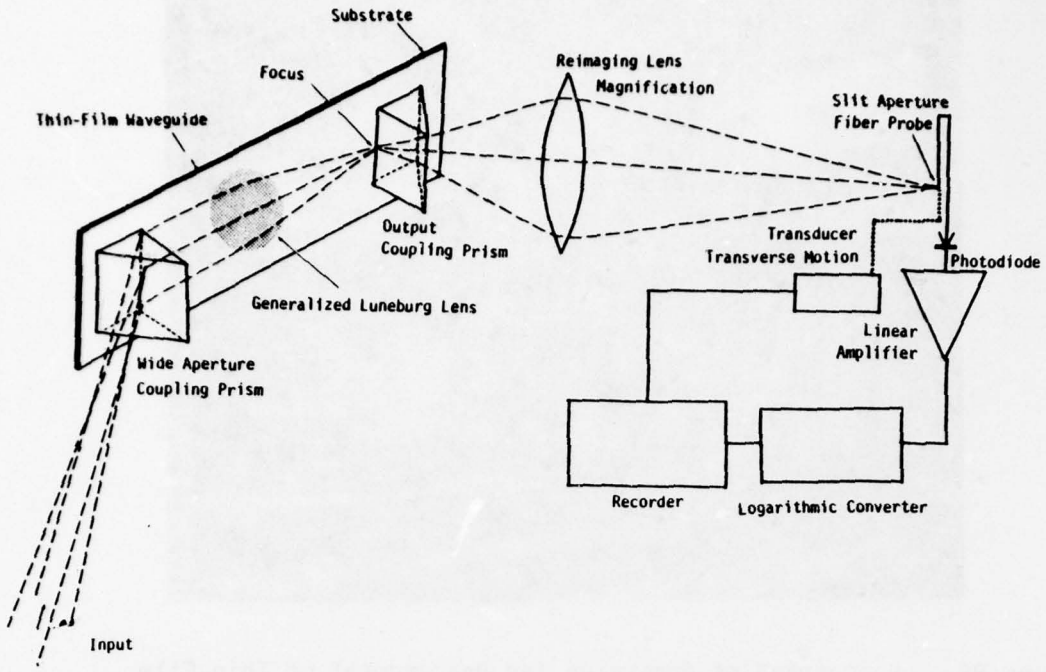

Figure 85. Schematic of Reimaging Technique to Characterize Thin-Film Waveguide Lens Performance.

compressed to give a logarithmic scale for the recorder. All experimental diffraction patterns reproduced herein have been measured in this manner. The physical apparatus showing the input beam alignment and coupling to the waveguide-lens substrate mounting fixture, followed by the relay lens and the slit-optical fiber probe, mechanical scanning fixture, are depicted in Figure 86 with the electronics and recorder. The relay lens is a Tropel diffraction-limited Fourier transform system having F/3 aperture with a focal length of 221mm.

Various methods of coupling from the waveguide lens substrate to the relay lens have been employed. Most of the experiments have utilized conventional prism couplers with special attention given to obtain a sharp defect-free edge. Another type of coupling which eliminates the prism utilizes a cleaved exit edge for the waveguide. A good cleaved edge close to the lens focus permits the use of a high-power microscope objective as the relay lens. A close-up view of such a configuration using an input coupling prism on a waveguide on a thermally-oxidized silicon substrate with a Ta_2O_5 overlay Luneburg lens is depicted in Figure 87. A scanning slit fiber optical probe is again used to measure the image distribution.

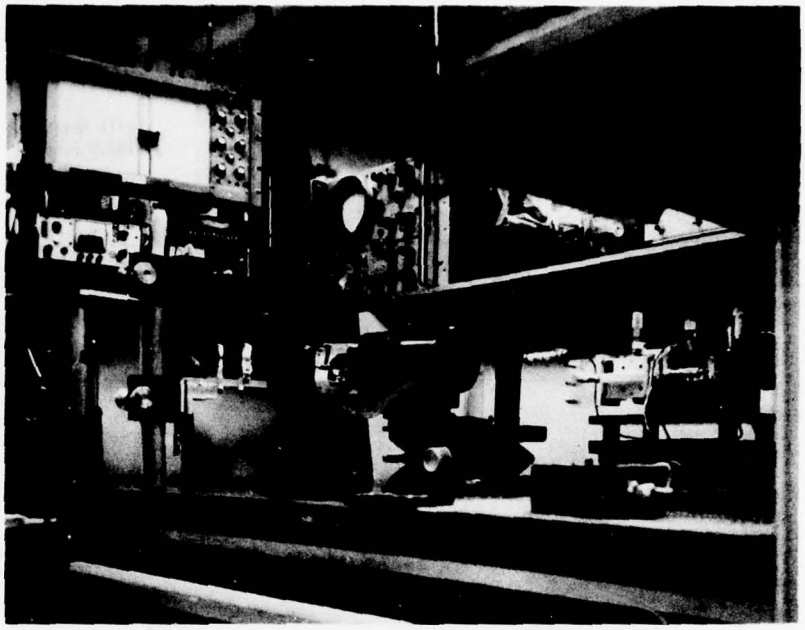

Figure 86. Photograph of Apparatus for Measurement of Thin-Film Waveguide Lens Performance Using Tropel F/3 Fourier Transform Lens Assembly (FL = 221mm) and Scanning Slit-Fiber Optical Probe.

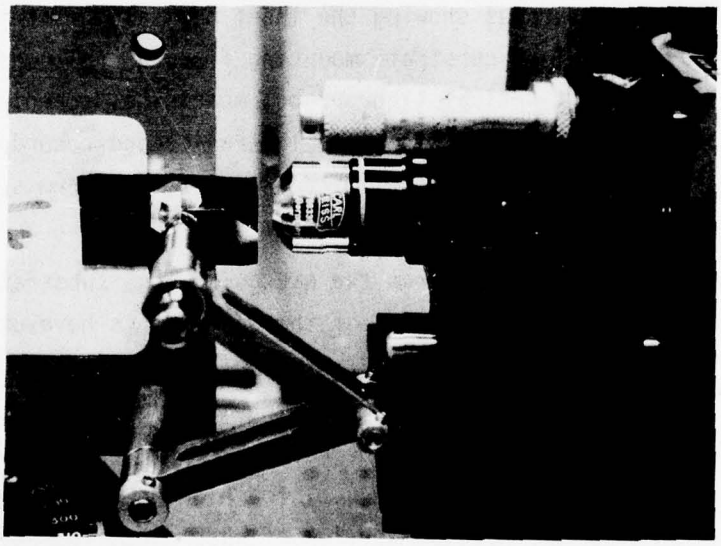

Figure 87. Close-up Photograph of Apparatus to Measure the Intensity Distribution From Waveguide and Lenses by Cleavage Through the Waveguide and Reimaging Using a Zeiss 40X Microscope Objective.

The use of a plane parallel optical plate introduced into a convergent or divergent beam introduces spherical aberration; and thus, the use of a prism coupler to extract radiation from waveguide containing lenses introduces an error into the measurement due to this added spherical aberration. Several methods were investigated to minimize or eliminate this effect. The most practical technique proved to be positioning of the coupler so that the coupling section straddles the focus equally and thus, in this position, cancels the spherical aberration. Two other techniques investigated to reduce the spherical aberration due to the coupler are illustrated in Figures 88 and 89. Thin spinel wafers edge mounted are shown in Figure 88. Effective coupling is obtained for 0.5mm thick wafers. An aplanatic prism with a spherical hypotenuse with its radial center located on the coupling edge can also eliminate spherical aberration. Such an aplanatic prism is depicted in Figure89. This concept is identical to an immersion microscope objective. However, it must be accurately positioned so that the spherical surface matches the emerging optical wavefront. Accurately positioning of the aplanatic prism is difficult to achieve routinely. Elimination of the prism using a cleaved edge of the waveguide also requires that the cleavage be accurately positioned at the focus of the lens to eliminate a spherical aberration introduced at the waveguide exit refraction.

Lens diffraction patterns are the convolution of the "true" lens diffraction pattern and the observational instrumentation. For the case at hand, the relay lens has been employed to provide magnification for a mechanical scanning of a slit across the reimaging diffraction pattern. As the lens performance is improved, the reimaging lens must exhibit comparable performance or superior performance. When couplers are employed, their distortions are also convolved.

Most of the measurements reported herein employed a Tropel F/3 lens designed for the Fourier transform as the relay lens. Further, some of the measurements have been performed using a Zeiss 40X microscope objective with a numerical aperture of 0.67.

The effect of this lens upon the measurements will be considered herein. For most of the measurements of F/4 Luneburg lens, the Tropel reimaging lens becomes a limiting factor, while the Zeiss lens is not. However, it requires a cleaved exit face accurately positioned at the focus.

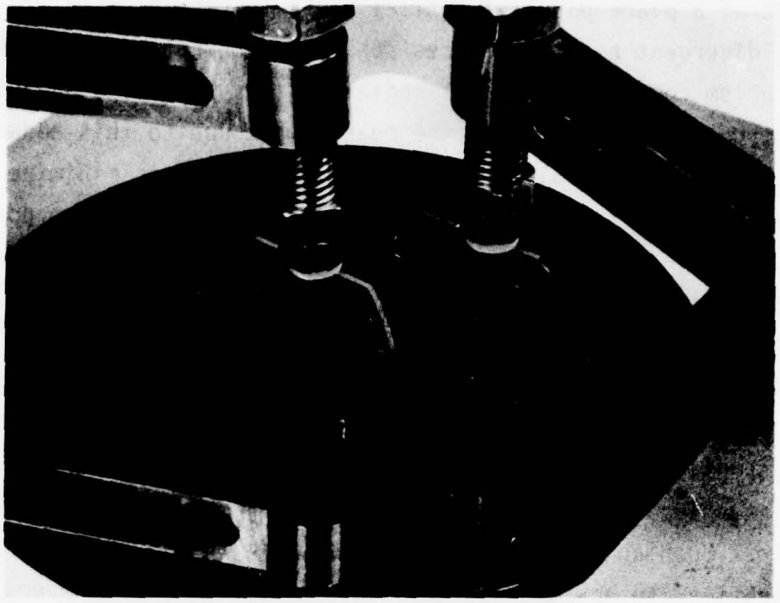

Figure 88. Thin Spinel Wafers Edge Coupled to Corning 7059 Waveguide on Thermally-Oxidized Silicon Substrate Used to Minimize Effective Prism Coupler Thickness.

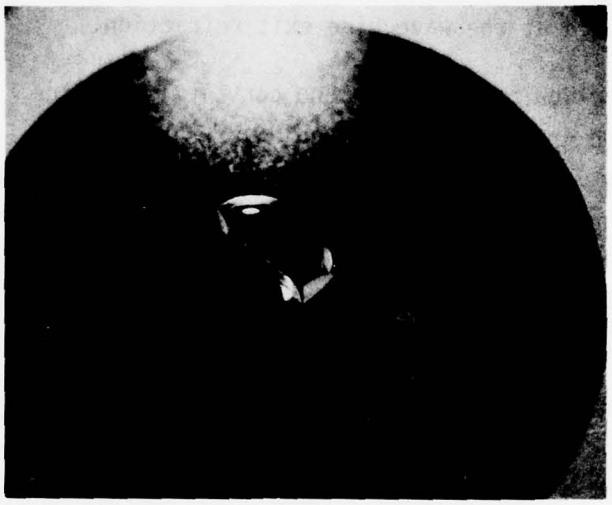

Figure 89. An Aplanatic Prism Coupler Fabricated from SF-6 Glass.

The Tropel lens is designed for a magnification of 2. Thus, for this Tropel lens, the effective f-number becomes

$$F_{eff} = F\left(1 + \frac{1}{M}\right) = 4.5 \tag{55}$$

The effective f-number is the actual f-number of the Tropel lens in the reimaging set up. Because of the index of refraction of the optical waveguide, which is 1.5, the F/4 Luneburg lens appears as an F/2.7 lens in air and is severely truncated by the F/4.5 Tropel lens reimaging system.

The effect of truncation on the beamwidth measurement for a Gaussian optical system will be discussed as follows. For a Gaussian optical-input beam with e^{-2} width of "a", the optical input amplitude function can be described by e^{-4x^2/a^2}. The optical amplitude distribution at the back focal plane of a planar lens is obtainable by taking a Fourier transformation of the input amplitude function. The optical intensity distribution at back focal plane is therefore,

$$I = |A|^2 = \left| \int_{-\infty}^{\infty} e^{\frac{-4x^2}{a^2}} \; e^{-j \frac{(kx_1)}{F} x} \; dx \right|^2$$

$$= \left| \left[\int_{-\infty}^{\infty} \frac{a}{2} \; e^{-\left(\frac{2x}{a} + j \frac{ak}{4F} x_1\right)^2} \; d\left(\frac{2x}{a} + j \frac{ak}{4F} x_1\right) \right] e^{-\left(\frac{ak}{4F}\right)^2 x_1^2} \right|^2$$

$$\sim e^{-2\left(\frac{ak}{4F}\right)^2 x_1^2} \tag{56}$$

where k is the optical propagation constant $\frac{2\pi}{\lambda}$, x_1 is the transverse coordinate in the back focal plane, and F is the focal length of a planar lens. The integral within the bracket is a constant related to the total optical power of the input optical beam. It is convenient to define the f-number of this focusing system as

$$f = \underline{\Delta} \; F/a \tag{57}$$

The beamwidth (i.e., spot width) at the back focal plane can be obtained from Equation (56). Converting Equation (56) to the dB notations, we have

$$\begin{aligned} \frac{I}{I_o} &= -8.69 \left(\frac{k}{4F}\right)^2 x_1^2 \quad \text{dB} \\ &= -21.44 \left(\frac{x_1}{\lambda F}\right)^2 \quad \text{dB} \end{aligned} \tag{58}$$

The e^{-2} beamwidth is twice the value of x_1 which makes $I/I_o = 8.79$ dB, while the half intensity spot width is twice the value of x_1 which makes $I/I_o = -3$ dB. Thus

$$\begin{cases} e^{-2} \text{ spot width} : 1.27\ \lambda F/a \\ 3 \text{ dB spot width} : 0.75\ \lambda F/a \end{cases} \tag{59}$$

In practical optical imaging system, all the lenses have limited aperture which truncates the Gaussian optical profile and causes the beam width to increase. Mathematically, the focal spot for truncated Gaussian beam has an intensity distribution of

$$I_t = \left| A * \text{sinc} \left(\frac{kDx_1'}{2F'}\right)\right|^2 \tag{60}$$

where the sinc x function denotes sinx/x, F' is the focal length of the reimaging lens, D is the aperture of the reimaging lens, x_1' is the coordinate in the reimaged plane, and $f' \triangleq F'/D$ is the effective f-number of the reimaging lens. To distinguish f and f', we shall call f the "optical beam f-number" and f' the "truncation f-number". The symbol "*" denotes the convolution operation. Equation (60) can be readily evaluated with a computer program for the simulation of actual coherent optical imaging system.

For systems involving multiple truncations, a chain of convolution operations may be performed. Because both the Gaussian function A and the sinc function resemble a delta-function when plotted at enlarged scales, it is obvious that (1) with little truncation $f' \ll f$, $I_t \approx |A|^2$ and (2) with extreme truncation, $f \ll f'$, $I_t \approx |\text{sinc} \frac{kx_1'}{2f'}|^2$. That is, the effect of truncation can be ignored when $f' \gg f$. For $f' \ll f$, the truncated beam

resembles an uniformly illuminated aperture of D focusing at the truncation f-number f′. The 3 dB beamwidth for the extremely truncated Gaussian beam is therefore the 3 dB width of sinc $\frac{kx_1}{2f'}$ and is 0.885 $\lambda f'$. Figure 90 shows the theoretical beamwidth size evaluation capability of the two testing lens systems employed. The straight line at a slope is the theoretical -3 dB focal beamwidth for untruncated Gaussian Beam. The -3 dB beamwidth is used because it is less confusing for non-Gaussian beams as well as truncated Gaussian beams. The horizontal lines are the limiting beamwidth for the two reimaging lenses used when they severely truncate a Gaussian beam. The curved lines are the theoretical expectation for the 3 dB focal beamwidth measured with the two systems. For simplicity, the optical waveguide lens is assumed not truncating the Gaussian beam at all, because the truncation ratio for the waveguide Luneburg lens involved in this report is $f/f_L \simeq 4$ which falls close to the "little truncation" category. It is noted that the convolution effect on the measured results, i.e., the curved lines, can be approximated by the commonly used square law given by Bracewell

$$\alpha_{a*\ell}^2 = \sigma_a^2 + \sigma_\ell^2 \qquad (61)$$

where σ's are the -3 dB beamwidth for the convolving systems. Eq. (61) is much easier to use than Eq. (56) and may also be extended to include other system aberrations, and truncation induced beam broadening effects.

For the beamwidth measurement system using the Tropel reimaging lens, the -3 dB beamwidth for a uniformly illuminated line aperture is

$$\sigma_\ell = 0.885\ (0.6328)\ 4.5 = 2.52 \text{ microns} \qquad (62)$$

assuming the Tropel lens is diffraction limited.

The -3 dB beamwidth for an F/4.1 waveguide Luneburg lens in a waveguide having an effective refractive index of 1.5, is

$$\sigma_g = 0.75\ (0.6328/1.5)\ \ 4.1 = 1.3 \text{ microns} \qquad (63)$$

Applying Snell's law for refraction into air, the equivalent beamwidth becomes

$$\sigma_a = 0.75\ (0.6328)\ \ 4.1/1.5 = 1.3 \text{ microns} \qquad (64)$$

Using Eq. (61) the measured -3 db beamwidth for a diffraction limited waveguide Luneburg lens is expected to be

$$\sigma_{a*\ell} = (1.3)^2 + (2.52)^2 = (2.84)^2$$

where our measured results are between 3.0 microns and 3.3 microns. We have tried to verify the value of σ_ℓ by placing a 1 micron diameter pin-hole in front of the Tropel lens and have experimentally measured σ_ℓ = 2.9 micron, which is 15% greater than the diffraction limited value. Using the measured σ_ℓ instead, the expected beamwidth becomes

$$\sigma^2_{a*\ell} = (1.3)^2 + (2.9)^2 = (3.18)^2 \tag{65}$$

which is in good agreement with the actual experimental result. It is concluded that the F/4.1 Luneburg lens performance is near the diffraction limit and, thus, the true beamwidth is approximately 1.3 microns in waveguide. From this discussion, it is clear that the reimaging lens is limiting the true measurement of the waveguide lens performance.

To improve our confidence of the waveguide Luneburg lens performance, the second measurement system using a Zeiss 40 X F/0.67 microscope objective lens as the reimaging lens and a (100) cleavage near the focal point instead of prism coupler, was constructed. Such system will provide a system limited beamwidth, σ_ℓ, of

$$\sigma_\ell = 0.885\ (0.6328)\ 0.67 = 0.38 \text{ micron} \tag{66}$$

An F/5.5 lens made of the same sputtering mask with different sputtering time was evaluated with this system. The theoretical beamwidth is expected to be

$$\sigma_g = \sigma_a = 0.75\ (0.6328)\ \ 5.5/1.5 = 1.74 \text{ micron} \tag{67}$$

The expected measurement result should be

$$\sigma^2_{a*\ell} = (1.74)^2 + (0.38)^2 = (1.78)^2 \tag{68}$$

whereas our measured result is 1.65 micron.

This measured result is 7% less than the calculated result probably due to the fact that the illumination beam could be slightly larger than the 2mm assumed which would lead to a reduced f-number. Thus, it is

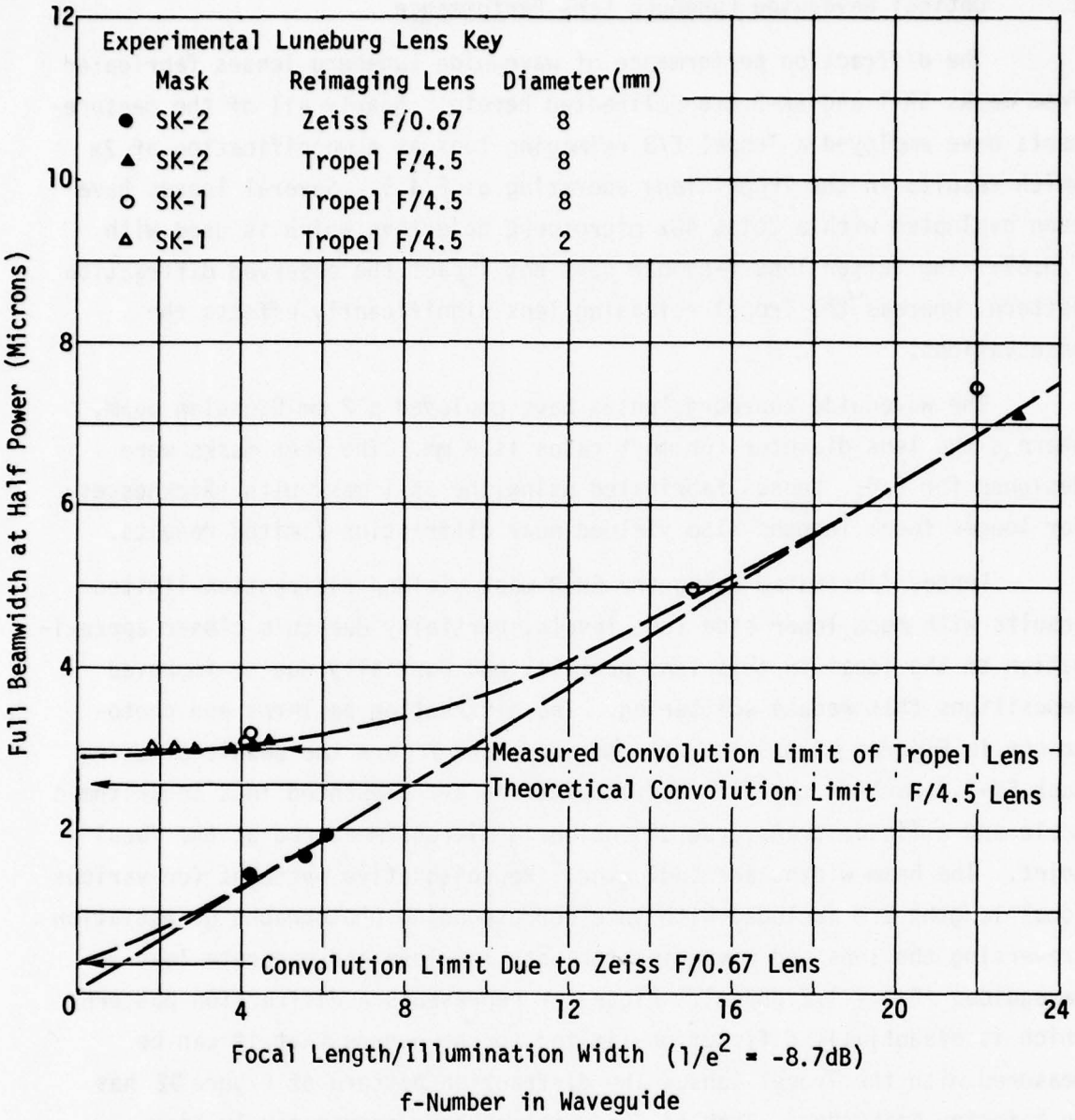

Figure 90. Measured Diffraction Pattern Beamwidth (3dB) as a Function of the f-Number in Waveguide, Limited by Convolution With the Reimaging Lens Showing Experimental Results.

verified that our Luneburg lenses are actually diffraction limited. Other measurements with waveguide Luneburg lenses of larger f-number have no problem with either of the measurement systems as shown in Figure 90.

2. Optical Waveguide Luneburg Lens Performance

The diffraction performance of waveguide Luneburg lenses fabricated from masks SK-1 and SK-2 are delineated herein. Nearly all of the measurements have employed a Tropel F/3 reimaging lens at a magnification of 2x which results in the Tropel lens operating as F/4.5. Several lenses have been evaluated with a Zeiss 40x microscope objective which is used with F/0.67. The latter lens f-number does not impact the observed diffraction pattern, whereas the Tropel reimaging lens significantly effects the observations.

The waveguide Luneburg lenses have employed a 2 mm Gaussian beam, whereas the lens diameter for most cases is 8 mm. The lens masks were designed for F/4. Lenses fabricated using the SK-1 mask with thicknesses for longer focal lengths also yielded near diffraction-limited results.

Lenses fabricated using the SK-2 mask yielded diffraction-limited results with much lower side lobe levels, partially due to a closer approximation to the ideal in this lens profile, and partially due to improved depositions that reduce scattering. The diffraction patterns and photographs in Figures 91,92 ,93 , 94 ,95 ,96 , and 97 are the result of using mask SK-1. Each of the diffraction patterns are presented in a logarithmic scale and a linear transverse dimension in microns measured at the focal point. The beam widths are indicated. Representative patterns for various focal lengths are included with some corresponding photographs of radiation traversing the lens and waveguide for both low-loss and moderate loss waveguides (0.2 = 1.2 dB/cm). Figure 91 represents a diffraction pattern which is essentially diffraction-limited to the degree that it can be measured with the Tropel lens. The diffraction pattern of Figure 92 has an inferior beamwidth. Both of the patterns have comparatively high shoulder lobes which indicate that the lens thickness profile is not fully corrected. The operation of the lens measured in Figure 92 is shown in Figure 93 used as a single lens and used as a beam expander in reverse. The scattered radiation and the throughput at the edge of the wafer are apparent.

The diffraction patterns for Figures 94 and 95 apply to F/22 and F/23 lenses with focal lengths of 44 and 46 mm. The losses of these

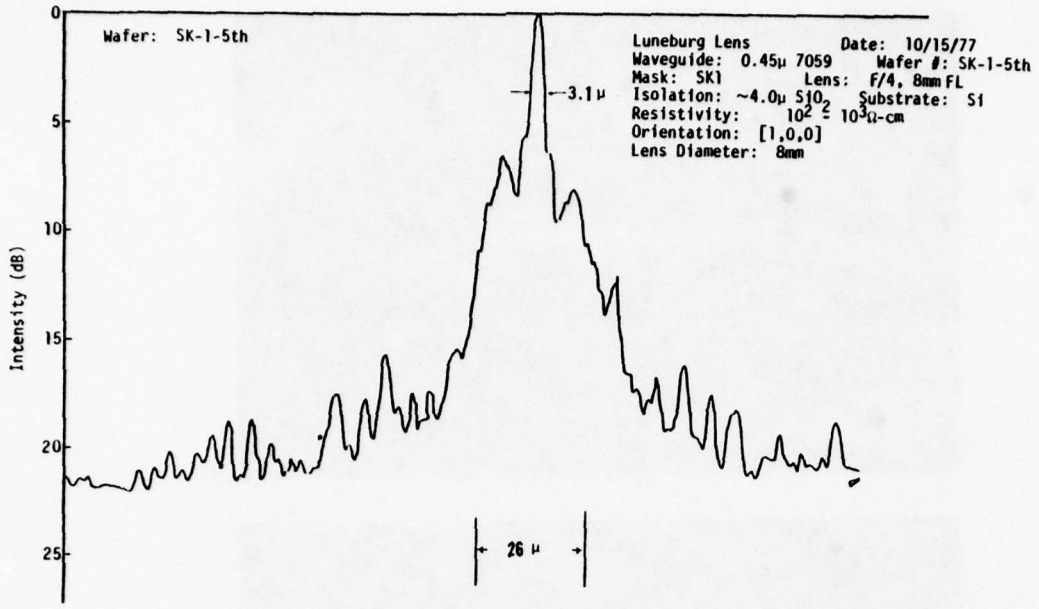

Figure 91. Measured Diffraction Pattern of Lens Using Mask SK-1 and Tropel F/3 Reimaging Lens Where Lens: F/4, FL = 8mm. Wafer: SK-1-5th

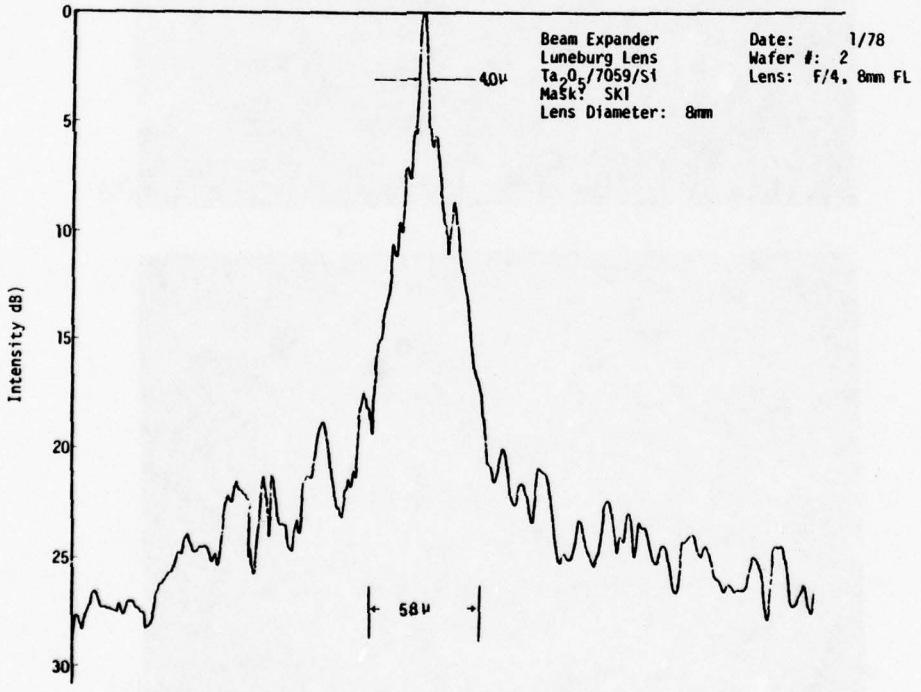

Figure 92. Measured Diffraction Pattern of Lens Using Mask SK-1 and Tropel F/3 Reimaging Lens Where Lens: F/4, FL = 8 mm on Wafer #2 Used in the Beam Expander Illustrated in Figure 93.

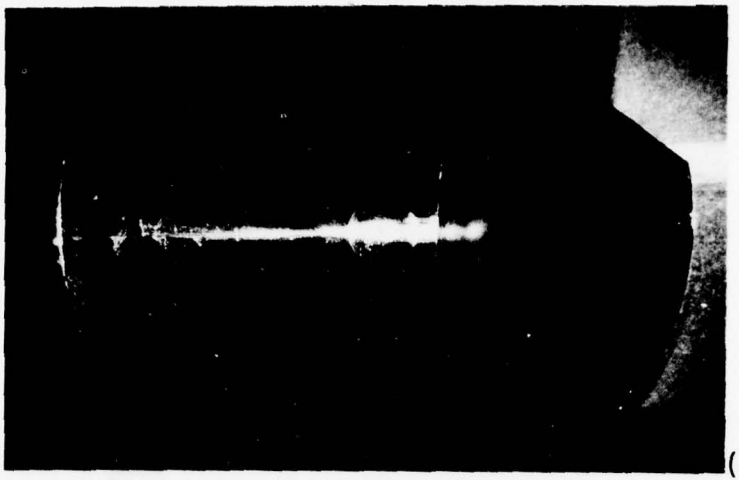

(a)

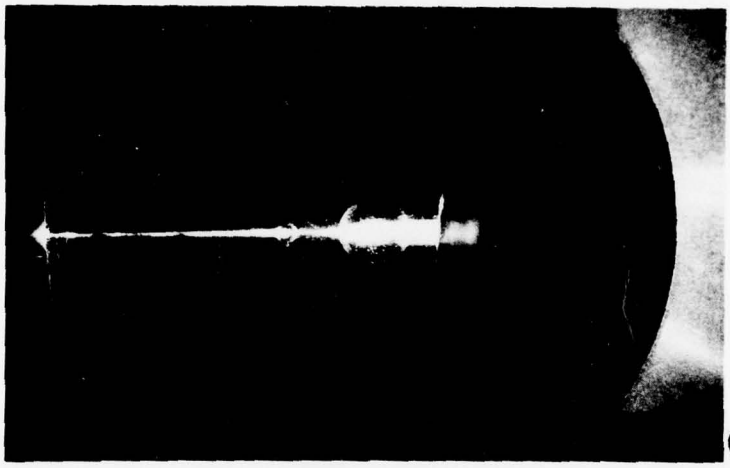

(b)

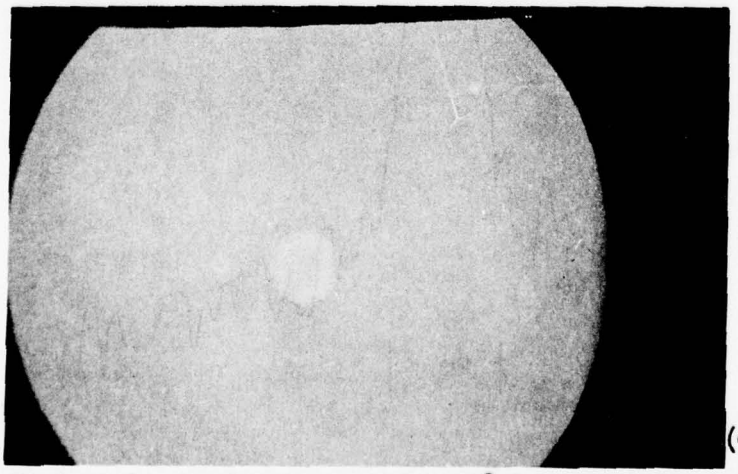

(c)

Figure 93 Typical Scattering Traces of 6328Å Radiation Traversing Ta_2O_5 Luneburg Lenses on Corning 7059 Waveguide on Thermally-Oxidized Silicon Substrate. Single Luneburg Lens (a), Beam Expander (b), and Lens Layout as Newton Rings (c).

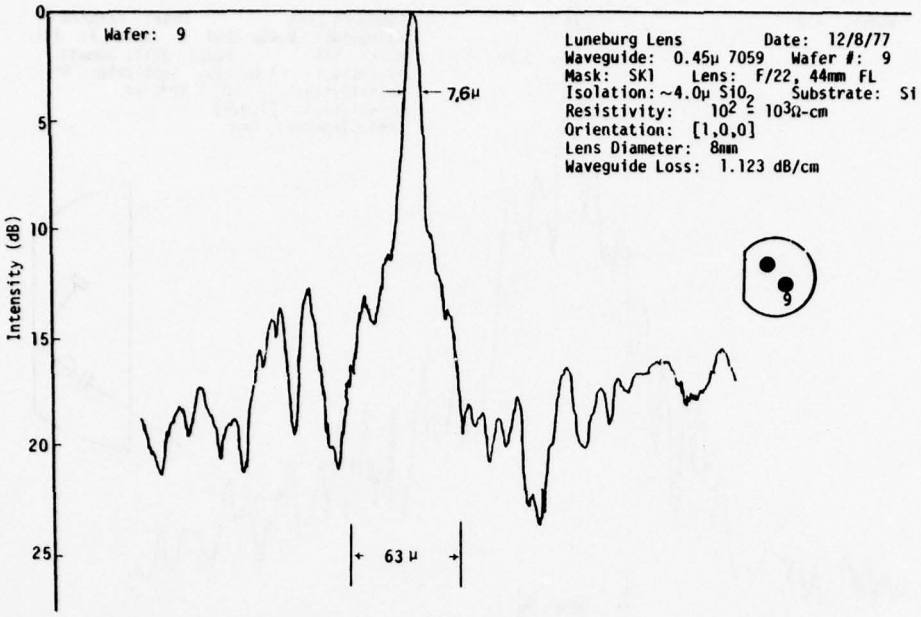

Figure 94 Measured Diffraction Pattern of Luneburg Lens Fabricated Using Mask SK-1 Using Tropel F/3 Reimaging Lens Where Lens: F/22 and FL = 44mm With 1.2dB/cm Waveguide Loss.

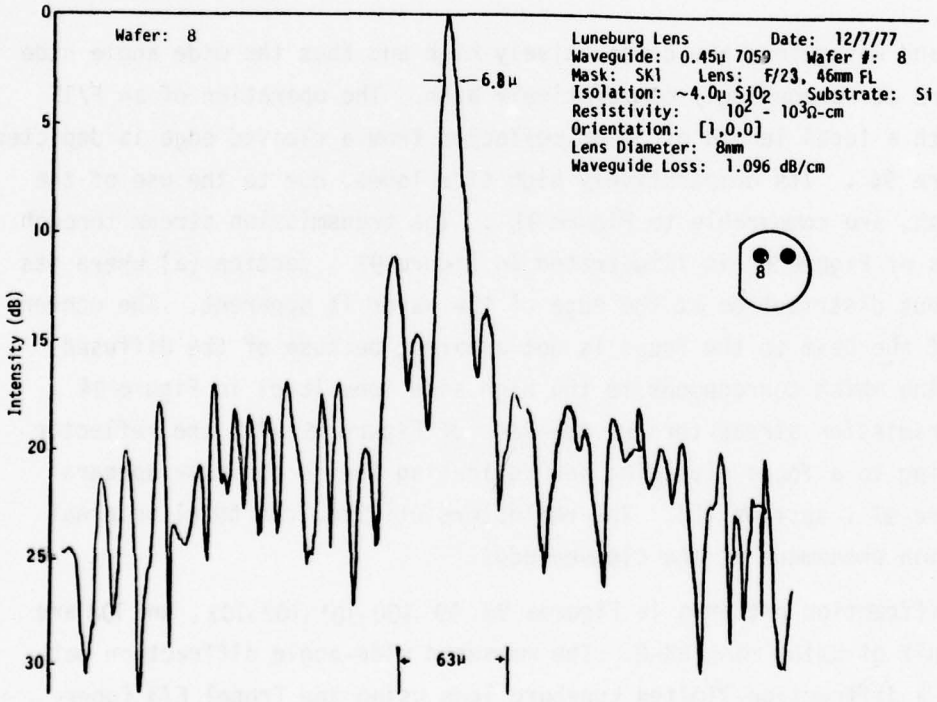

Figure 95 Measured Diffraction Pattern of Luneburg Lens Fabricated Using Mask SK-1 Using Tropel F/3 Reimaging Lens Where Lens: F/23 and FL = 46mm With 1.1dB/cm Waveguide Loss.

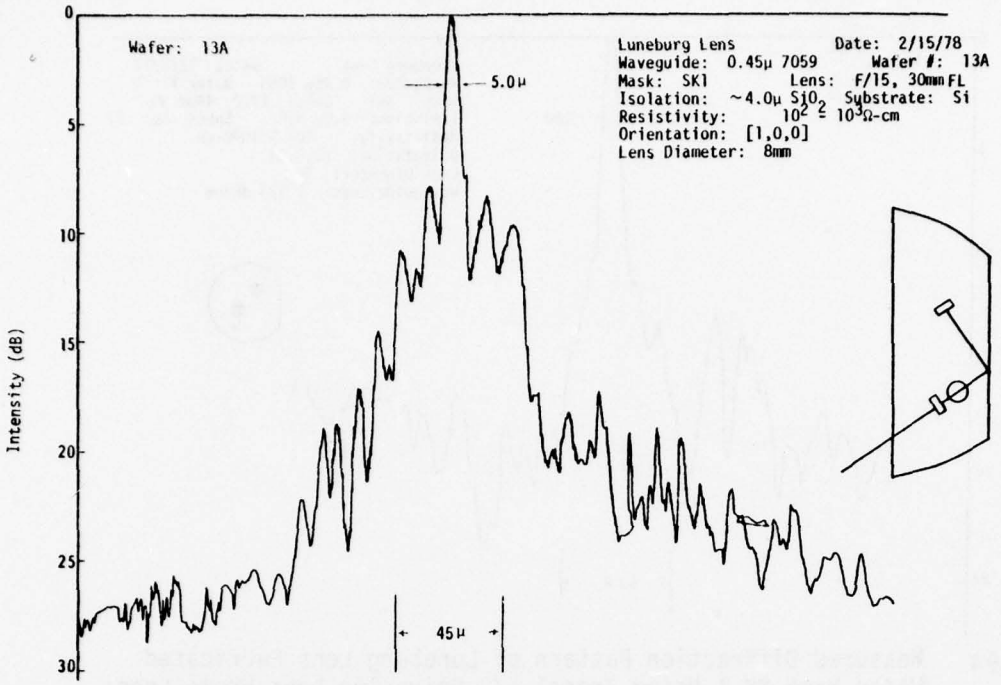

Figure 96 Measured Diffraction Pattern of Lens Using Mask SK-1 with a Cleaved Reflector Using Tropel F/3 Reimaging Lens Where Lens: F/15, FL = 30 mm.

lenses and waveguides are comparatively high and thus the wide angle side lobes are correspondingly comparatively high. The operation of an F/15 lens with a focal length of 30 mm reflected from a cleaved edge is depicted in Figure 96 . Its comparatively high side lobes, due to the use of the SK-1 mask, are comparable to Figure 91 . The transmission streak through the lens of Figure 95 is illustrated in Figure 97 , section (a) where its throughput distribution at the edge of the wafer is apparent. The convergence of the beam to the focus is not apparent because of the diffused scattering which corresponds to the high side lobe level in Figure 94 . The transmission streak through the lens of Figure 96 with the reflector converging to a focus diverging and reflecting the second time appears in Figure 97 , section (b). The reflectors utilized the total internal reflection phenomena at the cleaved edge.

Diffraction patterns in Figures 98, 99 ,100 ,101 ,102 ,103 , and 104 are the result of using mask SK-2. The measured wide-angle diffraction pattern of a diffraction-limited Luneburg lens using the Tropel F/3 (operating at F/4.5) reimaging lens is depicted in Figure 98 where the lens: F/4 and FL = 8mm. Its near-inside lobes are below 17dB and the decay

(a)

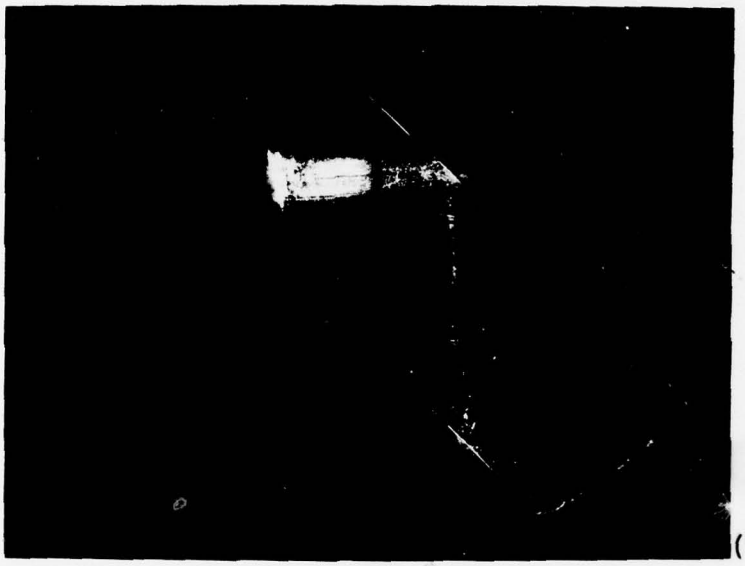

(b)

Figure 97 Propagation Streak Through a Luneburg F/25 Lens Fabricated With an SK-1 Mask With Throughput Distribution at the Edge of the Wafer in the Divergent Region (a) and Propagation Streak Through an F/15 Lens Fabricated With an SK-1 Mask With Two Total Internal Reflections From Cleaved Edges (b).

to 30dB within approximately 200 beamwidths. Beyond that range, the recorded signal is due to the instrumentation electronic noise. Another lens fabricated using mask SK-2 with F/5.5 which yields diffraction-limited results as measured with the Zeiss 40X objective is depicted in Figure 99 . Note that its beamwidth is 1.65 microns and that its near-

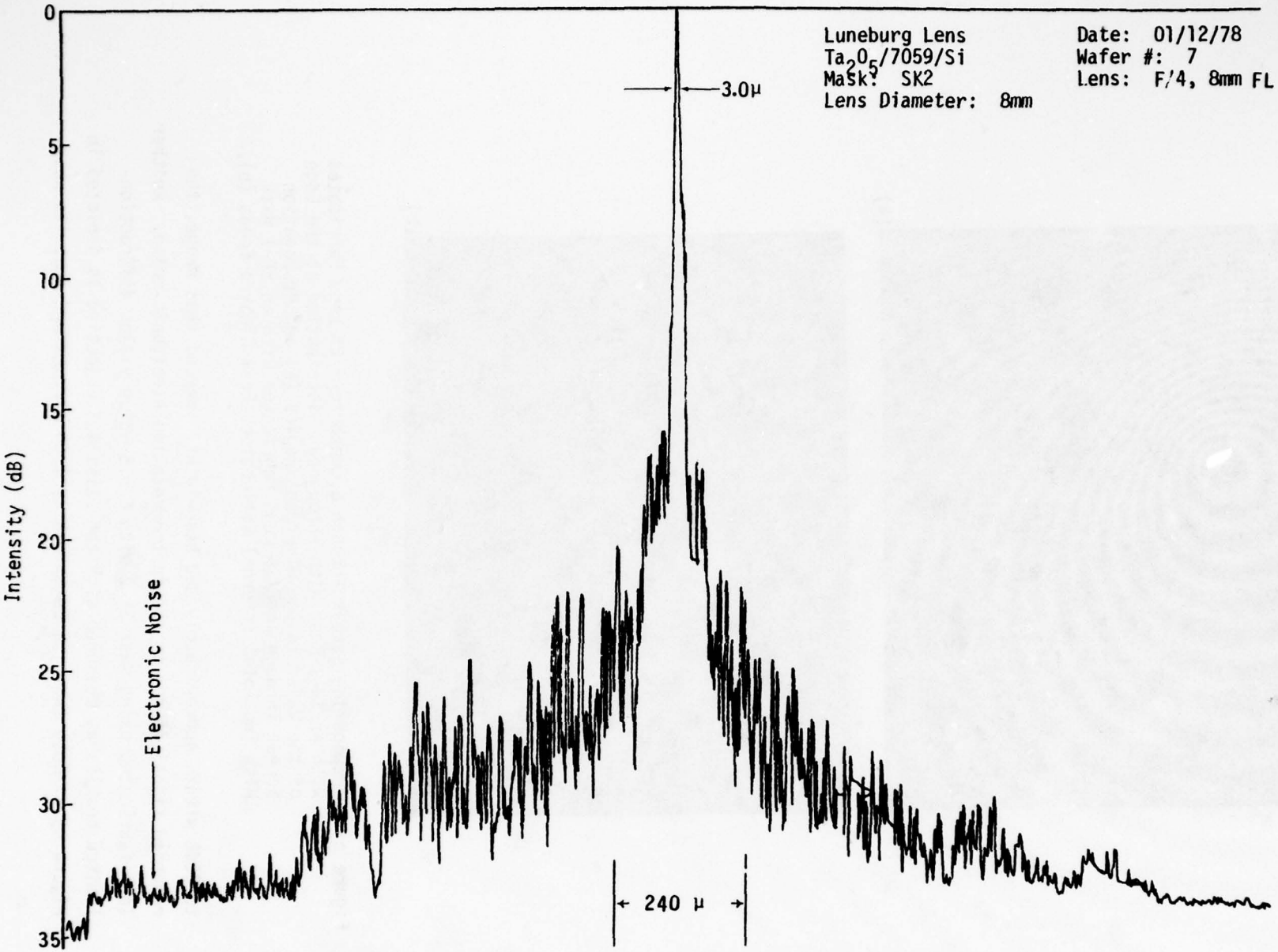

Figure 98. Wide Angle Measured Diffraction Pattern of Waveguide Luneburg Lens Using Mask SK-2 Using Tropel F/3 Reimaging Lens Where Lens: F/4 and FL = 8 mm.

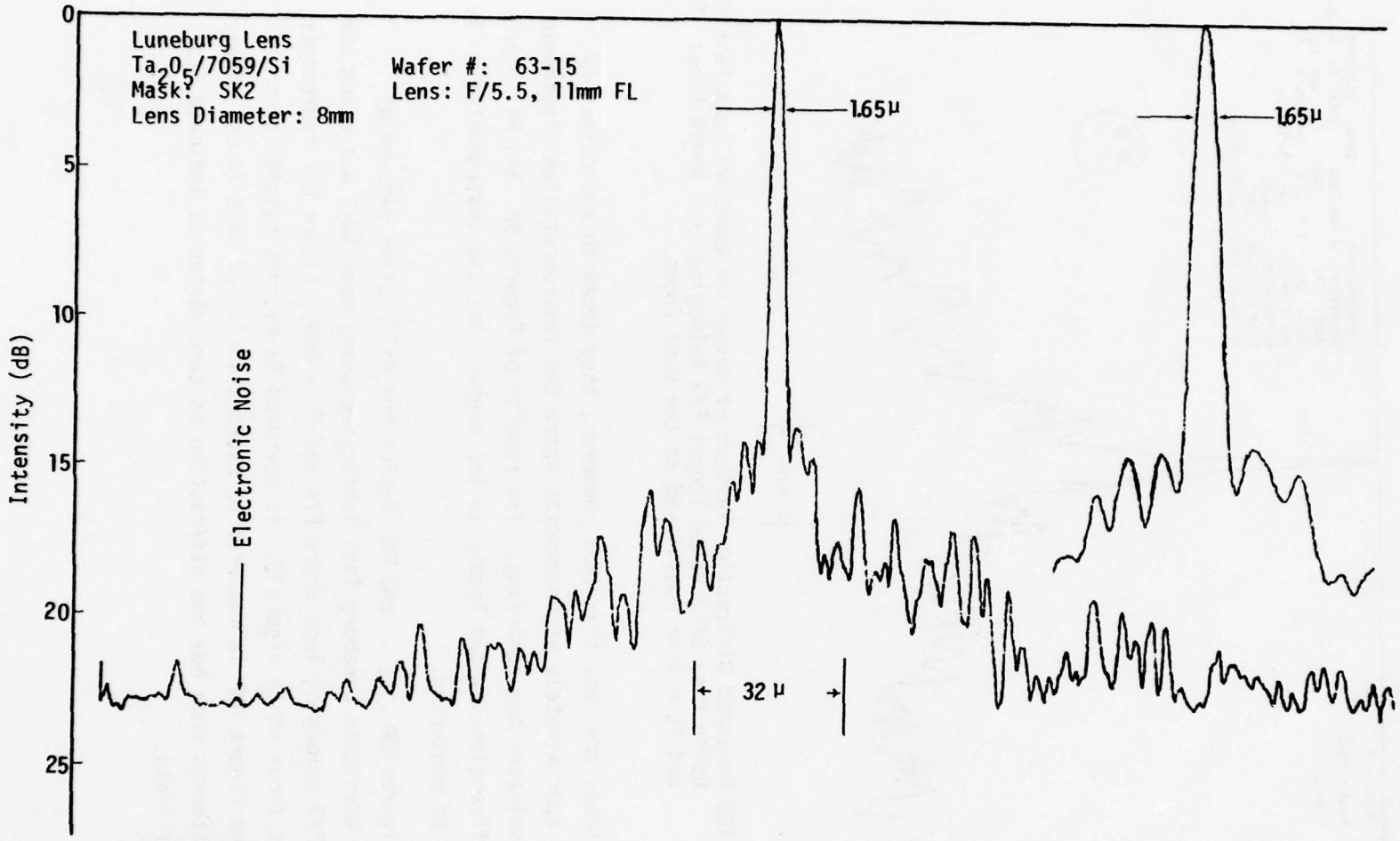

Figure 99 Measured Diffraction Pattern of Waveguide Luneburg Lens Fabricated Using Mask SK-2 Using a Cleaved Exit Face at the Focus and Zeiss X40, F/.67 Microscope Objective Showing Diffraction-Limited Performance Where Lens: F/5.5 and FL = 11mm (Expanded Scale Insert).

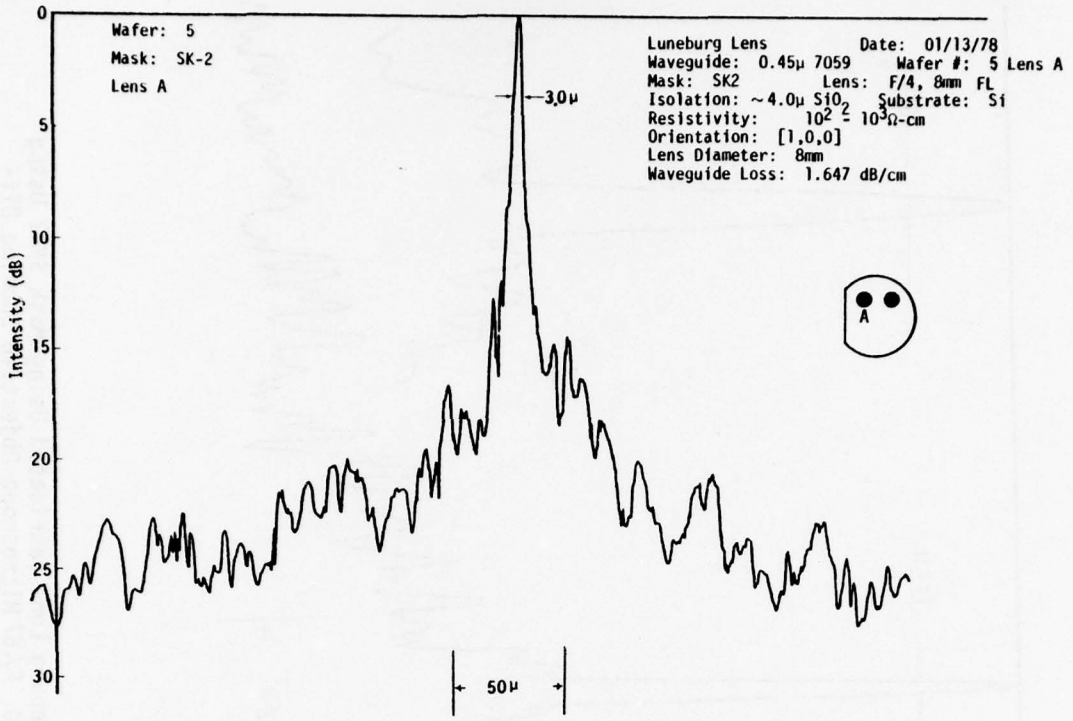

Figure 100 Measured Diffraction Pattern of Waveguide Luneburg Lens Fabricated Using Mask SK-2 Using Tropel F/3 Reimaging Lens Where Lens: F/4 and FL = 8 mm Positioned at the Best Focus.

inside lobes are less than 15dB, however, they decay to approximately 23dB in approximately 25 beamwidths where the instrumentation electronic noise dominates the recording. The results of Figures 98 and 99 represent diffraction-limited lenses to the degree that the instrumentation is capable of measuring.

Figures 100 , 101 , and 102 depict the diffraction pattern of another waveguide Luneburg lens fabricated using mask SK-2 and using the Tropel F/3 reimaging lens where F/4 and FL = 8mm. Figure 100 represents the best focus while Figure 101 is measured 62 microns outside of this focus and Figure 102 is measured 62 microns inside of this focus. These three patterns show how the diffraction pattern varies to indicate its depth of field.

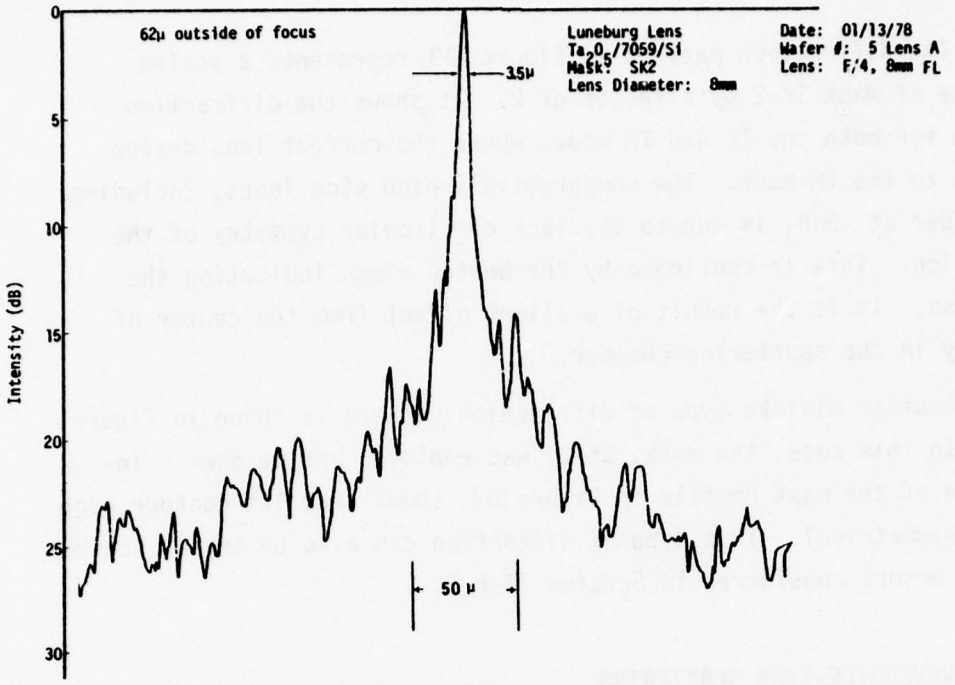

Figure 101 Same as Figure 100 Except Measured 62 Microns Outside of the Focus.

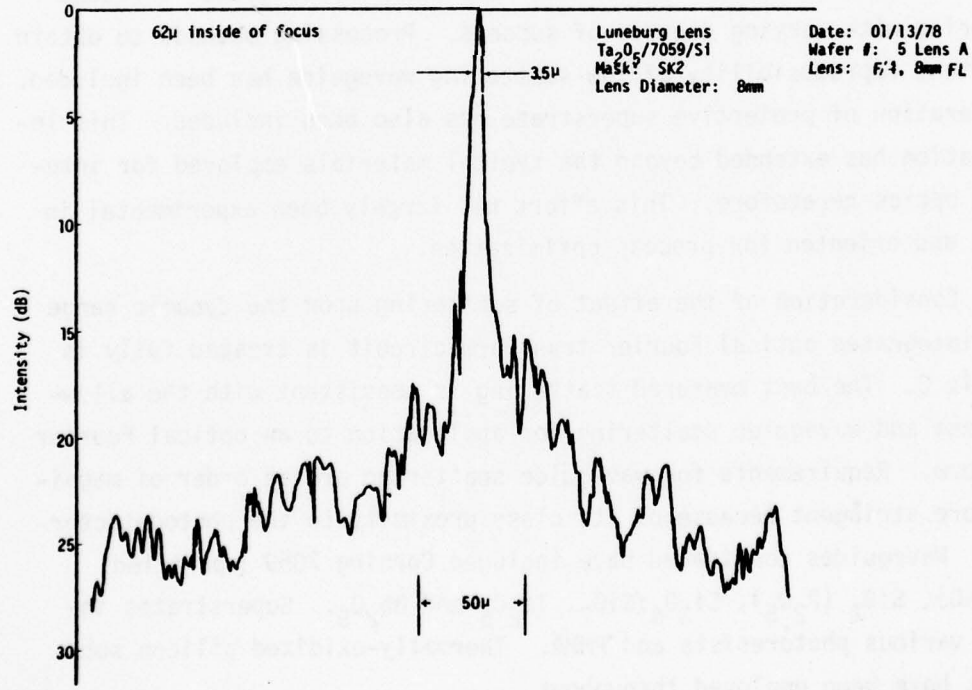

Figure 102 Same as Figure 100 Except Measured 62 Microns Inside of the Focus.

The diffraction pattern of Figure 103 represents a scaled increase of mask SK-2 by a factor of 2. It shows the diffraction pattern for both the TE and TM modes where the correct lens design applies to the TM mode. The comparatively high side lobes, including a shoulder at -5dB, is due to the lack of circular symmetry of the deposition. This is confirmed by the Newton rings indicating the thickness. It is the result of a slight offset from the center of symmetry in the sputtering chamber.

Another mistake type of diffraction pattern is shown in Figure 104. In this case, the mask, SK-2, was employed upside down. Inspection of the mask profile in Figure 104 shows that its contour edge is not symmetrical. This type of distortion can also be trace to the profile errors considered in Section II-B-5.

D. WAVEGUIDE-LENS SCATTERING

Mie and Rayleigh scattering in optical waveguide and waveguide lenses is an important consideration that may limit the application of integrated optical circuits. Various techniques have been investigated to reduce scattering with varying degrees of success. Processing methods to obtain consistent reproducibility of low-scattering waveguide has been included. Consideration of protective superstrate has also been included. This investigation has extended beyond the typical materials employed for integrated optics heretofore. This effort has largely been experimental in nature and oriented for process optimization.

Consideration of the effect of scattering upon the dynamic range of an integrated optical Fourier transform circuit is treated fully in Appendix C. The best measured scattering is consistent with the allowable lens and waveguide scattering for application to an optical Fourier transform. Requirements for waveguide scattering are an order of magnitude more stringent because of its close proximity to the photodetector array. Waveguides considered have included Corning 7059 (purified SiO_2:BaO), SiO_2 (P_2O_5), Si_3O_4:SiO_2, Ta_2O_5 and Nb_2O_5. Superstrates included various photoresists and PMMA. Thermally-oxidized silicon substrates have been employed throughout.

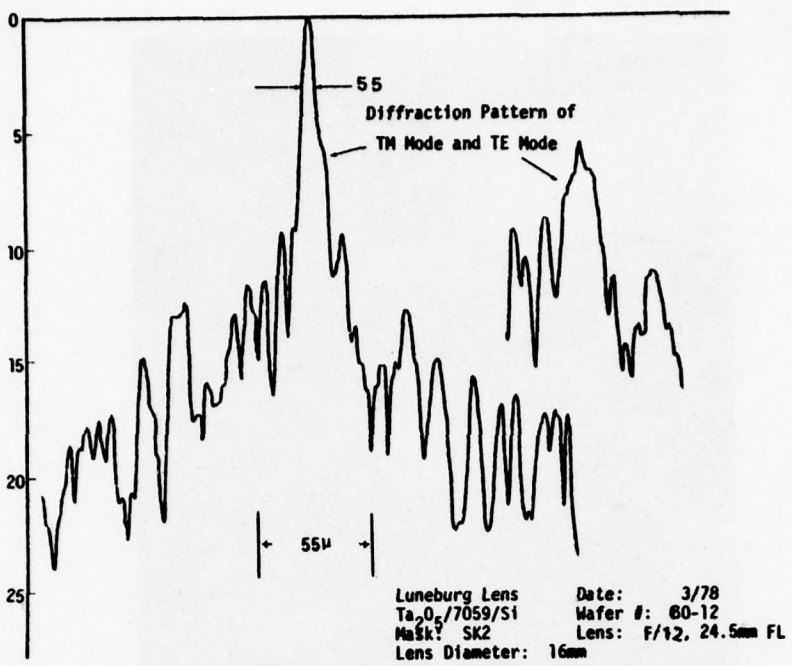

Figure 103 Measured Diffraction Pattern of Luneburg Lens Fabricated Using Mask SK-3 Using Tropel F/3 Reimaging Lens Where Lens: F/12.2 and FL = 25mm Showing the Results for Both TE and TM Modes.

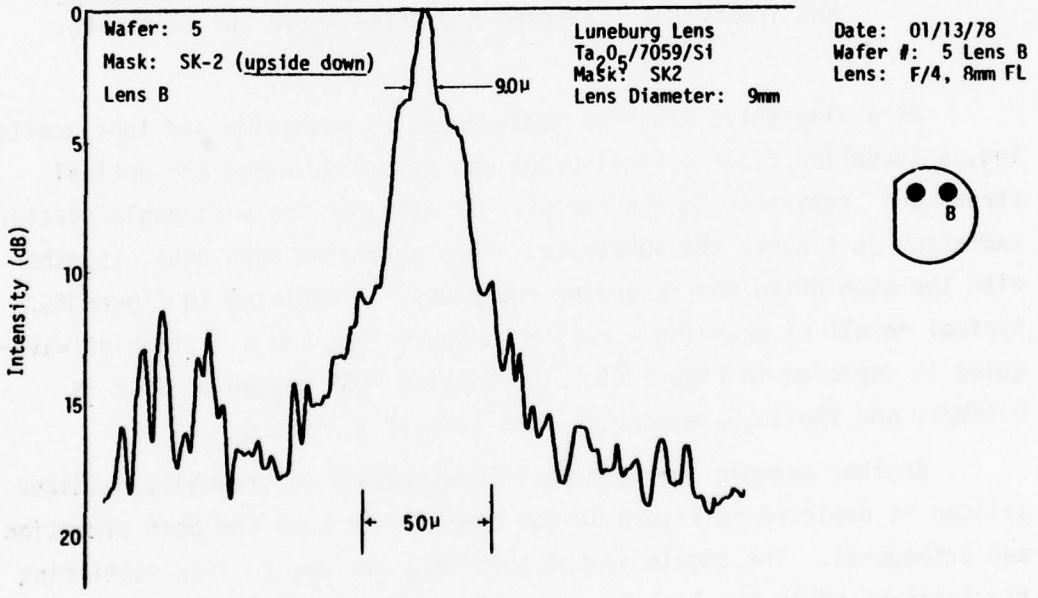

Figure 104 Measured Diffraction Pattern of Waveguide Lens Fabricated Using Mask SK-2 Turned Upside Down.

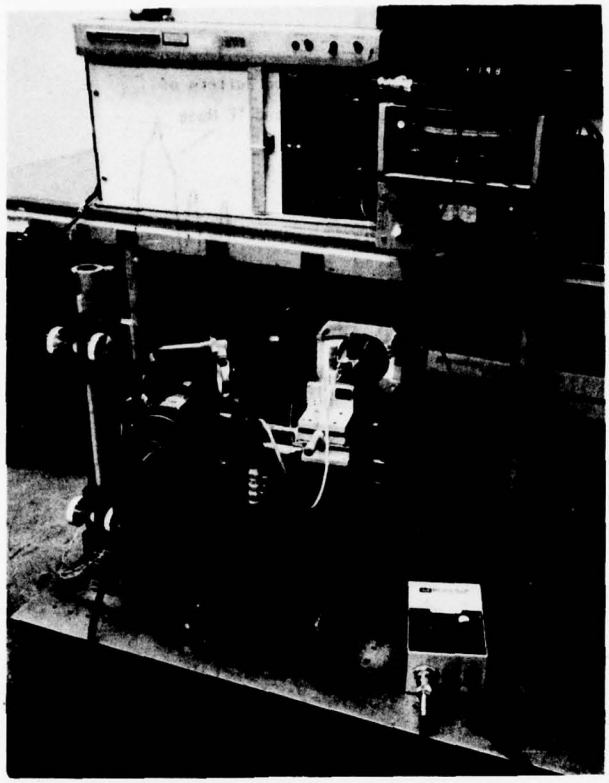

Figure 105 Traveling Fiber Optical Probe for Measuring Longitudinal and Transverse Scattered Radiation Above the Substrate.

As a diagnostic tool for measurement of waveguide and lens scattering, a traveling fiber optical probe was assembled along the optical streak and transverse to the streak. It measures the wide-angle scattered radiation just above the substrate. This automated apparatus, together with the scan drive and recording equipment, is depicted in Figure 105. A typical result of scanning across a Luneburg lens and a section of waveguide is depicted in Figure 106. The Corning 7059 waveguide loss is 0.4dB/cm and the Ta_2O_5 waveguide lens loss is 1.74dB/cm.

Another example for Corning 7059 waveguide on thermally-oxidized silicon is depicted in Figure 107 for wafer #7 in both the best direction and orthogonal. The angulations of this data are due to fine scattering fluctuations while the line is a computer-generated RMS slope. The streak of the waveguide in Figure 107 is barely perceptible to the eye.

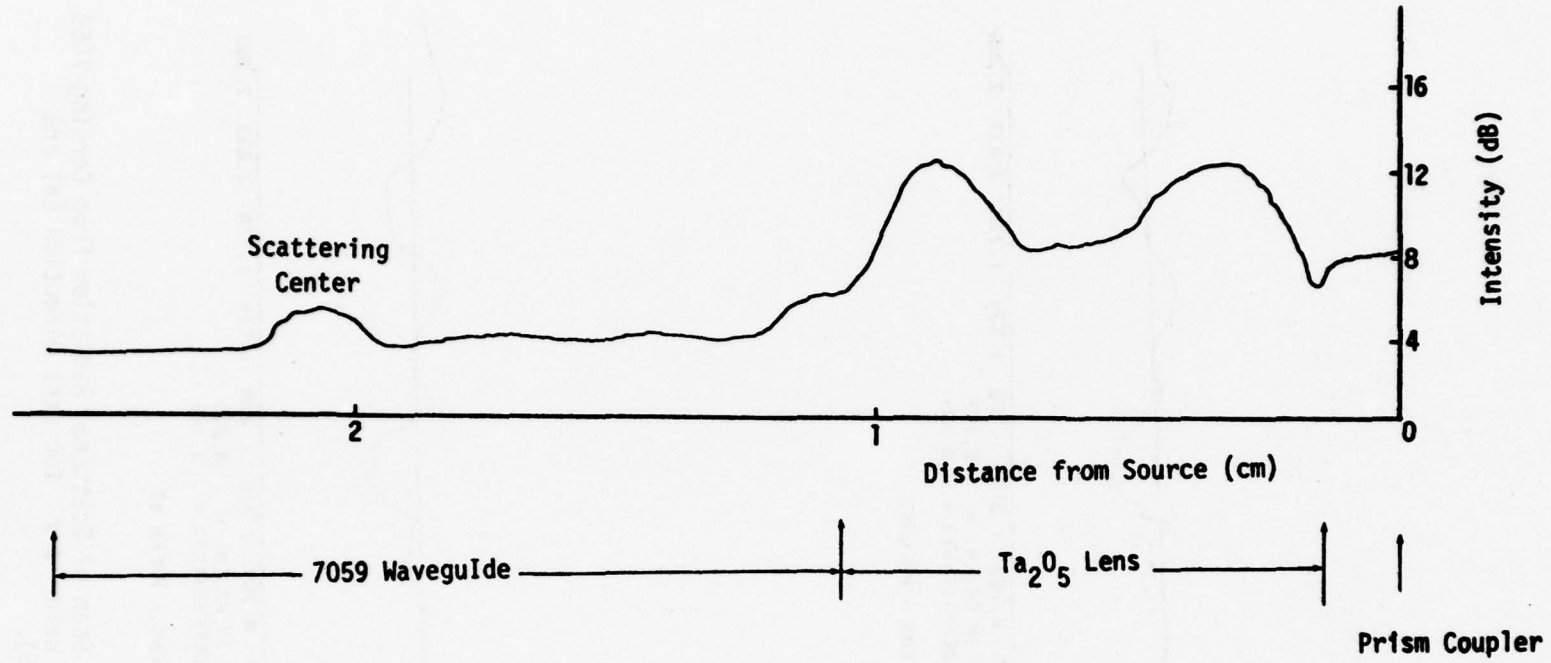

Figure 106 Waveguide Scattering Trace Across Ta_2O_5 Thin-Film Luneburg Lens and Subsequent Corning 7059 Waveguide.

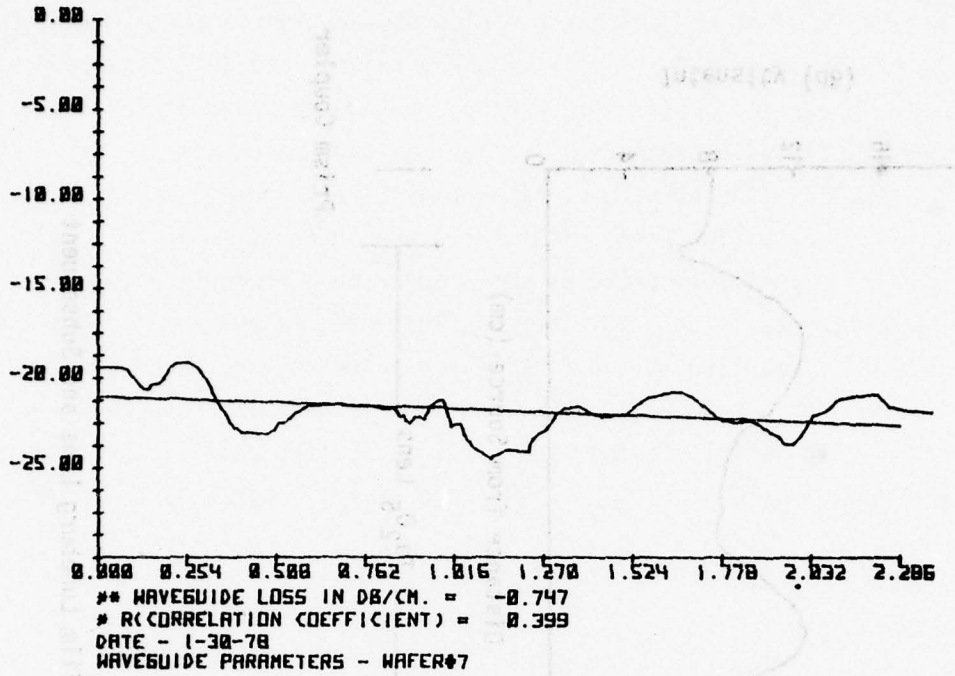

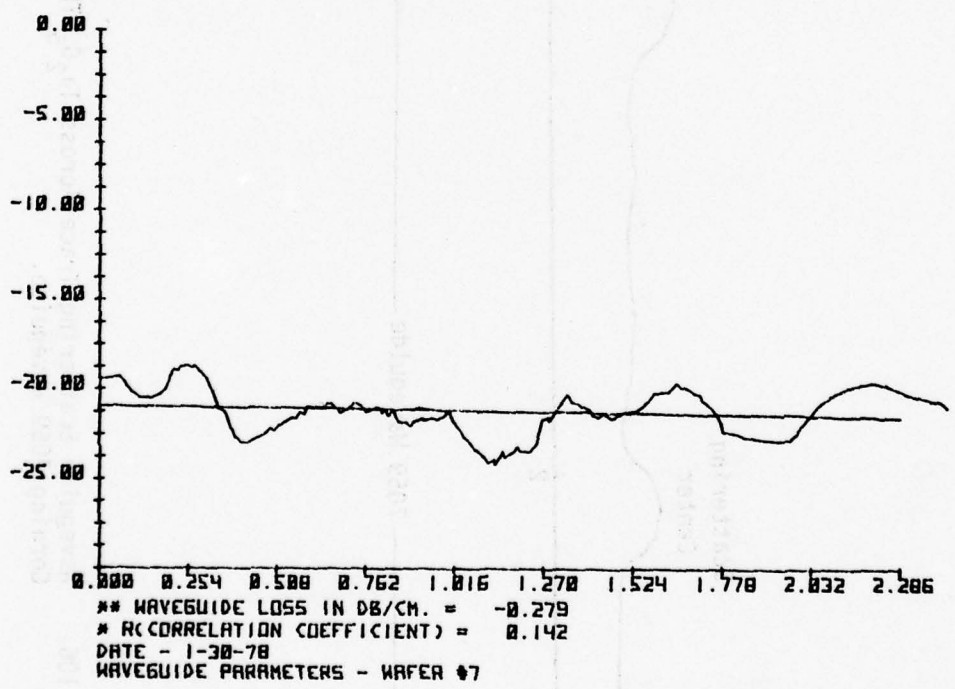

Figure 107 Longitudinal Scan of Scattered Radiation From Corning 7059 Waveguide on Wafer # 7 for Best Direction (a) and Orthogonal (b).

Another kind of waveguide scattering observation is depicted in Figure 108 showing scattering normal to the waveguide and 30° above the plane of the waveguide. Diffraction coupling has been used at the input cleaved edge. Close inspection of Section (a) shows a number of longitudinal streaks as fine structure. They have been traced to stepping of the cleaved edge. Two kinds of scatters are apparent in Section (a). The "snowball" effect for particles much larger than the optical wavelength is pronounced in both (a) and (b), while the relatively smooth fine-grained distribution is substantially reduced as the angles change. Another example of a Corning 7059 waveguide on a thermally-oxidized silicon substrate is illustrated in Figure 109. Unfortunately, the corresponding photograph is not available. The overall waveguide assembly effective measured loss is 2.8dB/cm. Three dashed curves are inserted for various segments which have a slope representative of 0.9dB/cm. The effect illustrated in Figure 109 has been traced to the cleaning process of the oxidized surface prior to the deposition of the waveguide. A smear appears corresponding to each of the dramatic steps in the scattering profile. Scattering at these points perturbes the confinement in the 7059 so that radiation is absorbed in the substrate. Thus, the actual streak traverses the guide at approximately 0.9dB/cm until it intersects the residue left from cleaning where a significant portion is scattered in the substrate and then continued at the 0.9dB/cm rate until it intercepts the next scattering section.

Another type of waveguide structure investigated employed a Corning 7059 waveguide on a phosphorous-doped silicate glass and thermally-grown SiO_2 on silicon substrate. The use of both isolation layers permits etching steps into the SiO_2 as may be required for a waveguide transition into a photodetector array. The addition of phosphorous reduces the melting temperature. The surface is heated until surface tension from the partial liquid state forms relatively smooth transitions over the steps. The results of this structure are illustrated in the photographs of Figure 110. Section (a) is taken at normal incidence and shows the typical streak and one scattering center at the first transition edge. The optical beam traverses three additional steps which are not apparent but each of the steps are reduced in height in

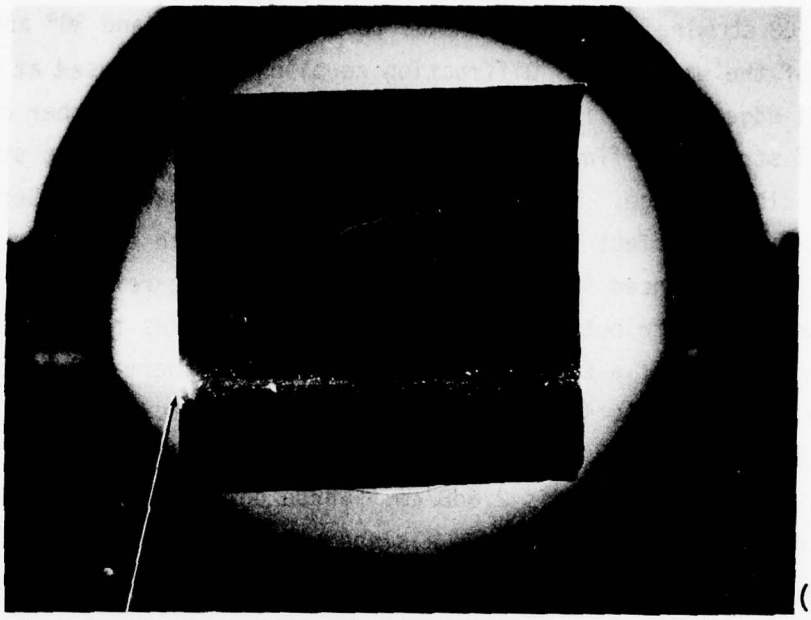

(a)

Diffraction Coupling to Cleaved Edge

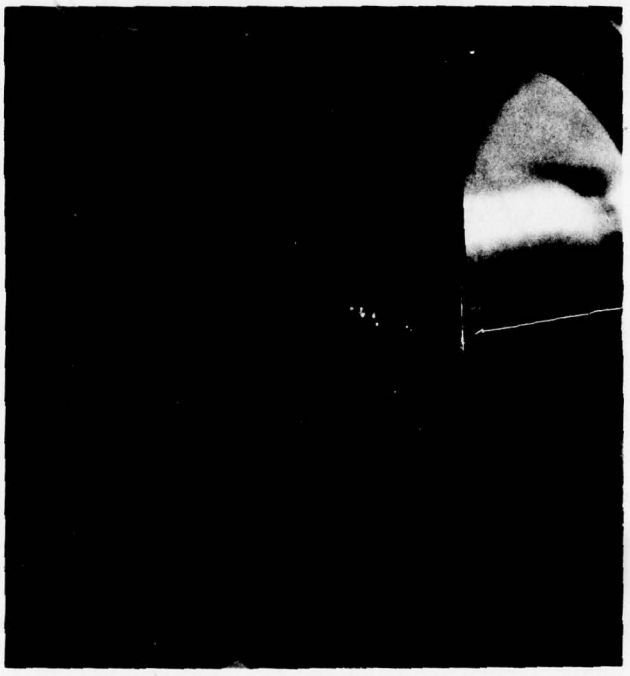

Tilted Substrate to Show Output Distribution

(b)

Figure 108 Photograph of Optical Streak through Corning 7059 Waveguide on Thermally-Oxidized Substrate at Normal Incidents (a) and at 30° above Plane Looking at the Output (b). Input Coupling Provided Focusing Radiation on Cleaved Edge.

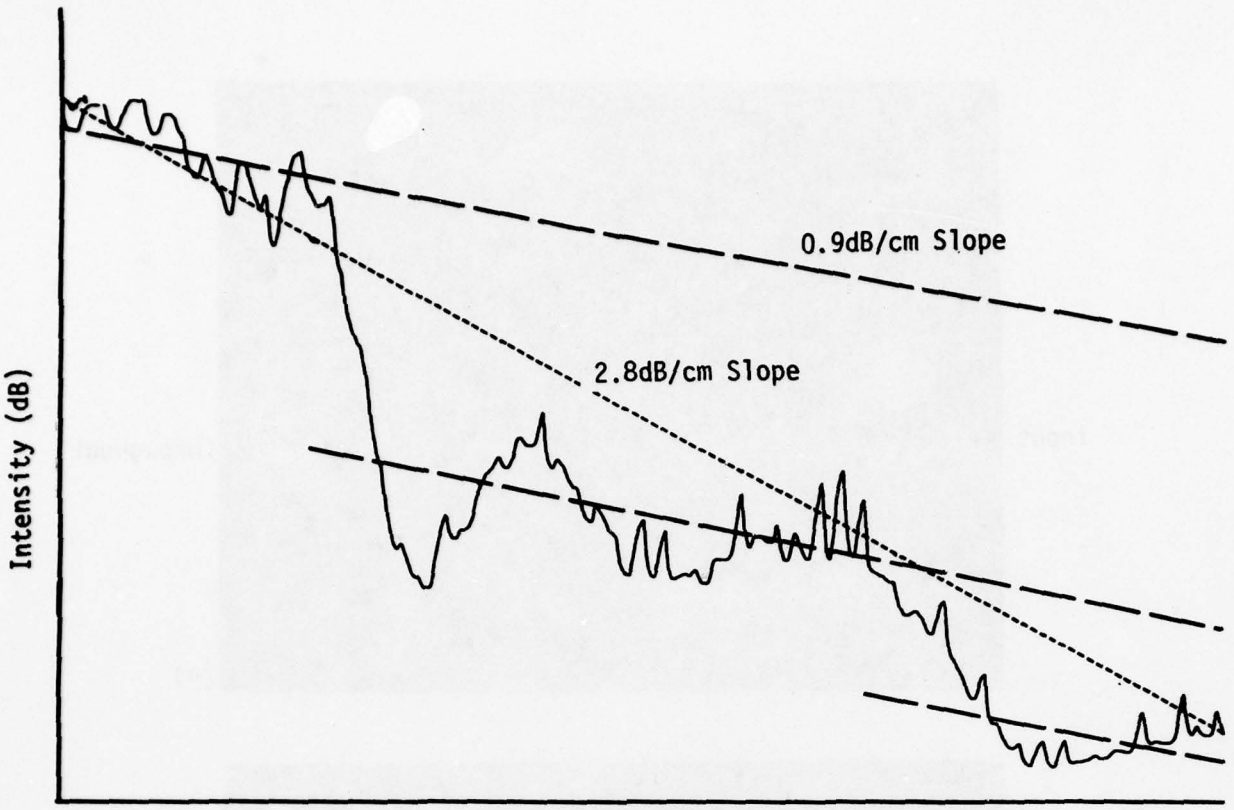

Figure 109 Measured Optical Waveguide Scattering for Corning 7059 Waveguide on a Thermally-Oxidized Silicon Substrate. Two Sharp Steps are due to Scattering Loss and Absorption in Silicon Substrate. Waveguide Assembly Effective Loss 2.8dB/cm. Reduced Slope Lines Represent 0.9dB/cm Loss.

descending order moving to the substrate edge. Section (b) of the photograph was taken at 45°. It shows a first-step transition to produce significant scattering in the forward direction and, thus, indicates that the step height is too much. The remainder of the trace to the end of the substrate is now apparent at the forward scatter angle. The use of reflowed phosphorous-doped silicate glass provides an important design freedom for integrated optical circuits and leads to a reduction of scattering. It is presumably due to the fact that its process reaches the liquid state so that the surface tension produces a smoothing effect.

The properties of silicon-oxynitride were investigated as an alternative to Corning 7059 and Ta_2O_5. The refractive index of this material can be changed from approximately 1.47 - 2.1 depending upon the SiO_2 and

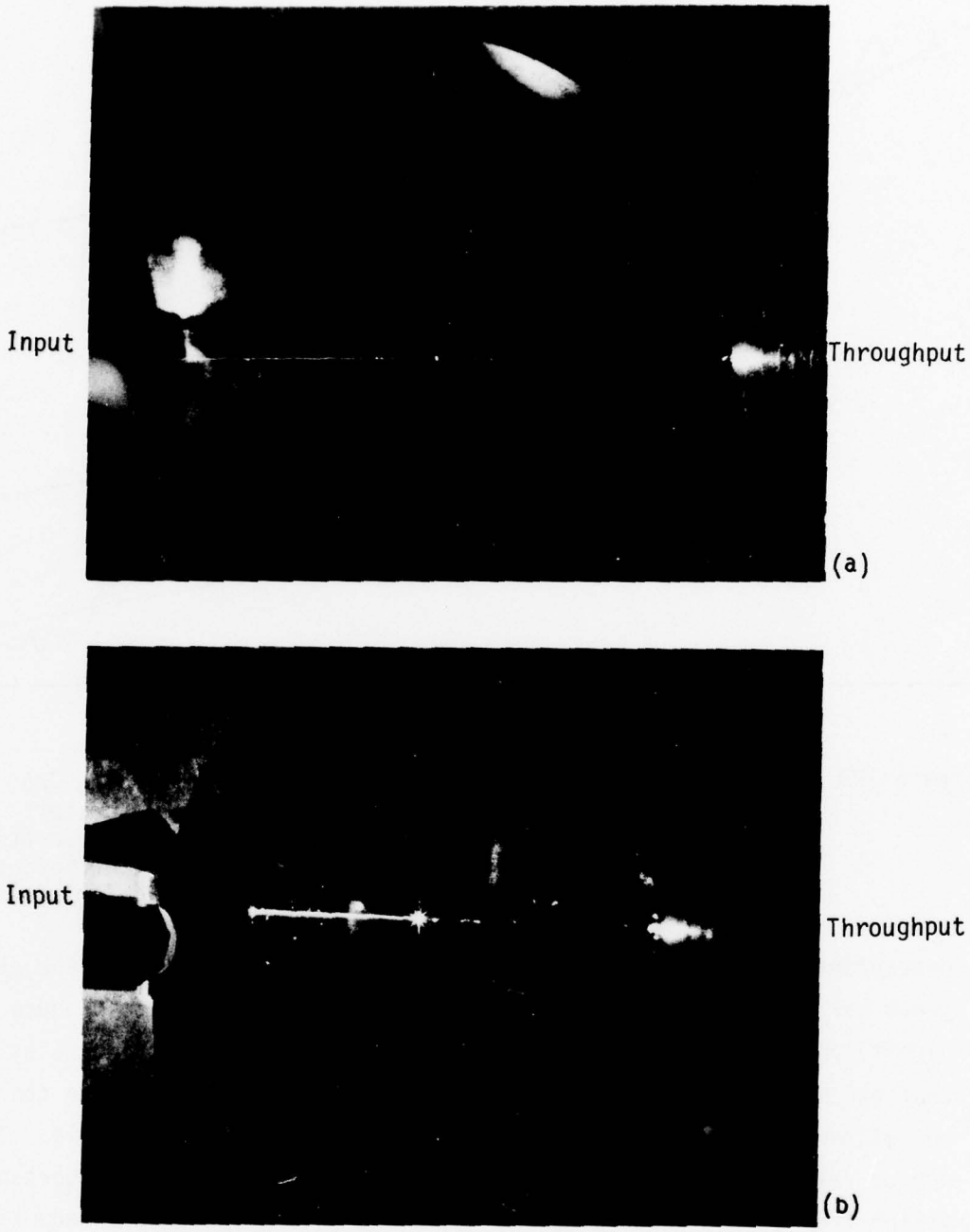

Figure 110 Photograph of Optical Waveguide Streak Normal to Substrate. 7059 Waveguide on Reflowed Phosporous Silica Glass on Thermally-Grown SiO_2 with Stepped Edges on Silicon Substrate (a), and Photograph of Forward Scattered Radiation at 45° (b).

Si_3N_4 proportions. The first result is shown in Figure 111, together with the measured scattering intensity profile. Careful inspection shows circular streaks which have been traced to a typical semiconductor cleaning procedure, spinning the wafer with solvents and a swab. The measured loss is 5.2dB. The film thickness is approximately 3000Å. A much better result is shown in Figure 112. The corresponding measured scattering profile has a slight slope indicating a loss of 0.5dB/cm. An expanded intensity scale has been included to show the minute fluctuations. The photograph of Figure 112 shows a throughput refraction from the cleaved edge and the transverse spatial distribution surrounding the streak contained within the waveguide. This gives an encouraging comparison with Corning 7059. If the process can be adapted for the formation of lens profiles and for the formation of waveguide, it will be possible to form the optical circuit using a single composition. In the region of the lens, a much larger percentage of Si_3N_4 would be used. The Si_3N_4 thin-film process employed for the waveguide in Figure 112 has utilized a chemical vapor deposition technique at high temperature and at high pressure. This process was used to obtain a higher concentration of Si_3N_4 and to obtain a larger thickness in a reasonable time. A corresponding low-pressure chemical vapor deposition process reported in the literature also yields good results but requires a considerably longer time to obtain the equivalent thickness.

Low-loss, low-scattering Corning 7059 waveguide is obtainable. Figure 113 illustrates a prism coupler with an optical beam propagating through the waveguide which exits from the cleaved face. The waveguide streak is not apparent to the eye or discernable by the available instrumentation. The wide collimated beam is refracted into the background in Figure 113 and is perfected with reflections photographed in Section (b) to show a well-defined diffraction pattern. A more typical low-loss propagation streak is shown in Figure 114 with its throughput. This streak has fine structure due to a less-than-perfect prism coupler edge. A scattering line defect is apparent at the output due to prior coupling of the prism. A measured transverse beam dis-

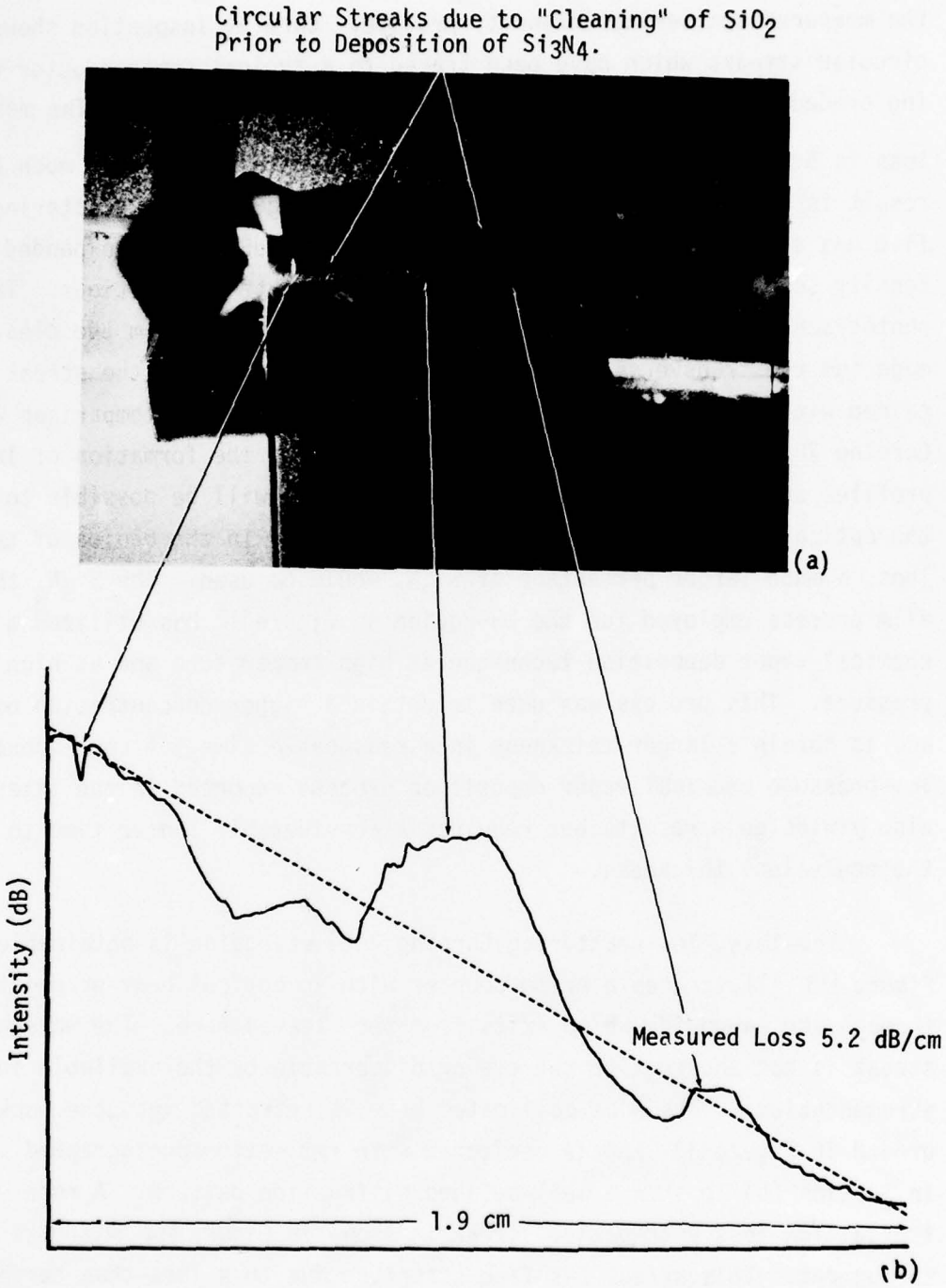

Figure 111. Photograph of Optical Waveguide (Very Poor) Streak for an Si_3N_4:SiO_2 Waveguide on a Thermally-Oxidized Silicon Substrate (a) Together with the Corresponding Measured Scattered Intensity Profiles by Travelling Fiber Probe Technique (b) of Specimen in (a)

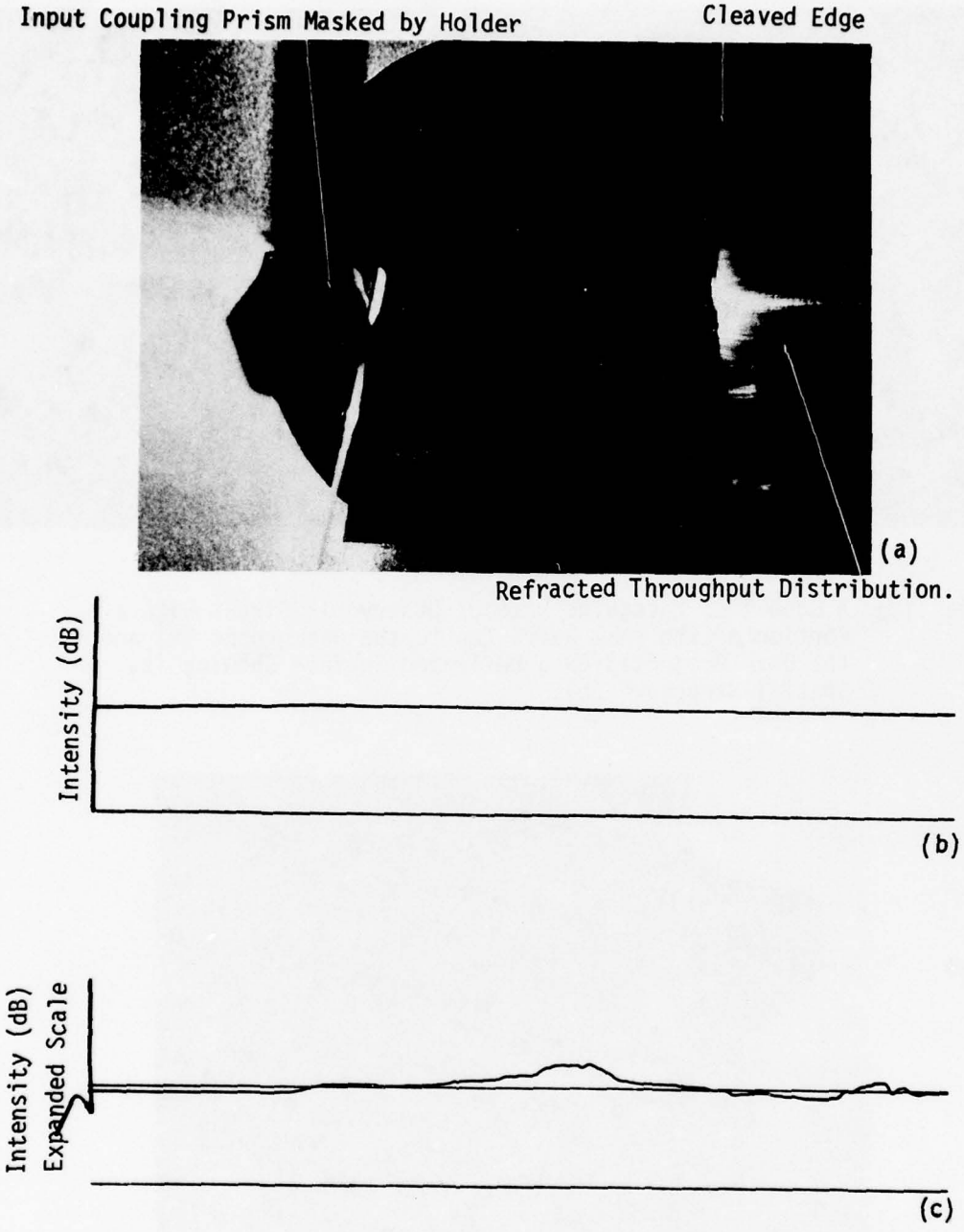

Figure 112 Photograph of Optical Waveguide (Good) Streak for an Si_3N_4:SiO_2 Waveguide on a Thermally-Oxidized Silicon Substrate (Increased Exposure) (a) Together with Two Corresponding Measured Scattered Intensity Profiles by Travelling Fiber Probe Technique (b) of Specimen in (a) and Expanded Scale of Profile (c).

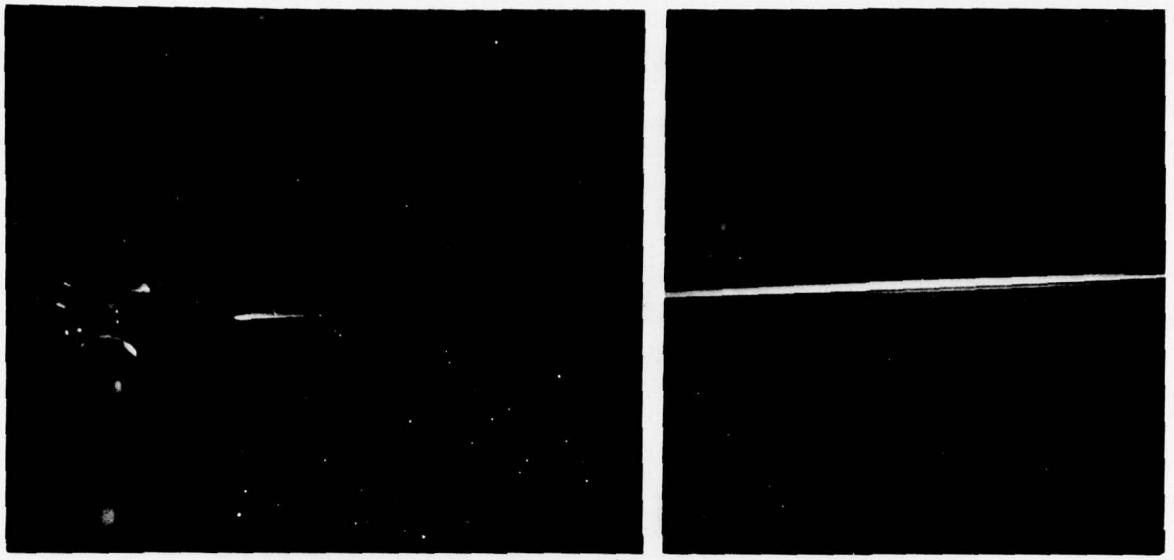

Figure 113 A Good 7059 Waveguide Without Observable Streak With a Portion of the Beam Refracted to the Background (a) and the Beam Projected on a Reflected Surface Showing its Spatial Structure (b).

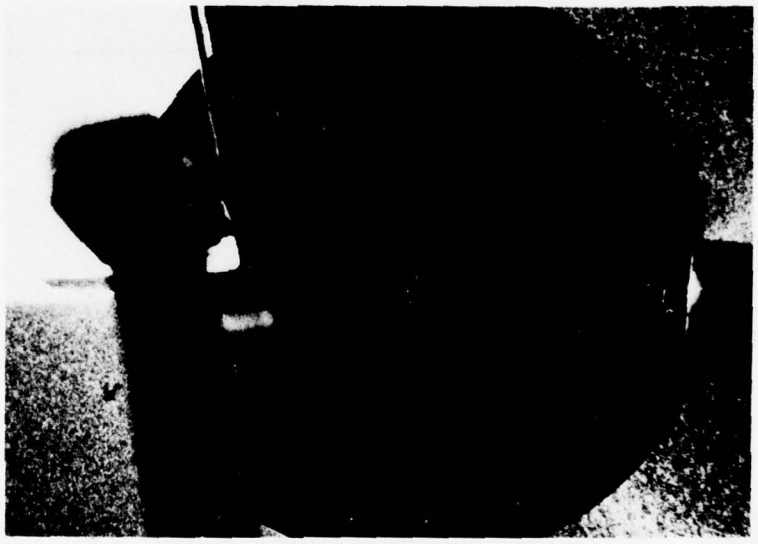

Figure 114 Another Propagation Streak for 7059 Waveguide Showing Structure Partially Due to a Less-Than-Perfect Prism Edge With its Throughput.

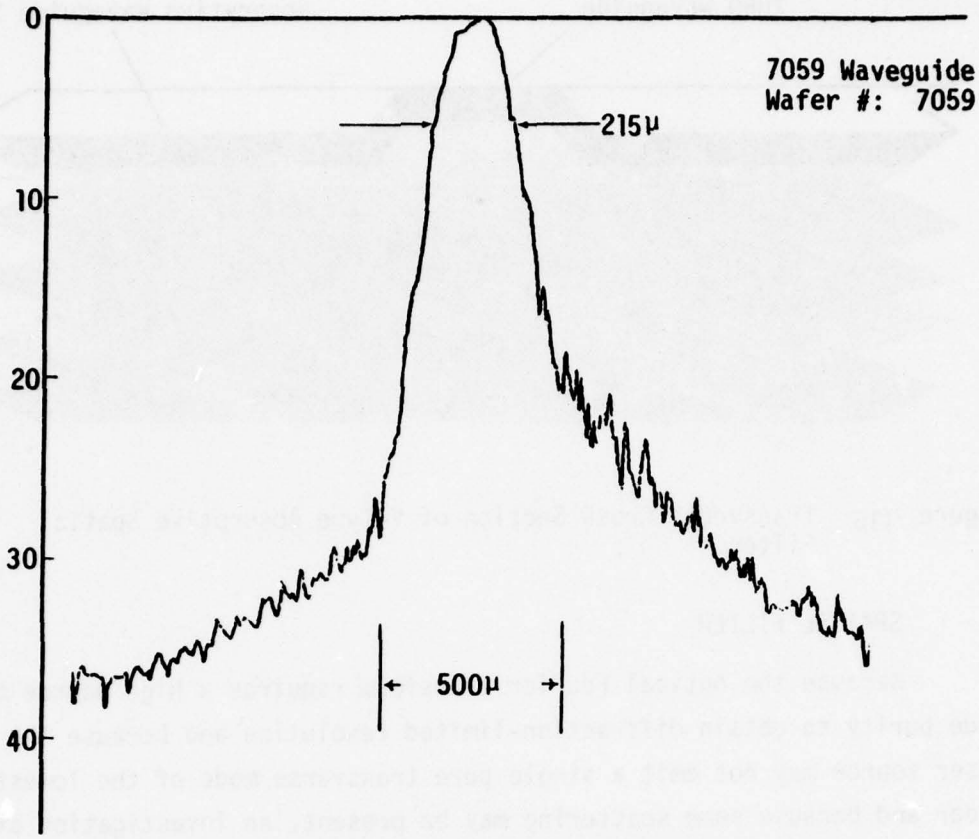

Figure 115 Transverse Beam Distribution of 6328Å Radiation Propagating Through 10 cm of 7059 Waveguide Corresponding to the Photograph of Figure 113.

tribution of a low-scattering, low-loss Corning 7059 waveguide is depicted in Figure 115 . This propagation loss is less than 0.1dB/cm. Loss measurements at this low scattering level requires further technique refinement.

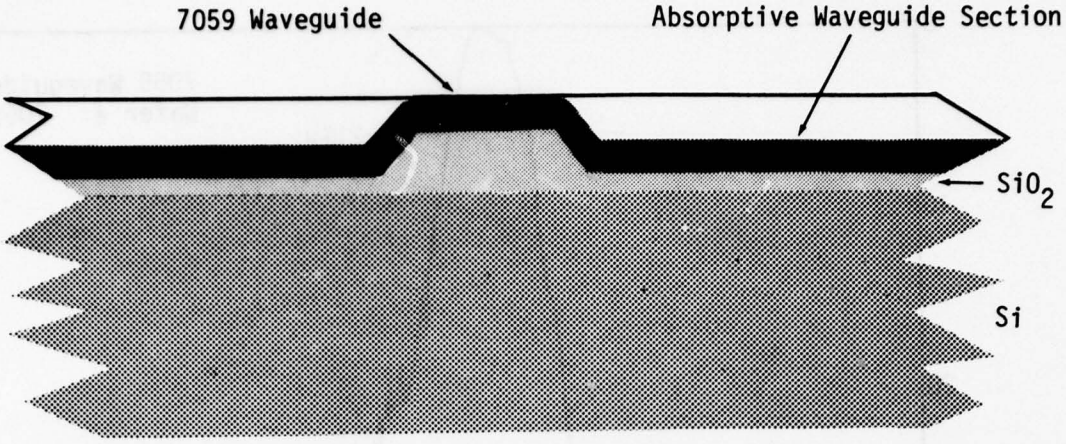

Figure 116 Transverse Cross Section of V-Type Absorptive Spatial Filter.

E. SPATIAL FILTER

Because the optical Fourier transform requires a high degree of mode purity to obtain diffraction-limited resolution and because the laser source may not emit a single pure transverse mode of the lowest order and because some scattering may be present, an investigation of a spatial filter has been included. Typical spatial filters consist of small aperture stops located at the focus of inverting beam expanders. They are largely reflective in nature with abrupt boundaries. The spatial filter considered herein for inverting beam-expansion lens systems employs an absorptive iris at the focus using a planar waveguide structure supported by a thermally-grown oxide isolation layer on a silicon substrate. The absorptive iris spatial filter is formed by removal of the thermally-grown oxide so that the planar waveguide is stepped down and is adjacent to the absorbed silicon substrate in the iris section. A transverse cross section through the V iris apex is shown in Figure 116 with a plan view of the stepped-down absorptive section shown in Section (a) of Figure 117. The V gap is 5 microns. Fiducial marks are used for accurate positioning in the focus of a Luneburg lens beam expansion system. The operation of this spatial filter is depicted in Section (b) of Figure 117 using a 6328Å radiation. The entrance beam

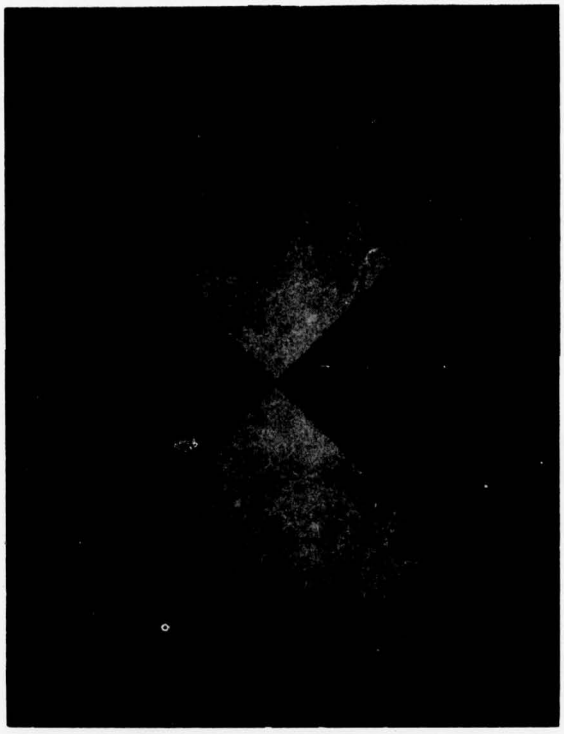

(a)

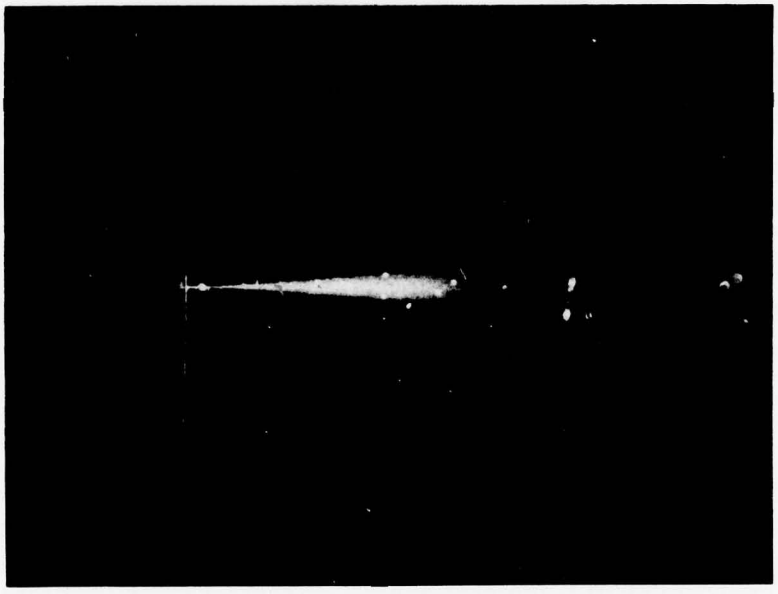

(b)

Figure 117 Photographs of V Spatial Filter (a) and its Operation (b).

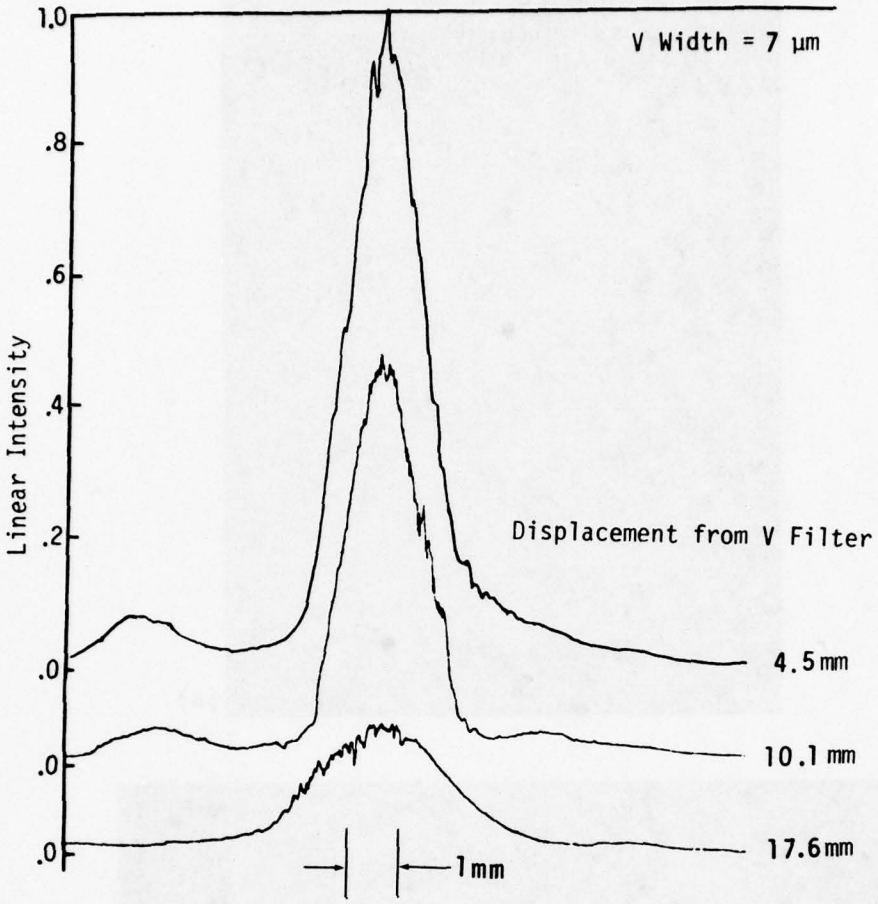

Figure 118 Cross Sections of Near Field Intensity in Output of V-Type Absorptive Spatial Filter.

is apparent together with the exit beam and a few scatterers (out of focus). The input beam is intentionally offset and exhibits a typical streak. Transverse profiles of another spatial filter through three sections of the beam at different displacements from the spatial filter are depicted in Figure 118 where the spatial filter aperture is 7 microns. The continuous-wave, power-handling capacity of Corning 7059 waveguide on thermally-grown SiO_2 at the focus is greater than 0.4×10^6 watts/cm^2.

The V-groove is appropriate for tightly focused beams, however, to introduce a more sharply defined beam truncation for a longer focal length than the system, the V shape has been altered to more closely approximate the hyperbolic beam contour near the focus. Figure 119 illustrates such a spatial filter plan view with a magnified view of the constricted waveguide section.

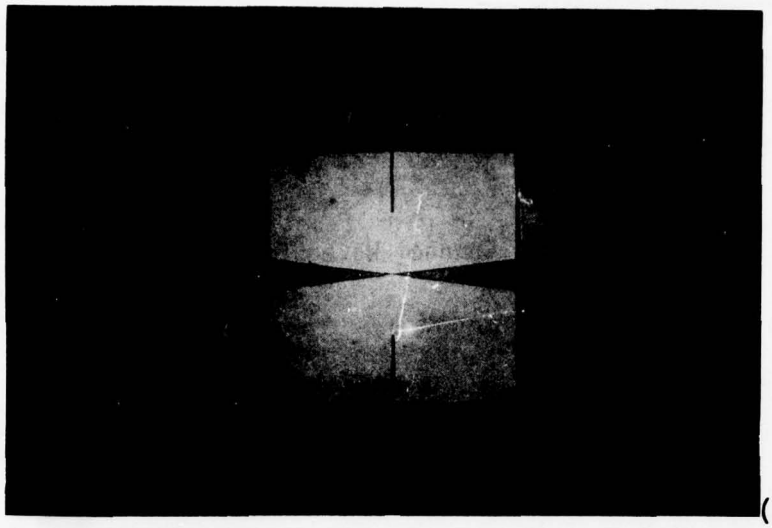

(a)

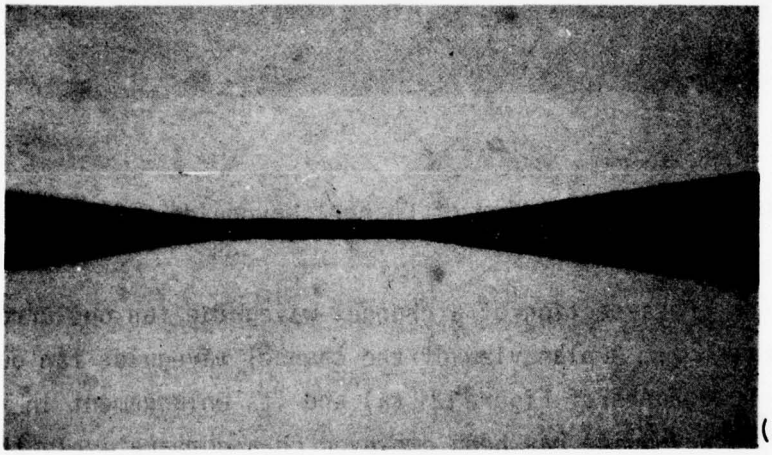

(b)

Figure 119 Macrophotograph of Absorptive Spatial Filter With Contoured Gap Designed for Use With F/4 Waveguide Lenses (a) and Detail Showing the Contoured Gap of 5.6 Microns (b).

F. CHANNEL WAVEGUIDE FAN OUT

For an integrated optical Fourier transform circuit, an optical waveguide fan out array was investigated to accommodate high density spatial information in the lens focal plane to a less dense photodetector linear array.

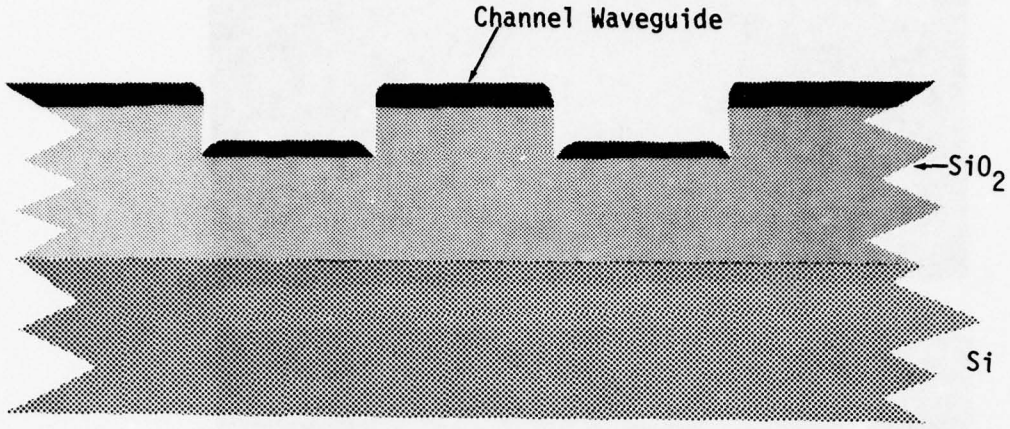

Figure 120 Transverse Cross Section of Channel Waveguide Fan-Out.

A transverse cross-section of a channel waveguide fan out array is depicted in Figure 120. A plan view of the channel waveguide fan out appears in the photographs of Figure 121 (a) and its enlargement in section (b). Corning 7059 waveguide has been employed on a comparatively thick thermally-grown SiO_2 isolation layer on a silicon substrate. Channel separation has been provided by photolithography using a chemical etch to define channels. The thermally-grown SiO_2 isolation layer thickness is typically 4 microns, while the etch depth defining the channels is approximately 1.5 microns deep. The Corning 7059 waveguide approximately 5000 Å thick will fill the separation channels to approximately 2000 Å due to the shadowing of the elevated waveguide. The operation of two channel waveguide fan out specimens is illustrated in Figure 122 for radiation where 6328 Å radiation has been coupled into and traverses a single channel waveguide. Some residual illumination discloses the presence of the other channels. Strong Mie scattering from the waveguide edges is apparent. The channel waveguide losses are unfortunately comparatively high (less

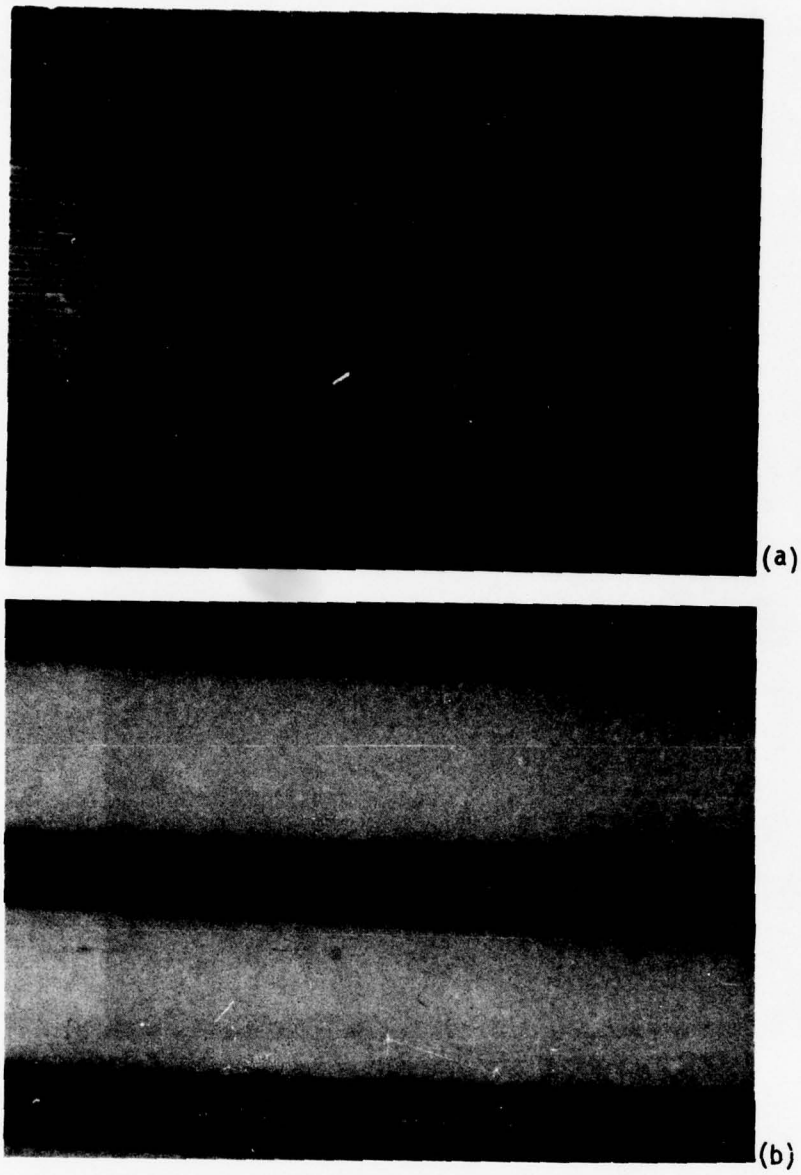

Figure 121 Plan View of Channel Waveguide Fan-Out (a) and Enlargement (b).

than 10 dB/cm), however, this loss should not impair the photodetector array because the waveguide fan out length probably will not exceed 2 millimeters. Coupling of radiation into a single waveguide channel at the end with a larger period shows that there is no significant coupling to adjacent channels as these waveguides converge.

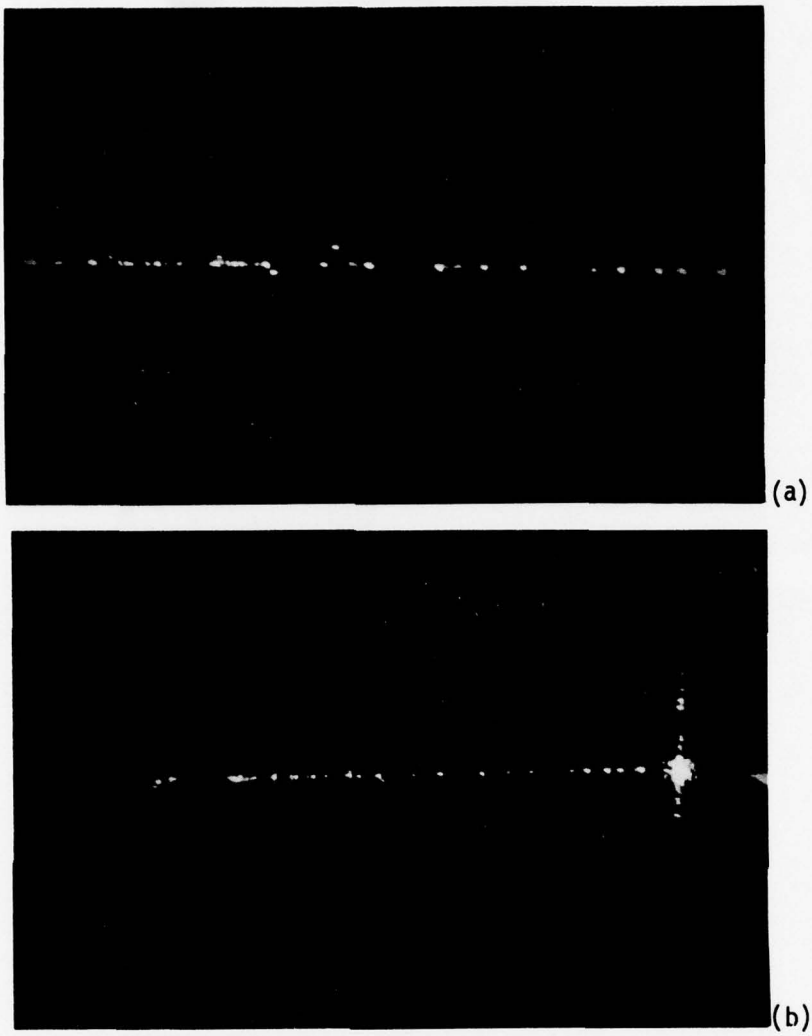

Figure 122. Plan View of Two Channel Waveguide Fan Out Arrays with 6328 Å Radiation Coupled into a Single Waveguide Traversing the Figure from Right to Left.

III. REVIEW

A. CONCLUSIONS

Integrated optical waveguide positive inhomogeneous refractors identified as the generalized Luneburg lenses have been investigated, calculating the performance and demonstrating their operation, yielding diffraction-limited results. A method to calculate and predict the performance and a method to synthesize the mask required to realize thin-film Luneburg lenses has been developed showing that the generalized Luneburg lens for integrated optics is on a sound, well-developed foundation. Further, the lenses exhibit the requisite properties for an optical Fourier transform "chip" that may be employed as a real-time microwave spectrum analyzer.

The approach has emphasized the application of Ta_2O_5 as the high-index lens film used, together with Corning 7059 as a waveguide, all of which are deposited upon thermally-grown SiO_2 as an isolation layer on a silicon substrate. This structure permits the integration of the optical components with their electronic counterpart on a single substrate. This material-structure and its associated processing is compatible with the processing of electronic circuit elements using processes familiar to the semiconductor industry.

The thin-film Luneburg lenses are formed by RF sputter deposition of the lens material through a circular mask with a prescribed edge shape on the waveguide. The procedure to synthesize the mask shape is included. Accurate synthesis of the "true" Luneburg lens profile yields diffraction-limited results verified experimentally.

A numerical procedure has been developed and applied to compute the performance of waveguide generalized Luneburg lenses. Starting with the waveguide lens thickness profile determining the ray traces in the waveguide leads to the ray intercepts in the image plane. With this data, the wavefront is determined and the resulting intensity diffraction pattern is calculated. The procedure allows the introduction of various types of waveguide thickness profile errors to be introduced and the calculation of the effect upon the diffraction pattern. Numerous examples have been included showing the effects for F/1, F/2.5 and F/4.5 lenses.

Waveguide Luneburg lenses with F/4 to F/25 have been realized with diffraction-limited beamwidths. The smallest beamwidth observed is 1.65 microns confirming the design value and the procedure. Decaying side lobes which can be held below 17dB for low-scattering lenses and waveguide can be achieved. The side lobes decay into the optical scattering level and/or instrumentation noise typically on the order of 30dB. These results have confirmed mask synthesis procedure. It has been found, experimentally, that a mask design for F/4 is applicable to longer focal length lens yielding diffraction-limited results.

The effects of optical waveguide scattering have been reduced by improved processing procedures so that consistent reproducibility has been achieved <0.3dB/cm while some results have broken the barrier below 0.1dB/cm. Corning 7059, 4 SiO_2:BaO, $SiO_2(P_2O_5)$, Si_3O_4:SiO_2 based waveguides were considered with Ta_2O_5 and Nb_2O_5 lenses. Consideration of the effect of waveguide and lens scattering upon the dynamic range and resolution of an integrated optical Fourier transform is treated showing that the best measured scattering is consistent with the allowable lens and waveguide scattering for this application.

Some further effort reducing the scattering by understanding the mechanism and introduction of process refinements is desirable. This is particularly true for the Ta_2O_5 and Nb_2O_5 lenses when the thickness is on the order of hundreds of Angstroms.

Other integrated optical circuit elements for the Fourier transform signal processing function include a spatial filter, reflectors and channel waveguide fan-out structures. Spatial filters using an absorptive V-type iris were demonstrated for use with inverting beam expansion lens systems. Several beam expansion lens systems have been demonstrated showing that the mask positioning can yield a collimated beam reproducibly. Cleavage through the substrate and overlaying films can produce an interface of sufficient perfection to implement total internal reflectors. Positioning of the cleavage to photolithographic patterns was demonstrated. For some integrated optical circuits, planar waveguide coupling to a discrete linear array of photodetectors is desirable. For this purpose, a high-linear density channel waveguide fan-out structure has been demonstrated.

The results of this effort and its predecessors have established a firm technology base for waveguide Luneburg lenses on a thermally-oxidized silicon substrate providing an attractive approach to implementing an integrated optical Fourier transform "chip" that may be used for spectral analysis and other signal processing functions where real-time bandwidth operation is essential. The approach uses well-known established manufacturing processes with some refinement and, thus, the "chip" can be implemented economically as quasi-monolithic optical circuit integrated with its associated electronics.

APPENDIX A

PREPRINT FOR THE TRANSACTIONS OF THE INSTITUTE OF ELECTRONICS
AND COMMUNICATIONS ENGINEERS OF JAPAN, MARCH 1978: SPECIAL ISSUE
Integrated Optics and Optical Fiber Communication

PROGRESS IN WAVEGUIDE LENSES FOR INTEGRATED OPTICS*

D. B. Anderson and R. R. August
Electronics Research Center
Rockwell International Corporation
Anaheim, California 92803 USA

SUMMARY

Thin-film waveguide Luneburg and geodesic lenses are being developed for near-infrared integrated optics. Considerations which yield a preference for these structures are enumerated, together with specifics, for generalized Luneburg lenses employing Ta_2O_5 (lens) with Corning 7059 (waveguide) on thermally-grown SiO_2 on Si substrates. Spheric geodesic lenses formed with the same waveguide, isolation layer, and substrate materials are included.

INTRODUCTION

Optical waveguide lenses, reflectors, and lens systems [1], together with surface elasto-optic spatial modulators [2] and waveguide coupled detectors [3], are being developed in an integrated optics format to perform the Fourier transform signal processing function.[4,5] Coherent optical signal processing requires near diffraction-limited performance, and the integration of these elements on a single substrate requires compatible materials-processing technology. For compactness and wavelength stability, a distributed-feedback electron injection laser is preferred. Economics, alignment stability, and small size compel the use of a single substrate which requires lenses of comparatively small f-number and reflectors for folding of the optical system so as to be contained within the available substrate area.

Two waveguide-material structures are receiving attention.[6] They are (1) in- or out-diffused $LiNbO_3$ waveguide [7] because of its low-loss and because of large piezoelectric coupling which leads to efficient wideband surface elasto-optic interactions and (2) Corning 7059 glass waveguide on

thermally-grown SiO_2 on silicon because of minimum cost considerations where sputtered ZnO is employed as the piezoelectric to launch Rayleigh waves.[8-10]

WAVEGUIDE LENS CONSIDERATIONS

The relatively large refractive index of $LiNbO_3$ and the lack of thin-film materials with substantially larger index forces the application of geodesic lenses with $LiNbO_3$. Geodesics employ curved surface topology which alters the propagation length because rays propagate according to Fermat's principle.[11-13] These surfaces do not conform to the normal concept of an integrated format; however, simple spherical depressions in the substrate are easily fabricated as exemplified by bifocal glasses. Fortunately, metal in- or out-diffusion on $LiNbO_3$ leads to low-loss waveguide with minimum scattering, the latter of which may compromise the transform's resolution and/or dynamic range. Experimental spheric depression geodesic lenses are illustrated in Figure 1, together with use of two lenses as a beam expander. Corning 7059 waveguide is employed on the thermally-grown oxide as the isolation layer on the silicon substrate. Three rays traversing the beam expander are shown with scattering at the sharp geodesic edges. Radiation (6328Å) traverses the sharp geodesic edge because of the inherent radius due to the thermal oxide growth. Mode conversion and scattering at the sharp planar-curved surface intersection can be minimized by a toroidal lip.[14]

Spherical geodesic lenses exhibit spherical and curvature of field aberrations, the former of which can be corrected and the latter is of no consequence to the Fourier transform. Spiller and Harper [15] have shown that use of a thin-film additional layer coincident with the geodesic can suppress the spherical aberration. Southwell [16] has shown that a toroidal lip may be used to reduce the spherical aberration. Computed ray traces through a spherical geodesic, with and without a toroidal lip, are shown in Figure 2 using Southwell's procedure. Vahey and Wood [17] have shown that the oblate spheroid can also be used to correct the spherical aberration. Perfect geometrical focusing can be achieved with the Rinehart[18]-Luneburg aspheric geodesic surface which focuses on the edge. For an arbitrary focal length, Morgan [19] has generalized the Luneburg class [20] of inhomogeneous lenses, and Southwell [16] has computed its geodesic analog. In general, the aspheric configurations are difficult to generate, polish sufficiently, and test when compared with spherics.

Spheric geodesic lenses have been fabricated using Ti-indiffused waveguide on $LiNbO_3$, Ag^+ion-exchange in glass, thermally-oxidized Si, and anodized GaAs substrates. Measured diffraction patterns clearly show evidence of spherical aberration and scattering due to less-than-perfect polish in and at the edge of the geodesic.

Thermally-grown SiO_2 on Si has yielded the smoothest low-scattering, low-loss substrate surface for the deposition of low-loss Corning 7059 waveguide with refractive elements. The loss of this waveguide can be in the 0.1-0.5 dB/cm range. The low cost of Si wafers with sufficient dimensions and the current mature processing technology of Si together with the fact that the optical circuit can be integrated with its electronic counterpart provides the stimulation for its exploitation. Tantalum pentoxide and Nb_2O_5 have been employed to form homogeneous and inhomogeneous thin-film lenses and lens systems. Their losses are in the 0.5-3 dB/cm range depending upon the deposition process. The larger value is usually obtained for very thin layers over Corning 7059, and the lower value may be obtained when immersed.

The cleavage of single-crystal Si can extend through the isolation and waveguide layers to form perfect reflectors, so as to permit folding of the optical system. A protective layer superstrate remains to be identified which will be probably an organic deposited from solution.

Because the waveguide effective refractive index is related to the film thickness, it is possible to create both homogeneous and inhomogeneous refractors using homogeneous materials. The maximum/minimum ratios of effective refractive indices are typically in the range of 1.4-0.7. The latter arises when the ambient waveguide is dense and the lens element thickness is reduced. Thus, it is possible to create positive or negative waveguide lens elements using either convex or concave interfaces. We avoid the homogeneous thin-film refractors because it is difficult to produce optically smooth interfaces lithographically.

The circular-symmetric inhomogeneous refractor due to Luneburg [20] has been demonstrated in optical thin films.[1,21] Interest in the Luneburg lens arises because it is free of all aberrations except curvature of field and because of its simplicity of fabrication as a thin-film waveguide structure. A Luneburg lens will form perfect geometric images of two given

concentric circles on each other,[19] and, if one is at infinity, the lens will focus a collimated beam from any direction on the opposite edge. This circular symmetry is of particular interest to integrated optics where the substrate area is limited because folding of the optical axis may use the same lens for several purposes.

Southwell [22,23] has developed a numerical technique for ray tracing through inhomogeneous, circular-symmetric, thin-film waveguide, generalized Luneburg lenses. Two examples are illustrated in Figure 3 for the "classic" [20] and the generalized Luneburg lens for Morgan's parameter S=2 [19]. Southwell's numerical procedure determines the ray intercept and uses Hamilton's theory to extract the pupil function phase error followed by the Fourier transform to determine the intensity diffraction pattern. The technique yields diffraction-limited results in the Hewlett Packard 9830A calculator. Computations and experiments show that errors in deposition time (waveguide thickness) lead to the defocused aberration which may be corrected. Errors of the waveguide lens radial refractive index profile may, thus, be traced to the resulting diffraction pattern and to the mask which shapes the lens deposition profile.

Generalized Luneburg lenses [19] have been fabricated with f-numbers of 0.5 (classical) to greater than 10 using a Ta_2O_5 overlayer, underlayer, or interleaved within the Corning 7059 waveguide. The interleaved symmetrical structure is preferred to suppress waveguide mode conversion as opposed to the overlay or underlay structure. Luneburg lenses with f-numbers greater than 6 have been realized using "all" 7059 thin films. These lenses have been formed by RF sputtering [24] from a wide-angle source through a conical mask [21]. In general, when the cone angle is reduced and the maximum thickness is reduced, an increase of focal length is obtained. The mask, to realize the required inhomogeneous lens profile, can be determined effectively from molecular geometric optics for the deposition process using the mask to control shadowing.

The operation of two thin-film overlay Ta_2O_5 Luneburg lenses as a beam expander (X3) is shown in Figure 4 where the full aperture of the expander lens is uniformly illuminated in one photograph, and a single ray is employed in the other to discern mode conversion in the expander overlay lens. Unfortunately, the effect of substrate damage extending into the

thermally-grown SiO_2 is apparent near the focus of the expansion system. Continuous power-handling capacity of Corning 7059 waveguide on thermally-grown SiO_2 at the focus is greater than 0.4×10^6 watts/cm^2. Damage due to attachment and detachment of coupling prisms prior to this photography is evident in both the input and output. The throughput exiting the Si wafer edge scattered from black paper is also evident. Control of lens position and thickness yields a collimated beam. The single 6328Å ray trace in Figure 4 enters the expansion lens as the TE_0 mode where it is partially converted to the TE_1 mode. After this mode traverses the expansion lens, it is reconverted to the TE_0 mode, so that two separate rays continue through the remainder of the expansion system as TE_0 modes.

A typical measured diffraction pattern of a generalized Luneburg lens, like the objective in Figure 4, is illustrated in Figure 5. Its beamwidth, 3 dB, is 5μ. Uniform illumination was employed and, thus, the increase of side lobe level and null fill-in is indicative of an error in the lens thickness profile, producing a $\pi/2$ quadratic phase error. The asymmetric wide angle side lobe can be traced to a Mie scatter in the lens.

CONCLUSIONS

A thin-film waveguide Luneburg lens is considered the most viable planar approach based upon the use of oxides; and when high refractive-index substrate materials must be employed, the geodesic becomes a feasible alternative. Accurate realization of the required Luneburg lens profile and correction of geodesic aberrations is continuing to receive attention. Further effort to reduce Rayleigh and Mie scattering in the waveguide is required because it limits the resolution and dynamic range of the Fourier transform.

ACKNOWLEDGMENTS

The research reported herein is supported by United States Air Force Avionics Laboratory; Dayton, Ohio. Use of ray trace results due to W. H. Southwell are gratefully acknowledged. Deposition of thin-film Luneburg lenses and characterization are due to R. L. Davis and for the geodesic lenses are due to V. G. Kreismanis. Stimulation discussions of Mr. M. C. Hamilton, U. S. Air Force Avionics Laboratory, are gratefully acknowledged.

* Research supported in part by Air Force Avionics Laboratory; Dayton, OH

REFERENCES

1. D. B. Anderson, R. L. Davis, J. T. Boyd and R. R. August: "Comparison of Optical-Waveguide Lens Technologies," IEEE J. Quantum Electronics, QE-13, 4, p.275 (April 1977)

2. C. S. Tsai, M. A. Alkaider, L. T. Nguyen and B. Kim: "Wide-Band Guided-Wave Acoustooptic Bragg Diffraction and Devices Using Multiple Tilted Surface Acoustic Waves," IEEE 64, 3, p.318 (March 1976), also Y. Omachi: "Acousto-Optical Light Diffraction in Thin Films," J. Appl. Phys. 44, 9, p.3928 (September 1973)

3. J. T. Boyd and C. L. Chen: "Integrated optical silicon photodiode array," Appl. Opt. 15, 6, p.1389 (June 1976)

4. M. C. Hamilton and D. A. Wille: "Acousto-Optic Diffraction in Optical Waveguides," *Digest of Technical Papers Topical Meeting on Integrated Optics*, New Orleans, LA, p. WA8-1, (January 1974)

5. D. B. Anderson, R. L. Davis, J. T. Boyd and R. R. August: "An Integrated-Optical Approach to the Fourier Transform," IEEE J. Quantum Electronics QE-13, 4, p.268 (April 1977)

6. M. C. Hamilton, D. A. Wille, and W. J. Miceli: "An Integrated Optical RF Spectrum Analyzer," *IEEE Trans. Sonics Ultrasonic Sym.*, Annapolis, MD.

7. I. P. Kaminow and J. R. Carruthers: "Optical Waveguiding Layers in $LiNbO_3$ and $LiTaO_3$," Appl. Phys. Lett. 22, 7, p.326, (April 1973), also R. V. Schmidt, I. P. Kaminow: "Metal-Diffused Optical Waveguides in $LiNbO_3$," Appl. Phys. Letter 25, 8, p.458 (October 1974)

8. F. S. Hickernell: "Zinc-Oxide Thin-Film Surface-Wave Transducers," Proc. IEEE 64, 5, p.193 (May 1976)

9. N. Chubachi, J. Kushibiki and Y. Kibuchi: "Monolithically Integrated Bragg Deflector for an Optical Guided Wave Made of Zinc-Oxide Film," Electron. Lett. 9, 10, p.193 (May 1973)

10. K. W. Loh, W. S. C. Chang, W. R. Smith and T. Grudkowski: "Bragg Coupling Efficiency for Guided Acoustooptic Interaction in GaAs," Appl. Opt. 15, 1, p.156 (January 1976)

11. T. van Duzer: "Lenses and Graded Films for Focusing and Guiding Acoustic Surface Waves," Proc. IEEE 58, 8, p.1230 (August 1970)

12. G. C. Righini, V. Russo, S. Sottini and G. Toraldo di Francia: "Geodesic Lenses for Guided Optical Waves," Appl. Opt. 12, p1477 (July 1973)

13. C. M. Verber, D. W. Vahey and V. E. Wood: "Focal Properties of Geodesic Waveguide Lenses," Appl. Phys. Lett. 28, 9, p.514 (May 1976)

14. V. E. Wood: "Effects of Edge-rounding on Geodesic Lenses," Appl. Opt. 15, 11, p.2817 (November 1976)

15. E. Spiller and J. S. Harper: "High Resolution Lenses for Optical Waveguides," Appl. Opt. 13, 9, p.2105 (September 1974)

16. W. H. Southwell: "Geodesic Optical Waveguide Lens Analysis," J. Opt. Soc. Am. 67, 10, p.1293 (October 1977)

17. D. W. Vahey and V. E. Wood: "Focal Characteristics of Spheroidal Geodesic Lenses for Integrated Optical Processing," IEEE J. Quantum Electronics, QE-13, 4, p.129 (April 1977)

18. R. F. Rinehart: "A Solution of the Problem of Rapid Scanning for Radar Antennae," J. Appl. Phys., 19, 9, p.860 (September 1948)

19. S. P. Morgan: "General Solution of the Luneburg Lens Problem," J. Appl. Phys., 29, 9, p.1358 (September 1958)

20. R. K. Luneburg: *MATHEMATICAL THEORY OF OPTICS*, University of California Press 1964 (Reprint of Notes Brown University Press 1944)

21. F. Zernike: "Luneburg Lens for Optical Waveguide Use," Opt. Commun., 12, 4, p.379 (December 1974)

22. W. H. Southwell: "Inhomogeneous Optical Waveguide Lens Analysis," J. Opt. Soc. Am., 67, P.8 (August 1977)

23. W. H. Southwell: "Index and Waveguide Thickness Profiles for Generalized Luneburg Lenses," J. Opt. Soc. Am., 67, p. 8 (August 1977)

24. D. H. Hensler, J. D. Cuthbert, R. J. Martin, and P. K. Tien: "Optical Propagation in Sheet and Pattern Generated Films of Ta_2O_5," App. Opt., 10, 5, p.1037 (May 1971)

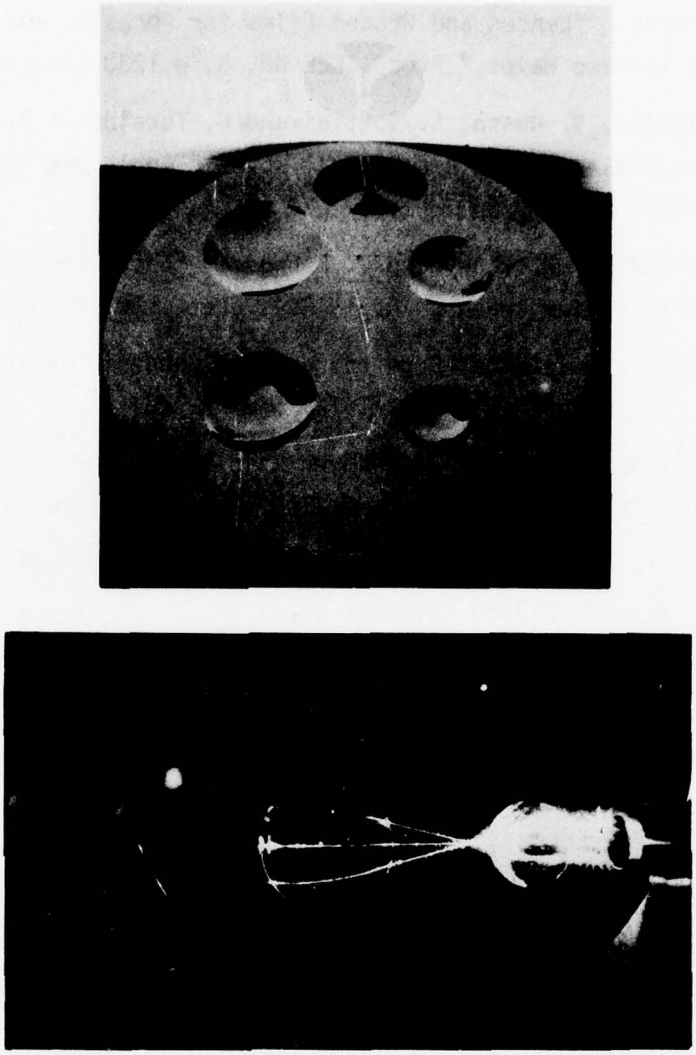

Figure 1. Concave Geodesic Lenses (a) Ground and Polished in a Si Substrate Thermally-Oxidized With Sputtered Corning 7059 Waveguide and (b) Operation of Two Geodesic Lenses as a Beam Expander Using 6328Å Radiation.

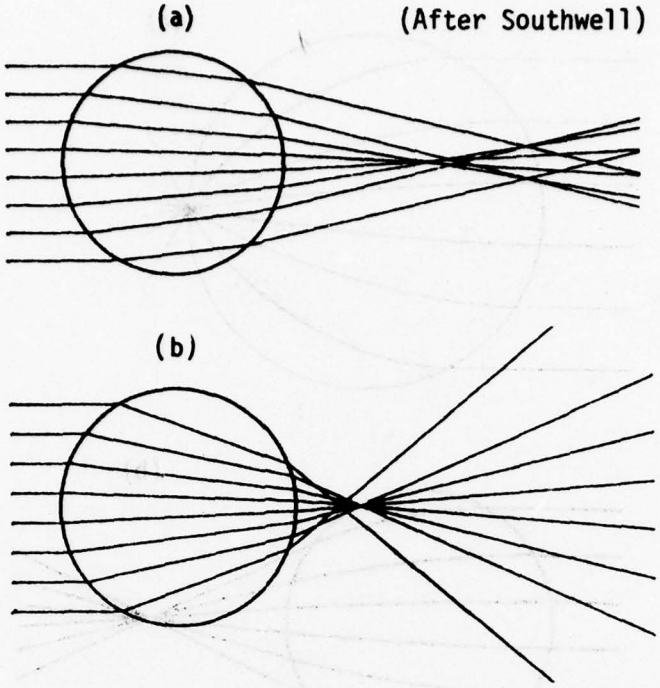

GEODESIC LENS PARAMETERS	(a)	(b)
Angular Radius	39.4°	39.4°
Geodesic Radius of Curvature	1.575	1.618
Toric Rim Radius	0	.1027
Lens Radius in Waveguide Plane	1.0000	1.0634
Toric Angle α	.6876	.6660
Paraxial Focal Length	2.211	1.597

Figure 2. Calculated Ray Traces Through Spheric Geodesic Lens Having (a) Sharp Edge and (b) Toroidal Lip for Parameters Listed.

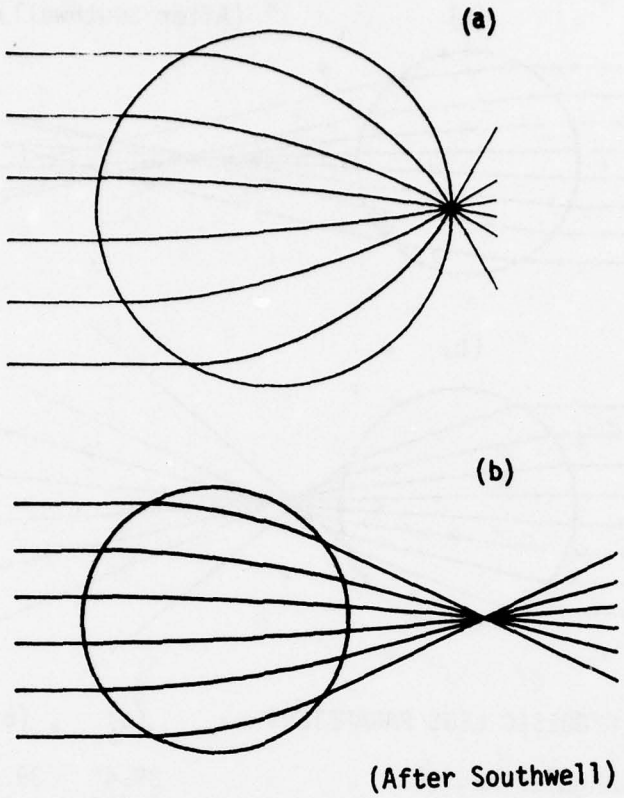

Figure 3. Calculated Ray Traces Through Luneburg Lenses for (a) "Classic" S=1, and (b) Generalized S=2 Derived From Waveguide Thickness Profiles Yielding Diffraction-Limited Results.

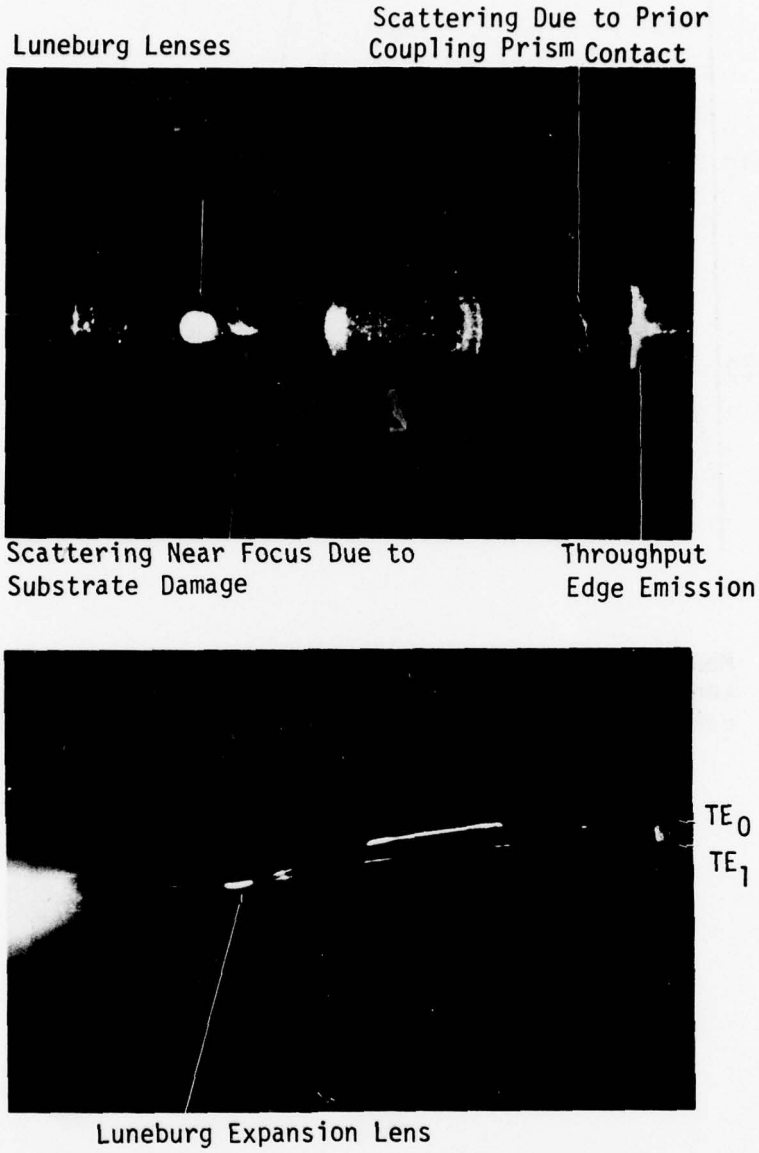

Figure 4. Luneburg Lens Beam Expander (X3) Employing Ta_2O_5 Lenses With Corning 7059 Waveguide on Thermally-Oxidized Si (a) Operation of Beam Expander Showing Lens Scatter, Defects and Throughput, and (b) a Single Ray Trace Through Same Beam Expander Showing Mode Conversion in Expansion Lens but With Both Rays Traversing the Remainder of the Waveguide as TE_0 Modes.

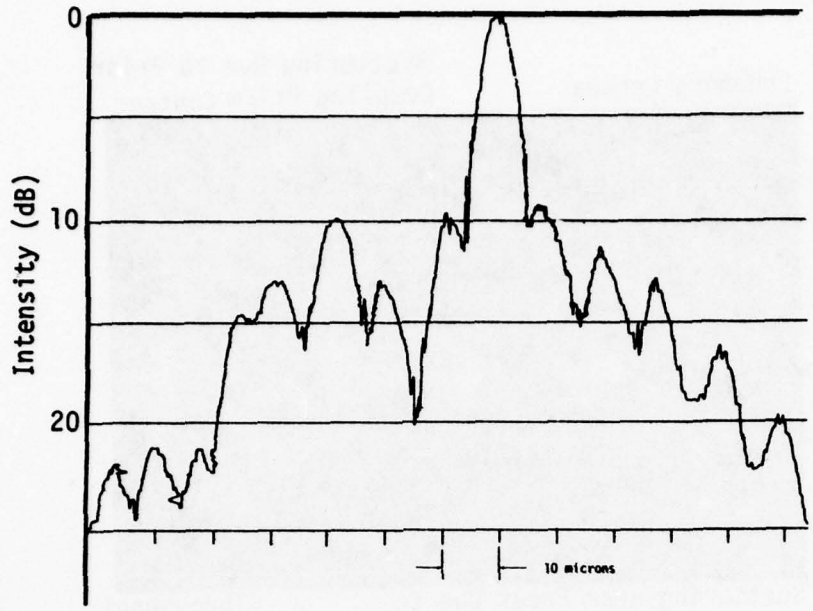

Figure 5. Measured Intensity Diffraction Pattern of Luneburg Lens, Focal Length 12mm and Uniform Illuminated Aperture 5mm Yielding 5μ Beam Width at Half-Power.

APPENDIX B

REPRINT PRESENTED AT THE TOPICAL MEETING ON INTEGRATED AND GUIDED WAVE OPTICS
JANUARY 16, 1978, SALT LAKE CITY, UTAH

MASK SYNTHESIS FOR DIFFRACTION-LIMITED WAVEGUIDE LUNEBURG LENSES*

S. K. Yao
D. B. Anderson
C. M. Oania
V. G. Kreismanis

Electronics Research Center
Rockwell International
Anaheim, CA 92803

An integrated optical circuit for RF signal spectral analysis requires a near diffraction-limited lens to perform the Fourier transform.[1,2] A thin-film waveguide Luneburg lens using Ta_2O_5 in the lens region with Corning 7059 waveguide on thermally-oxidized silicon substrate[4] is a low-cost approach providing for integration with a surface elasto-optic spatial modulator and a waveguide coupled photodetector array in the substrate. Waveguide Luneburg lenses are formed by sputtering high-index films through a circular mask with a shaped edge.

The generalized Luneburg lens is free of all aberrations except for curvature of field. It is a circular-symmetric, inhomogeneous lens requiring a specific radial refractive index profile and, thus, a waveguide thickness profile. Southwell[5] has developed a convenient technique for gradient-index ray-tracing and has applied it to generalized Luneburg lenses[6] determining ray intercepts, the corresponding phase wavefront and the intensity diffraction pattern. This ray-tracing technique is sufficiently accurate to yield diffraction-limited results for the "true" radial profile when executed with an HP 9830 calculator. The practical problem addressed herein is the synthesis of the mask edge shape such as to yield film thickness profiles that operate as Luneburg lenses with near diffraction-limited performance.

* Research supported by Air Force Avionics Laboratory; Dayton, OH

A computational procedure has been developed to derive the film thickness profile sputtered through masks with shaped edge. It is assumed that the molecules behave like optical rays, that their source distribution from the target is Lambertian, and that the mean-free path length is greater than the mask dimensions; and, thus, the problem reduces to shadowing from an incoherent extended source. The circular mask edge is simulated by an interconnected series of conical sections. The resulting radial thickness profile is converted into the effective waveguide refractive index profile for the designated mode kind and order. Southwell's ray-tracing program is then employed to evaluate the diffraction pattern in the focal line. Thus, knowing the effect of deviations from the "true" profile and recognizing the mask shadowing effects, it is possible to approximate the required "true" profile as demonstrated by the examples to be cited.

These procedures have been employed to derive the mask shape edge for thin-film waveguide Luneburg lenses having f-number of 4, which experimentally yields near diffraction-limited performance. The mask shape edge for our sputtering system geometry and the resulting calculated thickness profile is depicted in Figure 1 including an insert showing the measured edge profile. Using this radial thickness profile as an input to Southwell's ray-tracing program,[5] the resulting calculated ray traces, wavefront phase, and intensity diffraction pattern are shown in Figure 2. Note that the aperture has been limited, and that the simulation has allowed a wavefront phase error which does not seriously compromise the diffraction pattern. The lens employs an 8.2mm diameter overlay with thickness of 3000Å at the center on a Corning 7059 waveguide for a thickness of 4500Å.

The measured diffraction pattern for this Luneburg lens thickness profile, using a 2mm Gaussian input beam at 6328Å, is depicted in Figure 3 using a pair of prism couplers, an F/3.5 Tropel diffraction-limited relay lens providing a magnification of 2.5, and a traveling slit detector of 1μ width. The diffraction-limited beamwidth in the waveguide should be 2.2μ at the $1/e^2$ level; whereas, the measured width is 3.3μ. It should be noted that the relay lens diffraction pattern is convolved with the Luneburg lens diffraction pattern limiting the observed result to 3μ. The high level first side lobe is due to spherical

AD-A062 933 ROCKWELL INTERNATIONAL ANAHEIM CA ELECTRONICS RESEAR--ETC F/G 20/6
WAVEGUIDE OPTICS FOR COHERENT OPTICAL PROCESSING.(U)
JUN 78 D B ANDERSON , R R AUGUST, S K YAO F33615-77-C-1017

UNCLASSIFIED C77-210.13/501 AFAL-TR-78-83 NL

3 OF 3
AD
A062933

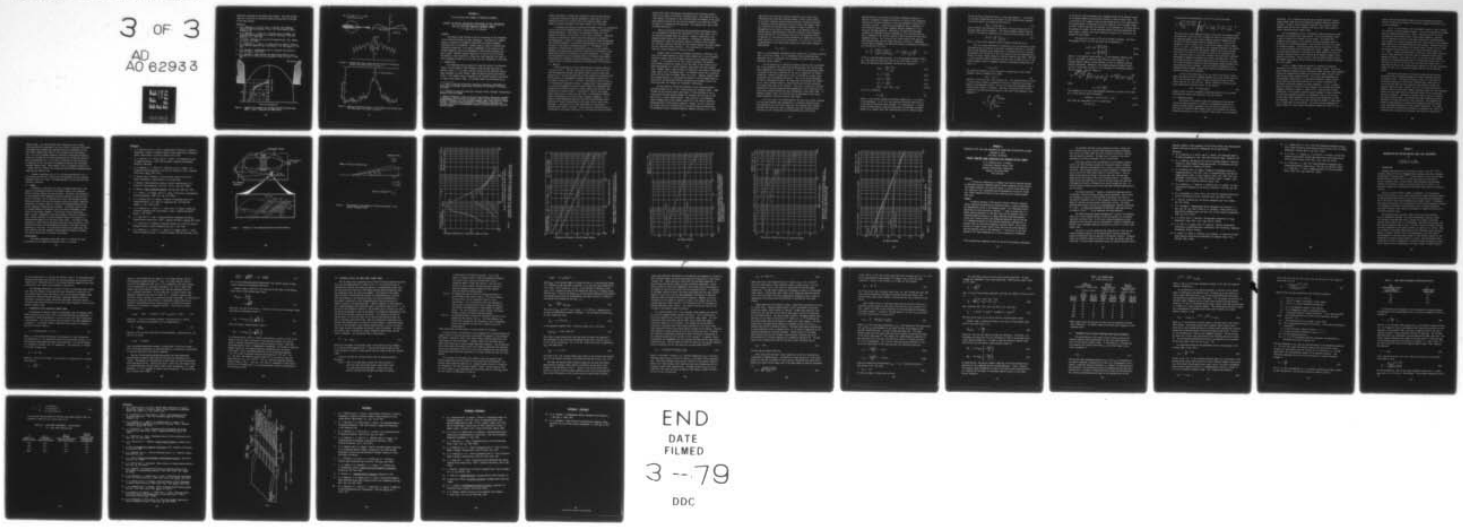

END
DATE
FILMED
3 -- 79
DDC

aberration introduced by the output prism coupler. The large shoulder lobes are in part due to scattering effects, particularly at the edge of the input coupler.

References

1. M. C. Hamilton, D. A. Wille, and W. J. Miceli, "An Integrated Optical RF Spectrum Analyzer," Proc. IEEE 1976 Ultrasonic Symp., Annapolis, MD.
2. D. B. Anderson, J. T. Boyd, M. C. Hamilton and R. R. August, "An Integrated-Optical Approach to the Fourier Transform," IEEE JQE, QE-13, No. 4, p. 268, 1977.
3. F. Zernike, "Luneburg Lens for Optical Waveguide Use," Opt. Commun., Vol. 12, p. 379, 1974.
4. D. B. Anderson, R. L. Davis, J. T. Boyd and R. R. August, "Comparison of Optical Waveguide Lens Technologies," IEEE JQE, QE-13, p. 275, 1977.
5. W. H. Southwell, "Inhomogeneous Optical Waveguide Lens Analysis," JQSA, Vol. 67, p. 1004, 1977.
6. W. H. Southwell, "Index Profiles for Generalized Luneburg Lenses and Their Use in Planar Optical Waveguides," JQSA, Vol. 67, p. 1010, 1977.

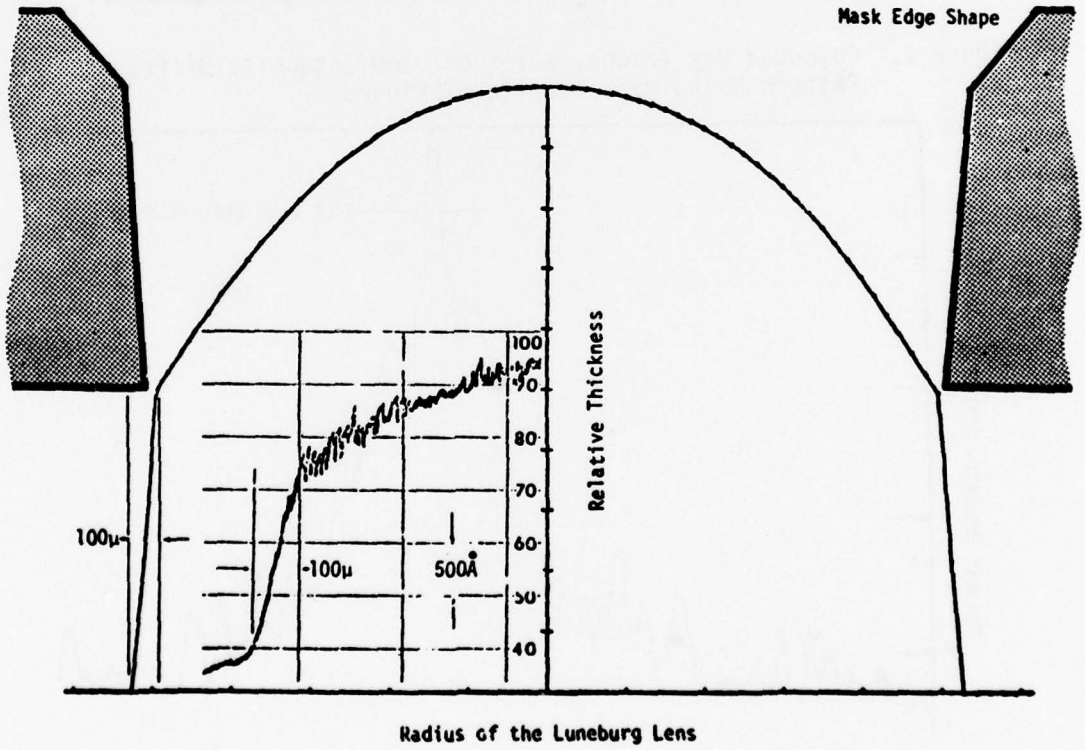

Figure 1. Computed F/4 Luneburg Lens Thickness Profile with Mask Edge Shape. Insert: Measured Lens Edge Profile.

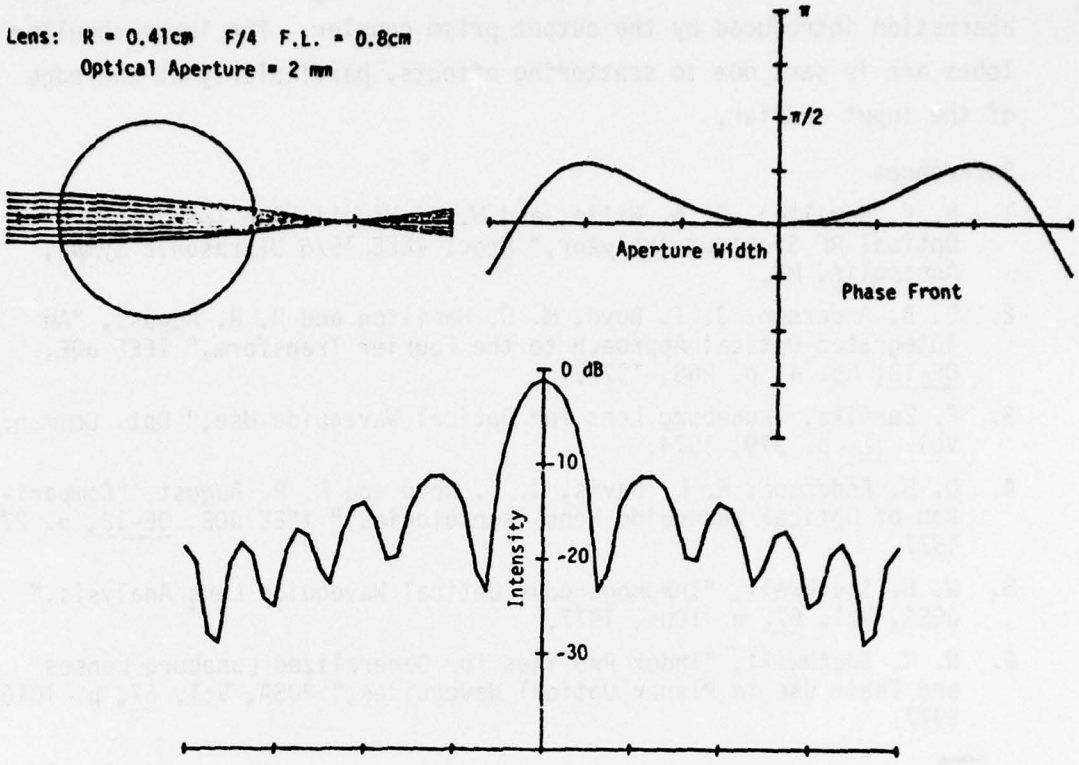

Figure 2. Computed Ray Traces, Wavefront and Intensity Diffraction Pattern Using Mask Profile of Figure 1.

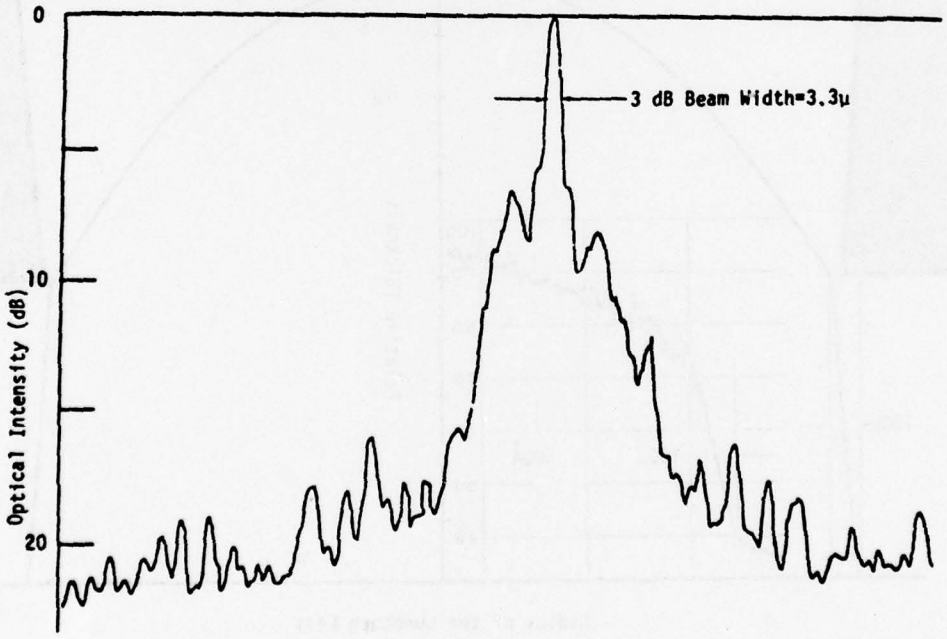

Figure 3. Measured Diffraction Pattern of F/4 Luneburg Lens Derived From Mask Edge Shape Illustrated in Figure 1.

APPENDIX C

TO BE PUBLISHED IEEE JOURNAL OF QUANTUM ELECTRONICS

EFFECT OF OPTICAL WAVEGUIDE SCATTERING ON THE INTEGRATED OPTICAL SPECTRUM ANALYZER DYNAMIC RANGE*

J. T. Boyd and D. B. Anderson

ABSTRACT

The dynamic range limited by optical scattering of the integrated optical spectrum analyzer has been considered. Calculations of dynamic range as a function of waveguide attenuation and surface roughness characteristics are presented. Dynamic range is found to decrease with increasing attenuation, to be nearly independent of the nature of the surface roughness, and to be independent of the Fourier transform lens focal length. Adjacent channel rejection is found to fall-off slowly. The effect of lens scattering is shown only to be important for cases in which waveguide scattering is very small and lens scattering is very high.

I. INTRODUCTION

The integrated optical approach to spectrum analysis of electronic signals in the hundreds of MHz frequency range has been described in previous papers.[1,2,3] In these previous discussions the important performance parameter of signal dynamic range has been discussed only qualitatively. This dynamic range is expected to be limited by optical scattering or sensor array dynamic range. We consider herein the limitation due to

---

J. T. Boyd is with the Solid-State Electronics Laboratory, Department of Electrical and Computer Engineering, University of Cincinnati, Cincinnati, Ohio 45221.

D. B. Anderson is with the Electronics Research Center, Rockwell International, Anaheim, California 92803

* Research sponsored in part by the Air Force Avionics Laboratory, Rockwell International, and for one of the authors (JTB), by the Air Force Office of Scientific Research, Air Force Systems Command, USAF, under Grant No. AFOSR 76-3032. The united States Government is authorized to reproduce and distribute reprints for Governmental purposes notwithstanding any copyright notation hereon.

optical scattering. Although some progress has been realized recently in reducing scattering in optical waveguides,[4] scattering is still expected to be more of a limiting factor than detector dynamic range. Numerical results presented in this paper support this conclusion.

To evaluate the effect of scattering on dynamic range in a configuration such as that of the integrated optical spectrum analyzer, a knowledge of scattering behavior in the plane of the waveguide surface due to an optical wave having a finite width in this plane is required. Theoretical analyses of scattering in optical thin-film waveguides are generally two-dimensional, in that it is assumed that the optical wave and waveguide have uniform properties in the direction perpendicular to the propagation direction in the plane of waveguide surface.[5,6] The emphasis is on obtaining a solution which is sufficiently simple so as to be readily amenable to an engineering calculation, rather than on performing a three dimensional analysis of scattering in optical waveguides. It is hoped that the numerical results presented herein will stimulate experimental investigation of scattering in optical waveguides in the plane of the surface similar to previous experimental two-dimensional investigations.[7]

II. ANALYSIS

A chip configuration of the integrated optical spectrum analyzer is shown in Fig. 1. The lens regions are circular in view of the fact that the generalized Luneburg and geodesic types currently appear most promising.[8,9] The size and positions of these regions are consistent with desired values of time-bandwidth products and frequency resolution.[2,3] The compact structure in Fig. 1 includes a semiconductor laser coupled to a silicon optical waveguide structure. Coherent laser light propagating in a thin-film waveguide is expanded and collimated by a waveguide lens system prior to being incident on a surface elastic wave which has been excited by the incoming signal. Diffraction of light by the surface elastic wave occurs in such a way that light is diffracted at different angles corresponding to different signal frequency components. For a range of signal frequencies and wave intensities the diffracted light amplitude is linearly proportional to the signal surface elastic wave amplitude. A waveguide lens is then positioned so as to perform a one-dimensional Fourier transform. Signal spectral information which is represented by the angular composition of light emerging from the surface

elastic wave region then becomes represented by the transverse spatial variation of light in the Fourier transform plane. The intensity of the light spatial distribution in the transform plane corresponds to the signal power density spectrum and can then be converted to an electrical signal by means of an integrated slab waveguide - CCD imaging array such as that discussed previously.[10]

Optical scattering affecting spectrum analyzer performance occurs in the waveguide surrounding the lens region, in the lens region, and in the transition between these two regions. However, scattering in the waveguide region adjacent to the detector is expected to dominate other contributions in that the acceptance angle of a detector array element for scattered radiation diminishes as the distance between the array element and the scattering center increases. This expectation is verified by numerical results presented in the next section.

Dynamic range as limited by waveguide scattering is defined as the ratio of the power reaching a single sensor element for a single frequency electronic signal input to the power scattered to the adjacent sensor element. It is assumed that the focal length, aperture, and detector array element spacing are chosen so that the width of the focused optical beam corresponding to a single frequency input equals the array element size. Dynamic range is thus defined as a measure of the number of resolvable signal levels for a narrowband input. For wideband signals more scattering occurs and thus fewer resolvable levels will exist. However, dynamic range for spectrum analysis is conventionally defined in the narrowband sense as above, while the additional effects associated with wideband signals are classified under the category of intersymbol interference.

We thus begin by considering operation of the integrated optical spectrum analyzer of Fig. 1 for a single electronic frequency input. Light incident on the surface elastic wave region is thus deflected at only a single angle and upon passage through the transform lens arrives for the most part at a single sensor element. Some light will reach adjacent sensor elements due to the inherent truncation in the Fourier transform associated with a finite optical aperture. However, we will assume for the present that for a suitable optical transverse beam variation along the waveguide surface (truncated Gaussian, Hamming, Hanning, etc.), side-

lobe levels will be minimal and thus essentially all of the optical information other than that scattered reaches a single sensor element. In an actual integrated optical spectrum analyzer it would be desirable if scattering could be suppressed to such an extent that dynamic range was limited by the sidelobe levels inherent in signal truncation. In propagating from the Fourier transform lens to the detector array the optical beam is attenuated due to interface scattering, bulk scattering, and bulk absorption. As scattering occurring at the waveguide surface is dominant in a high quality optical waveguide, we assume that all waveguide attenuation is due to this contribution. The ratio R_1 of the total scattered power to the signal power reaching the single sensor element is approximately

$$R_1 = e^{\alpha_s L} - 1 \tag{1}$$

where α_s is the waveguide attenuation factor (power) due to surface scattering and L is the focal length. In (1) variations in path length have been neglected, but (1) is expected to be reasonable for small scattering and moderately large f-numbers.

Of the fraction R_1 of radiation scattered, portions will be scattered out of the waveguide, into higher-order waveguide modes, and into the same mode propagating in a different direction. A high quality waveguide surface is assumed so that back scattering will be small in comparison to forward scattering. Radiative scattering will not be collected by a sensor array integrated into the waveguide structure.[10] This is one of the advantages of such an integrated structure. We assume that the waveguide will support only a single transverse mode of a given polarization so that scattering into higher-order modes is not possible. Thus, only a fraction of radiation scattered into the same waveguide mode propagating in other directions will reach sensor elements besides the one corresponding to the signal input. To determine dynamic range, this fraction must be determined for the sensor element adjacent to the one receiving signal power.

As a first step in this determination, the ratio R_2 of power scattered into the same waveguide mode propagating in a different direction within the waveguide to the sum of this power plus the scattered field radiated from the guide having the same k_y component along the waveguide surface transverse to the incoming beam can be determined from an intuitive

generalization of the coupling coefficients determined by Marcuse.[5,6] Marcuse's treatment of waveguide scattering is limited to two dimensions, ignoring the transverse dimension y along the waveguide surface which is of present interest. Scattering with propagation vector components in this direction require surface roughness spectral components in this direction for phase matching. Intuitively, we expect that the power scattered with propagation vector components k_y will be proportional to the k_y component of the spectral density of the y variation of the surface roughness function. For a given k_y this factor should be the same for both radiation modes and the single slab mode so that R_2 is independent of this spectral component and determined directly from Marcuse's[6] equations (9.4.10) and (9.4.11) to be:

$$R_2 = \left\{ 1 + \frac{4(\kappa d/2 + \kappa/\alpha_3)\,\Delta\eta}{\pi(n_2^2+3)\,\cos^2(\beta d-\phi_1)} \quad \tan^{-1}\left(\frac{2\Delta\eta}{\Delta\eta^2 + n_g^2 - 1}\right)\right\}^{-1} \tag{2}$$

In (2) d is the waveguide thickness, n_2 is the waveguide refractive index, n_g is the effective refractive index of the lowest order TE mode, κ, α_3, β and ϕ_1 are waveguide mode parameters defined by the equations:[11]

$$\tan\beta d = \frac{\beta(\alpha_1 + \alpha_3)}{\beta^2 - \alpha_1\alpha_3}\ , \tag{3-a}$$

$$\beta^2 + \kappa^2 = k_o^2 n_2^2\ , \tag{3-b}$$

$$-\alpha_3^2 + \kappa^2 = k_o^2 n_3^2\ , \tag{3-c}$$

$$-\alpha_1^2 + \kappa^2 = k_o^2 n_1^2\ , \tag{3-d}$$

$$\tan\phi_1 = \alpha_1/\beta,\ \tan\phi_3 = \alpha_3/\beta. \tag{3-e,f}$$

In (2) $\Delta\eta$ is defined as

$$\Delta\eta = \frac{1}{k_o \ell}\ , \tag{4}$$

where ℓ is the surface roughness correlation length and $k_o = 2\pi/\lambda$ where λ is the wavelength. In (3) n_1 is the substrate refractive index while n_3 is the overlay refractive index (assumed = 1 in calculations). In determining (2) from Marcuse's coupling coefficients,[6] we employed an approximation to an integral which sums contributions from all radiation modes.

We have previously described details of this approximation.[12] In deriving (2) we have followed Marcuse and assumed that the random surface roughness can be described by the autocorrelation function

$$R(u) = \sigma^2 \exp(-|u|/\ell) \tag{5}$$

where u measures the separation of two points along the surface and σ^2 is the mean square surface roughness. The surface roughness spectral density $|G(\eta)|^2$ is the fourier transform of the autocorrelation function, given as

$$|G(\eta)|^2 = \frac{2\sigma^2}{k_o} \frac{\Delta\eta}{\eta^2+(\Delta\eta)^2} , \tag{6}$$

where η is the surface roughness spatial frequency normalized to k_o.

Thus far we have determined an expression R_1 for the fraction of light scattered and R_2 the fraction of the total scattered field that is scattered into the same waveguide mode propagating in a different direction. We must now determine the fraction R_3 of the field scattered into the waveguide which reaches the sensor element adjacent to the one receiving the signal. Defining Θ as the scattering angle as measured from the z axis as shown in Fig. 2, the surface roughness spatial frequency required to phase-match scattering at an angle Θ is

$$\eta = 2n_g \sin\frac{\Theta}{2} \tag{7}$$

The scattering intensity of this direction is proportional to the surface roughness spectral component $S(\Theta)$, where

$$S(\Theta) = |G(\eta)|^2 \tag{8}$$

keeping in mind that Θ and η are related by (7). The scattered field arriving at a given sensor element is composed of the sum of radiation from various points on the waveguide surface. For each such point the acceptance angle of a given sensor element is different. With this in mind the ratio of field scattered to the adjacent sensor element to the total field scattered in the waveguide is

$$R_3 = \frac{\int_0^L \int_{\Theta_1(z)}^{\Theta_2(z)} S(\Theta)\,d\Theta\,dz}{L \int_{-\pi/2}^{\pi/2} S(\Theta)\,d\Theta} \tag{9}$$

In (9) $[\theta_1(z), \theta_2(z)]$ represents the acceptance angle of the adjacent sensor for scattered radiation originating a distance z from the focal plane. The y variation of this angular range has been neglected as a first approximation. This approximation is expected to be valid except for small f-number lenses. At first it would seem that the integral in the numerator of (9) would need to be weighted to account for the decreased width of the beam approaching the focal region. However, the field intensity increases so as to exactly compensate for this effect.

The expression R_3 give in (9) can be further evaluated. Utilizing the geometry in Fig. 2, $\theta_1(z)$ and $\theta_2(z)$ can be expressed as

$$\theta_1(z) = \tan^{-1}\left(\frac{ns - s_o/2}{z}\right) \tag{10-a}$$

$$\theta_2(z) = \tan^{-1}\left(\frac{ns + s_o/2}{z}\right) \tag{10-b}$$

where s is the detector array period, s_o is the elemental detector size, and n is the number of detectors away from the signal detector. To evaluate dynamic range as we have defined it, the n-1 adjacent detector would be considered. Generally, the acceptance angular interval $[\theta_1(z), \theta_2(z)]$ is quite small so that S( ) can reasonably be considered constant over this range. Thus (9) reduces to

$$R_3 = \frac{\sqrt{\Delta n^2 + 4n_g^2}}{2\pi L} \int_0^L \left[\frac{\Delta n}{\Delta n^2 + 4n_g^2 \sin^2 \frac{\theta_o}{2}}\right] \tan^{-1}\left(\frac{s_o z}{z^2 + n^2 s^2 - s_o^2/4}\right) dz \,, \tag{11}$$

where

$$\theta_o = \tan^{-1}\left(\frac{ns}{z}\right) \tag{12}$$

The integrand in (11) can be approximated accurately over most of the range of z in the interval [0,F] by assuming

$$\tan[\theta_2(z) - \theta_1(z)] \approx \theta_2(z) - \theta_1(z) \tag{13-a}$$

while over the range where (13-a) is significant

$$\tan \theta_o \approx \theta_o \quad . \tag{13-b}$$

Incorporating the approximations (13) into (11) gives the result

$$R_3 = \frac{\sqrt{s_o \, \Delta\eta \, \Delta\eta^2 + 4n_g^2}}{2\pi n_g^2 L} \int_0^L \frac{z^2}{\left[\frac{\Delta\eta^2}{n_g^2} \, z^2 + n^2 s^2\right]} \, \frac{z}{[z^2 + n^2 s^2 - s_o^2/4]} \, dz \, . \tag{14}$$

The second term in the integrand represents the effect of acceptance angle variation with z while the first includes the affect of the proportionality of scattering power to the surface roughness spectral component and the variation of the appropriate spectral component with z. A plot of the integrand in (14) is shown in Fig. 3 for the nth adjacent sensor element for n-1, 2, and 3. The magnitude of this integrand represents the relative scattering power received by the detector adjacent to the one receiving the signal as a function of the point of origin of the scattered radiation. Note that there is a position from which the scattering to adjacent photodetector elements originates which yields a maximum value. This is due to the variation in acceptance angle and by the increase in the angle of off-axis scattering required as the displacement between detector array and scattering center decreases. Note that peaks corresponding to the adjacent detector elements decrease with successive elements and that the maxima are progressively broadened.

In view of the definitions of R_1, R_2, and R_3, the ratio of optical power received by the first adjacent detector next to the signal receiving one to the received signal power is given by $R_1R_2R_3$ with each of these ratios given by (1), (2), and (14). Dynamic range DR as limited by waveguide scattering and defined earlier is thus given as

$$DR - -10 \log_{10}(R_1R_2R_3). \tag{15}$$

Dynamic range (limited by waveguide scattering) defined in (15) has been calculated and results are presented in the next section.

III. NUMERICAL RESULTS

The expression for dynamic range (15) determined in the previous section has been evaluated as a function of waveguide attentuation for typical spectrum analyzer parameters with the results plotted in Fig. 4. Note that, as expected, higher dynamic ranges are associated with smaller waveguide attenuation and thus situations in which there is less waveguide

acattering. Fig. 4 indicates that the use of smaller detectors lalows a larger dynamic range due to the decreased acceptance angle for scattered radiation. However, smaller detectors generally have a smaller device dynamic range and for such situations this may be the limiting factor in overall spectrum analyzer dynamic range.

For the parameters in Fig. 4 the dynamic range calculation has been repeated for different focal length lenses. The resulting dynamic range is nearly invarient with respect to focal length. For longer focal lengths we would expect R_3 to be smaller since the acceptance angle for scattering of the adjacent detector is much smaller over most of the range of scattering centers. Calculations agree with this expectation in that R_3 is seen to decrease with increasing focal length. However, this decrease is almost exactly offset by an increase in R_1 which measures the ratio of the total scattered field to that received by the detector element corresponding to the signal. The net result is that the product $R_1R_2R_3$ and thus the dynamic range remains nearly invarient with respect to Fourier transform lens focal length.

In Fig. 4 dynamic range was plotted as a function of waveguide attenuation for a fixed surface roughness correlation length. Since waveguide attentuation depends on both correlation length and mean square roughness, varying the attenuation and keeping the correlation length constant implies that the mean square roughness varies. Since these three parameters are interdependent, choosing one as a variable and keeping a second constant implies that the third varies with the first in order to maintain the functional relationship between the three parameters. In Fig. 5, dynamic range is plotted as a function of the reciprocal of the normalized surface roughness correlation length $\Delta\eta$, define in (4). Both the case in which attenuation is held constant with mean square roughness varying to maintain the functional dependence between it, attenuation, and $\Delta\eta$, and the case in which mean square roughness is held constant with attenuation variable are presented. The limit of very small correlation lengths or large values of $\Delta\eta$ is applicable to point defects. the nearly constant dependence of dynamic range on $\Delta\eta$ for constant attentuation coupled with curves in Fig. 4

clearly indicates that dynamic range varies with waveguide attenuation and very little with the nature of the surface roughness which gives rise to this attenuation.

In Fig. 6, the rejection ratio of adjacent channels in dB is plotted as a function of the nth adjacent channel. The curves correspond to a common value of waveguide attenuation of .1dB/cm, implying that the two curves correspond to two different values of mean square roughness. Rjection ratio is defined as the ratio of the power reaching the intended detector array element for a single frequency electronic signal input to the scattered power reaching the nth adjacent detector array element. Rejection ratio for n=1 is thus equal to the negative of dynamic range. We note in Fig. 6 that the rejection ratio drops faster for the large correlation length case ($\Delta\eta$ = .001). Surfaces characterized by localized or point defects thus give rise to slower decreased in rejection ratio as compared to those having smoother variations. Also shown in Fig. 6 is the locus of the sidelobe maxima for a truncated Gaussian beam in a diffraction limited system. We note that the rate of fall off for the long correlation length case is comparable to that for the sidelobe maxima, whereas for the small correlation length case this rate is much more gradual than that for the sidelobe maxima.

The previous calculations include only scattering contributions originating from the waveguide between the Fourier transform lens and the detector array. The question naturally arises as to the effect of scattering originating in the Fourier transform lens, particularly in view of the fact that the lens scattering rate generally exceeds the waveguide scattering rate. However, the lens is further away from the detector array so that detector element acceptance angles for lens scattering centers are much smaller than for scattering centers in the intervening section of waveguide. The effect of dynamic range is thus not as much as one might initially expect. We have used the same formalism previously described to include the effect of lens scattering. The waveguide lens region has been modeled as a region having waveguide properties similar to the surrounding waveguide but with a higher attenuation. This model should accurately characterize the effects of a geodesic lens, while, for a Luneburg lens, the model over-estimates the effects of scattering on

dynamic range. This over-estimate occurs because part of the light scattered within the waveguide in the lens region is scattered into higher order modes which radiate into the substrate at the termination of the lens region, whereas this effect is not included in the calculations. Fig. 7 is a plot of dynamic range as a function of waveguide attenuation. Curves are included for no lens scattering (similar to previous results), and for attenuations of 1.0, 3.16 and 10. dB/cm due to lens scattering. As expected, at very low values of waveguide scattering lens scattering dominates dynamic range. Note, however, that for waveguide attention of .1 dB/cm, only the 10 dB/cm lens scattering case noticeably degrades dynamic range and only then by 3 dB.

Computer evaluation of R_3 in (11) and the approximation of R_3 in (14) were carried out for a wide variety of parameters with very accurate agreement found in all cases. The approximations (13) are thus valid for practical situations.

IV. SUMMARY

An analysis of the effect of optical waveguide scattering in the plane of the waveguide surface on the dynamic range of the integrated optical spectrum analyzer has been performed. Initially, only scattering in the waveguide region between the Fourier transform lens and the focal plane is included. This is expected to be valid since acceptance angles become quite small for scattering centers outside this region. Numerical calculations of dynamic range as a function of waveguide attenuation and surface roughness properties were presented. The dynamic range is found to strongly depend on attenuation, but to be nearly independent of the nature of the surface roughness. Calculations indicate that dynamic range is nearly independent of the focal length of the Fourier transform lens. Channel rejection in the nth adjacent channel for variable n is determined and found to fall off quite slowly with n. The effect of lens scattering is numerically evaluated and shows that lens scattering is only important for cases in which waveguide scattering is very small and lens scattering is very high. This calculation confirms the expectations that only scattering from the waveguide region between the Fourier transform lens and the focal plane is of major significance.

ACKNOWLEDGMENT

The authors acknowlege discussions with M. C. Hamilton and some assistance with the computer calculations from J. A. Elliott.

REFERENCES

1. M. C. Hamilton and D. A. Wille, "Acousto-Optic Diffraction in Optical Waveguides," Digest of Technical Papers, Topical Meeting on Integrated Optics, New Orleans, Louisiana, January 21-24, 1974.

2. M. C. Hamilton, D. A. Wille, and W. J. Miceli, "An Integrated Optical RF Spectrum Analyzer," IEEE 1976 Ultrasonic Symposium Proceedings, Annapolis, Maryland.

3. D. B. Anderson, J. T. Boyd, M. C. Hamilton, and R. R. August, "An Integrated Optical Approach to the Fourier Transform," IEEE J. Quantum Electronics, QE-13, 268 (1977).

4. W. Stutius and W. Streifer, "Silicon Nitride Films on Silicon for Optical Waveguides," Applied Optics, to be published.

5. D. Marcuse, "Mode Conversion Caused by Surface Imperfections of a Dielectric Slab Waveguide," Bell Syst. Tech. J. 48, 3187 (1969).

6. D. Marcuse, Light Transmission Optics, Van Nostrand, New York, 1972.

7. D. J. Hannin, J. M. Hammer, and M. T. Duffy, "Scattering in ZnO/Sapphire Optical Waveguides," Appl. Opt. 14, 123 (1975).

8. D. B. Anderson and R. R. August, "Progress in Waveguide Lenses for Integrated Optics," Int. Conf. on Integrated Opt. and Fiber Opt. Commun., p. 231, Tokyo (1977).

9. D. B. Anderson, R. L. Davis, J. T. Boyd, and R. R. August, "Comparison of Optical Waveguide Lens Technologies", IEEE J. Quantum Electronics QE-13, p. 275 (1977).

10. J. T. Boyd and C. L. Chen, "Integrated Optical Waveguide and Charge Coupled Device Image Array," IEEE J. Quantum Electronics, QE-13, 282 (1977).

11. J. T. Boyd and D .B. Anderson, "Radiation Pattern of an End-Fire Optical Waveguide Coupler," Optics Communications 13, p. 353, 1975.

12. D. B. Anderson, R. L. Davis, J. T. Boyd, R. R. August, and R. E. Eisel, "Optical Waveguide Lenses," I, Technical Report AFAL-TR-76-54, May, 1976.

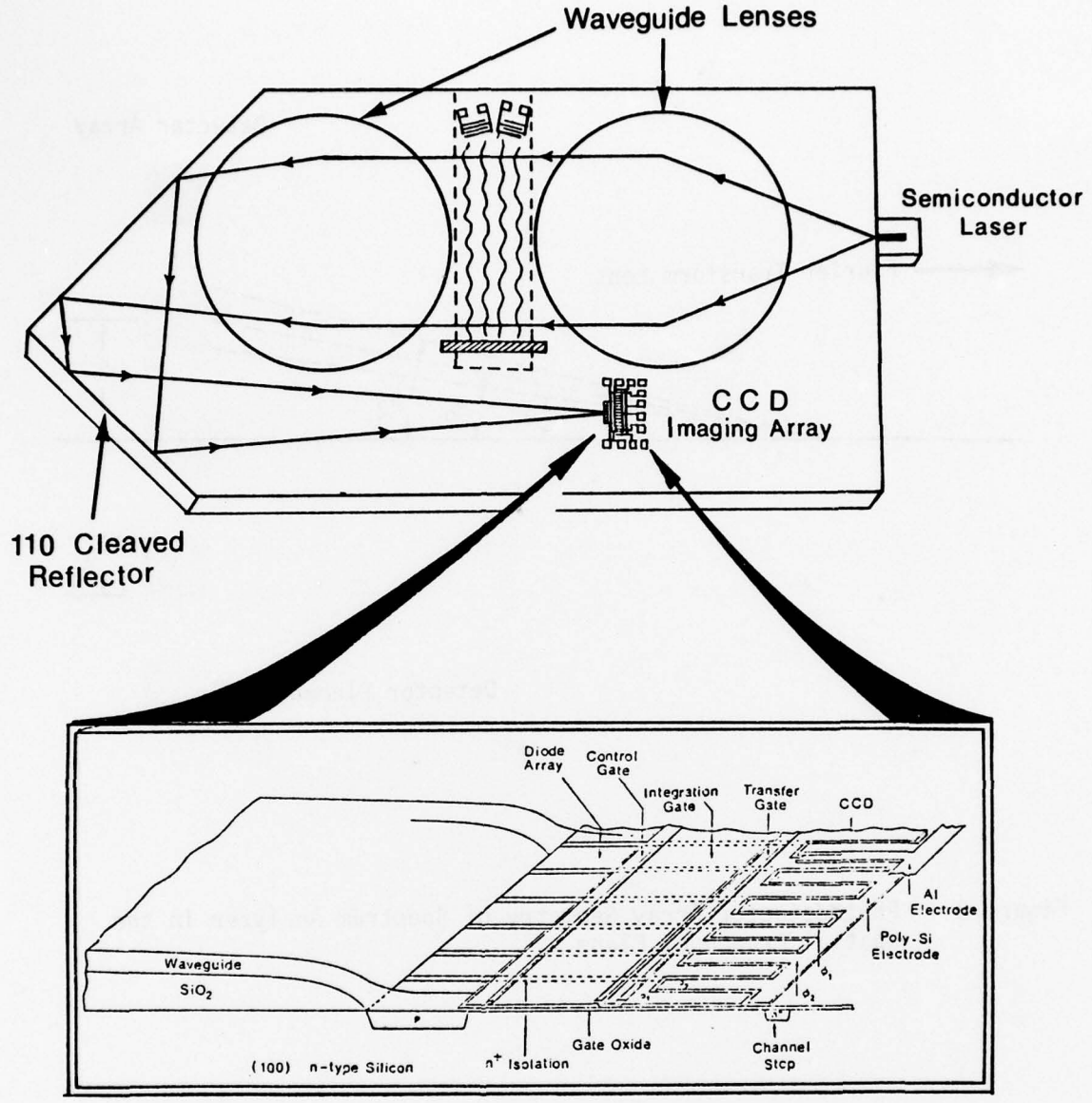

Figure 1 Schematic of the Integrated Optical Spectrum Analyzer.

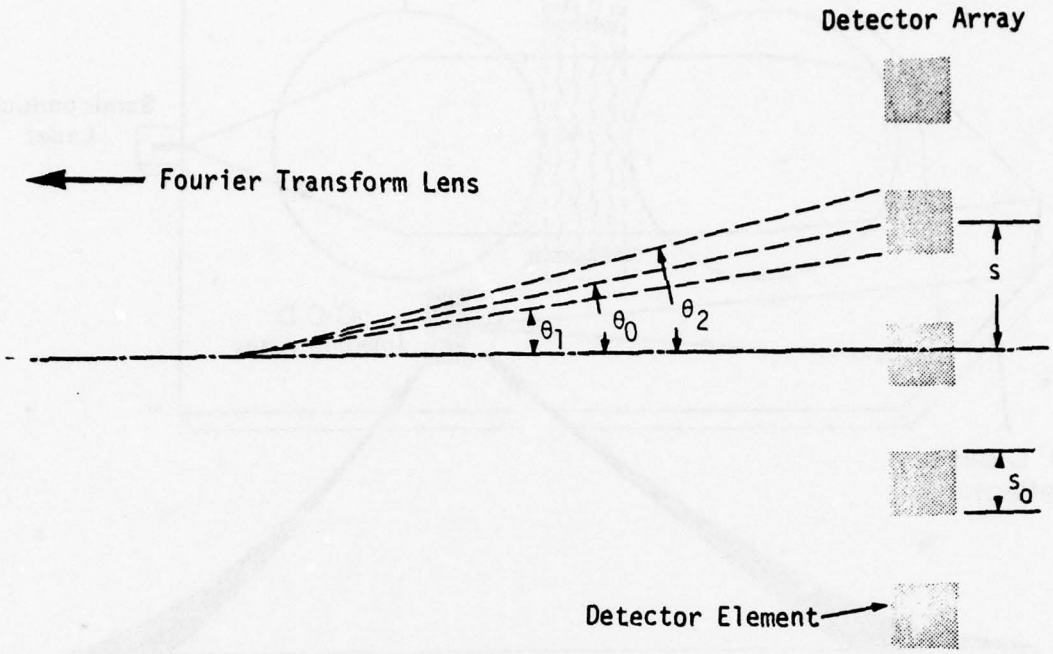

Figure 2 Photodetector Array Geometry of Spectrum Analyzer in the Spatial Frequency Plane.

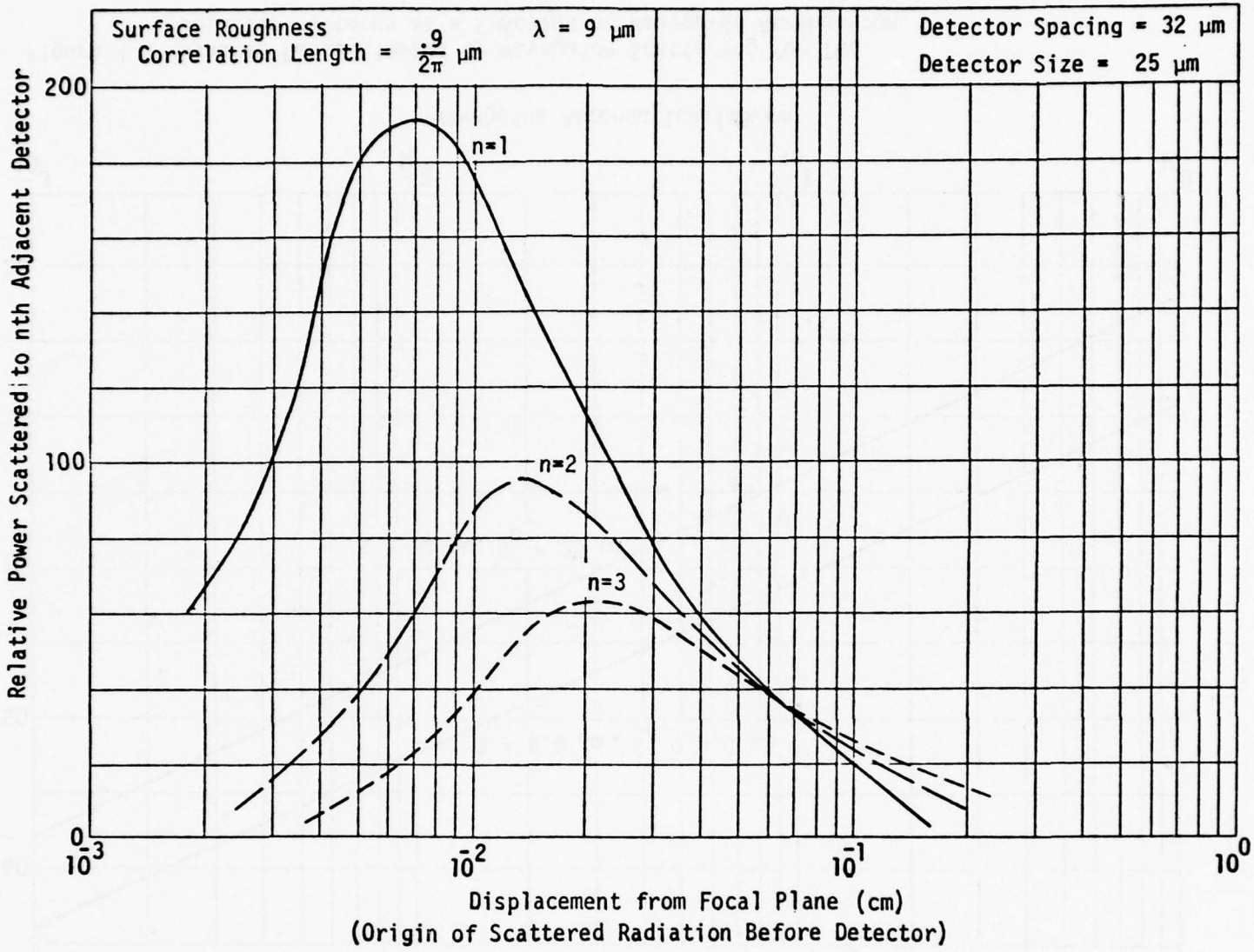

Figure 3 Scattered Power in Adjacent Detectors as a Function of the Separation of the Scattering Source from the Detector Plane.

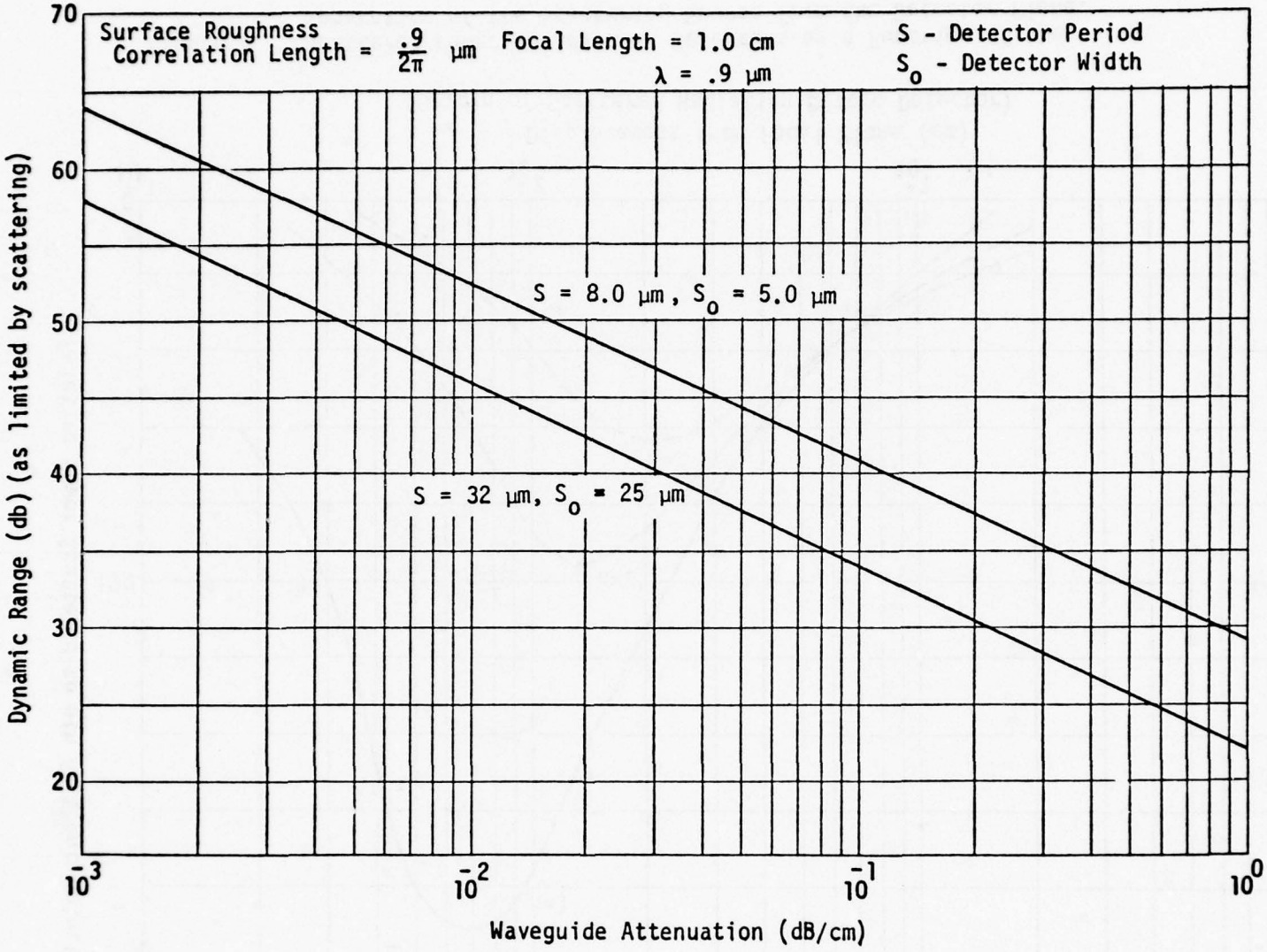

Figure 4 Dynamic Range Limited by Waveguide Scattering for Two Detector Patterns as a Function of Waveguide Attenuation.

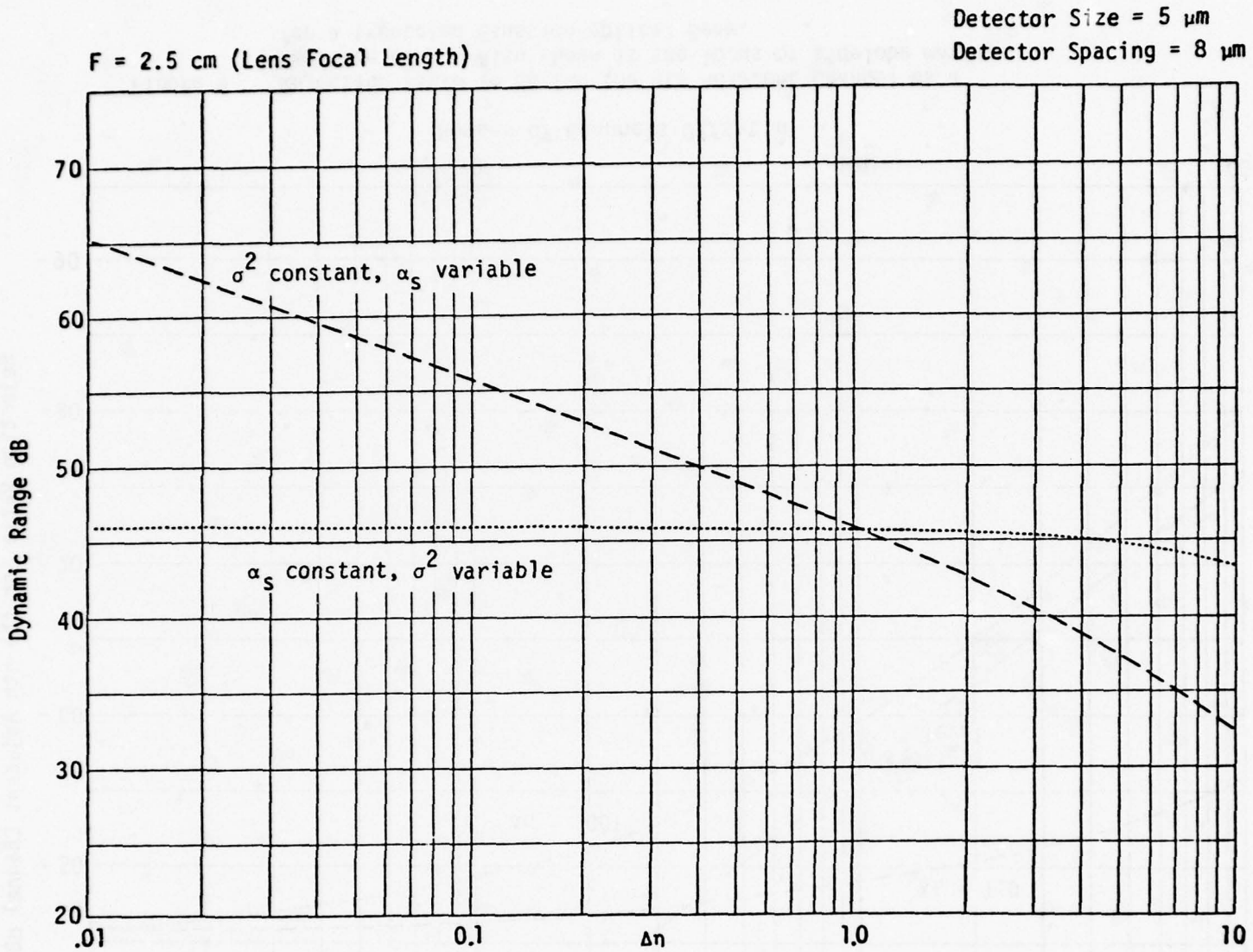

Figure 5 Dynamic Range as a Function of $\Delta\eta = \lambda/(2\pi\ell)$ for Constant Attenuation and Variable Mean Square Surface Roughness σ^2 and for Constant Mean Square Surface Roughness and Variable Attenuation.

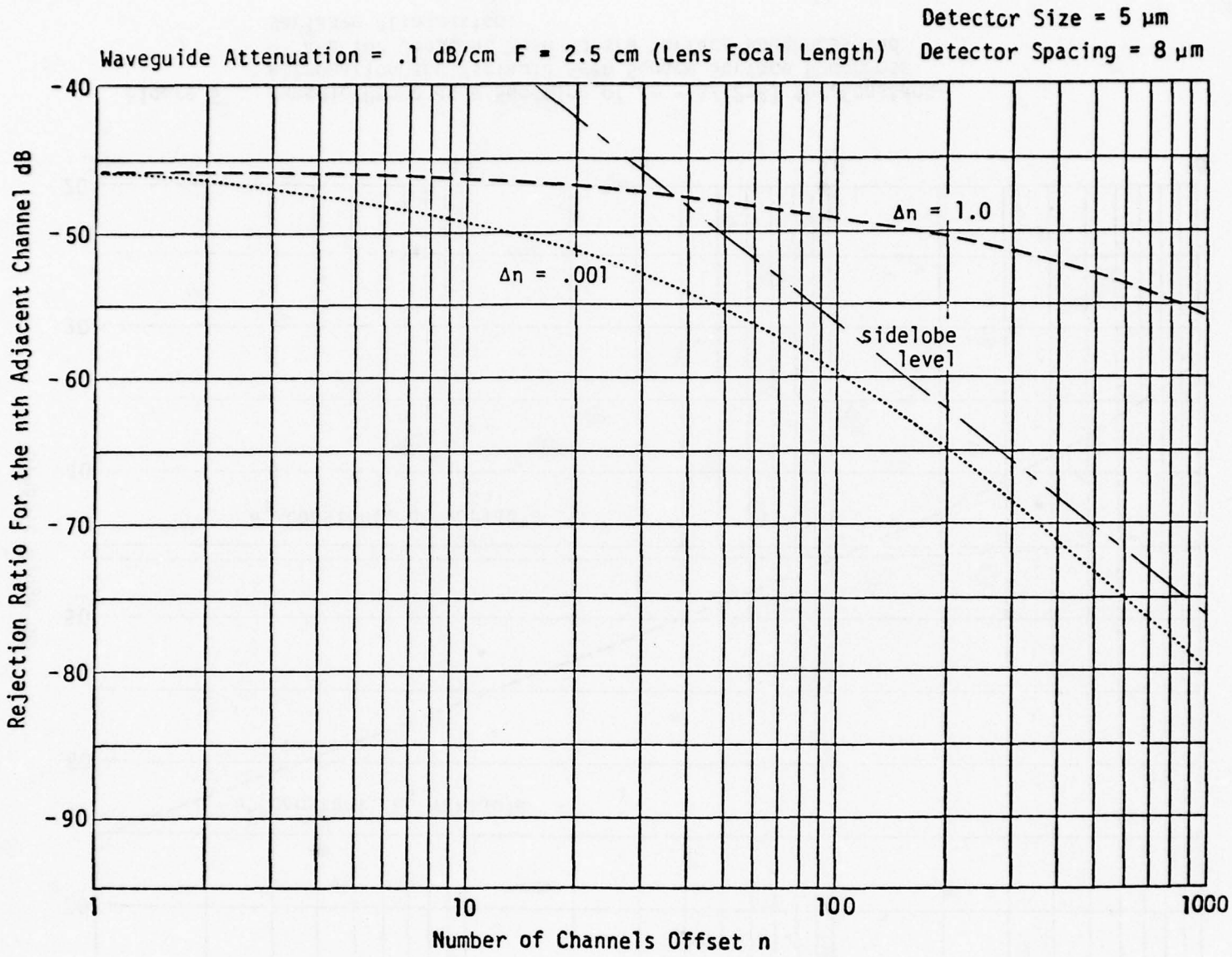

Figure 6 Rejection Ratio in dB for the nth Adjacent Channel as a Function of n. Also shown is the locus of sidelobe maxima for a truncated Gaussian optical Beam.

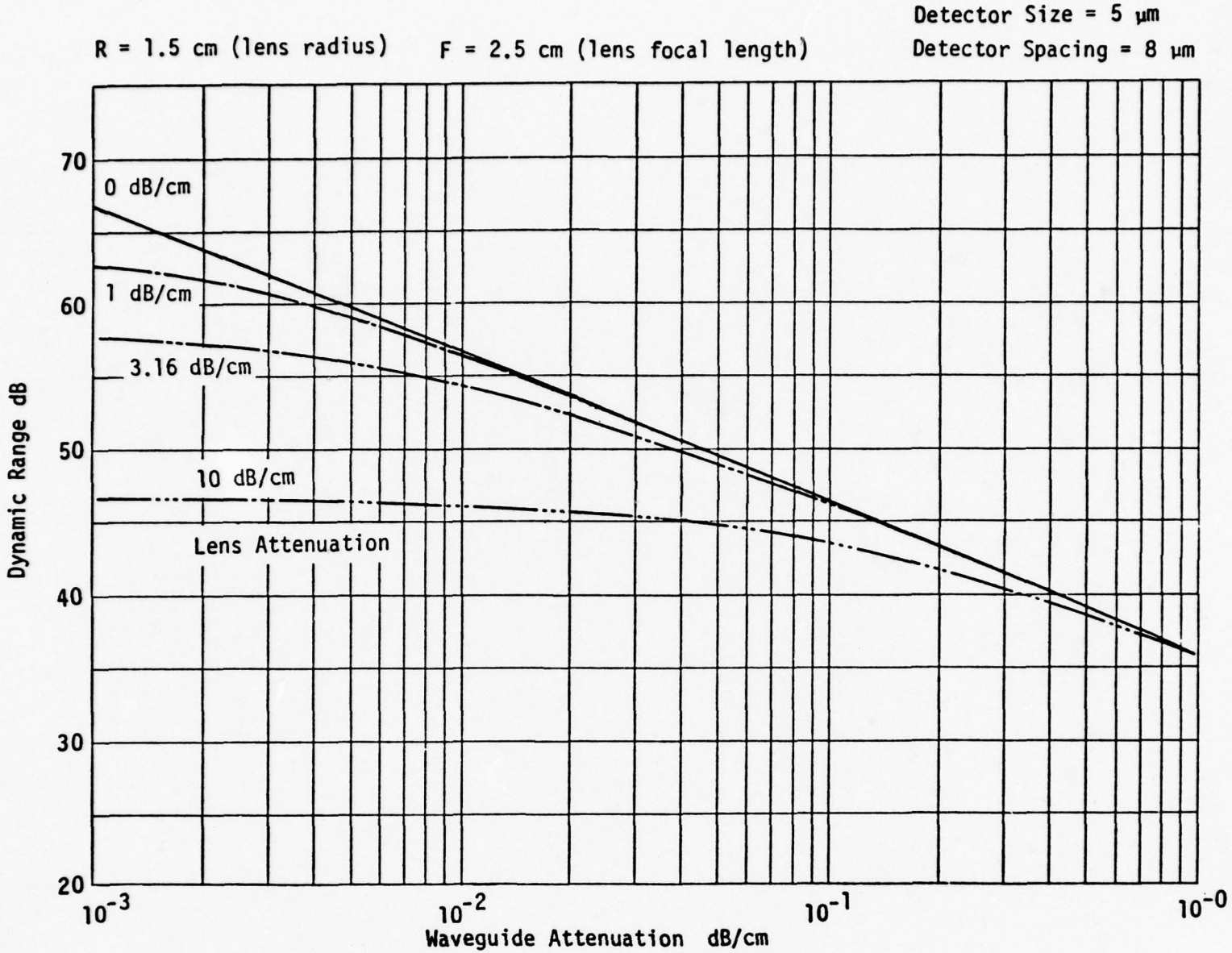

Figure 7 Spectrum Analyzer Dynamic Range in dB as a Function of Waveguide Attenuation Including the Effects of Lens Scattering.

APPENDIX D

PRESENTED AT THE IEEE IOSA CONFERENCE ON LASERS AND ELECTRO-OPTICAL SYSTEMS
February 8, 1978
San Diego, California

FOURIER TRANSFORM SIGNAL PROCESSING IN AN INTEGRATED OPTICAL FORMAT*

D. B. Anderson and R. R. August
Electronics Research Center, HA23
Rockwell International Corporation
Anaheim, California 92803
(714) 632-1881

ABSTRACT

A "first-cut" approach to a wideband real-time RF spectrum analyzer is described using an integrated optical planar waveguide circuit containing Luneburg expansion and transform lenses, a surface elasto-optic spatial modulator, and a waveguide-coupled photodetector array--all formed on a single thermally-oxidized silicon substrate with a hybrid-coupled GaAs laser.

SUMMARY

An optical approach to RF-spectral analysis requires a coherent source, appropriate expansion and transform lenses, a spatial modulator, and photodetector array in the frequency plane. Two integrated optical approaches are being pursued by industry.[1, 2] They are based upon (1) a hybrid coupling approach for the GaAs laser and the detector array to a diffused waveguide surface on a $LiNbO_3$ substrate containing geodesic lenses and a surface elastic wave Bragg-type modulator and (2) the use of a thermally-oxidized silicon substrate employing a multiplicity of overlay films for the planar waveguide, assorted lenses[3], and a piezoelectric to launch surface elastic waves and with the oxide removed to form the detector array in the substrate.[4] A "first-cut" at the integration of all these components on a silicon substrate is delineated.

* This research was supported in part by the Air Force Avionics Laboratory.

The thermally-oxidized silicon substrate provides a smooth low-loss isolation layer for a Corning 7059 waveguide extending throughout the circuit area except where the oxide is removed for optical coupling into the detector junctions. The GaAs laser is coupled to the planar waveguide by a butt-end technique[5] using a cleaved edge.

Thin Ta_2O_5 overlay films are employed to form Luneburg waveguide lenses[6] used for transverse expansion of the optical beam to encompass the spatial modulator time-aperture and to refocus, forming the Fourier transform. These Luneburg lenses are circular-symmetric, inhomogeneous and are void of all aberrations except for field curvature. They are formed by RF-sputtering through a circular mask where the mask edge shape controls the overlay film radial thickness profile. A synthesis technique has been developed to calculate the mask shape, the resulting film deposition profile, followed by ray tracing through the lens[7], to yield diffraction-limited results which have been confirmed experimentally for F/4 lenses.

The spatial modulator[8,9] employs a transverse Bragg-type surface elasto-optic interaction using an Nb_2O_5 overlay waveguide. Surface waves are launched by using an RF-sputtered ZnO piezoelectric film over an interdigital transducer array in the transducer section only with tapered edges for coupling into the surface elasto-optic section. The highly oriented ZnO overlay film yields an electromechanical coupling coefficient $k^2 = 0.015$. To obtain wide bandwidth (310-540 MHz), both beam steering[10] and angular tilting[11,12] array techniques have been employed.

The output waveguide-coupled photodetector[13] array in the frequency plane with a linear density period of 6 microns provides for a frequency resolution less than 1 MHz. An "all dry" processing approach has been employed for the detector using UV interferometric fringes to generate the detector array, waveguide coupling, and metallic contact in a single lithographic step.

The use of a silicon substrate with compatible thin films and processing procedures familiar to the semiconductor industry represents a potential significant low-cost approach to RF-spectral analysis. Waveguide losses and scattering impose an ultimate limit upon the dynamic range and resolution. Surface elastic absorption across the spatial modulator optical

aperature imposes a high frequency roll-off which affects the time-bandwidth-product which may be partially compensated for by equalization.

References

1. M. C. Hamilton, D. A. Wille, and W. J. Miceli, "An Integrated Optical RF Spectrum Analyzer," Proc. IEEE 1976 Ultrasonic Symp., Annapolis, MD.

2. M. C. Hamilton, "An Optical Thin-Film RF Spectrum Analyzer," Technical Session XI, Ninth Annual Electro-optics/Laser '77 Conference and Exposition, October 27, Anaheim, California.

3. D. B. Anderson and R. R. August, "Progress in Waveguide Lenses for Integrated Optics," 1977 Intl. Conf. on Integrated Optics and Optical Communications (IOOC '77 Conf. Digest), Tokyo, July, 1977; and to be published, Transactions of IECE (Institute of Elect. & Commun. Engrs. of Japan), Part E (English Edition), March, 1978.

4. D. B. Anderson, J. T. Boyd, M. C. Hamilton and R. R. August, "An Integrated-Optical Approach to the Fourier Transform," IEEE JQE, 13, 268, (1977).

5. R. G. Hunsperger, A. Yariv, and A. Lee, "Parallel End-Butt Coupling for Optical Integrated Circuits," Applied Optics, 16, 1026, (1977).

6. F. Zernike, "Luneburg Lens for Optical Waveguide Use," Opt. Commun., 12, 379, (1974).

7. W. H. Southwell, "Inhomogeneous Optical Waveguide Lens Analysis," J. Opt. Soc. Am., 67, 1004, (1977); W. H. Southwell, "Index Profiles for Generalized Luneburg Lenses and Their Use in Planar Optical Waveguides," JOSQ, 67, 1010, (1977).

8. D. A. Wille and M. C. Hamilton, "Acousto-Optic Deflection in Ta_2O_5 Waveguides," Appl. Phys. Lett., 24, 159-161, (1974).

9. S. K. Yao, R. R. August, and D. B. Anderson, "Surface Acousto-Optic Interaction on Non-Piezoelectric Substrates," 1977 Ultrasonics Symposium Proceedings, Phoenix, Arizona.

10. A. Korpell, R. Adler, P. Desmares, and W. Watson, "A Television Display Using Acoustic Deflection and Modulation of Coherent Light," Proc. IEEE 54, 1429, (1966).

11. L. T. Nguyen and C. S. Tsai, "Efficient Wideband Guided-Wave Acousto-Optic Bragg Diffraction Using Phased Surface Acoustic Array in $LiNbO_3$ Waveguides," Applied Optics, 16, 1297, (1977).

12. C. S. Tsai, L. T. Nguyen, S. K. Yao and M. A. Alhaider, "A High Performance Acousto-Optic Guided-Light Beam Device Using Intersecting Surface Acoustic Waves," App. Phys. Lett., 26, 140, (1975).

13. J. T. Boyd and C. L. Chen, "An Integrated-Optical Waveguide and a Charge-Coupled-Device Image Array," IEEE JQE, 13, 282-287, (1977); J. T. Boyd and C. L. Chen, "Integrated Optical Silicon Photodiode Array," Appl. Pot., 15, 1389-1393, (1976).

APPENDIX E

INTEGRATED OPTICAL SPECTRUM ANALYZER SIGNAL LEVEL REQUIREMENTS

By

Professor J. T. Boyd
University of Cincinnati

I. INTRODUCTION

Wideband spectrum analysis of electronic signals in the 10^8 - 10^9 Hz frequency range utilizing an integrated optical approach has been introduced and analyzed in previous papers.[1,2,3] Recent research in this area has been directed toward utilization of an SiO_2/Si substrate for fabrication of optical waveguide lenses, surface elastic wave transducers and waveguide coupled linear detector arrays with charge-coupled devices (CCDs). This substrate coupled with a semiconductor laser would then comprise the spectrum analyzer.

The use of SiO_2/Si offers a number of advantages. For the detector portion of the device, its use allows fabrication of sophisticated CCD readout or photodiode-amplifier detector arrays which provide both good performance and in the case of CCD arrays convenient serial signal output. Furthermore, such detector structures can be integrated into the optical waveguide structure.[4] This integration minimizes scattering which occurs in waveguide-detector coupling[4,5] and thus allows superior performance as compared with the use of an external detector array.

The present analysis considers signal levels for which a detector array is expected to operate. An array of photodiodes, possibly coupled to individual integrated amplifiers, provides the ultimate in spectrum analyzer signal output; that is, instantaneous, real-time signal output from each spectrum analyzer spectral point. We thus consider the signal handling and noise properties of this type of detector in Section II to follow. There are a number of anticipated applications of the integrated optical spectrum analyzer, however, in which it will be advantageous to sacrifice some of the advantages of real-time signal output for each spectral channel for the convenience of spectral signal output in a serial, time-multiplexed format. Conversion of spectral information in a parallel format represented as signal levels along an array of photodiodes to a serial format is simply effected

by the incorporation of a CCD into the detector array.[6] An integrated optical waveguide-CCD image array suitable for the above purpose has previously been demonstrated.[4] Detailed analysis of the signal handling capability and noise properties of this device are considered in Section III.

The knowledge determined in Sections II and III concerning signal ranges over which the detector arrays operate allows estimation in Section IV of the incident optical power required to fully utilize detector dynamic range. Estimation of detector quantum efficiency, waveguide-detector coupling efficiency, scattering losses, deflection efficiency, and laser coupling efficiency then allow calculation of the laser power required to fully utilize detector dynamic range.

II. INTEGRATED OPTICAL PHOTODIODE DYNAMIC RANGE

To determine the dynamic range of a photodiode, both the maximum signal handling capability and noise level of the photodiode must be determined. A photodiode is normally operated in a series circuit with a bias voltage and a load resistor. The load resistor may correspond to the input impedance of an amplifier. The optical signal is measured by the current I flowing in the series circuit, given as

$$I = -I_0 \left[\exp(-eV_r/kT) - 1\right] + I_L \quad , \tag{1}$$

where I_L is the current flowing due to the presence of light incident on the photodiode I_0 is the pn-junction reverse bias saturation current, V_r is the reverse voltage appearing across the pn-junction, e is electron charge, k is Boltzman's constant, and T is temperature. The voltage V_r is related to the bias voltage V_0 by

$$V_r = V_0 - IR_L \quad , \tag{2}$$

where R_L is the load resistance. The current I_L is proportional to incident light power as:

$$I_L = \frac{e\eta_q}{h\nu} P \quad , \tag{3}$$

where P is the incident optical power, $h\nu$ is the photon energy, and ηq is the photodiode quantum efficiency.[7] Thus, for a wide range of currents such that the exponential term in Eq. (1) is negligible, the total current is also proportional to light power through Eq. (1). But at large light levels, the current flowing increases such that the exponential term in Eq. (1) becomes significant. At this point Eqs. (1) and (2) form a transcendental equation which must be solved for I. Solutions indicate that the total current saturates for increasing incident light power. At the onset of saturation a departure from linearity in photodiode response thus occurs. We define the maximum optically excited current I_L as that value corresponding to a 1% deviation in response linearity. This value of current is a solution of

$$I_{L\,max} = V_o/R_L + (V_{th}/R_L) \ln (10^{-2} I_{L\,max}/I_o) \cong V_o/R_L \quad , \qquad (4)$$

where $V_{th} = kT/e$ is the thermal voltage. The value of R_L is usually related to the electrical bandwidth Δf of the photodiode by

$$\Delta f = \frac{1}{2\pi R_L C_d} \quad , \qquad (5)$$

where C_d is the junction capacitance of the photodiode. Substituting Eq. (5) into Eq. (4) gives

$$I_{L\,max} = 2\pi V_o C_d \Delta f \quad . \qquad (6)$$

Thus, the maximum photodiode response is proportional to the bias voltage and is inversely proportional to load resistance or, equivalently, proportional to junction capacitance and detector bandwidth.

Now that the maximum photodiode photocurrent has been determined, determination of dynamic range requires calculation of photodiode noise current. Photodiodes are characterized by both signal shot noise and thermal noise associated with R_L. Because shot noise is much less than thermal noise at minimum detectable incident optical power levels and because it is signal dependent, it is not included in dynamic range calculations. The rms current due to thermal noise $(\overline{I_{th}^2})^{1/2}$ is

$$(\overline{I_{th}^2})^{\frac{1}{2}} = \sqrt{\frac{4kT\Delta f}{R_L}} = \Delta f \sqrt{8\pi C_d kT} \quad . \tag{7}$$

This is the minimum detectable photocurrent since smaller values of photocurrent cannot be distinguished from noise.

Dynamic range is defined in the usual way as the ratio of the maximum signal level to the minimum signal level

$$DR_{ratio} = \frac{I_{L\ max}}{I_{L\ min}}$$

$$= V_o \sqrt{\frac{\pi C_d}{2kT}} \quad , \tag{8}$$

where Eqs. (6) and (7) were used. In terms of dB the electrical dynamic range applicable to photodiode current is

$$DR_e = 20 \log_{10} \left(V_o \sqrt{\frac{\pi C_d}{2kT}} \right) , \tag{9}$$

while the optical imaging dynamic range is

$$DR_o = 10 \log_{10} \left(V_o \sqrt{\frac{\pi C_d}{2kT}} \right) . \tag{10}$$

As deflected optical field is linearly proportional to acoustic field in the range of acoustic power applicable to the spectrum analyzer, the optical dynamic range DR_o characterizes the spectrum analysis process. Note that photodiode dynamic range is independent of bandwidth. We consider a numerical example similar to our integrated optical photodiode array previously fabricated.[8] The pn photodiode dimensions can be expected to approach 7 μm x 50 μm with a substrate impurity concentration of 10^{15} cm^{-3}. For V_o = 100 volts, the depletion region width is 11.5 μm, giving a junction capacitance of $C_d = 3.2 \times 10^{-15}$ F. For V_o = 100 volts spectrum analyzer dynamic range is DR_o = 50.4 dB. This value is comparable to that achievable with a CCD image array, as will become evident from the calculations in the following section.

III. INTEGRATED OPTICAL CCD IMAGE ARRAY DYNAMIC RANGE

The CCD image array integrated into an SiO_2/Si optical waveguide structure which has been demonstrated[4] is shown in Fig. 1. This particular device configuration provides for charge excitation in the photodiode regions with the gate potentials adjusted so that photo-excited charge accumulates under the integration gate for each array element. The presence of the photodiode provides an electrode-free surface for waveguide-detector coupling. With the presence of the integration gate, this device configuration is applicable to operation of the integrated optical spectrum analyzer in either a pulsed or an integrating mode. Charge integrates in the potential well formed underneath the integration gate in the device shown in Fig. 1. At the end of the integration period T_o, the transfer gate is turned on so that the charge accumulated in each array element is transferred simultaneously into the CCD shift register portion of the device. This parallel transfer of charge occurs in a time less than 1/2 of the CCD clock period so that the CCD is stationary during this time. Once this charge has transferred into the CCD, the transfer gate is turned off and the charge is transferred along the CCD to the end where, after suitable amplification, a serial, discrete-time signal emerges representing the spatial light distribution. As soon as the transfer gate is turned off, charge integration again begins and the cycle is repeated. The integration time is thus given as

$$T_o = N\tau = N/f_c \quad , \tag{11}$$

where N is the number of CCD stages equal to the number of array elements, f_c is the CCD clock frequency and τ is the CCD clock period equal to the time required to transfer a charge packet from one stage to the next adjacent stage.

We shall consider the following three cases of spectrum analyzer operation:

Case I - This is a pulsed mode in which the pulse duration is much less than the surface elastic wave transit time T_e across the optical aperature. Pulses occur once each T_e seconds occurring when the signal of interest

is positioned in the optical aperture. For a large number of spectral points (large time-bandwidth products), the transit time T_e may not provide ample time to completely empty a single CCD register. For such situations, we shall assume a CCD having several sections, each with separate output aligned one after another along the Fourier transform plane.

Case II - An integrating mode in which the integration period is on the order of the transit time T_e. The laser operates CW and we shall use an integration time T_e in our calculations. As in the previous case, the integration time T_e may not provide ample time to completely empty a CCD register corresponding to a large number of spectral points. For such situations we shall assume a CCD having several sections and several separate outputs.

Case III - An integrating mode in which the integration period is long compared to the transit time T_e. The laser operates CW, and we shall assume that the integration time is determined as the time required to shift out a single section CCD imaging device.

These three cases are applicable to a wide variety of situations.

In what follows, calculations will be presented for a Surface Channel CCD (SCCD) similar to the one previously fabricated[4] as opposed to a Bulk Channel CCD (BCCD). Generally, SCCD's have larger signal handling capabilities and larger dynamic ranges than BCCD's. However, BCCD's are characterized by lower noise levels and a larger maximum operating frequency. The calculations which follow could be altered to apply for a BCCD by replacing fast interface state noise applicable to SCCD's by a bulk state trapping noise and replacing the maximum charge handling capability of a surface channel by that of a bulk channel.

To calculate the CCD image array dynamic range, the maximum signal handling capability and noise level of the device must be determined. The maximum signal handling capability of a charge transfer device is limited by the breakdown of the SiO_2 insulator region.[6] Gauss' law then implies that the total charge $e\, n_{max}$ associated with the maximum electric-field E_{max} which the SiO_2 region can withstand is given as

$$e\, n_{max} = \varepsilon_o\, \varepsilon_{ox}\, E_{max}\, A \quad , \tag{12}$$

where n_{max} is the maximum number of charge carriers, e is the electron charge, A is the area of the electrode in question, ε_o is the free space permittivity ($\varepsilon_o = 8.85 \times 10^{-14}$ farad/cm.), and ε_{ox} is the dielectric constant of SiO_2 ($\varepsilon_{ox} \approx 4.0$). Because the area of the integration gate A_{ig} is slightly larger than the area of the CCD electrodes A_{sg} for the devices previously fabricated,[4] the maximum charge which can be handled by the overall device is limited to that which can be handled by the CCD, i.e.,

$$n_{max} = \frac{\varepsilon_o \varepsilon_{ox}}{e}\, E_{max}\, A_{sg} \quad . \tag{13}$$

The value of E_{max} varies[6,7] over a range $1 - 6 \times 10^6$ v/cm., depending on a variety of processing and material conditons. For the present calculations, we shall choose the value

$$E_{max} = 4 \times 10^6 \text{ v/cm.} \quad , \tag{14}$$

as the maximum allowable field. Using this value in Eq. (13) gives

$$n_{max}/A_{sg} = 8.85 \times 10^{12} \text{ cm}^{-2} \quad . \tag{15}$$

This value is more conservative than that given by Sequin and Tompsett.[6] The electrodes of the previously fabricated devices have a typical size of 10 μm x 125 μm, giving $A_{sg} = 125 \times 10^{-5}$ cm^2. Using this value in determining n_{max} from above gives

$$n_{max} = 1.11 \times 10^8 \quad . \tag{16}$$

The value in Eq. (15) is much greater than values of the surface state density Q_{ss}/e for the SiO_2/Si interface, justifying the omission of Q_{ss} in Eq. (13).

Now that the maximum signal handling capability has been calculated, determination of dynamic range requires calculation of the noise levels present in the CCD device in Fig. 1. Noise in this device arises from a variety of sources including output amplifier noise, noise associated with dark current fluctuations, noise associated with signal input circuitry,

noise associated with fluctuations in the emission and trapping of carriers by fast interface states, and noise associated with fluctuations in bias charge transfer loss. These sources of noise shall be considered separately in what follows with the net effect of noise eventually determined. As the various sources of noise are independent, their mean square fluctuations in the number of carriers will add to give the cumulative effect. In addition to the above sources of noise, shot noise associated with the input optical signal will also give rise to signal-dependent fluctuations in both the imperfect charge excitation and transfer processes. However, as the rms fluctuation in the number of carriers is equal to the square root of the average number of signal carriers, this fluctuation will be negligible at minimum detectable signal levels. This source of noise will thus not be included in the dynamic range calculation.

For surface channel CCD's, fast interface state trapping and emission can seriously degrade charge transfer efficiency. This is particularly true after operation for a period of time with no input signal. For such situations these traps empty and thus when signal charge does appear a significant amount of it is trapped. This problem can be overcome by injecting a continuous small bias charge referred to as fat zero so that trap occupation and thus free charge remain constant on the average. Emission and trapping of charge continue to occur but at balancing rates. Although this technique significantly improves transfer efficiency, fluctuations in the trapping and emission of carriers is still present. In general, these fluctuations are independent for each storage electrode and thus mean square fluctuations add. The rms number of noise electrons $\bar{n}_{is}$ due to fast interface state fluctuations for fat zero operation has been shown to be[10,11]

$$\bar{n}_{is} = \sqrt{kT\, N_{ss}\, \ln 2\, (2\, NA_{sg} + A_{ig})} \quad , \tag{17}$$

where k is Boltzman's constant, T is absolute temperature, N_{ss} is the fast interface state density in $ev^{-1}cm^{-2}$, and A_{ig} is the area of the integration gate. Note that although charge from all but one of the parallel channels travels less than N stages, fast interface state noise accumulates for all N stages in each signal charge packet. Although values of N_{ss} as low as $10^9 ev^{-1}cm^{-2}$ have been observed, we employ a more typical value[12] of $5x10^9$ $ev^{-1}cm^{-2}$ in Eq. (7) and find

$$\bar{n}_{is} = 47 \sqrt{N + 1.1} \quad , \tag{18}$$

where the area of the integration gate is taken as $A_{ig} = 2.87 \times 10^{-5} cm^{-2}$. The noise contribution of fast interface states as given by Eqs. (17) and (18) is an upper limit as this noise is suppressed[13] at low CCD signal frequencies. Low CCD signal frequencies correspond to analysis of broad band input signals. Narrow band input signals after undergoing spectrum analysis give rise to CCD signal variations approaching the Nyquist limit so that no suppression of the above noise contributions is expected for such input signals.

Output amplifier noise generally makes a significant contribution to overall device noise. Because charge packets in CCD's correspond to low-level electrical signals, amplification is required. An MOS reset amplifier integrated onto the same chip as the CCD has been found to be most satisfactory for this amplification. The reset process, however, introduces thermal noise generally on the order of 200 carriers.[14] White, et. al.,[15] introduced the correlated double sampling technique to remove this noise, however. We shall assume that correlated double sampling is employed so that this noise is removed from the CCD of present interest. The remaining primary contribution to output amplifier noise is thermal noise, as 1/f noise is suppressed at CCD operating frequencies of present interest. Careful design of the output amplification circuitry has yielded a device having a measured rms noise contirubtion of 27 carriers compared to a theoretical design of 25. We shall choose a more conservative value for the rms carrier fluctuation $\bar{n}_{oa}$ of

$$\bar{n}_{oa} = 100 \quad , \tag{19}$$

arising from the output amplifier.

Noise associated with dark current generation in CCD's is particularly significant in imaging devices. Fluctuations in dark current is a shot noise process so that the rms number of noise carriers associated with these fluctuations $\bar{n}_d$ is equal to the square root of the mean number of carriers generated; i.e.,

$$\bar{n}_d = \sqrt{\frac{J_o(A_{sg} + A_{ig})N}{e\, f_c}} \quad . \tag{20}$$

In Eq. (20) J_o is the dark current level which will be taken to be $J_o = 6 \times 10^{-9}$ A/cm^2 corresponding to measurements,[14] although lower values have been reported.[12] Using a clock frequency of 10 MHz, Eq. (20) becomes

$$\bar{n}_d = .39 \sqrt{N} \quad . \tag{21}$$

As in the case of fast interface state noise, Eq. (20) includes the fact that dark current accumulates throughout the entire device even though, with parallel entry, most signal charge is transferred over only a portion of the device.

Input thermal noise is significant both from the parallel injection of optically excited charge and from serial injection of a bias charge or fat zero. Again, 1/f noise is not significant at the high operating frequencies of present interest. In general, the rms number of carriers $\bar{n}_{in}$ associated with input thermal noise is given as[6,14]

$$\bar{n}_{in} = \frac{1}{e} \sqrt{kT(\alpha_{in}C_{in} + \alpha_{ig}C_{ig})} \quad , \tag{22}$$

where C_{in} is the input gate capacitance, C_{ig} is the integration gate capacitance and α_{in} and α_{ig} are parameters of the order of unity which depend on the specific input conditions. We shall assume both equal one. The input thermal noise due to fat zero injection can be reduced by reducing the width of the serial input gate.[14] This reduces the signal-handling capability of the input gate but, since only low-level bias charge is injected serially, it is of no consequence. For a serial input gate having dimensions 12 μm x 10 μm, the capacitance of the input gate and the integration gate are:

$$C_{in} = \frac{\varepsilon_o \varepsilon_{ox} A_{in}}{t_{ox}} = .04 \text{ pf} \tag{23a}$$

$$C_{ig} = \frac{\varepsilon_o \varepsilon_{ox} A_{ig}}{t_{ox}} = 1.02 \text{ pf} \quad , \tag{23b}$$

where we assumed the oxide thickness $t_{ox} = .1$ μm. Using these values of capacitance in Eq. (22) gives

$$\bar{n}_{in} = 414 \tag{24}$$

for the rms number of input noise carriers.

The significant sources of noise have now been quantified. As these sources are independent, their mean squares add. Denoting mean square values as n_x^2, where

$$\bar{n}_x = \sqrt{\overline{n_x^2}} \quad , \tag{25}$$

and x is any of the previous subscripts, the total rms number of noise carriers is

$$\bar{n}_t = \sqrt{\overline{n_{is}^2} + \overline{n_{oa}^2} + \overline{n_d^2} + \overline{n_{in}^2}} \quad . \tag{26}$$

Now, using Eqs.(18), (19), (21), and (24) in Eq. (26) gives

$$\bar{n}_t = \left[(414)^2 + (.39\sqrt{N})^2 + (47\sqrt{N+T})^2 + (100)^2 \right]^{\frac{1}{2}} \tag{27}$$

The total noise level $\bar{n}_t$ can now be used to calculate dynamic range.

Dynamic range is defined as before as the ratio of the maximum signal level to the noise level; i.e.,

$$DR_{ratio} = .9 \frac{n_{max}}{\bar{n}_t} \quad , \tag{28}$$

where Eqs. (16) and (27) need to be used for evaluation. The factor .9 is introduced to account for fat zero utilization of 10% of the maximum device signal handling capability. In terms of dB, the electrical dynamic range (CCD current) and the optical imaging dynamic range are

$$DR_e = 20 \log_{10} \left(.9 \frac{n_{max}}{\bar{n}_t} \right) \tag{29}$$

$$DR_o = 10 \log_{10} \left(.9 \frac{n_{max}}{\bar{n}_t} \right) \quad . \tag{30}$$

As noted earlier, the optical dynamic range DR_o is the one characterizing operation of the integrated optical spectrum analyzer. Table I presents this dynamic range information for each of the three cases discussed earlier as a function of the number of resolvable spectral points in the signal Fourier transform.

TABLE I CCD DYNAMIC RANGE

f_c = 10 MHz 10% Fat Zero

	Case I Pulsed Mode Pulsewidth <<Transit Time		Case II CW Mode Integration Time= Transit Time		Case III CW Mode Integration Time> Transit Time	
No. of Spectral Points	CCD Optical Dynamic Range (dB)	No. of Separate Outputs* Required	CCD Optical Dynamic Range (dB)	No. of Separate Outputs* Required	CCD Optical Dynamic Range (dB)	No. of Separate Outputs* Required
32	53	1	53	1	53	1
64	53	2	53	2	52	1
128	53	4	53	4	52	1
256	53	8	53	8	51	1
512	53	16	53	16	49	1
1024	53	32	53	32	48	1

*Fewer outputs would be required for those cases for operation at higher clock frequencies. The dynamic range varies slowly with frequency in this frequency range.

IV. INTEGRATED OPTICAL FOURIER TRANSFORM LASER POWER REQUIREMENTS

The determination of the range of signal levels over which the detector operates allows determination of the laser power required to fully utilize detector dynamic range. If laser power P_o is coupled into the waveguide with coupling efficiency η_{lc}, the initial power in the optical waveguide is

$$\eta_{lc} P_o \quad . \tag{31}$$

This optical power undergoes attenuation at a rate α_g as it propagates in the optical waveguide, attenuation at a rate α_l as it propagates in lens regions, reflection losses at reflectors (r = product of reflectivities at each reflector), and transmission losses at waveguide-lens and other discontinuities (t = product of transmissivities at each such discontinuity). The resulting undeflected optical power in the transform plan is thus

$$e^{-\alpha_l L_l} \; e^{-\alpha_g L_g} \; rt \; \eta_{lc} P_o \quad , \tag{32}$$

where L_l and L_g are the mean propagation lengths in the lens and waveguide regions, respectively.

In the operation of the spectrum analyzer, a portion of this optical power is deflected to the detector area. We define η_d as the fraction of optical power deflected with $\eta_{d\,max}$ as the maximum deflection efficiency, corresponding to maximum elastic wave power. For the present calculation, we consider single frequency surface elastic wave excitation having maximum intensity, so that all deflected optical power (except side lobe contributions) is incident on a single detector element. The maximum deflected optical power P_{inc} corresponding to maximum elastic wave power incident on a single detector element is thus

$$P_{inc} = \eta_{d\,max} \eta_{sl} \; e^{-\alpha_l L_l} \; e^{-\alpha_g L_g} \; rt \; \eta_{lc} P_o \quad , \tag{33}$$

where η_{sl} is the fraction of optical power in the main lobe of the focused optical beam. The maximum elastic wave intensity should ideally have a value which yields maximum deflection efficiency while maintaining linearity between the deflected optical field and the elastic wave field. Criteria for the maintenance of linearity are somewhat arbitrary. For the present we impose the criteria that the deviation from linearity should not exceed 1%. The corresponding deflection efficiency corresponding to the maximum elastic wave power should thus be $\eta_{d\,max} = .06$.

For photodiode detection the photodiode current corresponding to the incident power in Eq. (33) is

$$I_{inc} = \frac{e\eta_q}{h\nu} P_{inc} \quad , \tag{34}$$

similar to Eq. (3). As the incident deflected power P_{inc} corresponds to the maximum optical power which would ever reach a detector element, the current I_{inc} should equal the maximum current I_{Lmax} from Eq. (6) which a photodiode can pass while remaining within 1% of photoresponse linearity in order to fully utilize detector dynamic range. Thus, imposing the condition

$$I_{inc} = I_{L\,max} \quad , \tag{35}$$

in Eq. (34) and using Eq. (33) in Eq. (34), we can solve for the required laser power P_o to be

$$P_o = \frac{2\pi h\nu V_o C_d \Delta f \, e^{\alpha_l L_l} \, e^{\alpha_g L_g}}{e\eta_q \eta_{dmax} \eta_{sl} \eta_{lc} \, rt} \quad . \tag{36}$$

Equation (36) has been evaluated for the following parameters:

λ = .9 μm ($h\nu$ = 2.21 x 10^{-19} j)
α_l = .46 cm^{-1} (2 dB/cm. attenuation in lens region)
α_g = .115 cm^{-1} (.5 dB/cm. waveguide attenuation)
L_l = 2.5 cm (propagation length in lens region)
L_g = 10 cm (propagation length in waveguide region)
η_q = .8 (waveguide detector quantum efficiency = .8 has been measured[5])
η_{dmax} = .06 (maximum deflection efficiency which maintains nonlinear deviation < 1%)
η_{sl} = .95 (estimated fraction of power in main lobe)
η_{lc} = .45 (laser-waveguide coupling efficiency = .8 has been experimentally realized[16])
r = .9 (net fractional reflector losses = 1 - r)
t = .9 (net fractional transmission losses = 1 - t)
V_o = 10 volts (photodiode bias)
C_d = 3.2 x 10^{-15}F (photodiode junction capacitance corresponding to photodiode discussed in Section II)

The only parameter in Eq. (36) not specified above is the photodiode bandwidth Δf. For real-time output the spectrum analyzer can only resolve signal changes for times greater than the inverse of its resolution; i.e., T_e/TBW, where TBW is the time-bandwidth product of the spectrum analyzer. The photodiode bandwidth which will allow the detector to resolve the above changes is

$$\Delta f = \frac{TBW}{T_e} \quad . \tag{37}$$

For T_e = 3 μsec (corresponding to a 1 cm optical aperature) and TBW variable, we have evaluated Eq. (36) and the results are shown in Table II.

TABLE II. LASER POWER REQUIREMENTS-PHOTODIODE DETECTION

TWB (Time-Bandwidth Product) and the Number of Spectral Points	P_o Required Laser Power (mW)
32	1.8
64	3.6
128	7.2
256	14.4

For CCD detection the number of carriers excited at a detector element corresponding to the incident power in Eq. (33) and an integration time of T_x seconds is

$$n = \eta_q \frac{P_{inc}}{h\nu} T_x \quad , \tag{38}$$

where $h\nu$ is the incident photon energy and η_q is the detector quantum efficiency. The integration time T_x corresponds to the laser pulse duration for Case I operation, to the transit time T_e for Case II operation, and to the time T_o required to empty a single output CCD for Case III operation. The incident deflected power P_{inc} corresponds to the maximum optical power which would ever reach a detector element so the number of excited carriers n should be equal to the maximum number which the detector can handle; i.e., n_{max} in Eqs. (13) and (16) in order to fully utilize detector dynamic range. Thus, imposing the condition

$$n = n_{max} \quad , \tag{39}$$

in Eq. (38) and using Eq. (33) in Eq. (38), we can solve for the required laser power P_o to be

$$P_o = \frac{h\nu n_{max} e^{\alpha_l L_l} e^{\alpha_g L_g}}{\eta_q \eta_{dmax} \eta_{sl} \eta_{lc} r t T_x} \quad . \tag{40}$$

We have evaluated Eq. (40) for the above parameters along with f_c = 10 MHz, n_{max} given in Eq. (16) and N = TBW variable. The variable integration time T_x is

$$T_x = \begin{cases} .2\ \mu\text{sec Case I} \\ 3.2\ \mu\text{sec Case II} \\ 10^{-1}\ N\mu\text{sec Case III} \end{cases} \quad (41)$$

The results of the calculation of required laser power using Eq. (40) are tabulated in Table III for various values of N.

TABLE III. LASER POWER REQUIREMENTS - CCD DETECTION

P_o = Laser Power Required (mW)

N Number of Spectral Points	Case I Pulsed Mode Pulse Width=.2μsec	Case II CW Mode Integration Time=Elastic Wave Transit Time	Case III CW Mode Integration Time= Time Required To Empty CCD
128	73.6	4.6	1.15
256	73.6	4.6	.58
512	73.6	4.6	.29
1024	73.6	4.6	.14

REFERENCES

1. M. C. Hamilton and D. A. Wille, "Acousto-Optic Diffraction in Optical Waveguides," Digest of Technical Papers, Topical Meeting on Integrated Optics, New Orleans, La., Jan. 21-24, 1974.

2. M. C. Hamilton, D. A. Wille and W. J. Miceli, "An Integrated Optical RF Spectrum Analyzer," IEEE 1976 Ultrasonic Symposium Proceedings, Annapolis, Md.

3. D. B. Anderson, J. T. Boyd, M. C. Hamilton and R. R. August, "An Integrated Optical Approach to the Fourier Transform," IEEE J. Quantum Electronics QE-13, 268 (1977).

4. J. T. Boyd and C. L. Chen, "Integrated Optical Waveguide and Charge Coupled Device Image Array," IEEE J. Quantum Electronics QE-13, 282 (1977).

5. J. T. Boyd and C. L. Chen, "Integrated Optical Silicon Photodiode Array," Appl. Opt. 15, 1389 (1976).

6. C. H. Sequin and M. F. Tompsett, Charge Transfer Devices, Academic Press, 1975.

7. A. Yariv, Introduction to Optical Electronics, Holt, Rineholt and Winston, 2nd Edition, 1976.

8. D. B. Anderson, et. al., "Optical Waveguide Lenses, II," Technical Report, AFAL-TR-77-60, 1977.

9. A. S. Grove, Physics and Technology of Semiconductor Devices, John Wiley and Sons, Inc., 1967.

10. J. E. Carnes and W. F. Kosonocky, "Noise Sources in Charge-Coupled Devices," RCA, Rev. 33, 327 (1972).

11. M. F. Tompsett, "The Quantitative Effects of Interface States on the Performance of Charge-Coupled Devices," IEEE Trans. Elect. Dev. ED-20, 45 (1973).

12. R. W. Brodersen, C. R. Hewes and D. D. Buss, "A 500-Stage CCD Transversal Filter for Spectral Analysis," IEEE Trans. Elect. Dev. ED-23, 143 (1976).

13. K. K. Thornber and M. F. Tompsett, "Spectral Density of Noise Generated in Charge Transfer Devices," IEEE Trans. Elect. Dev. ED-19 , 456 (1972).

14. R. W. Brodersen and S. P. Emmons, "Noise in Buried Channel Charge-Coupled Devices," IEEE Trans. Elect. Dev. ED-23, 215 (1976).

15. M. H. White, D. R. Lampe, F. C. Blaha and I. A. Mack, "Characterization of Surface Channel CCD Imaging Arrays at Low Light Levels," IEEE J. Solid State Circuits SC-9 1 (1974).

16. R. G. Hunsperger, A. Yariv and A. Lee, "Parallel End-Butt Coupling for Optical Integrated Circuits," Appl. Opt. 16, 1026 (1977).

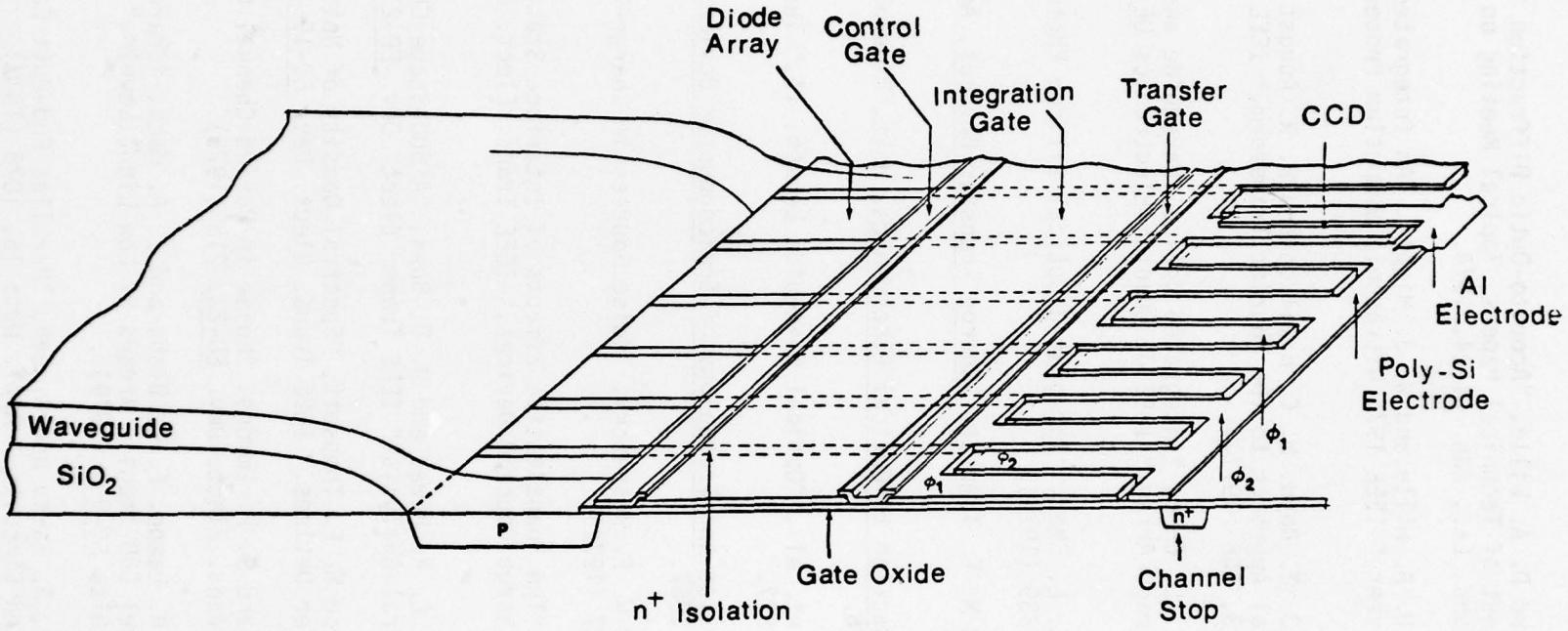

Figure 1. Integrated Optical Waveguide and CCD Detector Array

REFERENCES

1. M. C. Hamilton and D. A. Wille, "Acousto-Optic Diffraction in Optical Waveguides," Digest of Technical Papers, Topical Meeting on Integrated Optics, New Orleans, La., Jan. 21-24, 1974.

2. M. C. Hamilton, D. A. Wille and W. J. Miceli, "An Integrated Optical RF Spectrum Analyzer," IEEE 1976 Ultrasonic Symposium Proceedings, p 218, Annapolis, Md.

3. M. C. Hamilton, D. A. Wille and W. J. Miceli, "An Integrated Optical RF Spectrum Analyzer," Optical Eng. 16, 475 (1977).

4. D. B. Anderson, J. T. Boyd, M. C. Hamilton and R. R. August, "An Integrated Optical Approach to the Fourier Transform," IEEE J. Quantum Electronics, QE-13, 268 (1977).

5. D. B. Anderson and R. R. August, "Fourier Transform Signal Processing in an Integrated Optical Format," presented to the 1978 IEEE/OSA Conference on Laser and Electro-Optical Systems, February 8, 1978, San Diego, California.

6. L. J. Cutrona, E. N. Leith, C. J. Palermo and J. J. Procello, "Optical Data Processing and Filtering," IRE IT-6, 386 (1960).

7. J. T. Tippett, D. A. Berkowitz, L. C. Clapp, C. J. Koester and A. Vanderburgh, Editors, Optical and Electro-Optical Information Processing, MIT Press 1965.

8. K. Preston, Jr., Coherent Optical Computers, McGraw-Hill 1972.

9. D. B. Anderson, R. R. August and J. E. Coker, "Distributed-Feedback Double-Heterostructure GaAs Injection Laser with Fundamental Grating," Appl. Opt. 13, 2742 (1974).

10. D. B. Anderson, R. L. Davis, J. T. Boyd and R. R. August, "Comparison of Optical-Waveguide Lens Technologies," IEEE JQE, QE-13, No. 4, p 275, 1977.

REFERENCES (CONTINUED)

11. D. B. Anderson and R. R. August, "Progress in Waveguide Lenses for Integrated Optics," 1977 Intl. Conf. on Integrated Optics and Optical Communications (IOOC '77 Conf. Digest), Tokyo, July, 1977; and to be published, Transactions of IECE (Institute of Elect. & Commun. Engrs. of Japan), Part E (English Edition), March, 1978.

12. S. K. Yao, R. R. August and D. B. Anderson, "Surface Acousto-Optic Interaction on Nonpiezoelectric Substrates," 1976 IEEE Ultrasonics Symposium Proceedings, p. 439, 1976.

13. J. T. Boyd and C. L. Chen, "Integrated Optical Silicon Photodiode Array," Appl. Opt. 15, 1389 (1976).

14. D. B. Anderson, et. al., "Optical Waveguide Lens I," Final Technical Report, Rockwell International, AFAL-TR-76-54, Mar. 1976.

15. D. B. Anderson, et. al., "Optical Waveguide Lens II," Final Technical Report, Rockwell International, AFAL-TR-77-60, June, 1977.

16. J. T. Boyd and C. L. Chen, "Integrated Optical Waveguide and Charge Coupled Device Image Array," IEEE J. Quantum Electronics, QE-13, 282 (1977).

17. F. Zernike, "Luneburg Lens for Optical Waveguide Use," Optics Commun., Vol. 12, pp 379-381, 1974.

18. T. Tamir Ed., Integrated Optics, Springer-Verlag (1975) (Chapter 2).

19. M. Born and E. Wolfe, Principles of Optics, Pergamon Press, New York (1964).

20. R. K. Luneburg, The Mathematical Theory of Optics, University of California Press, Berkely, California (1954).

21. S. P. Morgan, "General Solution of the Luneburg Lens Problem, " J. Appl. Phys., Vol. 29, pp 1358-1369, 1958.

REFERENCES (CONTINUED)

22. W. H. Southwell, "Inhomogeneous Optical Waveguide Lens Analysis," J. OSA, 67, p. 1004, 1977.

23. W. H. Southwell, "Index Profiles for Generalized Luneburg Lenses and their use with Planar Optical Waveguides," J. OSA, 67, p 1010, 1977.

☆U.S.Government Printing Office: 1978 — 657-002/269